University of Strathclyde Glasgow

Viscoelastic Thermally-Driven Flows in Microgravity

A thesis presented in fulfilment of the requirements

for the degree of Doctor of Philosophy

by

Alessio Boaro

James Weir Fluids Laboratory

Department of Mechanical & Aerospace Engineering

University of Strathclyde, Glasgow

2022

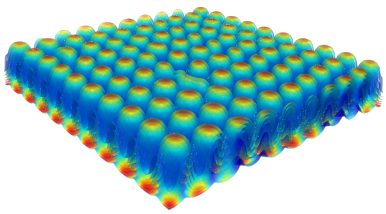

James Weir
Fluids Laboratory
University of Strathclyde

Declaration

This thesis is the result of the author's original research. It has been composed by the author and has not been previously submitted for examination which has led to the award of a degree.

Alessio Boaro,

University of Strathclyde, 18th December 2022

To my mum...

Solo una crescente efficacia nello spiegare consente una crescente capacità di capire...

Only growing effectiveness in explaining allows an ever-increasing capacity to understand...

– Piero Angela

Research output

Journal Articles

[J1] Lappa, M. & Boaro, A. 'Rayleigh–Bénard convection in viscoelastic liquid bridges'. In: *Journal of Fluid Mechanics* 904 (2020), A2. DOI: 10.1017/jfm.2020.608

[J2] Boaro, A. & Lappa, M. 'Multicellular states of viscoelastic thermovibrational convection in a square cavity'. In: *Physics of Fluids* 33.3 (2021), p. 033105. DOI: 10.1063/5.0041226. eprint: https://doi.org/10.1063/5.0041226. URL: https://doi.org/10.1063/5.0041226 [*Editor's Pick*]

[J3] Boaro, A. & Lappa, M. 'Competition of overstability and stabilizing effects in viscoelastic thermovibrational flow'. In: *Phys. Rev. E* 104 (2 Aug. 2021), p. 025102. DOI: 10.1103/PhysRevE.104.025102. URL: https://link.aps.org/doi/10.1103/PhysRevE.104.025102

[J4] Lappa, M. & Boaro, A. 'Viscoelastic Thermovibrational Flow Driven by Sinusoidal and Pulse (Square) Waves'. In: *Fluids* 6.9 (2021). ISSN: 2311-5521. DOI: 10.3390/fluids6090311. URL: https://www.mdpi.com/2311-5521/6/9/311

[J5] Lappa, M., Burel, T., Kerr, M., Crewdson, G., Boaro, A., Capobianchi, P., Bonnieu, S. V., Murphy, L., Randall, P. & Hens, S. 'Particle Vibration, an Instrument to Study Particle Accumulation Structures On Board the International Space Station'. In: *Microgravity Science and Technology* 34.3 (May 2022). DOI: 10.1007/s12217-022-09939-2

[J6] Boaro, A. & Lappa, M. 'On the competition of transverse and longitudinal modes of Marangoni convection in a three-dimensional layer of viscoelastic fluid'. In: *Physics of Fluids* 34.12 (Dec. 2022), p. 123103. DOI: 10.1063/5.0131461

[J7] Boaro, A., MacDowall, G. & Lappa, M. 'The symmetry properties and bifurcations of viscoelastic thermovibrational convection in a square cavity'. In: Ready for submission (2022)

Conference Papers

[C1] Crewdson, G., Boaro, A., Kerr, M. & Lappa, M. 'Supporting an ISS experiment as PhD students: a case study of the PARTICLE VIBRATION project'. In: *Proceedings of the 4th Symposium on Space Educational Activities*. Symposium on Space Educational Activities. 4th Symposium on Space Educational Activities, SSEA 2022 ; Conference date: 27-04-2022 Through 29-04-2022. SSEA, May 2022. doi: 10.5821/conference-9788419184405.017

Abstract

In the present thesis, non-linear and time-dependent numerical simulations are used to investigate the possible convective states of a specific category of non-Newtonian fluids under microgravity conditions, namely, the so-called Boger liquids. The "typical" microgravity phenomena examined include flows induced by vibrations and surface-tension in the presence of an imposed temperature gradient. The considered fluids are modelled using the classical Oldroyd-B model. However, the more sophisticated FENE-CR (Chilcott–Rallison finitely extensible nonlinear elastic) constitutive paradigm is also exploited to relax some of the mathematical difficulties inherent to this class of problems. A specific strategy of attack is implemented to clarify the flow dynamics, with situations of increasing complexity being analysed as the thesis progresses. First, thermovibrational flow is considered in a 2D square cavity, and it is shown that the relationship between the characteristic time scales (diffusivity, fluid elastic relaxation, and the period of vibrations) of these phenomena can lead to a kaleidoscope of states, which differ regarding the symmetry properties and the related spatiotemporal behaviours. Moreover, the fluid response in terms of hierarchy of bifurcations is extremely sensitive to the direction of vibrations. In all cases, an interesting parallelism can be drawn with respect to certain multi-component mechanical systems that undergo resonances and anti-resonances. When the constraint of two-dimensionality is removed and the flow is allowed to develop in an unbounded domain (infinite layer), very interesting patterns emerge, which are reminiscent of the superlattice structures typical of "complex order" in fluid-dynamics. The onset of thermovibrational convection in these cases occurs for values of the control parameter which are one order of magnitude smaller than the equivalent threshold to be exceeded in the companion Newtonian case, thereby lending evidence to the applicability of the concept of overstability to these circumstances. A

strong decrease of the critical parameter needed to produce a bifurcation also occurs in the Marangoni (thermocapillary) flow case. Rather than being driven by a complex interplay of harmonic and sub-harmonic modes of convection found in the thermovibrational case, however, the complex hierarchy of states displayed by Marangoni flow from an initial laminar condition up to fully developed chaos depends on the interplay between transverse (two-dimensional) and longitudinal (three-dimensional) disturbances. Moreover, in this case, elastic and inertial turbulence can coexist if specific conditions are considered.

Contents

List of Figures

List of Tables

List of Symbols

Dimensionless Groups

Γ	Non-dimensional amplitude of the external vibrational acceleration
Ω	Non-dimensional angular frequency of the external vibrations
Σ	Ratio beteween relaxations time and period of vibration
ϑ	Elasticity number
ξ	Solvent-to-total viscosity ratio
ζ	Viscosity ratio
AR	Aspect Ratio
Bi	Biot number
Gs	Gershuni number
Ma	Marangoni number
Nu	Area-averaged Nusselt number
$\overline{Nu}$	Area and time-averaged Nusselt number
Pr	Prandtl number
Ra	Rayleigh number
Ra_ω	Vibrational Rayleigh number

Physics Constants

α	Thermal diffusivity
β	Thermal expansion coeffitient
η_0	Dynamic viscosity of the Newtonian fluid
η_0	Total dynamic viscosity of the viscoelastic fluid
η_p	Dynamic viscosity of the polymer
η_s	Dynamic viscosity of the solvent
λ	Relaxation time of the visco-elastic fluid
ν	Kinematic viscosity
ρ	Density
σ	Surface tension
σ_T	Derivative of surface tension with respect to the temperature
c_p	Specific heat at constat pressure
g	Gravitational acceleration
h	Convective heat tranfer coefficient
k	Thermal conductivity

Other Symbols

$\boldsymbol{\gamma}$	Dimensional amplitude vector of the external vibrational acceleration
$\boldsymbol{\tau}$	Newtonian total stress tensor
$\boldsymbol{\tau}_s$	Dissipative part of the Newtonian total stress tensor
$\tilde{\boldsymbol{\tau}}$	Viscoelastic estra-stress tensor

$\boldsymbol{\tau}_\sigma$	Marangoni stress
$\mathbf{A}$	Conformation tensor
$\mathbf{g}$	Gravitational acceleration vector
$\mathbf{I}$	Unit tensor
$\mathbf{n}_\Omega$	Unit vector describing the direction of the vibrations
$\hat{\mathbf{n}}$	Unit vector orthogonal to the free surface
$\mathbf{q}$	Dumbbell spring end-to-end vector
$\mathbf{u}$	Velocity
ω	Dimensional angular frequency of the external vibrations
ε	Growth rate
ϖ	Flow field (usually velocity) angular frequency
A_{u_y}	Amplitude of the velocity signal's y component
b	Dimensional amplitude of the vibration's dispacement
EE	Global elasitic energy
$\overline{EE}$	Time-averaged global elastic energy
$\mathcal{I}$	Time interval, in CHAPTER 8 it reffers to an Integral quantity
K	Global kinetic energy
$\overline{K}$	Time-averaged global kinetic energy
ℓ	Generic characteristic length
L^2	Finite extensibility of the molecule
p	Pressure

$\mathcal{P}$	Power Spectral Density (PSD)
r	Reduced vibrrational Rayleigh number
T	Temperature
$T_{\mathcal{Q}}$	Oscillation period of the quantity $\mathcal{Q}$. If $\mathcal{Q} = \Omega$ (ω) it is reffered to the dimensionless (dimensional) vibration's period
t	Time
u_x, u_y, u_z	Components of $\mathbf{u}$ in x, y and z direction respectively

Subscripts

cr	Critical parameter
ref	Quantity at the reference temperature
c	Cold
h	Hot

Superscripts

T	Transpose operator
*	Indicates that the quantity is dimensional

Acknowledgement

Arriving at the end of this journey has certainly been a big challenge, doing it through a global pandemic and far away from home has not made things easier. Luckily, I am surrounded by amazing people that helped and sometimes pushed me not to give up.

The first big thanks go to my first supervisor, Dr Marcello Lappa, that has always believed in me and given me this life-changing opportunity. His precious advice and his love for science and research will always be an important part of my professional future. Another big thanks also go to my second supervisor Dr Mónica S. N. Oliveira, for the precious advice about viscoelastic fluid modelling techniques.

If finishing a PhD is difficult, starting it in the right way is absolutely crucial. In this regard, my thanks go to Dr Thomas Burel and Dr Paolo Capobianchi, that helped me get familiar with OpenFOAM and supported me in the first stage of this journey.

Of course, a PhD is not only about doing research but is also a beautiful opportunity to connect with other people. Even in this regard, I have been lucky to find great friends and office mates. Particularly, I would like to thank (in sparse order) Alessia, Philipp, Sarah, Jamie, Kieran, Miguel, Ronnie, and Silvia for making my days lighter. A special thanks go to Georgie, the other T-Paola PhD student and dear friend. Sometimes a long break and a laugh are maybe more important than good advice. Last but not least, I would like to thank Nadine, our long lockdown walks and silly chats have helped me finish this PhD more than you can expect.

Apart from the uni pals, I am extremely grateful to my lovely friends Pavel, Pier, Jox, Jose, Luca, Kyle and Fede. You are one of the main reasons I chose Glasgow as the place I want to live. It is a joy to be around you.

Although during the past three years it was not possible to see my Italian friends, they have always been with me. I would like to thank (in sparse order) Patrick, Cate L., Ale, Vale, Ila, Nick, Lau, Lisa, Cate S., Giulio, Sara, Chiara, Elisa, Gerghi, Pischio, Giacomo and Cristian for having been the amazing friends you are for more than 10 years. Even if the distance divides us, we will always be there for each other, no-matters what!

A special thanks go to my beautiful partner. You have changed my life more than a degree will ever do. You supported me in the toughest moments and showed me that, if I start enjoying life a bit more, everything will go better. Thank you for that.

Last but not least, the biggest thanks go to my lovely mum. You sacrificed a lot to allow me to be here and showed me what unconditional love means. I really hope that this work will make you proud of me!

Glasgow, 18th December 2022 Alessio Boaro

Thesis Aims and Scope

Our everyday experience suggests that if we heat a fluid, e.g. a pot of water, it will start moving *naturally* thanks to the energy provided by the heat source. This phenomenon is known as buoyancy or thermogravitational (often simply natural) convection. The mechanism behind this is relatively simple. The fluid closer to the heat source increases its temperature, expands, and in turn, its density decreases. The warmer and lighter fluid will become "buoyant" and, therefore, rise inside the surrounding colder fluid. As a consequence, the colder fluid will start sinking. As highlighted in Ref. [9], the buoyancy of the hotter fluid is resisted by the viscosity, which generates drag between fluid parcels with different density, and by thermal conductivity, which reduces the parcels' temperature (and density) difference.

Although the heat source is necessary to enable such a mechanism, it is insufficient to generate movement. Indeed, the other ingredient to establish buoyancy convection is the gravitational field (or, in other words, a steady acceleration), without which the idea of "heavier" or "lighter" would not make sense. Therefore, heating the same fluid container in space and on-ground will produce considerably different results.

Before introducing a fascinating example that shows how gravity can affect convective flows, let us introduce a new concept, i.e., *microgravity*. Microgravity can be defined as that condition in which a body appears to be weightless or, in other words, the effect of gravity is considerably reduced [10]. It is worth noting that microgravity or μg conditions occur in spacecraft orbiting the Earth, such as the International Space Station (ISS), just because they are in free-fall on the planet. Similarly, temporary μg conditions can be obtained on Earth using parabolic flights or drop towers.

At this point, let us introduce a trivial and relatable example that shows how gravity can affect convective flow. Particularly, let us focus on the behaviour of an open flame. A

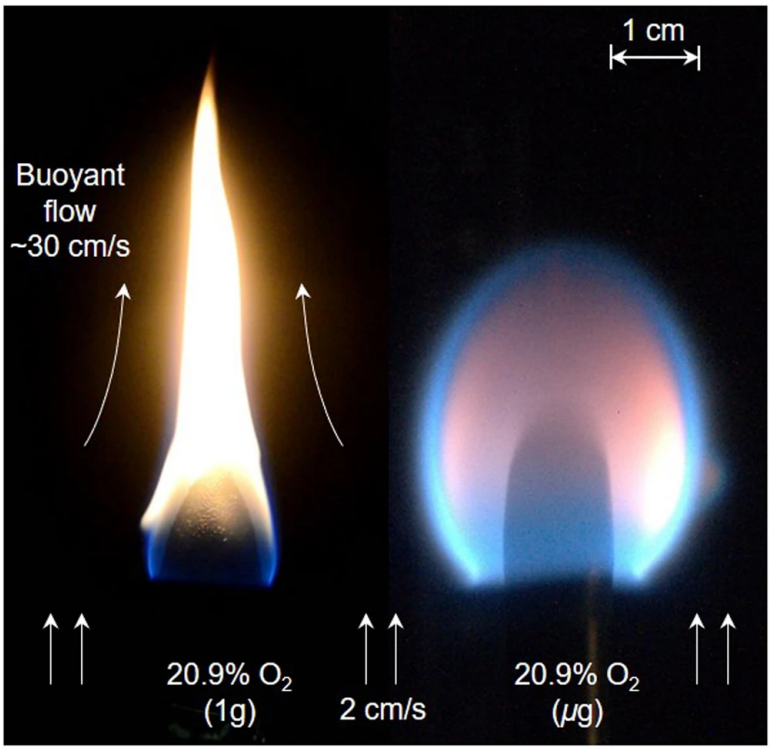

Figure 1: Comparison of a flame in normal gravity (left) and microgravity (right). Reproduced after Link et al., 2018 [11].

flame is the visible part of an exothermic chemical reaction, i.e. combustion. It involves an oxidant and an oxidiser. Let us consider that the oxidiser is oxygen and suppose ourselves to be in a typical gravity environment. Buoyancy convection is the fundamental mechanism through which the chemical reaction is sustained and enhanced. Once the combustion starts, the hotter oxidised fluid, rich in carbon dioxide, will become buoyant and rise in the surrounding colder air. Therefore, combustion exhibits a convective flow. This promotes the flow of colder and oxygen-rich air towards the flame.

Now, what happens to a flame in microgravity? In order to answer this question, several experiments were carried out. In particular, Figure 1 reports the result of a recent experiment carried out on the ISS [11]. While the flame has the typical elongated shape in the case of buoyant flow, it is rounded and symmetric in microgravity. Moreover, in microgravity, the flame's temperature is also considerably colder. All these three features can be ascribed to the lack of mixing between oxygen and the oxidant. Indeed, in the

absence of gravity, the only mixing effect is due to diffusion (known to be an inefficient mixing mechanism).

Although the flame example has been chosen for its immediate visual impact, it is easy to imagine that, similarly to the flame, other technological processes involving heated fluid will be affected in the absence of gravity.

The first experiments involving differentially heated fluids in microgravity revealed the existence of two different phenomena. Although in the absence of gravity, there is no buoyancy force acting on the fluid volume, scientists observed the presence of convective flow in specific problems characterised by a free-surface (see chapter 1 & 2 for a formal definition). This phenomenon happens because certain fluids' surface tension displays a dependency on temperature, similar to what happens to the density of a fluid in a gravitational field. The gradient of surface tension produces the so-called *thermocapillary* or *Marangoni* flow. Of course, this type of convection is present in normal gravity too, however, since the buoyancy force is much stronger, its effect has always been regarded as an external disturbance rather than an internal phenomenon. Thanks to these microgravity experiments, the "disturbance" observed on Earth was finally understood. The control of thermocapillary flows made it possible to perfect technological processes on Earth, increasing the quality of the final products (usually semiconductor crystals).

Thermocapillary convection arises only if there is a free surface. However, the scientists observed some residual convection even in closed containers. The cause of this phenomenon is the so-called *g-jitters*, i.e., vibrations induced on the spacecraft by crew and equipment operations, and aero-dynamical, and aero-mechanical forces [12]. In this case, we talk about *thermovibrational* convection. The flow is still driven by a difference in density, hence by buoyancy force. Notably, it is no longer due to the steady gravitational acceleration but rather to the time-dependent acceleration induced by the vibrations. Therefore, vibrations can give rise to an intrinsically time-dependent convective flow.

In a time when humans are more ready than ever to explore space, a proper understanding of convection in microgravity is fundamental. For this reason, space agencies

all around the world are investing considerable amount of resources to investigate how classical manufacturing techniques employed on Earth could be affected in microgravity or reduced gravity environments. To do so, over the years, several ad-hoc experiments were proposed.

Although experiments are necessary to understand the nature of certain instability, they are extremely expensive, require long preparation, and overall are limited to a particular type of "compatible" fluids. For this reason, in parallel to the development of experiments, scientists saw numerical and analytical methods as an excellent alternative (or rather an extra tool) for investigating convection in microgravity. Numerical tools, known as CFD (Computational Fluid Dynamics) methods, are used to identify significant set of parameters to be investigated experimentally, and in turn, the experiment can help the corroboration and improvement of CFD codes.

This research work should be regarded as an application of numerical techniques to open a new path of inquiry for future novel experimental investigations. Indeed, part of this work belongs to the Particle Vibration project, also known as T-Paola (Thermovibrationally-driven Particle self-Assembly and Ordering mechanisms in Low grAvity) [5, 8].

The T-Paola project

The T-Paola project is a collaboration between the University of Strathclyde, the UK Space Agency and ESA (European Space Agency) and aims to perform multiphase fluid dynamic experiments onboard the ISS.

Numerical simulations showed that if we consider a cavity (see Figure 2) filled with a Newtonian fluid, differentially heated, horizontally vibrated and seeded with solid particles having a density different from the one of the fluid medium, the particles can naturally accumulate and form well-ordered structures.

For this phenomenon to arise, microgravity is fundamental. Indeed, in normal gravity conditions, the particles will accumulate on the bottom (top) of the cavity since they are heavier (lighter) than the surrounding fluid. Replacing the gravitational force with vibrations allows the particles to aggregate in self-assembled structures.

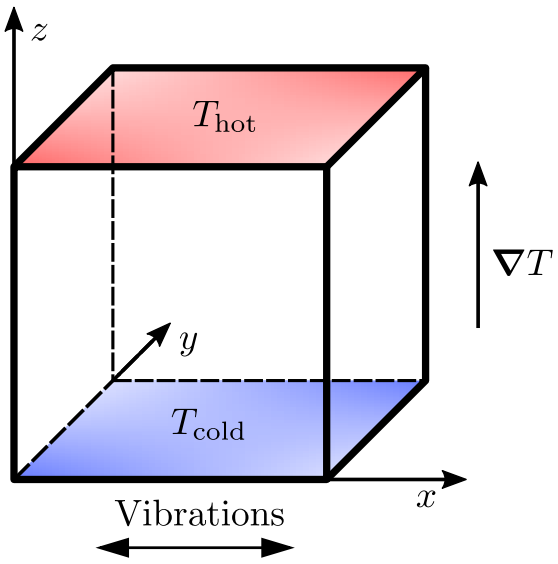

Figure 2: Sketch of the geometry and schematisation of the T-Paola experiment.

It is worth highlighting that, although thermovibrational convection was initially discovered thanks to the g-jitters acting on the spacecraft, for the case of T-Paola the vibrations are "artificially" imposed through a linear motor that generates a sinusoidal displacement. The use of well-defined vibrations enables complete control of the thermally driven flow and, in turn, the final particle structure.

In addition to the experiment, T-Paola also aims to expand the knowledge about thermovibrational flows. Indeed, this specific category of thermal convection has not enjoyed the same attention as its stationary counterpart (thermogravitational convection). This PhD project started paving the way for new microgravity convection experiments involving categories of fluid that do not follow the standard Newtonian behaviour.

Research question

Although experimental and numerical results exist for "standard" Newtonian fluid, i.e. a fluid in which the viscous stress arising because of the fluid motion is proportional to the local strain rate, far too little attention has been paid to fluids that do not follow a Newtonian behaviour. These fluids are widespread in industrial and biotechnological environments. However, they are also characterised by an intrinsic complexity in being represented mathematically. Moreover, this mathematical model cannot easily be integrated numerically due to instability problems that will be discussed later in this work. These facts are part of the reason why their investigation in the context of convective flows has not reached the same maturity as the Newtonian companion. Indeed, focusing on the sub-category of fluids analysed in this thesis, that is viscoelastic fluids, namely, liquids that can store or release elastic energy and, accordingly, can be subjected to

stresses even in the complete absence of velocity gradients, there are just a few works dealing with microgravity convection, while the case of standard buoyancy convection has been tackled mostly in simplified situations and with less-advanced numerical techniques.

For these reasons, this thesis, using non-linear and time-dependent numerical simulations, will analyse how microgravity convective flows (thermovibrational and thermocapillary) manifest themselves in a specific class of viscoelastic fluids known as Boger fluids.

More specifically, this thesis will answer the following questions:

- What is the patterning and temporal behaviour of viscoelastic convection in microgravity?
- Can superlattices-like structures (a situation where the convective disturbances are uniformly distributed in the domain and form well ordered structures) form in microgravity when viscoelastic fluids are considered?
- What is the effect of the "shape" of the vibrational waves on the convective disturbances dynamics?
- How do the fluid elasticity and the time-dependent forces (vibrations) interact with each other?
- Do the classical thermocapillary instabilities seen in Newtonian fluids manifest themselves in viscoelastic liquids?
- Can the concept of overstability originally proposed for thermogravitational convection in viscoelastic fluids be extended to thermovibrational and thermocapillary flows?

Thesis structure

In order to answer these questions, the following structure will be adopted:

Chapter 1 presents a literature review of convective instability in Newtonian and viscoelastic fluids.

Chapter 2 explains the microscopic derivation of the balance equations used to model Newtonian and viscoelastic fluids, along with the mathematical models to study thermal convection in microgravity. This chapter also introduces the non-dimensional balance equations and related non-dimensional numbers.

Chapter 3 introduces the numerical framework employed to solve the balance equations and related boundary conditions. Attention is paid to the stabilising techniques employed for the viscoelastic models' time-marching procedure.

Chapter 4 tackles the problem of thermovibrational convection in a square cavity subjected to vibrations orthogonal to the temperature gradient. The results for viscoelastic fluids are compared with their Newtonian counterpart.

Chapter 5 investigates the natural counterpart of the problem analysed in the previous chapter, i.e., thermovibrational convection in a square cavity subjected to vibrations parallel to the temperature gradient.

Chapter 6 explores the patterning evolution in an infinite layer of viscoelastic fluid vertically vibrated by sinusoidal vibrations (vibrations parallel to the temperature gradient).

Chapter 7 compares how thermovibrational convection manifests itself in an infinite layer when the vibrational waves' nature (or shape) is changed.

Chapter 8 studies thermocapillary convection in 2D and 3D finite layers of viscoelastic fluids.

Chapter 9 discusses some final remarks and ideas for future work.

Part I

Context and Methods

Chapter 1

Theoretical Background & Literature Review

This chapter presents an introduction to the general topic of thermal convection. Particularly, after a brief introduction on the instabilities affecting standard buoyancy or *thermogravitational* convection in more conventional (Newtonian) fluids, the chapter will focus on how convection can manifest itself in microgravity conditions. Eventually, it presents some insight into convective flows in viscoelastic fluids.

1.1 Thermogravitational Convection

In the Thesis aims and scope chapter, the fundamental mechanism that sustains thermogravitational convection has been introduced. Starting from those notions, this section aims to categorise different types of convective flows and explore their dynamic behaviour, i.e. understand the system's bifurcations and how they can affect the flow patterning distribution.

Let us start by introducing a dichotomy that is a common denominator of all the types of convective flows analysed in this thesis, i.e. the relative position between the temperature gradient and the direction of the acceleration (or the unit vector orthogonal to the free surface for thermocapillary flows). Particularly, the two vectors can be parallel or orthogonal.

In the framework of thermogravitational convection, we define accordingly two classes of flows, namely Rayleigh-Bénard and Hadley flows, when the vectors are parallel or orthogonal, respectively. As will be discussed in the following, although a density gradient drives both flows, the hierarchy of bifurcation is considerably different.

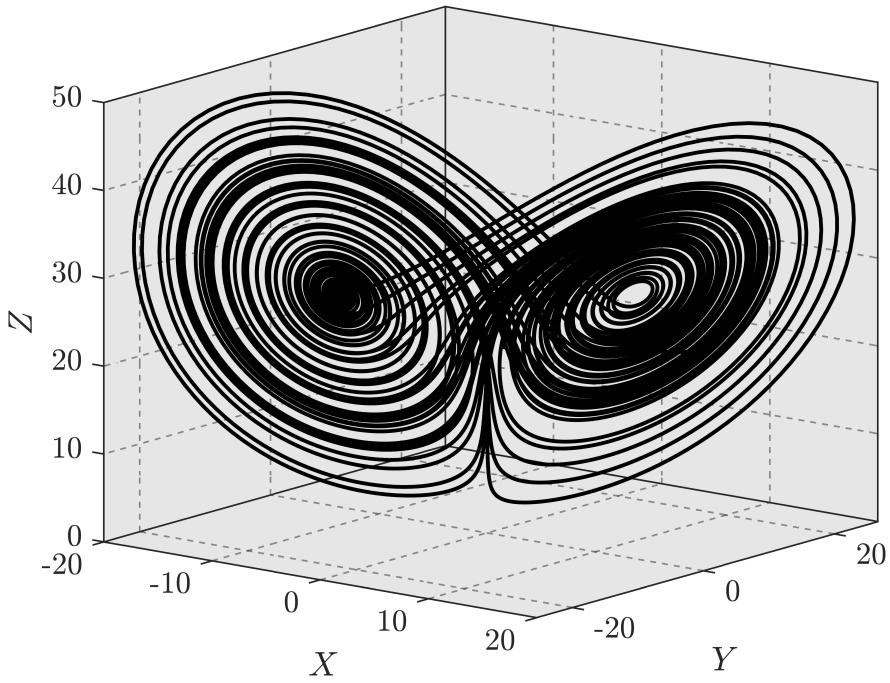

Figure 1.1: Lorenz (strange) attractor. X is the amplitude of convective, Y the temperature difference between rising and descending currents, and Z the temperature deviation with respect to a linear temperature profile.

1.1.1 Rayleigh-Bénard convection

In fluid dynamics Rayleigh-Bénard convection refers to convective flow arising in a fluid geometry when it is heated from below. This phenomenon takes its name from the two scientists that originally studied it theoretically (Lord Rayleigh, [13]) and experimentally (Bénard, [14, 15]).

The Rayleigh-Bénard archetype has enjoyed widespread popularity among the scientific community due to the intrinsic simplicity in modelling, simulating and investigating it experimentally, along with the complexity of dynamics that the system can undergo to [10, 16]. As an example, Rayleigh-Bénard systems are at the root of the first studies involving a systematic investigation of chaos. Indeed, the work of Lorenz (1963) [17], which is generally considered the precursor of the studies in non-linear dynamics and chaos, analysed a Rayleigh-Bénard system in the context of atmospheric flows. There, the non-linear behaviour of the system was visualised for the first time in the shape of a *strange attractor*, see Figure 1.1.

Apart from the strictly theoretical interest that this class of flows has attracted, Rayleigh-Bénard convection also has several industrial applications, spanning from producing semiconductors to heating private houses. There, thermal Rayleigh-Bénard convection can arise in complex geometry and non-straightforward configurations.

Nonetheless, in the context of this work, this section will primarily focus on the hierarchy of bifurcation the system can undergo and the related patterning configuration properties, in the specific case of two simple configurations, i.e. the infinite layer and the square cavity.

Let us introduce a few non-dimensional parameters that are fundamental to make this discussion rigorous, i.e. the Prandtl (Pr) and the Rayleigh (Ra) numbers. From a formal (mathematical) point of view, they will be derived and defined in section 2.3, however, here, it is worth recalling that Pr represents the ratio between momentum diffusivity (kinematic viscosity) and thermal diffusivity, while Ra is the ratio between buoyancy and viscous forces. It is also worth noting that while Pr solely depends on the fluid characteristics, Ra also depends on environmental properties, i.e. characteristic length scale of the fluid geometry, level of gravity and difference of temperature applied to the system (see eq. (2.76)).

In a Rayleigh-Bénard system, if Ra does not exceed a specific threshold, the dissipative effect of the viscosity and the stabilising effect of the thermal conductivity become prevailing, and the fluid will display a linearly distributed temperature profile. The critical value of the Rayleigh number ($Ra_{\mathrm{cr},1}$) for which the convective instabilities are sustained depends on the boundary conditions applied to the heated sides of the geometry. Lord Rayleigh, in its pioneering work [13], using the idealised *free-free* boundary conditions, i.e. both the heated sides are stress-free, estimated that for an infinite layer the critical Rayleigh number is $Ra_{\mathrm{cr},1} = 27/4\pi^4 \approx 657.5$. Although a geometry with top and bottom stress-free boundaries does not have a physical meaning, this simplification allowed Lord Rayleigh to find an analytical solution to this problem.

If only the top boundary is stress-free, i.e. the case corresponding to analysing a layer of fluid with a free-surface, the value of the critical Rayleigh number becomes 1101. Finally, if both the boundaries are rigid $Ra_{\mathrm{cr},1} = 1707$. This result was originally

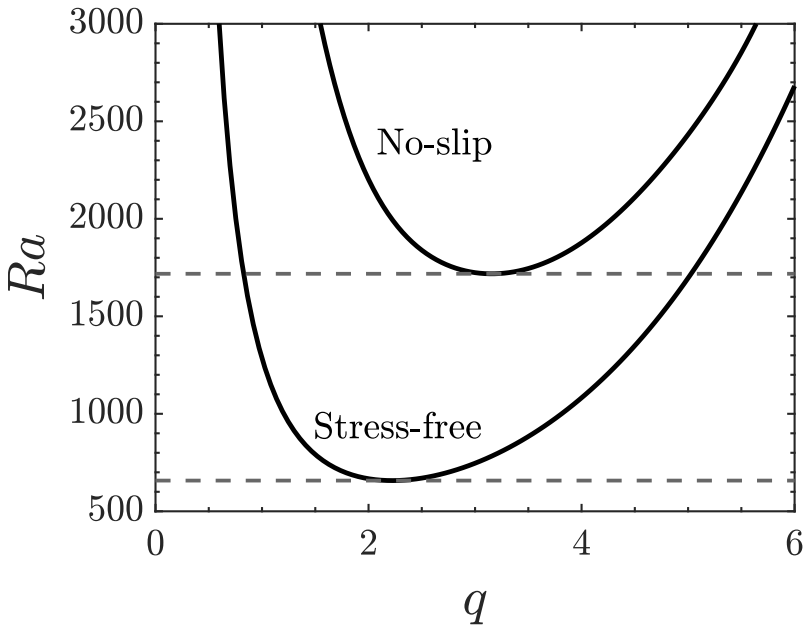

Figure 1.2: Marginal stability curves for Rayleigh-Bénard convection in an infinite layer for stress-free and no-slip boundary conditions. q represents the horizontal wave number at the onset of convection.

proposed in 1926 by Jeffreys [18, 19], where with a semi-empirical numerical approach he extrapolated this critical value.

However, it was only in the early 60s that light was shed on the nature of these instabilities. Indeed, thanks to the availability of more powerful computers, it was possible to carry out accurate linear and weakly non-linear stability analyses (see Figure 1.2 for the marginal curves). It was found that both for stress-free and no-slip conditions, the first bifurcation is stationary, i.e. the convective flow is steady after the critical threshold is exceeded [20–22].

Interestingly, the value of $Ra_{\mathrm{cr},1}$ does not depend on the Prandtl number, i.e. it does not depend on the particular type of fluid selected for the experiment but only on external factors such as the domain walls nature, the geometrical aspect ratios, and the thermal boundary conditions. The studies mentioned above also predicted that for the case of solid boundaries, the flow patterning configuration resembles straight parallel convective rolls (see, e.g. Figure 1.3a and c).

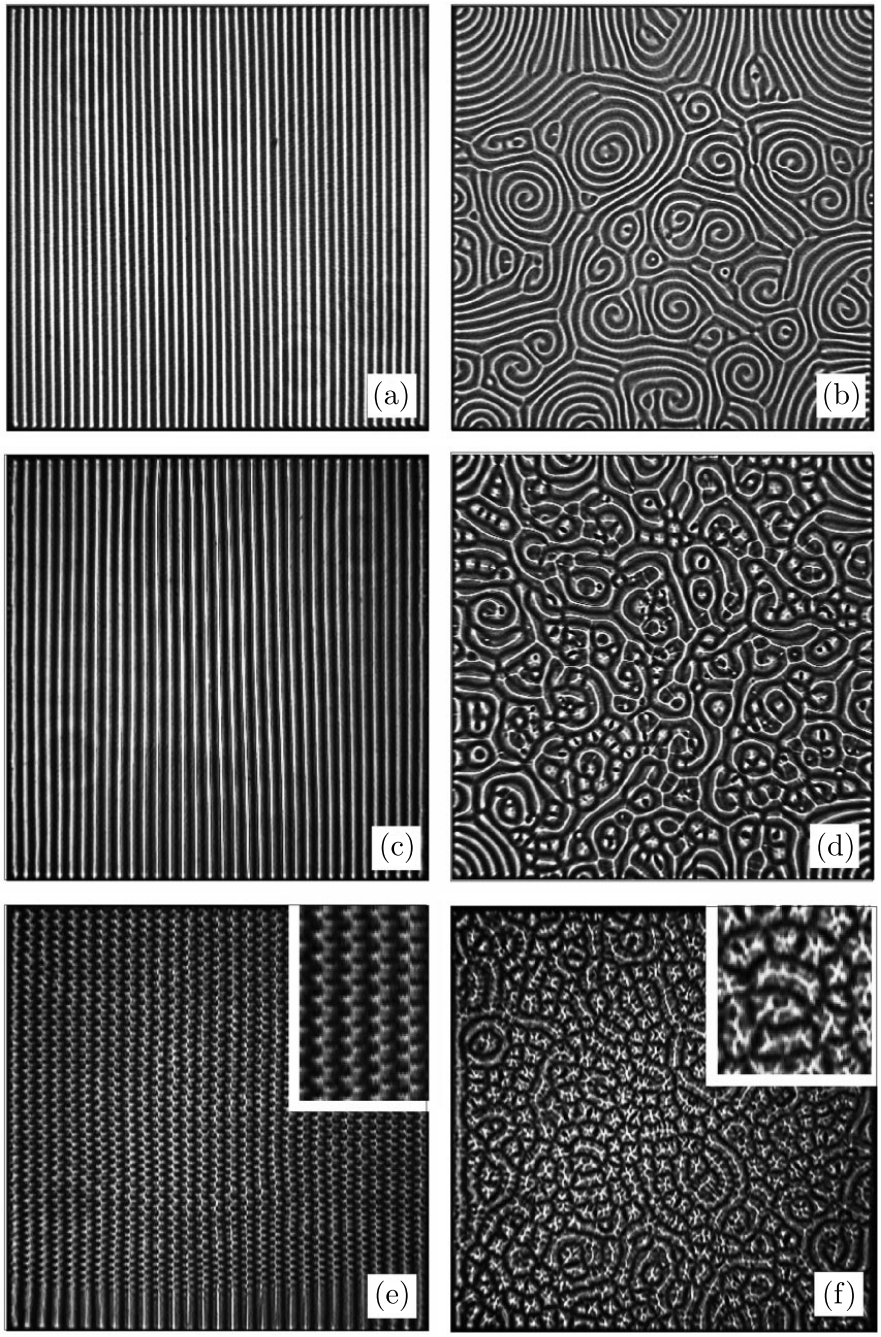

Figure 1.3: Example of possible patterning configuration in a Rayleigh-Bénardsystem. The left column represents the straight parallel convective rolls, while the right column represents spiral defect chaos. Stationary configurations (a) to (d) and oscillatory convection (e) and (f). Reprinted with permission from Cakmur, R. V., Egolf, D. A., Plapp, B. B. & Bodenschatz, E. 'Bistability and Competition of Spatiotemporal Chaotic and Fixed Point Attractors in Rayleigh-Bénard Convection'. In: *Phys. Rev. Lett.* 79 (10 Sept. 1997), pp. 1853–1856. doi: 10.1103/PhysRevLett.79.1853. url: https://link.aps.org/doi/10.1103/PhysRevLett.79.1853. Copyright 1997 by the American Physical Society.

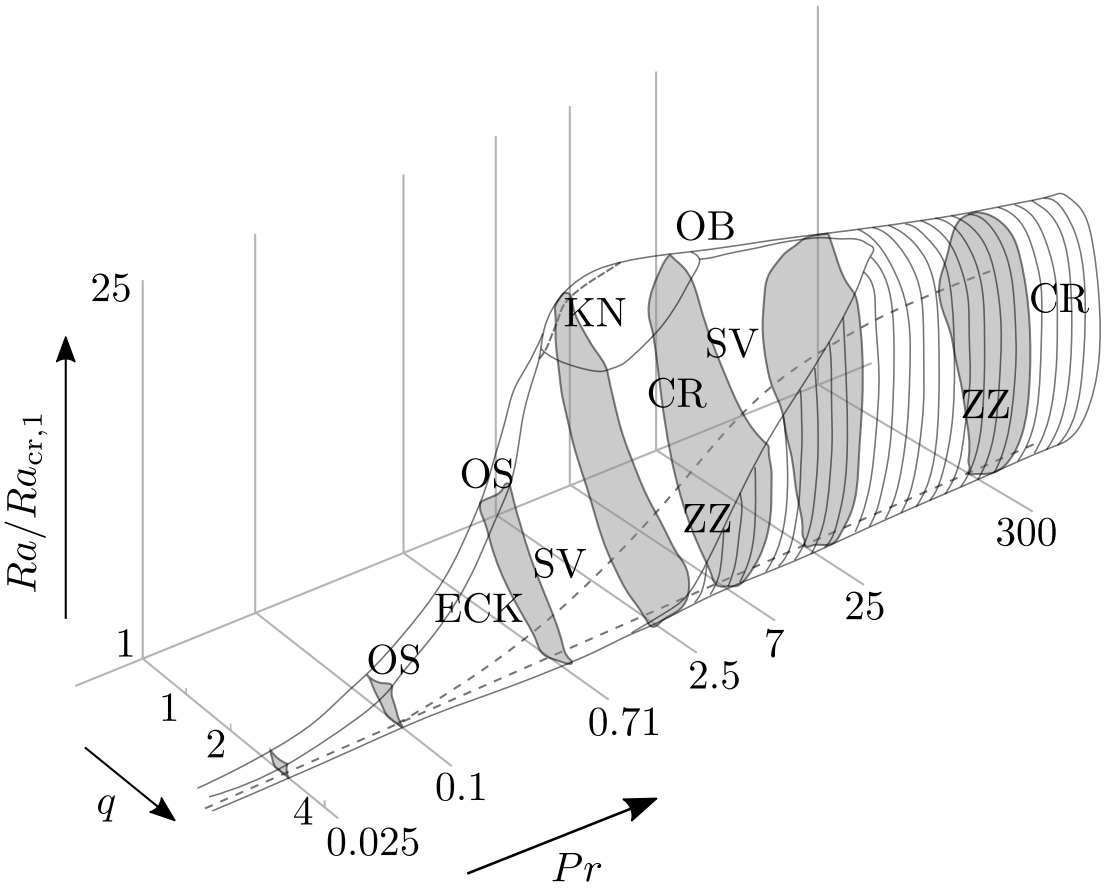

Figure 1.4: Busse balloon in three dimensions. The abbreviations outside the balloon indicate the Eckhaus instability (ECK), the oscillatory skewed varicose instability (SV), the cross-roll instability (CR), the oscillatory instability with travelling waves (OS), the zig-zag instability (ZZ), the knot instability (KN) and the oscillatory blob instability (OB). After Busse [26].

If starting from this stationary state Ra is further increased over a second critical boundary ($Ra_{\mathrm{cr},2}$), a myriad of states and patterning configurations become possible. In Figure 1.3 a few of these convective states are represented. This scenario is known as secondary modes of convection (see, e.g., Ref. [24, 25] for a complete classification of these modes) and, in this region of the parameter space, the flow field can also undergo a Hopf bifurcation, i.e., the flow becomes oscillatory. The value of $Ra_{\mathrm{cr},2}$ and the pattern that arises after the bifurcation strongly depends on the Prandtl number. This dependency can be summarised in the so-called *Busse balloon* [26], which is depicted in Figure 1.4.

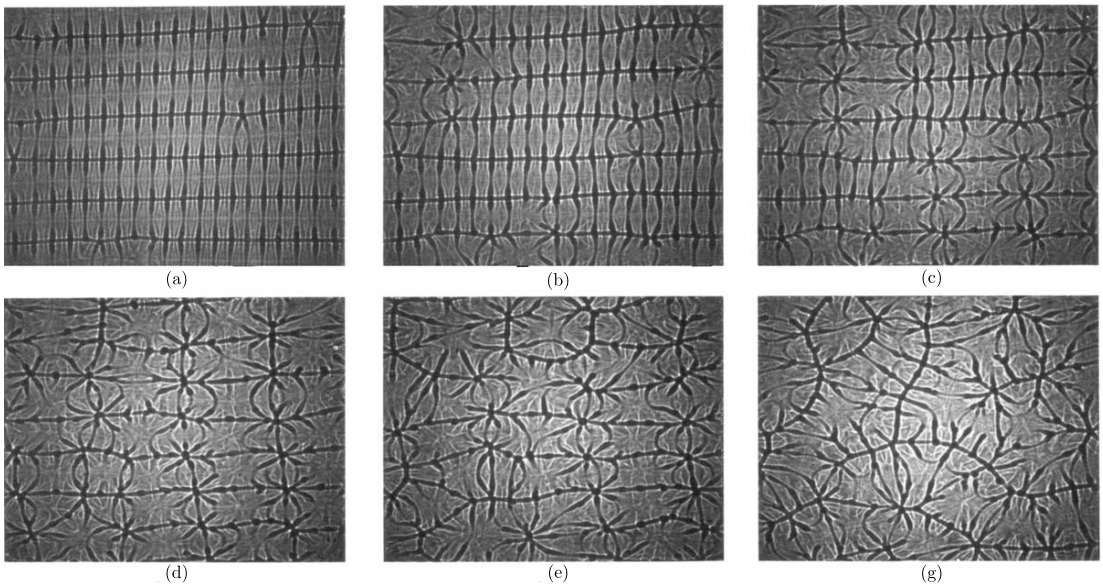

Figure 1.5: Transition form bimodal to spoke-pattern convection in a layer of fluid having $Pr = 63$. $Ra = 2.1 \times 10^6$ (a), and $Ra = 2.4 \times 10^6$ (b)-(f). The pattern becomes chaotic at the end of the transition (f). Reprinted with permission of Cambridge University Press from Ref. [27].

Interestingly, using this representation, it is evident that Pr does not affect the first stationary bifurcation. Indeed, comparing the "no-slip" curve of Figure 1.2 with the Busse balloon in Figure 1.4 we can observe that the critical wavenumber for the onset of convection is $q_c \approx 3.12$. Here, for $Ra = Ra_{\mathrm{cr},1}$ and regardless the value of Pr the bottom boundary of the Busse balloon can be drawn as a straight line ($q = q_c$). In this region of the parameter space, i.e. at the onset of convection, the diameter of the parallel rolls is $2\pi/q_c$. Inside the balloon, the rolls will change the diameter as a function of Ra and Pr, but overall, the parallel rolls pattern will remain stable. The solid lines of the balloon should be regarded as stability thresholds for the onset of the aforementioned secondary modes.

If Ra is further increased, a zoo of convection modes becomes possible. These modes are called tertiary and quaternary modes. As an example, Figure 1.5 reports [27] the transition between the so-called *bimodal* and *spoke-pattern* convection.

Until now, only infinite layers were considered, i.e. cases where the aspect ratio of the geometry is big enough so that the lateral walls have little impact on the flow field.

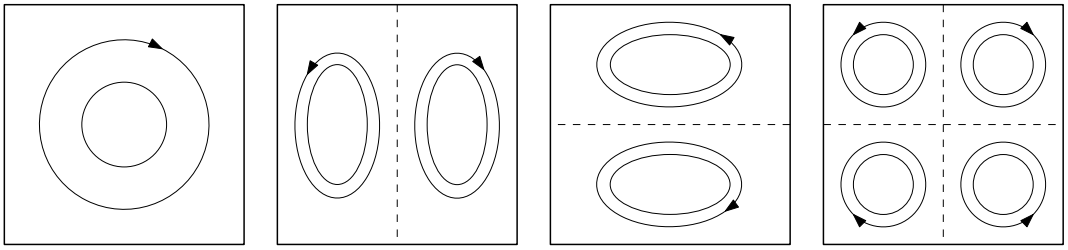

Figure 1.6: Categorisation of possible solutions of Rayleigh-Bénard convection in 2D finite enclosures in terms of related symmetries. **(aa)**: antisymmetric-antisymmetric mode, **(sa)**: symmetric-antisymmetric mode, **(as)**: antisymmetric-symmetric mode, **(ss)**: symmetric-symmetric mode.

However, as the reader might have realised, the type of boundaries has an important impact on the patterning configuration and critical threshold for the onset of convection.

Along with the archetype of the infinite layer, another geometrical model has enjoyed particular attention, i.e. the square cavity. For such a geometry, in the limiting case of 2D geometries and adiabatic side-walls, Kurzweg [28] first and Luijkx & Platten [29] later found that the critical Rayleigh number for the stationary bifurcation is $Ra_{\mathrm{cr},1} \approx 2585$. It is worth noting that the solid lateral boundaries have the effect of increasing the threshold for the onset of convection.

It was only Mizushima in 1995 [30] that carried out a proper categorisation of the symmetries that the flow field can display. In general, the distinct modes of convection allowed in a specific geometry can be identified a priori on the basis of the various possible symmetries that can be retained or broken by the emerging flow. For the square cavity, these are the reflection of the horizontal and vertical axis. The combination of these two properties can produce an additional possible solution, characterised by an even higher degree of symmetry, that is, the flow satisfying the so-called *centro-symmetry*. This makes the square geometry an ideal target to study many concurrent aspects. Based on these relatively simple arguments partially based on the earlier analysis by Mizushima [30], the set of possible modes relevant to the problems analysed in this work can immediately be partitioned into four fundamental classes (see Figure 1.6), namely:

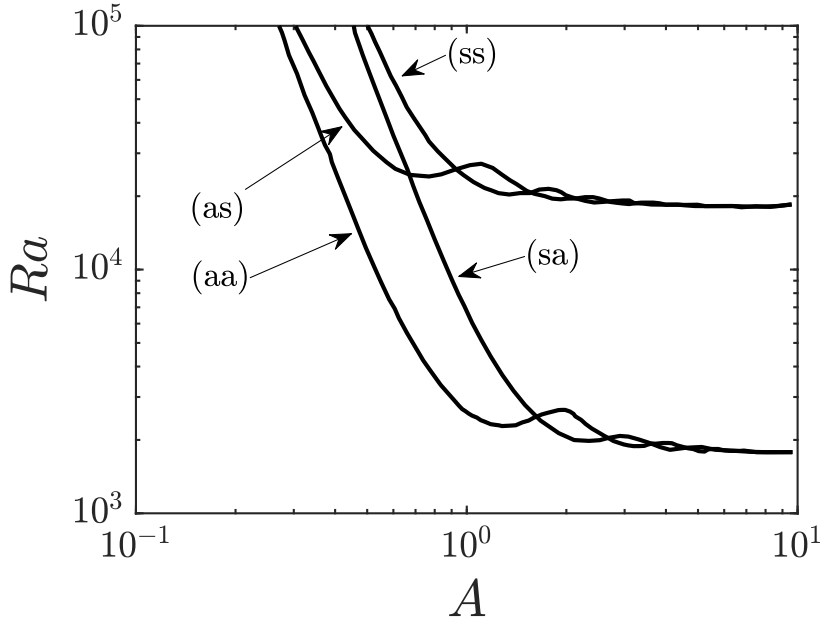

Figure 1.7: Critical Rayleigh number as a function of the enclosure aspect ratio (A = Horizontal length/depth) in the case of adiabatic sidewalls. After Mizushima, 1995 [30].

(aa) The antisymmetric-antisymmetric mode. Both the x- and y-symmetry are broken in this case, the flow typically displaying an odd number of rolls along both directions.

(sa) The symmetric-antisymmetric mode. Only the symmetry with respect to the (vertical) y axis is retained, the flow being typically characterised by an even number of rolls along the x and an odd number of rolls along y.

(as) The antisymmetric-symmetric mode. Only the symmetry with respect to the (horizontal) x axis is retained, the flow being typically characterised by an odd number of rolls along the x and an even number of rolls along y.

(ss) The symmetric-symmetric mode. This mode has an even number of vortex cells along both the x and y axes. It gives rise to a centro-symmetric configuration when the number of rolls along both the x and y directions is the same and to a columnar arrangement if the number of rolls along y is larger.

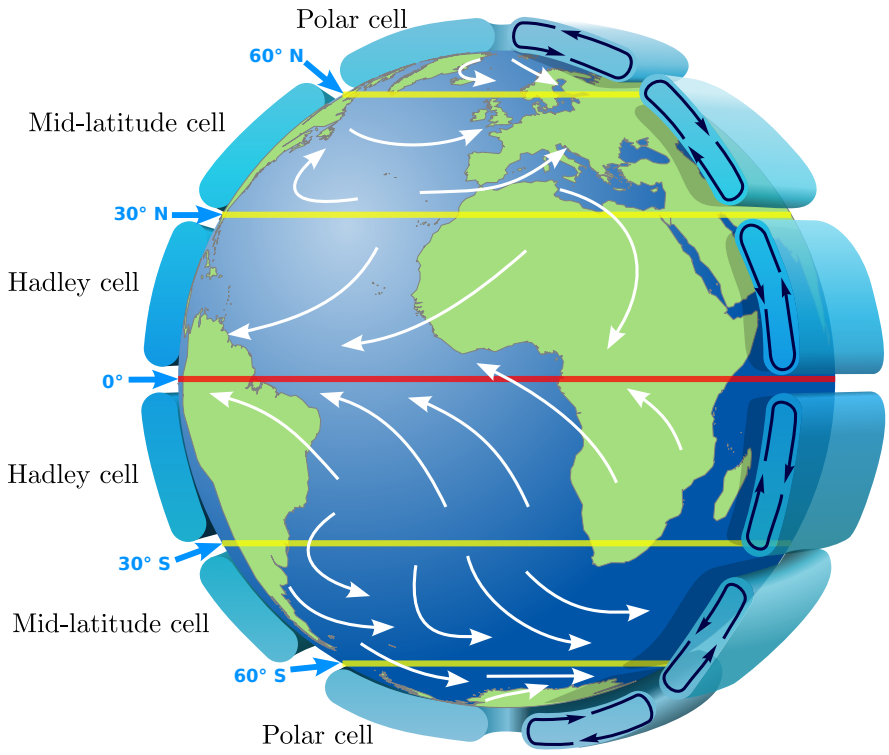

Figure 1.8: Schematisation of air recirculation between the equators (hot side) and the poles (cold side).

In Figure 1.7 the marginal curves for the onset of convection are sketched as a function of the aspect ratio. It is interesting to observe that in the limit of $A \to \infty$, the $Ra_{\mathrm{cr},1} \to 1707$, i.e., the critical Rayleigh number for the case of the infinite layer analysed earlier.

Without surprise, even in this case, when Ra is increased, the flow field can undergo several bifurcations that can allow complex and time-dependent patterning behaviour (see, e.g. Ref. [31]).

The case of the temperature gradient orthogonal to the gravitational acceleration vector will be analysed in the next section.

1.1.2 Hadley flow

In the attempt to formalise the flow of air between the equators and the poles, Hadley [32] proposed the model that now carries his name. The initial model was rather simple. Due to the temperature gradient between the equator and the poles, four con-

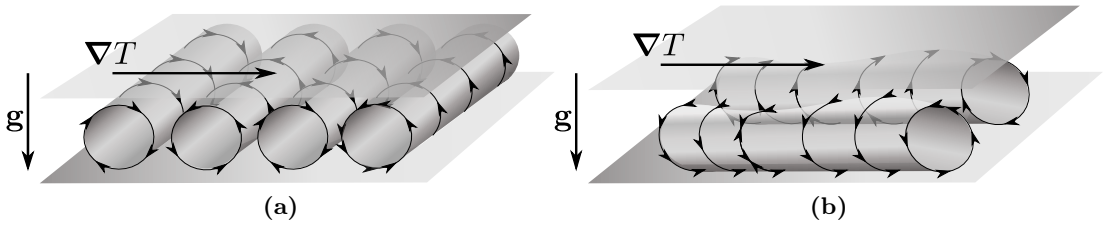

Figure 1.9: 2D hydrodynamic (or transverse) modes (a) and 3D longitudinal modes (b).

vective cells (two counter-rotating convective cells per hemisphere) were hypothesised to form. With the development of climate science, several sophisticated and more accurate models were proposed [33]. However, the basic idea remained the same (see Figure 1.8).

Although not accurate enough to adequately describe atmospheric flows, the model originally proposed by Hadley has enjoyed widespread popularity in the field of thermal convection due to its applications in several industrial processes [10, 34–37].

Considering once again the ideal case of the infinite layer, it is easy to prove (the reader might consider Ref. [10]) with analytical techniques that it does not exist any critical threshold for the onset of convection. Indeed, as soon as a temperature gradient is applied, convective flow will naturally arise, regardless of the intensity of such gradient. The flow manifests itself as a single convective cell known as the *Hadley cell*. This feature represents one of the main differences between Rayleigh-Bénard convection and Hadley flow.

The type of convective structure arising in the layer when the temperature gradient increases, or, in other words, when Ra is raised, strongly depends on the value of Pr. Indeed, two distinct cases can be considered, i.e. $Pr < 1$ and $Pr > 1$.

For low values of the Prandtl number, Hart [38, 39] focused on two different disturbances that can arise in the Hadley flow, namely, 2D transverse modes ad longitudinal modes. Around the same time, Gill [40] dedicated much effort to explaining the nature of the longitudinal roll configuration. The sketches related to these instability modes are depicted in Figure 1.9. As the reader can observe, while the transverse modes display rolls with the axis orthogonal to the temperature gradient, the longitudinal rolls' axis is in a parallel configuration. The outcome o such studies is that while the transverse

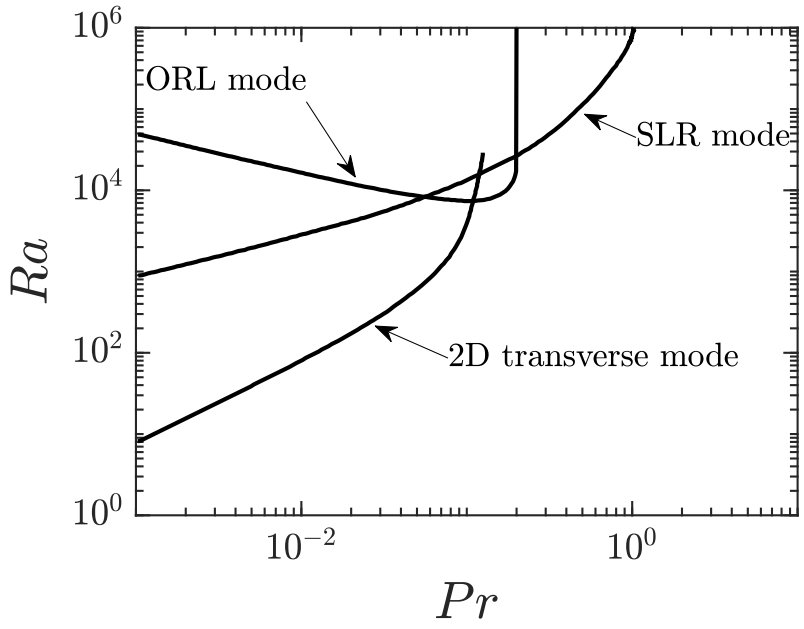

Figure 1.10: Critical Rayleigh number for the onset of secondary modes of the Hadley flow in an infinite horizontal layer as a function of Pr. Case of no-slip top and bottom boundary. After Kuo & Korpela,[41].

rolls arise due to a *shear instability* driven by the mean shear stress, the longitudinal rolls are caused by the interaction between mean shear stress and buoyancy force. The longitudinal rolls can be either stationary longitudinal rolls (SLR) or oscillatory longitudinal rolls (ORL). The dynamic behaviour strongly depends on the Prandtl number. Particularly in Ref. [41], using a linear stability analysis (LSA), the threshold of these modes was expressed as a function of Ra and Pr, as depicted in Figure 1.10.

A question naturally arise. What is the prevailing mode for the high Pr region? To answer it, Gershuni and co-workers [42], for the case of conducting top and bottom boundaries, discovered that another mode is prevailing, i.e. the so-called Rayleigh mode. It can be both 2D and 3D, depending on the value of the Rayleigh number. Indeed, in the case of high-Pr liquids, the fluid can stratify in the proximity to the conducting boundaries and eventually become unstable, trigging the aforementioned Rayleigh modes.

To conclude, it is worth mentioning the case of finite geometries heated from the sides. Similarly to the Rayleigh-Bénard case, the container's aspect ratio plays a crucial

role in the patterning configuration and instabilities the fluid can undergo. Remarkably, the aspect ratio influences the number of convective rolls that can arise in the container. Moreover, it is worth mentioning Ref. [43], which analyses the case of square cavities heated from the side, and found that for higher values of Pr, the most unstable convective modes are primarily 2D.

1.2 Thermovibrational Convection

So far, the case of standard thermogravitational convection has been analysed. Its natural extension to a microgravity environment is called thermovibrational convection. Ideally, this convective mechanism can be attained by replacing the steady gravitational acceleration with a time-dependent function (often sinusoidal). In practice, it is attained in microgravity environment when g-jitters or artificial (controlled) vibrations act on a differentially heated fluid container.

As anticipated, even in this case a natural dichotomy exists. Here, rather than the direction of gravity, the relative position between the direction of vibration and temperature gradient is the discriminant factor between two different flow regimes. If the vibrations are perpendicular to the temperature gradient, a flow is produced without the need to exceed any threshold. Instead, similarly to the case of Rayleigh-Bénard convection, when the vibrations are parallel to the temperature gradient, the fluid tends to remain in thermally diffusive and quiescent conditions until the control parameter exceeds a certain critical threshold.

Although a proper treatment of the mathematical modelling of such a category of flows will be presented in chapter 2, here, it is worth making a few considerations. Let us assume that the vibrations acting on the fluid are monochromatic harmonic functions. Therefore, once the harmonic function, i.e. the "shape" of the vibrations, has been fixed, two parameters affect the nature of the arising flow, i.e. amplitude and frequency of vibrations. Interestingly, another dichotomy arise: low-frequency-high-amplitude (lfha) and low-amplitude-high-frequency (lahf).

Before start reviewing the literature, it is worth adding another ingredient to the scenario presented so far. As remarked in Refs. [44–46], the velocity field $\mathbf{u}$ can be

decomposed in the sum of a time-average and an instantaneous component: $\mathbf{u} = \mathbf{u}_{\text{mean}} + \mathbf{u}'$. For the sake of completeness, $\mathbf{u}_{\text{mean}}$ is defined in eq. (2.81). Remarkably, the two decompositions of the velocity are function of two different non-dimensional numbers [47–50]. While $\mathbf{u}_{\text{mean}}$ is a function of the *Gershuni number* Gs, see eq. (2.80), the instantaneous component is related to the *vibrational* Rayleigh number Ra_ω, i.e. the natural extension of the Rayleigh number introduced in the preceding section where the modulus of the gravitational acceleration is replaced by the amplitude of the vibrations, see eq. (2.77).

Let us start analysing the case of high-frequencies vibrations. Historically, solving this case in its non-linear and time-dependent form (as this work aims to do) was prohibitive since, to track the effect of the vibration correctly, the time step must follow the Nyquist-Shannon sampling theorem. Put it simply, if the frequency $\Omega \to \infty$ then the discrete time-step $dt \to 0$, leading to an excessively big number of time integration iterations. Luckily, making appropriate order of magnitude analysis [44, 46, 51], it is possible to prove that a *potential flow* model exist [52–56]. Particularly, this model, also known as the Gershuni formulation, computes the time-average component of the velocity $\mathbf{u}_{\text{mean}}$ directly, saving a lot of computational recurses.

Let us analyse the case of the infinite layer. Using the Gershuni formulation, Gershuni & Zhukhovitskii [54, 55, 57] carried out an LSA to find the critical threshold for the onset of the time-average flow as a function of the angle ψ between the direction of vibrations and the temperature gradient (see Figure 1.11a). As outlined earlier, since the Gershuni formulation is used, the control parameter is the Gershuni number Gs.

This analysis's results are reported in Figure 1.11b. There, two interesting outcomes are evident. Particularly, in the limit of parallel configuration ($\psi = 0°$) the critical Gershuni number for the onset of a mean-flow $Gs_{\text{cr}} \to \infty$. Instead, in the limit of $\psi \to 90°$, $Gs_{\text{cr}} \to 2129$. Therefore, for the orthogonal configuration, the mean flow will arise only over this critical boundary. For these reasons, while in the orthogonal configuration, the pattern dynamics will be characterised in terms of the mean component of the velocity field, for the parallel case, the classification of the flow can only be made in function of the instantaneous component $\mathbf{u}' = \mathbf{u}$. Similar considerations were also made

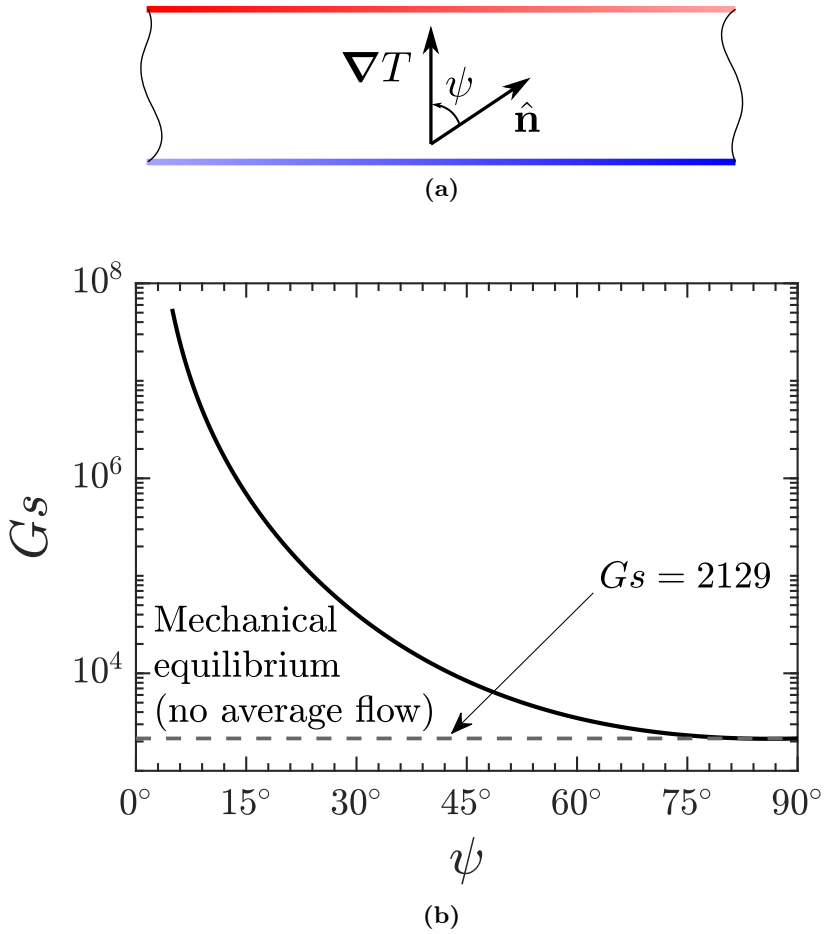

Figure 1.11: Scheme of the vibrated infinite layer where $\hat{\mathbf{n}}$ represent the direction of the vibrations (a) and related critical Gershuni number as a function of the angle between vibrations and temperature gradient (b).

on the basis of the solution of the balance equations in their non-linear and time-dependent form by Lappa [10] for the case of finite 2D cavities.

Moreover, it is worth remarking that the stability boundary described so far is valid *only* for the mean flow, meaning that, for the instantaneous part of the velocity vector, such a critical boundary will be considerably different, and, if $\psi = 90°$, the this critical threshold vanishes, i.e., a convective flow will instantaneously arise as soon the temperature gradient and the vibrations are applied.

Interestingly, similarly to the case of Rayleigh-Bénard convection ad Hadley flow, the mean velocity field can undergo multiple bifurcations when Gs is increased [57].

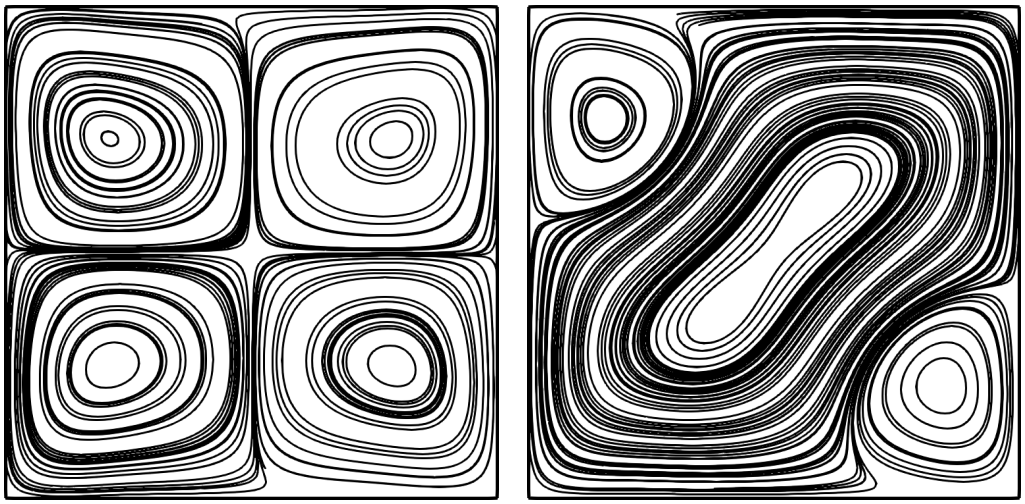

(a) (b)

Figure 1.12: Example of possible states of thermovibrational convection. The cavity is heated from below and cooled from above, while the vibrations are applied in the horizontal direction. Streamlines of the velocity time averaged component for $Pr = 10$, and non-dimensional frequency of the vibration $\Omega = 6 \times 10^3$. Quadrupolar cells for $Gs = 1.4 \times 10^3$ (a), and inversional pattern for $Gs = 9 \times 10^3$ (b).

Let us analyse the case of 2D square cavities. For the sake of brevity, only the case with $\psi = 90°$, i.e., vibrations orthogonal to the temperature gradient. In this case, for relatively small values of the Gershuni number, the (mean) flow exhibit the so-called quadrupolar cells pattern, i.e. a flow field with **(ss)** symmetry, see Figure 1.12a. A rise in Gs produces a flow bifurcation to an inversional pattern, i.e. two of the four cells merge together in the centre of the cavity, see Figure 1.12b. Interestingly, thanks to the more recent availability of long microgravity time, e.g. onboard the ISS and with parabolic flight, the transition between the two patterns have been observed not only numerically [58–60] but also experimentally [61–63].

For what concerns lower frequencies, the scenario is significantly different. Since the Gershuni formulation is no longer valid, the numerical analysis must be carried out using the complete form of the balance equations (see CHAPTER 2 for precise details).

Suppose the vibrations are applied orthogonally to the temperature gradient, for a 2D square cavity, a single cell that occupies the whole geometry forms. Interestingly, even in this case, the time-averaged (or mean) component of the velocity field can be

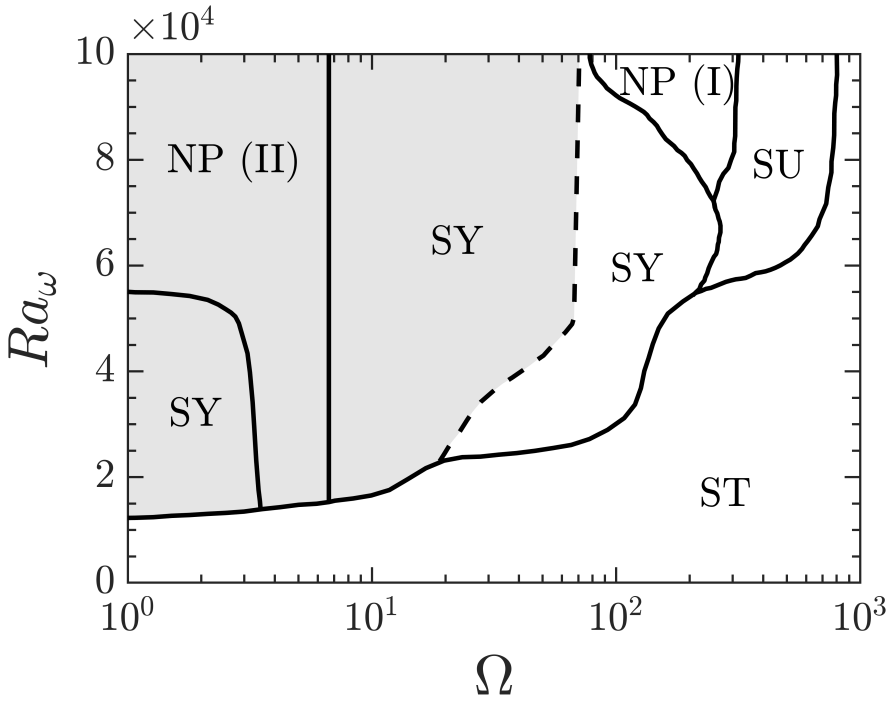

Figure 1.13: Response of the velocity field to the imposed vibrations as a function of Ω and Ra_ω in a 2D square cavity with conducting side-walls and filled with a liquid with $Pr = 7$. Vibrations parallel to the temperature gradient. The labels read: synchronous response (SY); half-subharmonic response (SU); non-periodic response (NP); stable (no-flow) response (ST). The shaded area represents the region where the fluid is stationary everywhere over some sub-interval during each period of vibrations. After Hirata, Sasaki & Tanigawa [65].

reconstructed (see eq. (2.81)). For lower frequencies, Crewdson & Lappa [64] showed that, not only the mean field can become time-dependent, but also turbulent if the Gershuni number is sufficiently increased.

The problem of vibrations parallel to the temperature gradient can finally be tackled in the low and medium vibration regimes. In this regard, it is worth mentioning the pivotal work by Hirata, Sasaki & Tanigawa [65], where, for a liquid having $Pr = 7$ they carried out a complete parametric study to discern the nature of the thermovibrational response of the flow field in a 2D square cavity. These result are summarised in Figure 1.13.

Let us start by observing that in this case, the control parameter is no longer the Gershuni number but rather the vibrational Rayleigh number Ra_ω. Indeed, only the instantaneous velocity field becomes meaningful for the parallel configuration and mid-

low vibration frequencies. Interestingly, Hirata and co-workers showed that the critical vibrational Rayleigh number $Ra_{\omega,\mathrm{cr}}$ strongly depends on the frequency of the external vibrations. Indeed, $Ra_{\omega,\mathrm{cr}}$ is a monotonic function of the vibrational frequency and tends to an infinite value as the frequency increases. In these circumstances, as $\Omega \to \infty$, the Gershuni regime is attained. Therefore, in the Gershuni regime, when the vibrations are parallel to the temperature gradient, not only does the time-averaged velocity field vanishes (see Figure 1.11b) but also all the instantaneous convective disturbance are suppressed [66, 67]. Therefore, high-frequency vibrations in the parallel configuration have a *stabilising* effect.

For lower values of Ω, the flow field can display a synchronous, half-subharmonic, or non-periodic response. It is worth noting that the same type of response is also possible for the orthogonal configuration [64].

1.3 Thermocapillary Convection

To conclude the review of standard convective flow, this section focuses on surface-tension driven or thermocapillary convection. To occur, this type of convective flow requires not only a temperature gradient but also the presence of a *free surface*, which can be defined as a situation where there is a negligible thickness separating two immiscible fluids (two liquids or a liquid and a gas) [68].

As anticipated at the beginning of this chapter, and in line with thermogravitational and thermovibrational flows, the relative direction between the temperature gradient and the unit vector normal to the free surface creates a natural dichotomy. When the two vectors are parallel, the related convective flow is generally known as Marangoni-Bénard convection, while when they are perpendicular, it is generally known as Marangoni convection. Both flow, take the name from the Italian physicist Carlo Marangoni that was the first to study the surface tension dependency upon temperature [69]. This dependence typically leads to a surface stress imbalance, which results in the emergence of surface flow and, eventually, ensuing bulk fluid motion driven by viscous effects [70].

Later Bénard, in its experimental investigation about Rayleigh-Bénard convection [14, 15], found that hexagonal cells (also known as Bénard cells) were emerging on the

top free surface of the liquid container. At that point, he did not realise that those cells were not forming only because of the buoyancy effect, as discussed in section 1.1, but they were arising as an interaction between buoyancy and surface tension-driven forces [71, 72]. For these historical reasons, where the temperature gradient is orthogonal to the free surface, we talk about *Marangoni-Bénard* convection.

Regardless of the relative direction between the temperature gradient and the normal vector to the free surface, in problems involving surface tension-driven convection, the control parameter is the Marangoni number (Ma), formally defined in eq. (2.78).

Similarly to the structure of section 1.1, let us start discussing the Marangoni-Bénard problem. It is worth remarking that here, we will only discuss "pure" Marangoni-Bénard convection and not the "mixed" variant discovered by Bénard, i.e. the system will be considered in a microgravity environment.

Traditionally, in studies involving problems with a free surface, another important effect has always been considered, i.e. the heat exchanged at the interface. This quantity is accounted with the Biot number Bi, defined in section 2.3.

The first complete theoretical study of Marangoni-Bénard convection can be ascribed to Pearson, [72] which studied the critical threshold for the onset of Marangoni convection as a function of the Biot number. Indeed, similarly to the Rayleigh-Bénard problem, the basic state is quiescent and diffusive until a critical value of the control parameter is exceeded.

In Figure 1.14, we can observe the marginal curves for the onset of Marangoni-Bénard convection in an infinite layer in zero-g conditions. For $Bi = 0$, i.e. the ideal case where the free surface is adiabatic, $Ma_{\text{cr}} = 79.607$. This case is purely ideal since, both with non-linear numerical simulations and experimentally, if the free surface is adiabatic, the fluid will eventually have a uniform temperature equal to the one of the heated boundary. However, this result is still valid within the limit of an LSA. More interesting is the overall trend of these curves as Bi is increased. Indeed, Ma_{cr} raises as the heat exchange between fluid and the surrounding environment becomes stronger. Regardless of the value of Bi, similarly to the case of Rayleigh-Bénard convection, the bifurcation from a quiescent state is stationary.

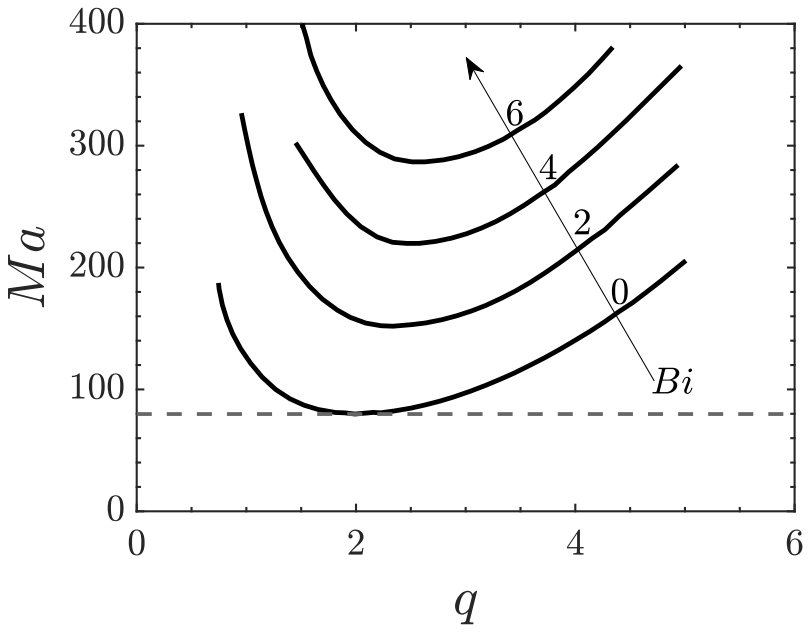

Figure 1.14: Marginal stability curves for Marangoni-Bénard convection in an infinite layer for different values of the Biot number (Bi). q represents the horizontal wave number at the onset of convection. After Pearson [72].

Although the LSA approach is a powerful tool for identifying the instability regions, it cannot predict the "shape" of the convective cells. In the first experiments carried out by Bénard the emerging flow displayed a honeycomb structure (see Figure 1.15 for an example of such a pattern). However, in those circumstances, buoyancy played an important role. For obvious reasons, back in those times, an experiment in microgravity to clarify these aspects would have been impossible. Nonetheless, thanks to the evolution of computer science, bifurcation theory and more advanced CFD techniques, i.e. use of non-linear simulation, it was proved that once the 2D disturbance that arises at the onset of convection saturates, hexagonal cells are the preferred mode in pure Marangoni-Bénard configurations [73–75]. Interestingly, it was also shown that these disturbances are selected by non-linear effects. In light of what explained here, the experimental results of Bénard [14, 15] should be re-interpreted.

Unlike the Rayleigh-Bénard configuration, in this case, the Prandtl number plays an important role on the emerging flow. Indeed, although the emerging pattern will still have a hexagonal configuration, for $Pr > 1$, the fluid will move toward the free surface

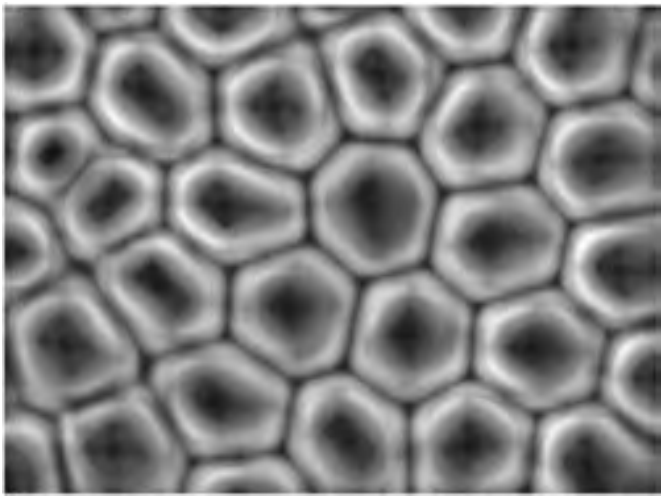

Figure 1.15: Bénard cells on a thin layer of silicone oil. Thermographic image digitally enhanced. Courtesy of M. Lappa.

from the centre and sink at the edges of the cell [71]. For $Pr << 1$ (liquid metals) the situation is exactly the opposite[76, 77]. In both cases, increasing the Marangoni number allow a plethora of different pattern to arise and undergo an oscillatory bifurcation when a critical threshold is exceeded [78–83].

Similarly to what was discussed in the context of thermogravitational flow, when the temperature gradient is rotated until it is parallel to the free surface, the hierarchy of bifurcations changes considerably. In this case, i.e. Marangoni convection, as soon as a temperature gradient is applied, the fluid will start flowing naturally. For the sake of brevity, let us focus only on finite shallow layers. In this case, the emerging flow will resemble a single cell that occupies the whole geometry (flow parallel to the free surface) [84]. Interestingly, in this case, the Prandtl number influences the position of a second roll that forms inside the primary single cell, in proximity to the solid lateral boundaries, upon increasing the Marangoni number. If $Pr << 1$, the secondary convective roll will form in the proximity to the cold wall, while at high-Pr, the roll will be located on the hot side [85, 86].

The most interesting effects happen when Ma is further increased. The first studies in this regard were carried out by Smith & Davis [88, 89] and Peltier & Biringen [90] which studied the problem of the infinite layer. Later Priede & Gerbeth [87]

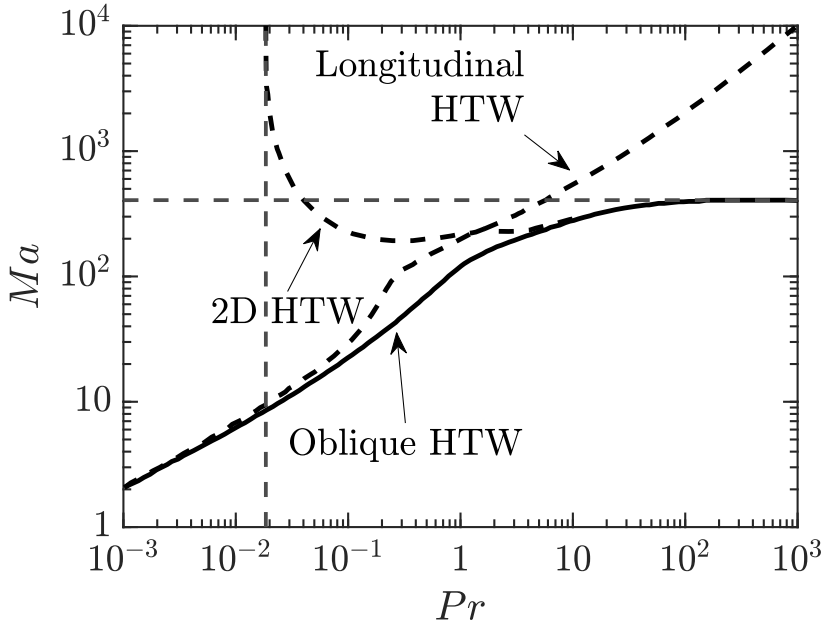

Figure 1.16: Critical Marangoni number and emerging flow as a function of the Prandtl number in an infinite layer with return flow and adiabatic free surface. After Priede & Gerbeth [87].

investigated the infinite layer with return flow problem. They paid attention to the nature of the emerging flow after the bifurcations when the layer has an adiabatic bottom boundary and free surface. Three possible mechanisms can be distinguished, namely, oblique hydrothermal waves (HTW), 2D HTW, and longitudinal HTW, as depicted in Figure 1.16. Hydrothermal waves are disturbances that propagate (or travel) from the cold to the hot boundaries of a layer [91–93]. An example of 2D HTW will be presented in chapter 3 in the context of the numerical framework validation (see Figure 3.2).

Interestingly, when the 2D constraint is removed in a finite layer, the disturbances become intrinsically 3D for $Pr < 1$, while the approximation of two-dimensionality remains valid for $Pr > 1$.

1.4 Convective Flows in Viscoelastic Fluids

So far, only Newtonian fluids have been considered. However, a myriad of different fluids exist in nature. Specifically, in this thesis, fluids that exhibit viscoelastic behaviour

are analysed. Viscoelastic fluids are generally liquids that exhibit both a viscous and elastic behaviour, i.e. when subjected to external velocity gradient, not only do they dissipate energy through viscous effect (as happens in a standard Newtonian fluid), but they are also capable of storing part of the supplied energy in the form of elastic energy. This class of fluid can display a flow even when the external force is removed, thanks to the extra energy previously stored.

Apart from the purely theoretical interest that attaches to the mathematical representation of viscoelastic fluids and their non-linear dynamics, these liquids find a wide spectrum of versatile applications in many fields of science and engineering. Relevant examples range from the development of plastic materials to a variety of complex fluids, which include (but are not limited to) colloids, polymer solutions and particulate suspensions with often counter-intuitive fluid mechanical behaviour.

For these reasons, over the years, viscoelastic fluids have been the subject of interest both in academia and industry. As a natural consequence of viscoelasticity, a variety of interesting phenomena can be produced due to their intrinsically non-linear behaviour, such as *rod-climbing* [94], *extrude swell* or "*die swell*" effect (Ref. [95] and references therein), *the tubeless siphon* [96], *the Uebler* effect [97], *elastic recoil* [98] and *vortex inhibition* [99] just to mention some of them.

More recently, significant interest has been attracted by flows of "natural" origin, i.e. convection produced by thermogravitational flow or surface-tension effects. As will be revealed in this section, whereas thermal convection in Newtonian fluids can be organised in well-defined universality classes, the interpretation of viscoelastic flow realisations is always more challenging, due to the inherent complexity and unpredictability.

The first pioneering theoretical analysis about Rayleigh-Bénard convection in viscoelastic fluids was carried out by Green in 1968 [100] which investigated the onset of RB convection in an infinite layer with stress-free top and bottom boundaries. Interestingly he found an unusual phenomenon arising in the fluid. Starting from a quiescent and diffusive state, the flow does not undergo a stationary bifurcation as in the case of Newtonian fluids. Instead, the flow field directly undergoes a Hopf (oscillatory) bifurcation. In addition, the critical value of the Rayleigh number is smaller if compared with

the Newtonian counterpart. This phenomenon was later studied by Vest & Arpaci [101] and Sokolov & Tanner [102]. These authors formalised a new concept, i.e. *overstability*. From a mathematical standpoint, overstability occurs when in an LSA, the real part of a pair of conjugate stability exponents becomes positive on passage through the critical boundary. Put it simply, from a physical point of view, due to the competition between the processes of viscous relaxation and thermal diffusion, viscoelastic fluids can produce convective modes that become unstable at a Rayleigh number that is smaller than that predicted for the corresponding stationary convection in Newtonian fluids, and at the same time, the flow can displays oscillatory behaviour [103].

Before moving forward with the current discussion, it is worth mentioning a few details about how this class of fluids is modelled. Let us remark that a complete discussion about viscoelastic fluid modelling will be provided in chapter 2, and that the scope of this paragraph is only to highlight the non-dimensional parameters that define the problem. The most common models used in computational rheology [104] are based on the idea that a viscoelastic fluid can be modelled as a mixture between a Newtonian solvent and a polymeric (elastic) solute. From this modelling, two extra non-dimensional number naturally arise, i.e. the elasticity number ϑ and the solvent-to-total viscosity ratio ξ (see section 2.3 for a complete definition).

Martínez-Mardones & Pérez-García [105] were the first to analyse the case of the infinite layer with solid top and bottom boundaries. The results of such analysis are reported in Figure 1.17. Interestingly, in the same paper, the authors assess that, in this case, the instability threshold depends on the Prandtl number. However, for $Pr > 10$, this dependency becomes almost negligible.

Another critical parameter for assessing the flow characteristic at the onset of convection is the elasticity of the fluid, which is quantified through the elasticity number ϑ. Interestingly, LSA studies [106, 107] showed that there are two "regions" or regimes in the space of the parameters, namely, weakly elastic regime (WER) and strongly elastic regime (SER). If $\vartheta < \vartheta_{\text{cr}}$, the flow attains a WER and the liquid behaves similarly to a Newtonian fluid, i.e. the first bifurcation is stationary. On the contrary, the fluid un-

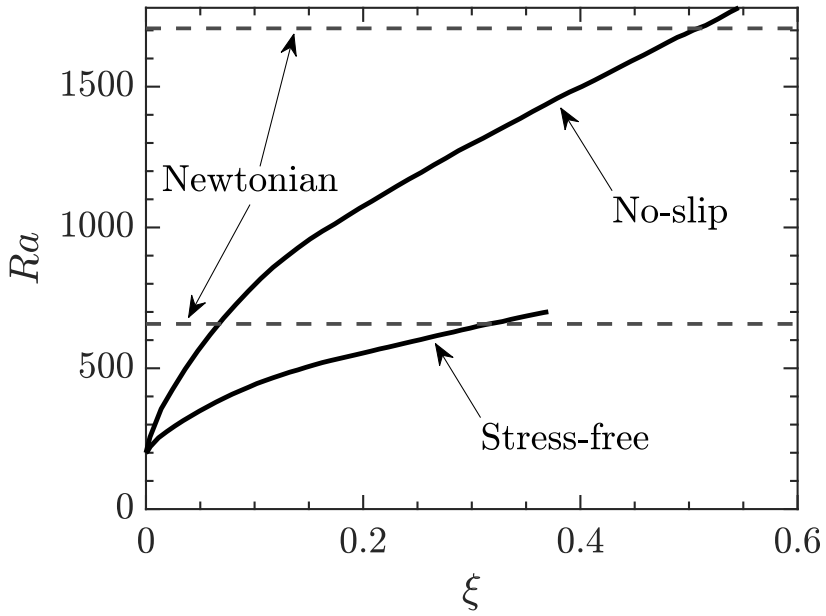

Figure 1.17: Marginal stability curves for viscoelastic Rayleigh-Bénard convection in an infinite layer for stress-free and no-slip boundary conditions as a function of the solvent-to-total viscosity ratio ξ, for $Pr = 10$ and $\vartheta = 0.1$. The horizontal dashed lines represent the critical threshold for Newtonian fluids. After Martínez-Mardones & Pérez-García [105].

dergoes a Hopf bifurcation for higher values of the elasticity number (SER), displaying overstable behaviour.

So far, only the temporal behaviour at the onset of convection has been described. However, nothing has been said about the patterning configuration of the flow. To bridge this gap, several authors [77, 106–111] analysed the same problem in the framework of a weakly non-linear analysis. For the WER, it was proved that, if in a layer of viscoelastic fluid heated from below with stress-free top boundary, both 2D rolls (similar to the ones depicted in Figure 1.3a and c) and 3D patterns with square and hexagonal cells are possible. Whether the flow is 2D or 3D depends on the value of the solvent-to-total viscosity ratio [107]. For higher values of the elasticity number (SER), it was predicted that, close to the critical threshold, the preferred mode of oscillatory convection resembles a standing wave, i.e. the convective cells "pulsate" and continuously change the sense of rotation over time with a specific oscillation frequency.

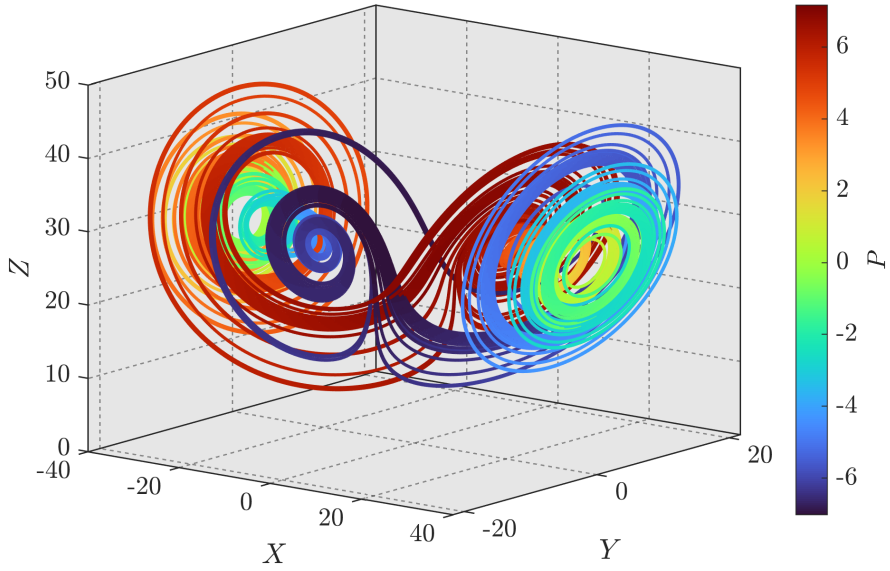

Figure 1.18: Lorenz-Khayat (strange) attractor. X is the amplitude of convective, Y the temperature difference between rising and descending currents, and Z the temperature deviation with respect to a linear temperature profile. The curve is coloured with the amplitude of viscoelastic stress P. The initial condition and the convective parameters are the same of Figure 1.1 with the addition of the elastic component with $\vartheta = 3.8$ and $\xi = 0.1$.

When the control parameter (Ra or ϑ) is further increased, similarly to the case of Newtonian fluid, chaos can arise in the flow. In this regard, Khayat [112] developed an extension of the Lorenz model to account for the viscoelastic effect. A comparison between Figure 1.1 and 1.18 reveals how different the system dynamics can be when the elastic effect is enabled in the fluid.

On a different note, recently Lappa & Boaro [1] discovered a new mode of convection using numerical simulations accounting for the complete non-linear and time-dependent formulation of the infinite layer problem (FENE-CR model) with no-slip top and bottom boundaries. Its dynamics is depicted in Figure 1.19. As the reader can observe, parallel rolls continuously break and reform in a position that is orthogonal to the original one. Due to this feature, this dynamic has been called *breaking-roll* pattern. Comparing Figure 1.19a and 1.19c (or Figure 1.19b and 1.19d), it might appear that the pattern undergoes a standing wave mechanism, where the rolls change sense of rotation in time. Instead, this is just the effect of multiple breakage and reorganisation of the

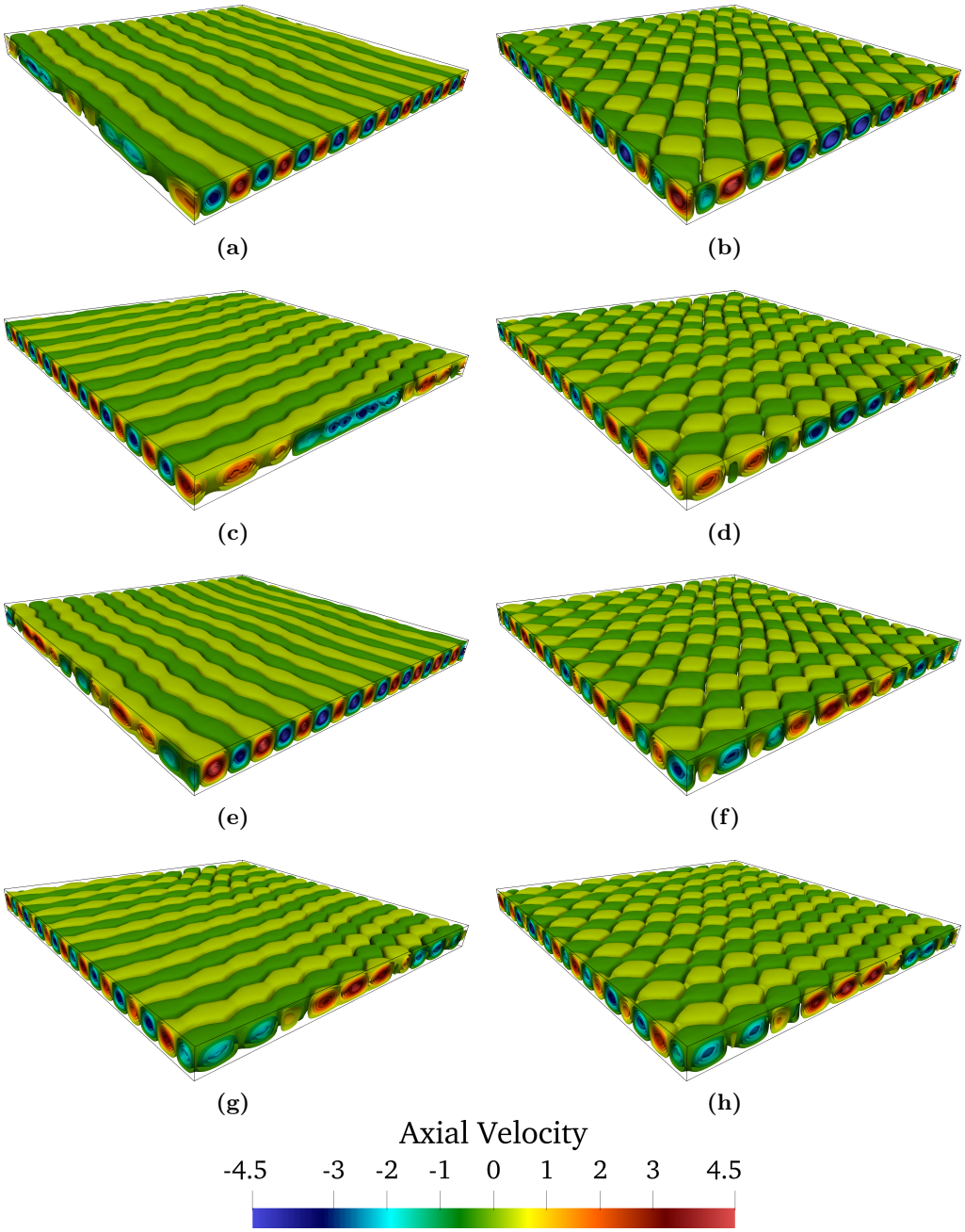

Figure 1.19: Rayleigh-Bénard convection in a layer of viscoelastic fluid ($15 \times 15 \times 1$ domain) delimited by solid horizontal walls, heated from below and cooled from above and periodic lateral boundary conditions. Snapshots of the isosurfaces of the vertical component of velocity evenly distributed over the oscillation period for $\xi = 0.5$, $Pr = 8$, $Ra = 2000$, $\vartheta = 0.1$. Non-dimensional angular frequency of oscillation $\varpi = 7.9$. After Lappa & Boaro [1].

rolls. In doing so (right column of Figure 1.19), the flow field displays a checkerboard pattern.

Similarly to the case of Newtonian fluids, after analysing the ideal case of the infinite layer, researchers focused on the study of finite geometries paying particular attention to the SER regions using linear [113, 114] and non-linear [115–118] analysis techniques. For this case, few non-linear and time-dependent studies are available in the literature [119–124]. Interestingly, the development of these studies is accompanied by new stabilising techniques for the solution of the non-linear equations for viscoelastic fluids. Further details on this topic will be provided in CHAPTER 3. For now it is worth noting that Park, Shin & Sohn [120] using a *grid-by-grid* inversion approach, studied the onset of convection in a rectangular cavity having aspect ratio AR = width/height = 2 for highly elastic fluids (SER). They found that, similarly to the case of the infinite layer, the solution appears as a standing wave. However, upon increasing the Rayleigh number, it bifurcates to a travelling wave.

The only study presenting non-linear and time-dependent results in a 3D finite geometry is due to Lappa & Boaro [1] where, apart from the case of the infinite layer analysed above, that studies the Rayleigh-Bénard problem in a cylindrical geometry with stress-free lateral boundary. There, they found that apart from the common solutions that arise in this class of domains for Newtonian fluids, namely standing and travelling waves, the breaking-roll mechanism can arise for shallow cavities. They also found the presence of multiple solutions that coexist for the same set of non-dimensional parameters and are selected starting from a specific initial condition.

Additionally, it is worth mentioning the experimental work by Kolodner [125] that studied thermogravitational convection in an annular pool arising in a solution containing long DNA chains. In Ref. [126], an analysis of the oscillation frequency reveals that the experiment is carried out in the WER sub-region of the parameters space. Another exciting experiment was more recently carried out by Métivier et al. [127] which studied the Rayleigh-Bénard problem in elasto-viscoplastic gels where travelling waves were found to replace standing waves when the yield number (formally

proportional to the Rayleigh number) exceeds a critical threshold. These results are in good agreement with the numerical results presented above.

Apart from Rayleigh-Bénard systems, also Marangoni-Bénard convection in viscoelastic fluids has enjoyed particular popularity. For the sake of brevity, here it is worth recalling just a few results. Let us start with the LSA by Lebon et al. [128] where mixed Rayleigh-Bénard Marangoni-Bénard was considered. Particularly these authors focused on the influence of different control parameters on the onset of stationary or oscillatory convection. As an example, Figure 1.20 represents the marginal curves for different thermal boundary conditions of the free surface (Biot number Bi). It is easy to observe that the oscillatory mode is the preferred one at the onset, even for $Ra = 0$ (pure Marangoni-Bénard convection). Therefore, even this class of flows become overstable if the elasticity of the fluid is high enough [129–131]. An effort was also put to study Marangoni-Bénard convection with deformable free surface, enabling thermorheological effects and other (more complex) configurations by means of LSA techniques [132–134].

Recently Lappa & Ferialdi [135] studied pure viscoelastic Marangoni-Bénard convection using 3D non-linear and time-dependent simulations. The study revealed that non-only multiple solutions are possible even in these circumstances, but also that the flow displays a more chaotic behaviour if compared to the Newtonian counterpart. Moreover, it was also found that a less regular patterning behaviour takes over the hexagonal cells that are characteristic of standard (Newtonian) fluids.

At this stage, the reader might have realised that the discussion about thermally driven flow has only concentrated on Rayleigh-Bénard and Marangoni-Bénard systems, without even mentioning other convective flows analysed earlier in the context of Newtonian fluids, namely, Hadley, Marangoni, and thermovibrational flows. Unfortunately, this is not due to a lack of attention from the present author. Indeed, up to the author's knowledge, there are just a few LSA dealing with viscoelastic Marangoni and mixed thermogravitational-thermovibrational flows in the literature.

Starting with the viscoelastic Marangoni flow, some guidance on this matter is provided by the investigations by Hu et al. [136–138] where it has been shown that in an infinite layer with temperature gradient parallel to the free-surface, in the case of

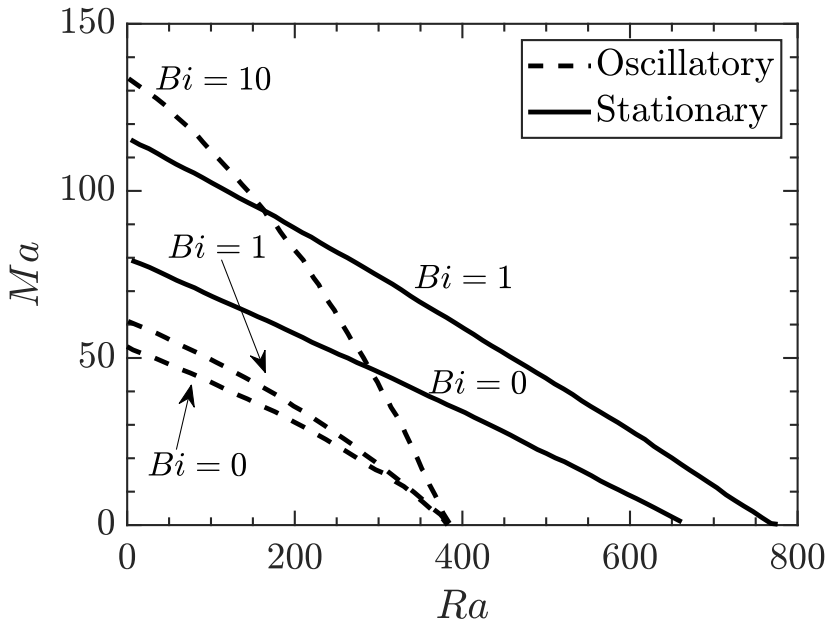

Figure 1.20: Critical Marangoni number for viscoelastic mixed Rayleigh-Bénard Marangoni-Bénard convection in an infinite layer as a function of the Rayleigh ad Biot numbers, for $Pr = 200$ and $\vartheta = 0.2$, $\xi = 0.1$. After Lebon et al. [128].

high-Pr fluids, elasticity can cause a swap in the direction of propagation of the HTW (enabled as a result of the primary Hopf bifurcation of the flow). More precisely, the disturbances start spreading in the downstream direction, i.e. from the hot to the cold boundary, when the elasticity overcomes a given level. Eventually, steady longitudinal convection modes completely replace them if a second threshold is exceeded. In such circumstances, steady rolls with axes parallel to the imposed temperature gradient are produced in place of the standard ones with perpendicular axes. More recently, Patne, Agnon & Oron [139, 140] have extended this line of inquiry by considering layers subjected to both parallel and perpendicular temperature differences (inclined temperature gradient), thereby revealing a variety of stabilising and destabilising effects depending on the dominant mechanism. Although these studies are paving a new path of enquiry, they analyse the ideal case of the infinite layer. As discussed up to a certain extent, the effect of lateral solid boundaries has a significant impact on the flow field, especially in the case of Marangoni flow. Therefore, these studies do not give any insight into the variety of patterning and dynamic behaviour that could be enabled in a finite layer.

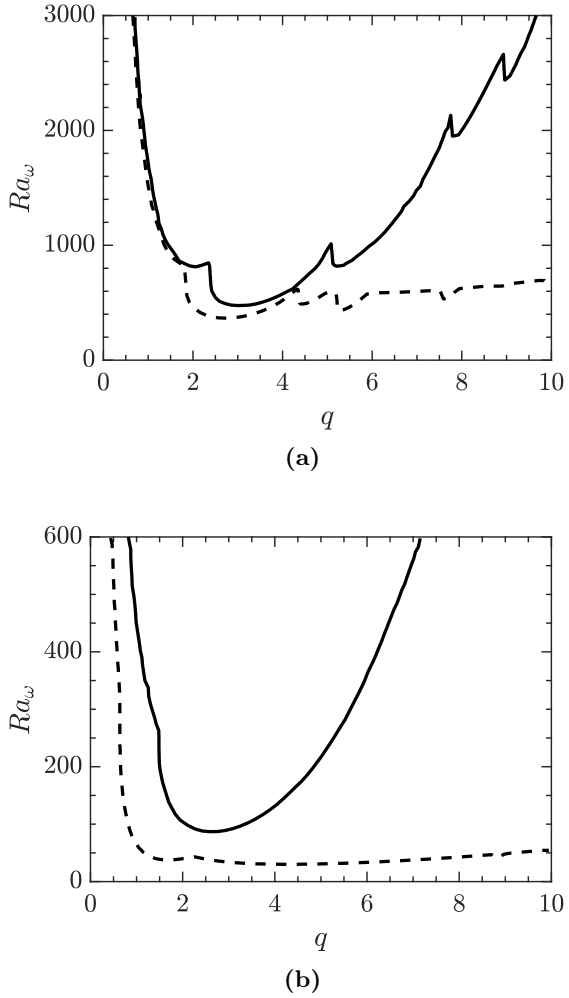

Figure 1.21: Marginal stability curves for modulated Rayleigh-Bénard convection in an infinite layer of viscoelastic fluid delimited by horizontal stress-free walls. For $Pr = 7$, $\Omega = 26.5$, $\Gamma = 1$, $\xi = 0.1$ and $\vartheta = 0.06$ (a) and $\vartheta = 0.38$ (b). Dashed and solid lines represent the Maxwell and Oldroyd-B model results, respectively. After Yang [141] and Lyubimova & Kovalevskaya [142].

For what concerns the case of pure viscoelastic thermovibrational flow, there are no studies that directly tackle this problem. However, a few papers deal with modulated Rayleigh-Bénard convection in an infinite layer, i.e. the fluid is subjected to a steady gravitational acceleration and vibrations that are both parallel to the temperature gradient. In particular, these works are due to Yang [141] which analysed the problem in the framework of the Maxwell model, and Lyubimova & Kovalevskaya [142] that tackled the same problem using an Oldroyd-B model. As a peculiarity, both

these studies carried out an LSA using square (or pulse) vibrational waves, while the majority of the studies presented in section 1.2 employed sinusoidal waves to model the vibrational motion. The results of these two studies are presented in Figure 1.21.

From these curves, we can observe that, in accordance with other studies dealing with viscoelastic Rayleigh-Bénard convection, an increase in the elasticity number has the effect of lowering the threshold for the onset of convection. Moreover, it is also worth mentioning another outcome of the study made by Lyubimova & Kovalevskaya, i.e. similar to what was found by Hirata, Sasaki & Tanigawa [65], the flow field response to the vibration can be synchronous and half-subharmonic or quasi-periodic. However, a synchronous and harmonic solution was not predicted for viscoelastic liquids.

At this stage, it is evident that some effort should be paid to studying how convection in viscoelastic fluids can manifest itself once the influence of gravity is removed. To do so, following a classical path in the field of microgravity convection, this work aims to carry out numerical simulations to better understand the behaviour of these complex systems. The following chapter will introduce and derive the mathematical model used to describe convective flows in Newtonian and viscoelastic fluids.

Chapter 2

Mathematical Model

This chapter presents an introduction to the mathematical formulation of the balance equations that describe the phenomena presented in Chapter 1. Specifically, the chapter starts presenting the microscopic derivation of the balance equations for Newtonian fluids. The derivation is later expanded to fluids that exhibit a viscoelastic rheology. Finally, it introduce the set of non-dimensional balance equations and the related dimensionless groups.

2.1 The balance equations for Newtonian fluids: a microscopic derivation

In engineering, the balance equations for mass, momentum and energy are generally derived macroscopically, i.e. balancing the aforementioned quantities over a control volume infinitesimally small but still bigger than the mean free path of the fluid molecules. This approach is justified on the one hand by its simplicity and on the other by the fact that microscopic and macroscopic quantities can be directly correlated. On the contrary, there is no straightforward macroscopic approach to discerning the whole set of balance equations for a viscoelastic fluid.

For this reason, this section presents a microscopic derivation for the mass, continuity and energy balance equations. It will follow the same rationale underpinned in the seminal work by Kirkwood [143] and Irving & Kirkwood [144], where, using a statistical mechanics approach, they develop a complete theory that links the microscopic structure of a Newtonian fluid to its macroscopic balance equations. Moreover, since this derivation can be pretty tedious, some simplifications inspired by the work of Lappa [10] will be made in an attempt to keep this section as concise as possible.

Let us consider a group of N particles of fluid. For simplicity and without losing generality, the fluid is assumed to be single-component and single phase, and the whole ensemble of molecules only interacts via central forces (binary interaction).

After defining an arbitrary reference frame, each particle is identified by its position $\mathbf{r}_i$, velocity $\mathbf{c}_i(=\dfrac{d\mathbf{r}_i}{dt})$ and mass m_i. It is worth noting that, by defining the momentum of each particle as:

$$\mathbf{p}_i = m_i \frac{d\mathbf{r}_i}{dt} = m_i \mathbf{c}_i \tag{2.1}$$

we can describe the whole system only using the position and momentum of each particle. Moreover, since both $\mathbf{r}_i$ and $\mathbf{p}_i$ are 3D vectors, the system lays in a $6N$–dimesional phase space D_{6N}.

Before deriving the balance equations, another fundamental concept must be introduced, i.e. the probability distribution function denoted by $f(\mathbf{r}_1, \ldots, \mathbf{r}_N, \mathbf{p}_1, \ldots, \mathbf{p}_N, t)$, which, from a purely mathematical standpoint, represents the relative density of representative points in the phase space.

This function undergoes the normalisation condition $\int_{D_{6N}} f \, dD_{6N} = 1$, while its evolution in time is described by the so-called *Liouville* equation:

$$\frac{\partial f}{\partial t} = -\sum_{i=1}^{N} \left[\frac{\mathbf{p}_i}{m_i} \cdot \boldsymbol{\nabla}_{\mathbf{r}_i} f + \frac{\partial \mathbf{p}_i}{\partial t} \cdot \boldsymbol{\nabla}_{\mathbf{p}_i} f \right] \tag{2.2}$$

Given a distribution function and a generic dynamical property of the system a, the expectation value (or in other words the stochastic average value) of the quantity a is defined as:

$$\langle a \rangle = \int_{D_{6N}} a(\mathbf{r}_1, \ldots, \mathbf{r}_N, \mathbf{p}_1, \ldots, \mathbf{p}_N) f(\mathbf{r}_1, \ldots, \mathbf{r}_N, \mathbf{p}_1, \ldots, \mathbf{p}_N, t) \, dD_{6N} \tag{2.3}$$

In the following, this definition will simply be applied without introducing any distribution functions.

It is worth noting that a is only a function of spatial (phase space) variables $(\mathbf{r}_1, \ldots, \mathbf{r}_N, \mathbf{p}_1, \ldots, \mathbf{p}_N)$ but does not explicitly depend on the time [144]. Therefore, taking into account these consideration, eq. (2.2) can be plugged into the rate of change

of eq. (2.3), and using the Green's theorem, it is straightforward to conclude that:

$$\frac{\partial}{\partial t}\langle a\rangle = \sum_{i=1}^{N}\left\langle \frac{\mathbf{p}_i}{m_i}\cdot\boldsymbol{\nabla}_{\mathbf{r}_i}a + \frac{\partial \mathbf{p}_i}{\partial t}\cdot\boldsymbol{\nabla}_{\mathbf{p}_i}a\right\rangle \tag{2.4}$$

Moreover, considering the linearity property of the integral and sum operators, it is easy to proof that $\sum_i\langle A_i\rangle = \langle\sum_i A_i\rangle$, for every mathematical entity A_i.

The concepts just introduced can be used for the derivation of the balance equations. Using the average operator defined in eq. (2.3), the probability that the i-th particle is at the position $\mathbf{x}$ at a specified instant of time t is given by $\langle\delta(\mathbf{r}_i-\mathbf{x})\rangle$, where δ is the *Dirac delta* function:

$$\delta(x) = \begin{cases} 0 & \text{if} \quad x\neq 0 \\ \infty & \text{if} \quad x = 0 \end{cases} \tag{2.5}$$

Given a quantity ϕ related to the molecules, its total (macroscopic) density at a given location $\mathbf{x}$ and time t, reads:

$$P_\phi = \sum_{i=1}^{N}\langle\phi_i\delta(\mathbf{r}_i-\mathbf{x})\rangle \tag{2.6}$$

and its rate of change is:

$$\frac{\partial P_\phi}{\partial t} = \sum_{i=1}^{N}\left[\langle\frac{\partial}{\partial t}\phi_i\delta(\mathbf{r}_i-\mathbf{x})\rangle + \langle\phi_i\frac{\partial}{\partial t}\delta(\mathbf{r}_i-\mathbf{x})\rangle\right] \tag{2.7}$$

Accounting for eq. (2.4), eq. (2.7) becomes:

$$\begin{aligned}\frac{\partial P_\phi}{\partial t} &= \sum_{i=1}^{N}\Big[\langle\frac{\partial}{\partial t}\phi_i\delta(\mathbf{r}_i-\mathbf{x})\rangle + \sum_{j=1}^{N}\Big\langle\phi_i\underbrace{\frac{\mathbf{p}_j}{m_j}\cdot\boldsymbol{\nabla}_{\mathbf{r}_j}\delta(\mathbf{r}_i-\mathbf{x})}_{=0 \text{ if } i\neq j} + \phi_i\underbrace{\frac{\partial\mathbf{p}_j}{\partial t}\cdot\boldsymbol{\nabla}_{\mathbf{p}_j}\delta(\mathbf{r}_i-\mathbf{x})}_{=0\,\forall\, j}\Big\rangle\Big] \\ &= \sum_{i=1}^{N}\Big[\langle\frac{\partial}{\partial t}\phi_i\delta(\mathbf{r}_i-\mathbf{x})\rangle + \Big\langle\phi_i\mathbf{c}_i\cdot\boldsymbol{\nabla}_{\mathbf{r}_i}\delta(\mathbf{r}_i-\mathbf{x})\Big\rangle\Big]\end{aligned} \tag{2.8}$$

where in the last step the velocity of the i-th molecule $\mathbf{c}_i$ has been written explicitly.

2.1.1 Continuity equation

The continuity equation simply formalises the fact that in a system the mass is always conserved. In this particular case, since the number of molecules is fixed and equal to N, the total mass remains constant:

$$\sum_{i=1}^{N} m_i = \text{ constant} \tag{2.9}$$

Let us use the theory developed in the preceding part of this chapter to calculate the density of mass. Using the classical notation, and eq. (2.6) the density of mass $\rho(t, \mathbf{x})$ can be written as:

$$\rho(\mathbf{x}, t)) = P_m = \sum_{i=1}^{N} \langle m_i \delta(\mathbf{r}_i - \mathbf{x}) \rangle \tag{2.10}$$

while, using eq. (2.8) and taking into account that the mass of each molecule is *always* constant in time ($\partial m_i / \partial t = 0$, $\forall i$, t), its rate of change is:

$$\begin{aligned} \frac{\partial}{\partial t} \rho(\mathbf{x}, t) = & \sum_{i=1}^{N} \Big\langle m_i \mathbf{c}_i \cdot \boldsymbol{\nabla}_{\mathbf{r}_i} \delta(\mathbf{r}_i - \mathbf{x}) \Big\rangle \\ = & - \sum_{i=1}^{N} \Big\langle \boldsymbol{\nabla} \cdot [m_i \mathbf{c}_i \delta(\mathbf{r}_i - \mathbf{x})] \Big\rangle \end{aligned} \tag{2.11}$$

were in the last passage the base of the nabla operator was changed from the phase space to the macroscopic phase, using the property $\boldsymbol{\nabla}_{\mathbf{r}_i} \delta(\mathbf{r}_i - \mathbf{x}) = -\boldsymbol{\nabla}_{\mathbf{x}} \delta(\mathbf{r}_i - \mathbf{x})$ and omitting the $\mathbf{x}$-subscript to indicate the macroscopic (standard) nabla.

The right hand side of eq. (2.11) can also be expressed as a function of macroscopic quantities considering that the density of momentum can be written as $\rho(\mathbf{x}, t)\mathbf{u}(\mathbf{x}, t)$, where $\mathbf{u}$ is the macroscopic mean velocity of the ensemble of molecules, but it can can also be calculated through eq. (2.6):

$$\rho(\mathbf{x}, t)\mathbf{u}(\mathbf{x}, t) = P_{m\mathbf{u}} = \sum_{i=1}^{N} \langle m_i \mathbf{c}_i \delta(\mathbf{r}_i - \mathbf{x}) \rangle \tag{2.12}$$

Replacing eq. (2.12) in eq. (2.11), it follows that:

$$\frac{\partial}{\partial t}\rho(\mathbf{x},t) = -\boldsymbol{\nabla}\cdot[\rho(\mathbf{x},t)\mathbf{u}(\mathbf{x},t)] \tag{2.13}$$

which is the classical *continuity* equation.

Eq. (2.13) can be further simplified if the nature of the fluid is considered. Indeed, the present work considers only *incompressible* fluid, i.e. fluid having a constant density. It follows that the derivatives of the density, both with respect time and space go to zero, and the final continuity equation for incompressible fluids becomes:

$$\boldsymbol{\nabla}\cdot\mathbf{u}^*(\mathbf{x},t) = 0 \tag{2.14}$$

Here we introduced the superscript $(^*)$ to underline that the quantity is written in dimensional form (the reason for this will become clearer later).

2.1.2 Momentum equation

With an approach similar to the one adopted in the preceding section, the momentum conservation equation is now derived. The density of momentum is calculated in eq. (2.12). Let us note that, instead of assuming that the macroscopic momentum is given by $\rho\mathbf{u}$, it can be calculated assuming that the velocity of every molecule can be split into two contributions, one given by the random microscopic motion ($\mathbf{C}_i$) and one given by the mean macroscopic motion ($\mathbf{u}$). Therefore, the velocity of each fluid particle reads:

$$\mathbf{c}_i = \mathbf{C}_i + \mathbf{u} \tag{2.15}$$

and the right hand side of eq. (2.12) becomes:

$$\begin{aligned}\sum_{i=1}^{N}\langle m_i\mathbf{c}_i\delta(\mathbf{r}_i-\mathbf{x})\rangle &= \cancelto{\mathbf{0}}{\sum_{i=1}^{N}\langle m_i\mathbf{C}_i\delta(\mathbf{r}_i-\mathbf{x})\rangle} + \sum_{i=1}^{N}\langle m_i\mathbf{u}\delta(\mathbf{r}_i-\mathbf{x})\rangle \\ &= \mathbf{u}\sum_{i=1}^{N}\langle m_i\delta(\mathbf{r}_i-\mathbf{x})\rangle = \rho\mathbf{u}\end{aligned} \tag{2.16}$$

where, because of its randomness, the density of the momentum due to the random motion is statistically $\mathbf{0}$.

Using eq. (2.8) and the results of eqs. (2.12) and (2.16), the change of rate of the density of momentum is represented by:

$$\frac{\partial}{\partial t}[\rho(\mathbf{x},t)\mathbf{u}(\mathbf{x},t)] = \sum_{i=1}^{N}\Big[\Big\langle \underbrace{\frac{\partial}{\partial t}(m_i\mathbf{c}_i)}_{=\mathbf{f}_i}\,\delta(\mathbf{r}_i-\mathbf{x})\Big\rangle + \Big\langle m_i\mathbf{c}_i\mathbf{c}_i\cdot\boldsymbol{\nabla}\delta(\mathbf{r}_i-\mathbf{x})\Big\rangle\Big] \tag{2.17}$$

were $\mathbf{f}_i$ is the external force applied to each molecule. Hence, the macroscopic density of body force acting on the particle ensemble is:

$$\mathbf{f}_b = \sum_{i=1}^{N}\langle \mathbf{f}_i\delta(\mathbf{r}_i-\mathbf{x})\rangle \tag{2.18}$$

which correspond to the first therm of eq. (2.17) that now reads:

$$\frac{\partial}{\partial t}[\rho(\mathbf{x},t)\mathbf{u}(\mathbf{x},t)] = \mathbf{f}_b + \underbrace{\sum_{i=1}^{N}\langle m_i\mathbf{c}_i\mathbf{c}_i\cdot\boldsymbol{\nabla}_{\mathbf{r}_i}\delta(\mathbf{r}_i-\mathbf{x})\rangle}_{\mathcal{A}} \tag{2.19}$$

The second term of the right hand side $\mathcal{A}$ must be tackled. To do so, let us apply the same transformation of eq.(2.11), accounting for the linearity of average, sum and divergence operators, and consider eq. (2.15):

$$\begin{aligned}
-\mathcal{A} &= \sum_{i=1}^{N}\langle\boldsymbol{\nabla}\cdot[m_i\mathbf{c}_i\mathbf{c}_i\delta(\mathbf{r}_i-\mathbf{x})]\rangle \\
&= \boldsymbol{\nabla}\cdot\sum_{i=1}^{N}\Big\langle m_i\mathbf{u}\mathbf{u}\delta(\mathbf{r}-\mathbf{r}_i)\Big\rangle + \boldsymbol{\nabla}\cdot\sum_{i=1}^{N}\Big\langle m_i\mathbf{C}_i\mathbf{u}\delta(\mathbf{r}-\mathbf{r}_i)\Big\rangle \\
&+ \boldsymbol{\nabla}\cdot\sum_{i=1}^{N}\Big\langle m_i\mathbf{u}\mathbf{C}_i\delta(\mathbf{r}-\mathbf{r}_i)\Big\rangle + \boldsymbol{\nabla}\cdot\sum_{i=1}^{N}\Big\langle m_i\mathbf{C}_i\mathbf{C}_i\delta(\mathbf{r}-\mathbf{r}_i)\Big\rangle \\
&= \boldsymbol{\nabla}\cdot\Big[\sum_{i=1}^{N}\Big\langle m_i\delta(\mathbf{r}-\mathbf{r}_i)\Big\rangle\mathbf{u}\mathbf{u}\Big] + \boldsymbol{\nabla}\cdot\Big[\underbrace{\sum_{i=1}^{N}\Big\langle m_i\mathbf{C}_i\delta(\mathbf{r}-\mathbf{r}_i)\Big\rangle}_{=\mathbf{0}}\mathbf{u}\Big]
\end{aligned}$$

$$+ \boldsymbol{\nabla} \cdot \Big[\mathbf{u} \underbrace{\sum_{i=1}^{N} \Big\langle m_i \mathbf{C}_i \delta(\mathbf{r} - \mathbf{r}_i) \Big\rangle}_{=\mathbf{0}} \Big] + \boldsymbol{\nabla} \cdot \underbrace{\sum_{i=1}^{N} \Big\langle m_i \mathbf{C}_i \mathbf{C}_i \delta(\mathbf{r} - \mathbf{r}_i) \Big\rangle}_{-\boldsymbol{\tau}}$$

$$= \boldsymbol{\nabla} \cdot (\rho \mathbf{u}\mathbf{u}) - \boldsymbol{\nabla} \cdot \boldsymbol{\tau} \tag{2.20}$$

The new quantity $\boldsymbol{\tau}$ just introduced is known as *viscous stress tensor*. For the sake of brevity, let us underline that although the stress tensor is now a function of microscopic entities, for Newtonian fluids, it is possible to correlate it to macroscopic and measurable quantities using the CHAPMAN & ENSKOG theory. In this regard, the reader is referred to Ref. [109] for a complete derivation of such a correlation. The outcome of this process is that the stress tensor can be written as:

$$\boldsymbol{\tau} = -p\mathbf{I} + 2\eta \left[\frac{\boldsymbol{\nabla}\mathbf{u} + (\boldsymbol{\nabla}\mathbf{u})^{\intercal}}{2} - \frac{(\boldsymbol{\nabla} \cdot \mathbf{u})\mathbf{I}}{3} \right] \tag{2.21}$$

where p is the pressure, $\mathbf{I}$ is the unit tensor, and η is the dynamic viscosity of the fluid.

This formulation is generic to every Newtonian fluid, however, considering only incompressible fluids and accounting for the continuity equation (eq. (2.14)), eq. (2.21) can be simplified as:

$$\boldsymbol{\tau} = -p\mathbf{I} + \eta[\boldsymbol{\nabla}\mathbf{u} + (\boldsymbol{\nabla}\mathbf{u})^{\intercal}] \tag{2.22}$$

To conclude this section, considering the result of eqs. (2.18), (2.20), and (2.22), the rate of change of density of momentum for an incompressible fluid, that is the balance equation for the conservation of momentum, reads:

$$\rho \frac{\partial \mathbf{u}^*}{\partial t} + \rho \boldsymbol{\nabla} \cdot (\mathbf{u}^* \mathbf{u}^*) = -\boldsymbol{\nabla} p^* + \eta \nabla^2 \mathbf{u}^* + \mathbf{f}_b^* \tag{2.23}$$

where ∇^2 is the Laplacian operator, the viscosity η and the density ρ are assumed to be constant and, again, the symbol $(^*)$ is used to highlight that the quantities are dimensional.

2.1.3 Energy equation

Let us continue with the same rational adopted so far and consider the density of microscopic kinetic energy. The kinetic energy of a molecule is $e_i = 1/2 m_i c_i^2$, where c_i is the magnitude of the particle velocity, and using eq. (2.6), its density is:

$$\rho e = P_e = \sum_{i=1}^{N} \langle \frac{1}{2} m_i c_i^2 \delta(\mathbf{r}_i - \mathbf{x}) \rangle \tag{2.24}$$

Using eq. (2.15), c_i^2 can be rewritten as:

$$c_i^2 = \mathbf{c}_i \cdot \mathbf{c}_i = (\mathbf{u} + \mathbf{C}_i) \cdot (\mathbf{u} + \mathbf{C}_i) = u^2 + 2\mathbf{u} \cdot \mathbf{C}_i + C_i^2 \tag{2.25}$$

and eq.(2.24) becomes:

$$\begin{aligned} \rho e &= \sum_{i=1}^{N} \langle \frac{1}{2} m_i u^2 \delta(\mathbf{r}_i - \mathbf{x}) \rangle + \sum_{i=1}^{N} \langle m_i \mathbf{u} \cdot \mathbf{C}_i \delta(\mathbf{r}_i - \mathbf{x}) \rangle + \sum_{i=1}^{N} \langle \frac{1}{2} m_i C_i^2 \delta(\mathbf{r}_i - \mathbf{x}) \rangle \\ &= \frac{1}{2} u^2 \underbrace{\sum_{i=1}^{N} \langle m_i \delta(\mathbf{r}_i - \mathbf{x}) \rangle}_{=\rho} + \mathbf{u} \cdot \underbrace{\sum_{i=1}^{N} \langle m_i \mathbf{C}_i \delta(\mathbf{r}_i - \mathbf{x}) \rangle}_{=\mathbf{0}} + \underbrace{\sum_{i=1}^{N} \langle \frac{1}{2} m_i C_i^2 \delta(\mathbf{r}_i - \mathbf{x}) \rangle}_{\rho e_{\text{int}}} \end{aligned} \tag{2.26}$$

were e_{int} represents the internal energy per unit of mass. Therefore, the density of microscopic kinetic energy reads:

$$\rho e = \frac{1}{2} \rho u^2 + \rho e_{\text{int}} \tag{2.27}$$

As usual, the rate of density of kinetic energy can be calculated using eq. (2.8):

$$\begin{aligned} \frac{\partial}{\partial t}(\rho e) &= \sum_{i=1}^{N} \Big\langle \frac{\partial}{\partial t} \Big(\frac{1}{2} m_i c_i^2 \Big) \delta(\mathbf{r}_i - \mathbf{x}) \Big\rangle + \sum_{i=1}^{N} \Big\langle \frac{1}{2} m_i c_i^2 \mathbf{c}_i \cdot \boldsymbol{\nabla}_{\mathbf{r}_i} \delta(\mathbf{r}_i - \mathbf{x}) \Big\rangle \\ &= \underbrace{\sum_{i=1}^{N} \Big\langle \frac{\partial}{\partial t} \Big(\frac{1}{2} m_i c_i^2 \Big) \delta(\mathbf{r}_i - \mathbf{x}) \Big\rangle}_{=\mathcal{B}} - \boldsymbol{\nabla} \cdot \underbrace{\sum_{i=1}^{N} \Big\langle \Big[\frac{1}{2} m_i c_i^2 \mathbf{c}_i \delta(\mathbf{r}_i - \mathbf{x}) \Big] \Big\rangle}_{=\mathcal{C}} \end{aligned} \tag{2.28}$$

For the sake of simplicity, let us analyse each term ($\mathcal{B}$ and $\boldsymbol{\mathcal{C}}$) separately. Starting with $\mathcal{B}$:

$$\begin{aligned}\mathcal{B} &= \sum_{i=1}^{N}\Big\langle \mathbf{c_i}\cdot \underbrace{\frac{\partial}{\partial t}\Big(m_i\mathbf{c_i}\Big)}_{=\mathbf{f}_i}\delta(\mathbf{r}_i-\mathbf{x})\Big\rangle \\ &= \mathbf{u}\cdot\sum_{i=1}^{N}\Big\langle \mathbf{f}_i\delta(\mathbf{r}_i-\mathbf{x})\Big\rangle + \underbrace{\sum_{i=1}^{N}\Big\langle m_i\mathbf{C}_i\cdot\frac{\partial \mathbf{c}_i}{\partial t}\delta(\mathbf{r}_i-\mathbf{x})\Big\rangle}_{=0} \\ &= \mathbf{f}_b\cdot\mathbf{u} \end{aligned} \tag{2.29}$$

that correspond to rate of work done by the body forces on the ensemble of particles.

For what concerns the term $\boldsymbol{\mathcal{C}}$:

$$\begin{aligned}\boldsymbol{\mathcal{C}} &= \sum_{i=1}^{N}\Big\langle\Big[\frac{1}{2}m_i(u^2+2\mathbf{u}\cdot\mathbf{C}_i+C_i^2)(\mathbf{u}+\mathbf{C}_i)\delta(\mathbf{r}_i-\mathbf{x})\Big]\Big\rangle \\ &= \sum_{i=1}^{N}\Big\langle\Big[\frac{1}{2}m_iu^2\mathbf{u}\delta(\mathbf{r}_i-\mathbf{x})\Big]\Big\rangle + \sum_{i=1}^{N}\Big\langle\Big[\frac{1}{2}m_iu^2\mathbf{C}_i\delta(\mathbf{r}_i-\mathbf{x})\Big]\Big\rangle \\ &+ \sum_{i=1}^{N}\Big\langle\Big[\frac{1}{2}m_i(2\mathbf{u}\cdot\mathbf{C}_i)\mathbf{u}\delta(\mathbf{r}_i-\mathbf{x})\Big]\Big\rangle + \sum_{i=1}^{N}\Big\langle\Big[\frac{1}{2}m_i(2\mathbf{u}\cdot\mathbf{C}_i)\mathbf{C}_i\delta(\mathbf{r}_i-\mathbf{x})\Big]\Big\rangle \\ &+ \sum_{i=1}^{N}\Big\langle\Big[\frac{1}{2}m_iC_i^2\mathbf{u}\delta(\mathbf{r}_i-\mathbf{x})\Big]\Big\rangle + \sum_{i=1}^{N}\Big\langle\Big[\frac{1}{2}m_iC_i^2\mathbf{C}_i\delta(\mathbf{r}_i-\mathbf{x})\Big]\Big\rangle \\ &= \frac{1}{2}u^2\mathbf{u}\underbrace{\sum_{i=1}^{N}\Big\langle m_i\delta(\mathbf{r}_i-\mathbf{x})\Big\rangle}_{=\rho} + \frac{1}{2}u^2\underbrace{\sum_{i=1}^{N}\Big\langle m_i\mathbf{C}_i\delta(\mathbf{r}_i-\mathbf{x})\Big\rangle}_{=\mathbf{0}} \\ &+ \mathbf{u}\cdot\underbrace{\sum_{i=1}^{N}\Big\langle m_i\mathbf{C}_i\delta(\mathbf{r}_i-\mathbf{x})\Big\rangle}_{=\mathbf{0}}\mathbf{u} + \mathbf{u}\cdot\underbrace{\sum_{i=1}^{N}\Big\langle m_i\mathbf{C}_i\mathbf{C}_i\delta(\mathbf{r}_i-\mathbf{x})\Big]\Big\rangle}_{=-\boldsymbol{\tau}} \\ &+ \mathbf{u}\underbrace{\sum_{i=1}^{N}\Big\langle\Big[\frac{1}{2}m_iC_i^2\delta(\mathbf{r}_i-\mathbf{x})\Big]\Big\rangle}_{\rho e_{\text{int}}} + \underbrace{\sum_{i=1}^{N}\Big\langle\Big[\frac{1}{2}m_iC_i^2\mathbf{C}_i\delta(\mathbf{r}_i-\mathbf{x})\Big]\Big\rangle}_{=\boldsymbol{\Phi}} \\ &= \Big(\frac{1}{2}\rho u^2+\rho e_{\text{int}}\Big)\mathbf{u}+\boldsymbol{\Phi}-\mathbf{u}\cdot\boldsymbol{\tau}\end{aligned} \tag{2.30}$$

where $\mathbf{\Phi}$ is the flux of internal energy due to the random motion of the molecules. This quantity can be express as a function of macroscopic quantities through the well-known Fourier law:

$$\mathbf{\Phi} = -k\boldsymbol{\nabla}T \tag{2.31}$$

where T is the macroscopic temperature and k is the thermal conductivity of the fluid.

Therefore, plugging eqs. (2.29), (2.30) and (2.31) into eq. (2.28), the complete equation for the rate of change of energy density reads:

$$\frac{\partial}{\partial t}\Big(\frac{1}{2}\rho u^2 + \rho e_{\text{int}}\Big) + \boldsymbol{\nabla}\cdot\Big[\Big(\frac{1}{2}\rho u^2 + \rho e_{\text{int}}\Big)\mathbf{u}\Big] = \boldsymbol{\nabla}\cdot(k\boldsymbol{\nabla}T) + \boldsymbol{\nabla}\cdot(\mathbf{u}\cdot\boldsymbol{\tau}) + \mathbf{f}_b\cdot\mathbf{u} \tag{2.32}$$

With the assumption that the fluid is incompressible (ρ constant) and that the thermal conductivity is constant, eq. (2.32) can be further simplified:

$$\rho\frac{\partial}{\partial t}\Big(\frac{1}{2}u^2 + e_{\text{int}}\Big) + \rho\boldsymbol{\nabla}\cdot\Big[\Big(\frac{1}{2}u^2 + e_{\text{int}}\Big)\mathbf{u}\Big] = k\nabla^2 T + \underbrace{\boldsymbol{\nabla}\cdot(\mathbf{u}\cdot\boldsymbol{\tau})}_{=(\boldsymbol{\nabla}\cdot\boldsymbol{\tau})\cdot\mathbf{u}+\boldsymbol{\tau}:\boldsymbol{\nabla}\mathbf{u}} + \mathbf{f}_b\cdot\mathbf{u} \tag{2.33}$$

where the (:) operation represents the tensorial double inner product.

Eq. (2.33) can be further simplified if the contribution of kinetic and internal energy is split into two equations. Indeed, it is worth noting that the balance of kinetic energy can be accounted for with the momentum equation without the need to solve another equation. On the contrary, the calculation of the internal energy needs an extra balance equation to be assessed.

Let us multiply (dot product) the momentum equation for incompressible fluids by the velocity:

$$\rho\frac{\partial\mathbf{u}}{\partial t}\cdot\mathbf{u} + \rho\boldsymbol{\nabla}\cdot(\mathbf{u}\mathbf{u})\cdot\mathbf{u} = (\boldsymbol{\nabla}\cdot\boldsymbol{\tau})\cdot\mathbf{u} + \mathbf{f}_b\cdot\mathbf{u} \tag{2.34}$$

and with a few mathematical manipulation, the transport equation for the kinetic energy becomes:

$$\frac{1}{2}\rho\frac{\partial u^2}{\partial t} + \frac{1}{2}\rho\boldsymbol{\nabla}\cdot(u^2\mathbf{u}) = (\boldsymbol{\nabla}\cdot\boldsymbol{\tau})\cdot\mathbf{u} + \mathbf{f}_b\cdot\mathbf{u} \tag{2.35}$$

The balance equation for the internal energy is obtained subtracting eq.(2.35) from (2.33):

$$\rho\frac{\partial e_{\text{int}}}{\partial t} + \rho\boldsymbol{\nabla}\cdot(e_{\text{int}}\mathbf{u}) = k\nabla^2 T - \boldsymbol{\tau} : \boldsymbol{\nabla}\mathbf{u} \tag{2.36}$$

where the $\boldsymbol{\tau} : \boldsymbol{\nabla}\mathbf{u}$ accounts for kinetic energy degradation due to viscous dissipation. In practical thermal-convection problem, this term can be neglected since its order of magnitude is smaller than the other therms in the equation.

Before concluding this section, it is worth noting that this is not the usual form of the energy equation used in thermal convection problems, where the macroscopic temperature represents the unknown. Luckily, internal energy and temperature are proportional:

$$de_{\text{int}} = c_V dT \tag{2.37}$$

where c_V is the specific heat at constant volume.

Moreover, for incompressible fluids, $c_V \approx c_P$, where c_P is the specific heat at constant pressure. Therefore, neglecting the viscous dissipation therm and accounting for eq. (2.37), eq. (2.36) becomes:

$$\rho c_P\frac{\partial T}{\partial t} + \rho c_P\boldsymbol{\nabla}\cdot(T\mathbf{u}) = k\nabla^2 T \tag{2.38}$$

Eventually, defining the thermal diffusion coefficient as $\alpha = \frac{k}{\rho c_P}$, the energy balance equation reads:

$$\frac{\partial T^*}{\partial t} + \boldsymbol{\nabla}\cdot(T^*\mathbf{u}^*) = \alpha\nabla^2 T^* \tag{2.39}$$

where even in this case the asterisks indicate that the quantity is dimensional.

2.1.4 The Oberbeck–Boussinesq approximation

In the preceding sections, the assumption that the fluid has a constant density (hypothesis of incompressibility) made it possible to simplify the balance equations considerably. However, variations of density due to a temperature difference are the only driven force in different types of convective flows, namely, thermogravitational

and thermovibrational convection, as discussed up to a certain extent in Chapter 1. Therefore, there is a need to account for the density's dependency on the temperature.

Moreover, up to this point, the (density of) body force $\mathbf{f}_b$ has not been characterised yet, but rather has been considered as a generic term in the momentum balance equation. To tackle the issue of constant density, we can suppose that the only macroscopic force acting on the fluid is the weight of the fluid itself. Therefore, the body force reads:

$$\mathbf{f}_b = \rho' g \mathbf{i}_g \tag{2.40}$$

where g is the magnitude of the steady gravitational acceleration and $\mathbf{i}_g$ is the unit vector pointing in the direction of gravity. Let us note that the density in this term differs from the density in the rest of the equation. This is the basis of the so-called Oberbeck-Boussinesq (O-B) approximation. In particular, this framework initially introduced by Oberbeck [145] and Boussinesq [146], states that the density can be considered constant in every term of the momentum balance equation except for in the buoyancy term, where it is a function of the temperature. Specifically, for convective flow, the density can be approximated as the linear Taylor expansion of the density function $\rho'(T)$:

$$\rho' = \rho + \frac{d\rho}{dT}(T - T_{\text{ref}}) \; [+\mathcal{O}(T - T_{\text{ref}})^2] \tag{2.41}$$

where $\rho'(T_{\text{ref}}) = \rho$.

Moreover let us note that the thermal expansion coefficient can defined as $\beta_T = -d\rho/dT$, and that neglecting the non-linear terms eq.(2.41) becomes:

$$\rho' = \rho - \beta_T(T - T_{\text{ref}}) \tag{2.42}$$

Before presenting the balance equation for the momentum accounting for the buoyancy term, it is convenient to consider that, in general, the pressure can be written as the sum of a hydrostatic and a hydrodynamic term, i.e. $p = \rho g h + \tilde{p}$, where $\tilde{p}$ is the hydrodynamic pressure, and h is the depth of the fluid along the direction of the gravity.

The pressure gradient appearing in the momentum equation becomes:

$$\boldsymbol{\nabla} p = \boldsymbol{\nabla} \tilde{p} + \rho g \boldsymbol{\nabla} h = \boldsymbol{\nabla} \tilde{p} + \rho g \mathbf{i}_g \tag{2.43}$$

At this point it is clear that introducing the O-B approximation and summing up the pressure gradient and buoyancy term, leads to:

$$-\boldsymbol{\nabla} p + [\rho - \beta_T (T - T_{\text{ref}})] g \mathbf{i}_g = -\boldsymbol{\nabla} \tilde{p} - \beta_T (T - T_{\text{ref}}) g \mathbf{i}_g \tag{2.44}$$

Moreover, it is worth noting that usually, when dealing with the O-B approximation in a CFD context, the fact that the pressure under analysis is the *dynamic* one is so obvious that the "˜" is simply omitted. From now on, this work will follow the standard notation, that is, the pressure p will simply refer to the hydrodynamic pressure.

2.1.5 The effect of unsteady acceleration

Before casting the momentum equation for Newtonian fluids in its final form, it is worth it generalising the buoyancy term, i.e. accounting for unsteady accelerations. Indeed, this work will primarily focus on convection induced by vibrations.

The easiest way to introduce vibrations to the system is supposing that it is excited by a sinusoidal displacement:

$$\mathbf{s}(t) = b \sin(\omega t) \mathbf{n}_\omega \tag{2.45}$$

where b is the amplitude, ω is the angular frequency($\omega = 2\pi f$, f being the frequency), and $\mathbf{n}_\omega$ is the direction of the vibrations.

The resulting acceleration can easily be obtained considering the displacement second derivative with respect to time:

$$\mathbf{a}_\omega(t) = \boldsymbol{\gamma} \sin(\omega t) \tag{2.46}$$

where $\boldsymbol{\gamma} = -b\omega^2 \mathbf{n}_\omega$.

It is straightforward to observe that different "shapes" of vibrational waves can be considered by changing the sinusoidal law in eq. (2.46). For example, in this work, square (pulse) waves are also considered. In that case, the acceleration can be modelled as:

$$\mathbf{a}_\omega(t) = \boldsymbol{\gamma} \tanh[10 \sin(\omega t)] \tag{2.47}$$

To conclude, accounting for the O-B approximation and general periodic accelerations, the balance equation for the momentum equation (eq. (2.23)) in dimensional form becomes:

$$\rho \frac{\partial \mathbf{u}^*}{\partial t} + \rho \boldsymbol{\nabla} \cdot (\mathbf{u}^* \mathbf{u}^*) = -\boldsymbol{\nabla} p^* + \eta \nabla^2 \mathbf{u}^* + \rho \beta_T (T^* - T^*_{\text{ref}})(g \mathbf{i}_g + \mathbf{a}^*_\omega) \tag{2.48}$$

where the p simply represents the hydrodynamic pressure, as explain in section 2.1.4.

2.1.6 Thermocapillary flow: the Marangoni boundary condition

Until now, only buoyancy-driven convection (with steady and unsteady driven force) has been considered. However, as discussed in CHAPTER 1, another type of convection, not driven by buoyancy, but rather by a gradient of surface tension, may arise if the fluid volume has a *free surface*.

Similarly to the density, in these circumstances the surface tension of a fluid can be modelled as a function of the the temperature ($\sigma = \sigma(T)$). Developing this function in Taylor series and truncating it to the first order, the surface tension can be written as:

$$\sigma(T) = \sigma_{\text{ref}} - \sigma_T (T - T_{\text{ref}}) \tag{2.49}$$

where $\sigma_{\text{ref}} = \sigma(T_{\text{ref}})$ and $\sigma_T = -d\sigma/dT|_{T=T_{\text{ref}}} (> 0)$.

Therefore, if a temperature gradient is applied within the geometry, on turn, it will generate a tangential stress, know as Marangoni stress, on the free surface:

$$\boldsymbol{\tau}_\sigma = (\mathbf{I} - \hat{\mathbf{n}}\hat{\mathbf{n}}) \boldsymbol{\nabla} \sigma = \sigma_T (\mathbf{I} - \hat{\mathbf{n}}\hat{\mathbf{n}}) \boldsymbol{\nabla} T \tag{2.50}$$

where $\mathbf{I}$ is the unit tensor and $\hat{\mathbf{n}}$ is the unit vector orthogonal to the free surface.

Let us now consider a non deformable free surface. On this boundary, the Marangoni stress must be balanced by the dissipative stress tensor in the liquid (in the following also referred to as Newtonian stress tensor). As derived in subsection 2.1.2, the Newtonian stress reads:

$$\boldsymbol{\tau}_s = \eta[\boldsymbol{\nabla}\mathbf{u} + (\boldsymbol{\nabla}\mathbf{u})^\intercal] \tag{2.51}$$

Mathematically, the boundary condition (the stress balance) can be simply cast in the form $\boldsymbol{\tau}_s + \boldsymbol{\tau}_\sigma = \mathbf{0}$, leading to:

$$\eta[\boldsymbol{\nabla}\mathbf{u}^* + (\boldsymbol{\nabla}\mathbf{u}^*)^\intercal] \cdot \hat{\mathbf{n}} = -\sigma_T(\mathbf{I} - \hat{\mathbf{n}}\hat{\mathbf{n}})\boldsymbol{\nabla}T^* \tag{2.52}$$

2.2 The balance equations for viscoelastic liquids

The balance equations derived in the previous section (eqs. (2.14), (2.48) and (2.39)), along with the Marangoni boundary condition (2.52) can properly describe convective flows in Newtonian fluids.

However, they are insufficient to tackle similar issues where non-Newtonian fluids are considered. Fortunately, with a few modifications, the balance equations for Newtonian fluids derived in the preceding section can still be used.

Before moving forward with the derivation of the balance equations, it is worth highlighting that this thesis will only treat a sub-category of non-Newtonian fluid, i.e. viscoelastic liquids. More specifically, Boger fluids, which are fluids that exhibit constant viscosity over a wide range of shear rates, are analysed in this work. Among different models employed for the investigation of viscoelastic fluid dynamic phenomena, in this study, only the Oldroyd-B and the FENE–CR (Finite Extendable Non-linear Elastic – Chilcott and Rallison) models will be used.

As anticipated, there is no straightforward macroscopic approach to derive the balance equations in these circumstances. Hence, in this thesis, they will be inferred through microscopic considerations. Let us start from the so-called *dumbbell* archetype, which hypothesise that a viscoelastic fluid is a solution of a Newtonian solvent, having dy-

namic viscosity η_s, and an elastic (polymeric) solute with a dynamic viscosity η_p. The resulting solution will have a total dynamic viscosity $\eta_0 = \eta_s + \eta_p$. According to the dumbbell archetype, the polymeric solute can be modelled as a spring that interconnects two beads, as depicted in Figure 2.1. The spring represents the entropic tendency of the polymeric molecule to stretch and bring the beads back together as it is subjected to external forces. For this reason, the system combining the Newtonian solvent and the polymer molecules mimics the generation and the retention of elastic force typical of viscoelastic liquids.

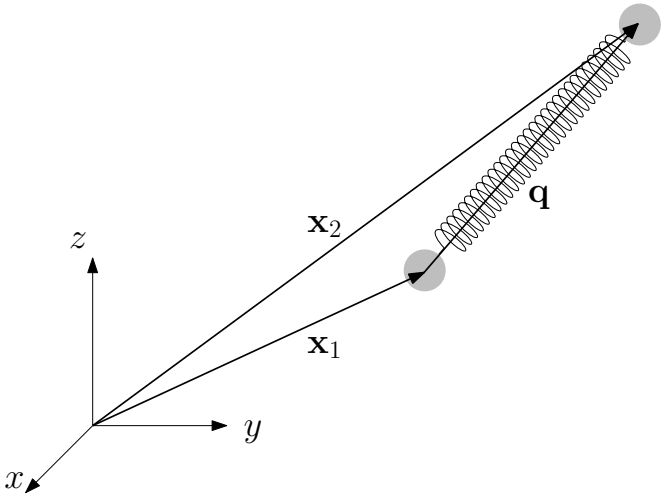

Figure 2.1: Sketch of the dumbbell model.

Using this approach, the total stress tensor (without the pressure contribution) can be split into two contributions [147, 148], i.e. the dissipative Newtonian stress $\boldsymbol{\tau}_s$, given by eq.(2.51) where now $\eta = \eta_s$, and an extra stress due to the elastic component of the fluid $\tilde{\boldsymbol{\tau}}$:

$$\boldsymbol{\tau}_{\text{tot}} = \boldsymbol{\tau}_s + \tilde{\boldsymbol{\tau}} \tag{2.53}$$

Therefore, the momentum equation can be simply modified by adding the divergence of to extra stress tensor ($\boldsymbol{\nabla} \cdot \tilde{\boldsymbol{\tau}}$) to the right-hand-side of eq. (2.48):

$$\rho \frac{\partial \mathbf{u}^*}{\partial t} + \rho \boldsymbol{\nabla} \cdot (\mathbf{u}^* \mathbf{u}^*) = -\boldsymbol{\nabla} p^* + \eta \nabla^2 \mathbf{u}^* + \boldsymbol{\nabla} \cdot \tilde{\boldsymbol{\tau}}^* + \rho \beta_T (T^* - T^*_{\text{ref}})(g \mathbf{i}_g + \mathbf{a}^*_\omega) \tag{2.54}$$

The problem now reduces to finding a way to mathematically close the set of differential balance equations, i.e. find an expression that links $\tilde{\boldsymbol{\tau}}$ to the other macroscopic quantities that characterise the fluid.

For this purpose, let us apply Newton's second law to a dumbbell immersed in a Newtonian solvent. Three different forces act on each bead:

1. The drag force due to the motion of fluid around the bead ($\mathbf{F}_D$),

2. The force caused by the *Brownian* motion ($\mathbf{F}_B$),

3. The spring force ($\mathbf{F}_S$).

Therefore we can write the Newton's second law for the i-th bead as:

$$m_i \frac{d^2\mathbf{x}_i(t)}{dt^2} = \mathbf{F}_{Di}(t) + \mathbf{F}_{Bi}(t) + \mathbf{F}_{Si}(t) \tag{2.55}$$

where, as sketched in Figure 2.1, $\mathbf{x}_i$ and m_i are the position and mass of the i-th bead.

The drag force acting on each bead is simply given by:

$$\mathbf{F}_{Di}(t) = 6\pi\eta_s a \left[\mathbf{u}(\mathbf{x}_i(t)) - \frac{d\mathbf{x}_i(t)}{dt} \right] \tag{2.56}$$

where a is the molecule radius of gyration (considered constant for every molecule dispersed in the fluid) and $\mathbf{u}(\mathbf{x}_i(t))$ is the macroscopic velocity of the solvent around the i-th bead.

In order to evaluate the elastic force exerted on each bead, it is convenient to classify two different types of springs, namely linear and non-linear. The first one, the most simple spring, reacts to a displacement with a force that is linearly proportional to the displacement itself. The linearity implies that, from a mathematical standpoint, the spring can be infinitely extended. On the contrary, different types of non-linear springs can exist. However, in modelling viscoelastic fluids, finite extensible springs are commonly employed, which means that it exists a limit over which the dumbbell cannot be further stretched.

Regardless of the type of spring that is considered, the extra polymeric stress generated by the elasticity can be evaluated on the basis of simple arguments.

Firstly, let us recall that, macroscopically, the force applied on the surface of a control volume of a Newtonian fluid can be evaluated as:

$$\mathbf{F} = \int_S \boldsymbol{\tau} \cdot \mathbf{n}\, dS \tag{2.57}$$

where $\boldsymbol{\tau}$ is given by eq (2.22) and $\mathbf{n}$ is the unit vector normal to the surface. The extra-stress due to the elasticity of the polymer can be evaluated similarly. Let us consider a single dumbbell flowing through a control volume, as depicted in Figure 2.2. The related spring force $\mathbf{F}_{S_j}$ reads:

$$\mathbf{F}_{S_j}(t) = \kappa \mathbf{q}_j(t) \tag{2.58}$$

where $\mathbf{q}_j(t) = \mathbf{x}_{2,j}(t) - \mathbf{x}_{1,j}(t)$ is the spring elongation or end-to-end vector and describes the orientation of the j-th molecule in the physical space, and κ is the spring stiffness. Moreover, we can define the entropic tendency of a dumbbell to cross the control volume as $\mathbf{q}_j \cdot \mathbf{n}\, dS$.

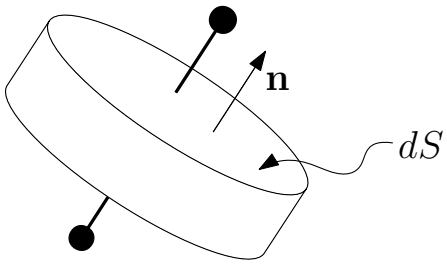

Figure 2.2: Schematisation of a dumbbell flowing though the surface of a generic control volume.

Therefore the density of force exerted by the j-th dumbbell on the surface can be evaluated as the average elastic force over all the possible configurations of the dumbbell (the averaging function is similar to the one defined in eq. (2.3)):

$$\begin{aligned} \mathbf{F}_j &= \int_S \langle \mathbf{F}_{S_j} \mathbf{q}_j \cdot \mathbf{n}\, dS \delta(\mathbf{x} - \mathbf{x}_{\mathrm{cm},j}) \rangle \\ &= \int_S \langle \mathbf{F}_{S_j} \mathbf{q}_j \delta(\mathbf{x} - \mathbf{x}_{\mathrm{cm},j}) \rangle \cdot \mathbf{n}\, dS \end{aligned} \tag{2.59}$$

where $\mathbf{x}$ is the generic position in space and $\mathbf{x}_{\mathrm{cm},j}$ is the the dumbbell centre of mass position.

The same force can also be evaluated using eq. (2.57), where the Newtonian stress tensor is replaced by the viscoelastic extra-stress tensor $\tilde{\boldsymbol{\tau}}_j$ exerted by the single molecule. It follows that:

$$\int_S \tilde{\boldsymbol{\tau}}_j \cdot \mathbf{n}\, dS = -\int_S \langle \mathbf{F}_{S_j} \mathbf{q}_j \delta(\mathbf{x} - \mathbf{x}_{\mathrm{cm},j}) \rangle \cdot \mathbf{n}\, dS \tag{2.60}$$

where the minus on the right hand side has been introduced due to the nature of the elastic force (negative for positive displacement of the spring, and vice versa).

Since this equation must be valid for every control volume, hence $\forall\, S$ and $\mathbf{n}$, the integral operator and the dot product $(\cdot\mathbf{n})$ can be dropped, leading to:

$$\tilde{\boldsymbol{\tau}}_j = -\langle \mathbf{F}_{Sj}\mathbf{q}_j\delta(\mathbf{x}-\mathbf{x}_{\mathrm{cm},j})\rangle \tag{2.61}$$

Moreover, if in the fluid there are dispersed N_p particles, the macroscopic expression of the viscoelastic extra-stress tensor can be considered as the sum of each molecule's contribution to the stress $\tilde{\boldsymbol{\tau}}_j$, implying that:

$$\tilde{\boldsymbol{\tau}}(t) = \sum_{j=1}^{N_p} \tilde{\boldsymbol{\tau}}_j = -\sum_{j=1}^{N_p} \langle \mathbf{F}_{Sj}(t)\mathbf{q}_j\delta(\mathbf{x}-\mathbf{x}_{\mathrm{cm},j})\rangle \tag{2.62}$$

that is, the extra-stress introduced by the polymeric chains can be seen as the (statistic) average value of the elastic force over all the possible configuration of the molecules, for all the molecules dispersed in the fluid.

2.2.1 The Oldroyd–B model

To derive the equations for the *Oldroyd–B* model a linear spring is considered. The stiffness of a molecule can be evaluated on the basis of thermodynamic forces as [147]:

$$\kappa = \frac{3k_BT}{a^2} \tag{2.63}$$

where k_B is the *Boltzmann constant*. This quantity is directly related to the entropy of the polymeric chain. Therefore, accounting for eq. (2.58), eq. (2.62) becomes:

$$\tilde{\boldsymbol{\tau}}(t) = -\frac{3k_BT}{a^2}\sum_{i=1}^{N_p} \langle \mathbf{q}_j\mathbf{q}_j\delta(\mathbf{x}-\mathbf{x}_{\mathrm{cm},j})\rangle \tag{2.64}$$

It is straightforward to observe that the polymeric stress changes in time and depends not only on the velocity of the surrounding solvent, but also on the average level of deformation of the springs dispersed in the Newtonian fluid matrix. Therefore, tracking the global rate of change in polymeric deformation level seems necessary. This operation

will lead to an additional equation that will be solved along with the balance equations introduced for Newtonian fluids.

For the sake of brevity, the complete derivation of the balance equation for $\tilde{\boldsymbol{\tau}}(t)$ is reported in Appendix A. Here, let us simply report the final result of such an exercise:

$$\lambda\left(\frac{\partial\tilde{\boldsymbol{\tau}}^*}{\partial t}+\mathbf{u}^*\cdot\boldsymbol{\nabla}\tilde{\boldsymbol{\tau}}^*\right)+\tilde{\boldsymbol{\tau}}^*=\eta_p\Big(\boldsymbol{\nabla}\mathbf{u}^*+(\boldsymbol{\nabla}\mathbf{u}^*)^{\intercal}\Big)+\lambda\Big(\tilde{\boldsymbol{\tau}}^*\cdot\boldsymbol{\nabla}\mathbf{u}^*+(\boldsymbol{\nabla}\mathbf{u}^*)^{\intercal}\cdot\tilde{\boldsymbol{\tau}}^*\Big) \quad (2.65)$$

Along with eqs. (2.14), (2.54) and (2.39), eq. (2.65) can properly describe convective flows in viscoelastic fluid with constant viscosity (Boger fluids).

2.2.2 The FENE–CR model

Although the Oldroyd-B model represents the reference framework for most studies on isothermal and non-isothermal flows in viscoelastic fluids, it is derived from the (unphysical) assumption that the molecules are infinitely extensible. In turn, this assumption can lead to numerical instabilities when the set of balance equations is numerically integrated. Moreover, the Oldroyd-B model is not adequate for several applicative problems (the interested reader is referred to, e.g. Refs [151, 152] and references therein). For these reasons, other models were proposed. The simplest way to tackle the problem mentioned above is to replace the linear spring with a non-linear finite extensible one. This leads to a class of models known as FENE (Finite Extensible Non-linear Elastic) models. FENE-type models come in different variants. One of the most popular is known as FENE-P (the "P" stands for Peterlin [153, 154], the name of the researcher that initially proposed it) steams from consideration similar to the ones used to the derive the Oldroyd-B framework, and therefore, it has a direct physical interpretation [147].

However, the FENE-P model cannot be used to study Boger fluids since it accounts for shear-thinning effects, i.e. the viscosity is not constant. In other words, if the final goal is to study the sole effect of viscoelasticity on a particular flow, the FENE-P is not a good candidate. For this reason, Chilcott & Rallison [155] proposed a simplified model, known as FENE-CR, accounting for finite extensible molecules without displaying any viscosity change (shear-thinning) effects. The model is a simple mathem-

atical modification of the FENE-P. Hence, there is no direct microscopic derivation and can be seen as a compromise between the Oldroyd-B and FENE-P models. Therefore, the balance equation for the extra-stress tensor can still be used to study the category of Boger fluids and can be regarded as a modification of the Oldroyd-B equation (eq. (2.65)):

$$\lambda\left(\frac{\partial\tilde{\boldsymbol{\tau}}^*}{\partial t}+\mathbf{u}^*\cdot\boldsymbol{\nabla}\tilde{\boldsymbol{\tau}}^*\right)+f[\mathrm{tr}(\tilde{\boldsymbol{\tau}}^*)]\tilde{\boldsymbol{\tau}}^*=\eta_p f[\mathrm{tr}(\tilde{\boldsymbol{\tau}}^*)]\left(\boldsymbol{\nabla}\mathbf{u}^*+(\boldsymbol{\nabla}\mathbf{u}^*)^\intercal\right)+\lambda\left(\tilde{\boldsymbol{\tau}}^*\cdot\boldsymbol{\nabla}\mathbf{u}^*+(\boldsymbol{\nabla}\mathbf{u}^*)^\intercal\cdot\tilde{\boldsymbol{\tau}}^*\right) \tag{2.66}$$

where $f[\mathrm{tr}(\tilde{\boldsymbol{\tau}}^*)]$ is a quantity related to the possible deformation of the polymeric molecule and reads:

$$f[\mathrm{tr}(\tilde{\boldsymbol{\tau}}^*)]=\frac{L^2+\frac{\lambda}{\eta_p}\mathrm{tr}(\tilde{\boldsymbol{\tau}})}{L^2-3} \tag{2.67}$$

where L^2 is the so-called *finite extensibility* parameter of the polymer molecule.

Interestingly, if $L^2\to\infty$, $f[\mathrm{tr}(\tilde{\boldsymbol{\tau}}^*)]\to 1$ and eqs. (2.65) and (2.66) become equal. Therefore, by selecting a high value of the finite extensibility parameter, the two models will return similar results. These properties will be used in the following part to validate the numerical solver.

2.2.3 The Marangoni boundary condition for viscoelastic fluids

At this point, it is clear that the effect of the buoyancy force can be modelled independently from the viscoelasticity of the fluid and can be fully accounted for with eq. (2.54). On the contrary, the Marangoni boundary condition for Newtonian fluids (eq. (2.52)) must be further modified to account for the elastic contribution. It is worth noting that eq. (2.50) is still valid. Therefore it will be sufficient to replace the Newtonian stress tensor with the total stress tensor given by eq. (2.53). The stress balance on the free surface reads:

$$\eta_s[\boldsymbol{\nabla}\mathbf{u}^*+(\boldsymbol{\nabla}\mathbf{u}^*)^\intercal]\cdot\hat{\mathbf{n}}+\tilde{\boldsymbol{\tau}}^*\cdot\hat{\mathbf{n}}=-\sigma_T(\mathbf{I}-\hat{\mathbf{n}}\hat{\mathbf{n}})\boldsymbol{\nabla}T^* \tag{2.68}$$

2.3 The non-dimensional balance equations and related characteristic numbers

In the preceding sections, the final balance equations for mass, momentum energy, rate of extra stress, and stress on the free surface were characterised by an asterisk (*) to highlight the fact that all the quantities are *dimensional*. Nonetheless, it is common practice to generalise these equations through a non-dimensionalisation procedure. This leads to another advantage, i.e. the non-dimensional groups (or characteristic numbers) that characterise a problem will appear as coefficients of each equation term.

To non-dimensionalise the equations, let us consider the characteristic length of the geometry hosting the fluid ℓ. Of course, this quantity is strictly related to the problem under analysis and will be defined in more detail in the Results part of this work before presenting each specific case.

Once the characteristic length has been defined, different scaling quantities can be derived, namely, α/ℓ for the velocity, ℓ^2/α for the time, $\rho\alpha^2/\ell^2$ for the pressure, $\Delta T = T_h - T_c$ for the temperature (the subscript h and c indicate the temperature of the hot and cold boundary, present in all the problems analysed in this thesis), $\eta_0\alpha/\ell^2$ for the viscoelastic stress tensor. The complete set of balance equations in non-dimensional form can be written as:

$$\boldsymbol{\nabla}\cdot\mathbf{u} = 0 \tag{2.69}$$

$$\frac{\partial \mathbf{u}}{\partial t} + \boldsymbol{\nabla}\cdot(\mathbf{u}\mathbf{u}) = -\boldsymbol{\nabla}p + Pr\xi\nabla^2\mathbf{u} + Pr\boldsymbol{\nabla}\cdot\tilde{\boldsymbol{\tau}} + PrRaT\mathbf{i}_g + PrRa_\omega T\mathbf{a}_\Omega \tag{2.70}$$

$$\frac{\partial T}{\partial t} + \boldsymbol{\nabla}\cdot(T\mathbf{u}) = \nabla^2 T \tag{2.71}$$

$$\vartheta\left(\frac{\partial\tilde{\boldsymbol{\tau}}}{\partial t}+\mathbf{u}\cdot\boldsymbol{\nabla}\tilde{\boldsymbol{\tau}}\right)+f[\mathrm{tr}(\tilde{\boldsymbol{\tau}})]\tilde{\boldsymbol{\tau}} = \zeta\xi f[\mathrm{tr}(\tilde{\boldsymbol{\tau}})]\Big(\boldsymbol{\nabla}\mathbf{u}+(\boldsymbol{\nabla}\mathbf{u})^\intercal\Big)+\vartheta\Big(\tilde{\boldsymbol{\tau}}\cdot\boldsymbol{\nabla}\mathbf{u}+(\boldsymbol{\nabla}\mathbf{u})^\intercal\cdot\tilde{\boldsymbol{\tau}}\Big) \tag{2.72}$$

where the non-dimensional vibrational acceleration for the case of sinusoidal and square waves vibrations respectively, reads:

$$\mathbf{a}_\Omega = -\sin(\Omega t)\mathbf{n}_\omega \tag{2.73}$$

$$\mathbf{a}_\Omega = -\tanh[10\sin(\Omega t)]\mathbf{n}_\omega \tag{2.74}$$

Moreover the Marangoni boundary condition, written in its compact form reads:

$$\boldsymbol{\tau}_{\text{tot}} \cdot \hat{\mathbf{n}} = -Ma(\mathbf{I} - \hat{\mathbf{n}}\hat{\mathbf{n}})\boldsymbol{\nabla} T \tag{2.75}$$

As anticipated before, a plethora of non dimensional groups appear as equations coefficient, specifically, $Pr = \nu_0/\alpha$ is the Prandtl number, $\xi = \eta_s/\eta_0$ is the solvent-to-total viscosity ratio, $\zeta = \eta_p/\eta_s = (1-\xi)/\xi$ is the viscosity ratio, $\vartheta = \lambda\alpha/\ell^2$ is the elasticity number, $\Omega = \ell^2\omega/\alpha$ is the non-dimensional (angular) frequency, Ra is the *classical* Rayleigh number, defined as:

$$Ra = \frac{g\beta_T \Delta T \ell^3}{\nu_0 \alpha} \tag{2.76}$$

Ra_ω is the *vibrational* Rayleigh number, that is:

$$Ra_\omega = \frac{b\omega^2\beta_T \Delta T \ell^3}{\nu_0 \alpha} \tag{2.77}$$

and eventually

$$Ma = \frac{\sigma_T \Delta T \ell}{\eta_0 \alpha} \tag{2.78}$$

is the Marangoni number.

Although these parameters are sufficient to completely define a thermal convection problem, in the following sections, other non-dimensional quantities will be instrumental in properly describing convective phenomena arising in these complex fluids. It seems appropriate to introduce these quantities in this section.

Let us start introducing the non-dimensional amplitude of the oscillatory acceleration, useful in mixed thermogravitational-vibrational convection problems, as:

$$\Gamma = \frac{b\omega^2}{g} = \frac{Ra_\omega}{Ra} \tag{2.79}$$

In addition, it is known that, if the vibrations are orthogonal to the temperature gradient, the mean flow field is not properly described by the vibrational Rayleigh number but rather by the so-called Gershuni number:

$$Gs = \frac{(b\omega\beta_T\Delta T\ell)^2}{2\nu_0\alpha} = \left(\frac{Ra_\omega}{\Omega}\right)^2 \frac{Pr}{2} \tag{2.80}$$

Specifically, in these type of problem the velocity of the fluid can be split into a time-average component $\mathbf{u}_{\text{mean}}$ and a periodic component that oscillates with the same (or multiple) frequency of the imposed vibrations: $\mathbf{u} = \mathbf{u}_{\text{mean}} + \mathbf{u}'$, where:

$$\mathbf{u}_{\text{mean}} = \frac{1}{T_\Omega}\int_{T_\Omega} \mathbf{u}\, dt \tag{2.81}$$

where T_Ω is the period of the non-dimensional vibrational acceleration.

So far, there are two non-dimensional groups related to time-constants, i.e., the elasticity number, that is the ratio between the characteristic time of the polymer (the relaxation time λ) and the characteristic thermal diffusion time ($t_\alpha = \ell/\alpha$), and the non-dimensional frequency Ω, that is the ratio between the period of oscillations ($T_\omega = 2\pi/\omega$) and t_α. Given these arguments, it seems natural to introduce another dimensionless number to account for the relative "weight" between polymer and oscillations time scale, that is, the ratio between λ and T_ω:

$$\Sigma = \frac{\lambda}{T_\omega} = \frac{\Omega\vartheta}{2\pi} \tag{2.82}$$

At this point, it is also worth introducing the well-known *Nusselt* number, a non-dimensional number used to assess the strength of the convective flow or, to be more precise, the ratio between heat transfer due to convection and conduction (or diffusion).

This parameter comes in different forms, i.e. local and time-dependent form, the area-averaged and time-dependent form, and the area-and-time-averaged form. In this work, only the last two forms will be considered. They are respectively defined as:

$$Nu(t) = \frac{1}{A}\int_A \boldsymbol{\nabla} T \cdot \mathbf{n}_{\text{plate}}\, dA \tag{2.83}$$

$$\overline{Nu} = \frac{1}{T_{Nu}}\int_{T_{Nu}} Nu(t)\, dt \tag{2.84}$$

where $\mathbf{n}_{\text{plate}}$ is the unit vector normal to the heated boundary, A is its area, and T_{Nu} is the oscillation period of the area-averaged Nusselt number.

Similarly to the Nusselt number that accounts for the thermal energy exchange at the boundary of the system, we can define the kinetic and elastic energy that come in local and time-dependent form, the global or volume-averaged and time-dependent form, and the volume-and-time-averaged form. Again, only the last two forms will be used in the present work. We can use a similar definition to eqs. (2.83) and (2.84). Therefore, for the kinetic energy, they respectively read:

$$K(t) = \frac{1}{V}\int_V \mathbf{u} \cdot \mathbf{u}\, dV \tag{2.85}$$

$$\overline{K} = \frac{1}{T_K}\int_{T_K} K(t)\, dt \tag{2.86}$$

while, for the elastic energy :

$$EE(t) = \frac{1}{V}\int_V \text{tr}(\tilde{\boldsymbol{\tau}})\, dV \tag{2.87}$$

$$\overline{EE} = \frac{1}{T_{EE}}\int_{T_{EE}} EE(t)\, dt \tag{2.88}$$

where V is the volume of the fluid domain, and T_K and T_{EE} are the oscillation period of global kinetic and elastic energy respectively.

Eventually, if a free surface is considered, it is worth defining the well-known Biot number since it accounts for the ratio between the heat exchanged through conduction

inside the liquid bulk and the heat exchanged via convection with the environment surrounding the free surface. It is defined as $Bi = h\ell/k$, where h is the convective heat transfer coefficient at the free surface.

Before moving forward with the description of the numerical method, it is worth adding some information about the parameter used to account for the elasticity of the fluid, i.e. the elasticity number ϑ. This parameter has been obtained by dividing the relaxation time by the characteristic diffusion time in the fluid. As underlined by Li & Khayat [107], this parameter, in general, is not the best way to represent the influence of normal stresses. Indeed, the diffusion time does not carry any information about the fluid velocity time scale. A better parameter to account for this influence would be the so-called Deborah number De. Indeed, this non-dimensional number is directly calculated using a characteristic velocity of the flow. In problems like channel flow, it is relatively simple to asses which velocity should be used for calculating De, this being, in general, the inlet velocity. On the contrary, in problems dealing with flows of natural origin, especially when the flow field displays an oscillatory nature, choosing a characteristic velocity is not an easy task. For this reason, the majority of the studies dealing with thermal convection in viscoelastic liquids use only the elasticity number for the assessment of the effect of the elasticity.

Moreover, as proved by Li & Khayat, if ϑ is not too large (as in the present work), the elasticity number is still a suitable parameter for adequately representing the effect of elasticity. For this reason and for continuity with the existing literature, throughout this thesis, the only parameter that will be employed is the elasticity number ϑ.

The following chapter presents the numerical framework for solving the balance equations presented in the preceding sections.

Chapter 3

Numerical Method

The previous chapter derived a generic mathematical framework for studying thermal convection in viscoelastic (but also Newtonian) fluids. Solving the complete set of equations, along with the related boundary conditions, is not an easy task. Indeed, putting aside for now the complexity introduced by the viscoelastic nature of the fluid, the Navier-Sokes equation has represented, and still do, a challenge for generations of mathematics and physicist. Their hyperbolic and highly non-linear nature allows their direct (analytical) solution, only in simplified cases, far from the actual and real applications.

The introduction of fluids that do not follow the rheological Newtonian behaviour increases the non-linearity level of the set of balance equations, amplifying even further the difficulties associated with their solution. On a different note, experimental activities related to fluid behaviour in microgravity conditions come with a high cost and logistic complexities that make this field of enquiry hard to explore.

For these reasons, the natural way to tackle these problems consists of solving the balance equations numerically, i.e. algebraically solving the discretised (approximated) version of the balance equations and related boundary conditions. To do so, in the present work, the computational platform OpenFOAM® was employed. In particular, OpenFOAM is an open-source software designed for the solution of partial differential equations by mean of the Finite Volume (also known as Control Volume) Method (FVM). This methodology is particularly efficient for the solution of fluid dynamics problems [156].

Therefore, given some initial and boundary conditions, OpenFOAM will calculate $\mathbf{u}$, p, T, and $\tilde{\boldsymbol{\tau}}$ (for viscoelastic fluids). We can observe that for incompressible flows, while there is a balance equation for $\mathbf{u}$, T, and $\tilde{\boldsymbol{\tau}}$, namely momentum, energy

and viscoelastic stress transport equation, the same thing is not valid for the pressure field. Therefore, to overcome this problem, during the years were proposed several techniques. For example, very popular is the solution of the balance equations equation in their stream-function and vorticity form. However, this technique is only limited to 2D geometries. For the class of primitive variable techniques, the algorithms available can be divided into two big categories, namely coupled [157] and segregated (also known as projection) methods. Although OpenFOAM allows the user to choose between coupled and segregated solvers, the second ones are more indicated for time-marching problems. Therefore, the category of projection method algorithms will be used throughout this work. More specifically, OpenFOAM relies on the solution of the balance equation on a co-located grid where the Rhie & Chow interpolation scheme [158] for the pressure is used to avoid checkerboarding. Moreover, the Piso (Pressure-Implicit with Splitting of Operators) algorithm is particularly indicated for problems involving heat exchange and convective flows.

A brief explanation of the rationale behind segregated algorithms like Piso will be presented hereafter.

3.1 The projection method

As introduced above, the need for an algorithm that couples velocity and pressure stems from the fact that there is no balance equation for the pressure that closes the set of balance equations. The category of the projection methods stems from the so-called *Hodge decomposition theorem* [159] which states that any type of vector field can be expressed as the sum of a divergence-free and a curl-free part, i.e. the gradient of a scalar potential. In this case, the vector field is the velocity, while the pressure represents the scalar potential.

Following Ref. [160] and the Hodge decomposition theorem, the velocity $\mathbf{u}$ can be divided into the sum of an intermediate $\mathbf{u}'$ and correction $\widehat{\mathbf{u}}$ component ($\mathbf{u} = \mathbf{u}' + \widehat{\mathbf{u}}$). Accordingly, the pressure can be decomposed as $p = p' + \widehat{p}$, where p' and $\widehat{p}$ are the pressure intermediate and correction components respectively. In a time marching

procedure, the intermediate component of the pressure is usually selected equal to the pressure at the preceding time step.

For the sake of simplicity and without losing the generality of such an approach, let us consider the momentum equation for an incompressible Newtonian fluid subjected to a generic body force as the one in eq. (2.23). Let us discretised this equation in time and rewrite it for the intermediate field omitting the (*) to indicate the fact that the quantities are in dimensional form:

$$\rho\frac{\mathbf{u}' - \mathbf{u}^n}{\Delta t} = -\rho\boldsymbol{\nabla}\cdot(\mathbf{u}^n\mathbf{u}') - \boldsymbol{\nabla}p' + \eta\nabla^2\mathbf{u}' + \mathbf{f}_b \tag{3.1}$$

where Δt is the integration time-step and the superscript n represents the quantity at the previous time-step. Here, for the sake of simplicity the time-integration schemes resemble an implicit first order scheme with a classical Picard linearisation in the convective term.

The solution of this equation will give the intermediate velocity field $\mathbf{u}'$ characterised by the fact that it has a non-zero divergence, hence, it does not follow the continuity equation. Moreover the correction components of velocity and pressure are related through the following equality:

$$\rho\frac{\mathbf{u}^{n+1} - \mathbf{u}'}{\Delta t} = \rho\frac{\widehat{\mathbf{u}}}{\Delta t} = -\boldsymbol{\nabla}\widehat{p} \tag{3.2}$$

Indeed, adding eq. (3.2) to eq. (3.1), we can observe that the time-discretised momentum balance equation is recovered.

Moreover, for the incompressibility constrain:

$$\boldsymbol{\nabla}\cdot\mathbf{u}^{n+1} = 0 \tag{3.3}$$

Therefore, *projecting* eq. (3.2) in eq. (3.3), a closure equation for the correction pressure is obtained:

$$\nabla^2\widehat{p} = \frac{\rho}{\Delta t}\mathbf{u}' \tag{3.4}$$

This equation is known as the elliptic equation for pressure. Therefore, velocity and pressure field are *segregated* into two different equations.

The solution of eq. (3.4) is $\widehat{p}$. It follows that $p^{n+1} = p' + \widehat{p}$, and that the correction velocity can be calculated as:

$$\widehat{\mathbf{u}} = \frac{\Delta t}{\rho} \boldsymbol{\nabla} \widehat{p} \tag{3.5}$$

leading to the correct solenoidal velocity field $\mathbf{u}^{n+1} = \mathbf{u}' + \widehat{\mathbf{u}}$.

Although the Piso algorithm [161] is fragmented in more steps when compared to the one just presented, the two share the same rationale.

Moreover, it is worth highlighting that the reason why other methods such as the Pimple [156] (generally faster than the Piso) were not used for the present simulations can be explained as follow. In the problems analysed in this work, the time-step is "constrained" by two different aspects: (i) the frequency of the vibrations, (ii) the stability of the viscoelastic model (not related to the classical Courant number). The time-step must be sufficiently small to avoid aliasing with respect to the external vibrations and to guarantee the stability of the viscoelastic model at the same time. For these reasons, the advantages associated with other computational variants such as the Pimple, i.e. marching with a Courant number greater than 1, become irrelevant (while related drawbacks, such as the increased computational cost and selection of under-relaxation factors would be retained) [162].

3.2 Stabilising techniques for viscoelastic models

Although the segregated algorithms, especially when the time-integration scheme is implicit, are reliable, robust and stable when using the classical Newtonian model, when dealing with viscoelastic fluids, special attention must be paid to the coupling and time integration of the balance equation. As explained in the section above, the time step is constrained by the stability of the viscoelastic model. Indeed, the extra stress transport equation is hyperbolic in nature. This property increases the level of non-linearity and, at the same time, makes the system of balance equations more challenging to solve.

In particular, defining a new non-dimensional number known as the Weissenberg number $Wi = \lambda \mathcal{U}/\ell$, where $\mathcal{U}$ is the characteristic velocity of the problem, if Wi exceeds a critical threshold that is problem-related, the time-marching algorithm becomes

unstable. This leads to numerical singularities that can generate numerical divergence of the calculation [163–168]. This class of problems is known as *high Weissenberg number problems* (HWNP).

More specifically, let us recall that when defining the properties of the conformation tensor $\mathbf{A}$, it was underlined that it is a positive-definite tensor. When the HWNP occurs, the conformation tensor can lose its positiveness. In turn, the loss of positiveness can lead to the so-called Hadamard instability that can ultimately jeopardise the whole time-marching procedure [169, 170].

Several techniques were proposed to mitigate or at least retard the appearance of these singularities. Here, only two techniques employed in this study will be briefly discussed.

The simplest techniques is know as Both Side Diffusion (BSD) and it equivalent to the DEVSS (Discrete Elastic-Viscous-Split-Stress) method originally proposed by Guénette & Fortin, 1995 [171] in the context of the finite element method. Following the implementation of Favero et al. [172] eq. (2.70) can be written in non-dimensional form as:

$$\frac{\partial \mathbf{u}}{\partial t} + \boldsymbol{\nabla} \cdot (\mathbf{uu}) - Pr\xi(1+\zeta)\nabla^2\mathbf{u} = -\boldsymbol{\nabla} p - Pr\xi\zeta\nabla^2\mathbf{u} + Pr\boldsymbol{\nabla}\cdot\tilde{\boldsymbol{\tau}} + PrRaT\mathbf{i}_g + PrRa_\omega T\mathbf{a}_\Omega \tag{3.6}$$

This numerical implementation presents an additional diffusive term $Pr\xi\zeta\nabla^2\mathbf{u}$ at the left and right-hand sides of eq. (2.70). Hence, from a purely mathematical point of view, eq. (2.70) and (3.6) are equivalent. Nevertheless, to increase the "ellipticity" of the momentum equation appreciably and therefore improve the numerical stability of the time-marching procedure, one extra term is discretised in an implicit way while the other is implemented explicitly. The beneficial stabilisation stems from the fact that the different treatment of the right- and left-hand-side term produces a quantitatively negligible numerical diffusion, which, however, appreciably improves the robustness of the solver [104].

A more complicated but also more stable method is known under the heading of *log-conformation*. Originally proposed by FATTAL & KUPFERMAN [173], this method stems from the fact that the Hadamard instability is caused by the loss of positive-definiteness of the conformation tensor during the time-and-space integration procedure. The change in positiveness is triggered by physiological discretisation errors that are introduced in every numerical solver. In turn, this causes numerical divergence. Luckily, there are different techniques to "force" positiveness, such as the log-conformation technique.

First of all, let us rewrite the transport equation of $\mathbf{A}$, derived for the Oldroyd-B in eq. (A.17), for the more generic FENE-CR model:

$$\frac{\partial}{\partial t}\mathbf{A}(\mathbf{x},t)+\mathbf{u}\cdot\boldsymbol{\nabla}\mathbf{A}(\mathbf{x},t)+\frac{\tilde{f}[\mathrm{tr}(\mathbf{A})]}{\lambda}(\mathbf{A}(\mathbf{x},t)+\mathbf{I})=\mathbf{A}(\mathbf{x},t)\cdot\boldsymbol{\nabla}\mathbf{u}+(\boldsymbol{\nabla}\mathbf{u})^{\intercal}\cdot\mathbf{A}(\mathbf{x},t) \quad (3.7)$$

where $\tilde{f}[\mathrm{tr}(\mathbf{A})]=L^2/[L^2-\mathrm{tr}(\mathbf{A})]$. Of course, the Oldroyd-B model is recovered when $\tilde{f}=1$ or equivalently when $L^2\to\infty$. The generic Kramers correlation (defined for the Oldroyd-B in eq. (A.13)) becomes [104]:

$$\tilde{\boldsymbol{\tau}}^{*}=\frac{\eta_p\tilde{f}[\mathrm{tr}(\mathbf{A})]}{\lambda}(\mathbf{A}-\mathbf{I}) \quad (3.8)$$

where, again, it is straightforward to recover the correlation for the Oldroyd-B.

The first step of the log-log conformation techniques is to solve a modified version of the balance equation for $\mathbf{A}$ (eq. (3.7)), and then calculate the extra-stress tensor though the correlation of eq. (3.8). The modified version of eq. (3.7) is obtained replacing $\mathbf{A}$ with its logarithm:

$$\boldsymbol{\Theta}=\ln(\mathbf{A})=\mathbf{R}\ln(\boldsymbol{\Lambda})\mathbf{R}^{\intercal} \quad (3.9)$$

where, using the positive definitiveness and symmetry of $\mathbf{A}$, it has always real and positive eigenvalues, and therefore it can always be diagonalised into a matrix $\boldsymbol{\Lambda}$ thank to the matrix for the change of basis $\mathbf{R}$ formed with the eigenvectors of $\mathbf{A}$. Let us remark, as noted by FATTAL & KUPFERMAN that if $\mathbf{A}=\mathbf{R}\boldsymbol{\Lambda}\mathbf{R}^{\intercal}$ then $\ln(\mathbf{A})=\mathbf{R}\ln(\boldsymbol{\Lambda})\mathbf{R}^{\intercal}$. In addition, the same authors also observe that the velocity gradient can be decomposed

as:

$$\boldsymbol{\nabla}\mathbf{u} = \boldsymbol{\Omega} + \mathbf{B} + \mathbf{N}\mathbf{A}^{-1} \tag{3.10}$$

where $\boldsymbol{\Omega}$ and $\mathbf{N}$ are antisymmetric tensors representing pure rotations, while $\mathbf{B}$ is symmetric, traceless, and commutes with the conformation tensor $\mathbf{A}$.

Therefore, eq. (3.7) written for $\boldsymbol{\Theta}$ reads [174]:

$$\frac{\partial}{\partial t}\boldsymbol{\Theta} + \mathbf{u}\cdot\boldsymbol{\nabla}\boldsymbol{\Theta} = \boldsymbol{\Omega}\boldsymbol{\Theta} - \boldsymbol{\Theta}\boldsymbol{\Omega} + 2\mathbf{B} + \frac{\tilde{f}[\mathrm{tr}(\mathbf{A})]}{\lambda}(e^{-\boldsymbol{\Theta}} + \mathbf{I}) \tag{3.11}$$

Since the unknown is now Θ, and this quantity is forced to be always definite positive by the logarithmic transformation, the instability problem are consistently mitigated and HWNP can be tackled in a more agile way.

After this equation is solved numerically, the conformation tensor is recovered through an exponential transformation ($\mathbf{A} = e^{\boldsymbol{\Theta}}$) and using eq. (3.8) it is straightforward to recover the extra stress tensor $\tilde{\boldsymbol{\tau}}$. In addition, to increase the stability and robustness of the time marching algorithm, as extensively discussed in Refs. [174–176] it also increases the precision of the solver in areas where there is an exponential growth of the stress. In this work, this approach has shown particular accuracy in predicting the critical threshold for the onset of supercritical convective flow.

For the numerical implementation of the log-conformation approach, this work uses the OpenFOAM library rheoTool by Pimenta & Alves [177].

3.3 Regularisation of the Marangoni boundary condition

Last but not least, attention has also been paid to the intrinsic singularities of Marangoni flow in finite-size geometries. These can manifest regardless of the elastic or non-elastic nature of the considered liquid (i.e. also in Newtonian fluids [178–180]) as they are not associated with specific equations but rather stem from the inconsistency of the velocity boundary conditions used for the free interface and the isothermal walls in the corners of the cavity (which explains why they are generally referred to as “viscous singularities”).

For convenience, a heuristic interpretation for their origin can be briefly provided as follows. On the solid boundary where the no-slip condition is applied, the viscous stress is $\mathbf{0}$, while, on the free surface, in general, it is not zero as the Marangoni stress condition is effective there (right-hand side of eq. (2.68)). Due to such an unphysical imbalance, a singularity is produced in the computational cell located between the interface and the perpendicular wall. While for low Prandtl number fluids ($Pr << 1$), the singularity can be implicitly bypassed by the finite precision associated with the local approximation used for the discretisation of the derivatives, for high-Prandtl number fluids, it typically manifests itself causing an unlimited growth of the velocity in this cell as the cell size is reduced. As a result, a need arises for the physical consistency to be recovered, and, from a mathematical point of view, this can be achieved if the Marangoni stress is forced to vanish at the solid walls while keeping a continuous behaviour. This is typically obtained by using a "regularisation function".

In the present work, in particular, to "regularize" the flow (Refs [178–180]), eq. (2.68) has been modified as follows:

$$\eta_s\Big[\nabla\mathbf{u}^* + (\nabla\mathbf{u}^*)^\intercal\Big]\cdot\hat{\mathbf{n}} = \mathcal{R}(x)\Big[-\tilde{\boldsymbol{\tau}}^*\cdot\hat{\mathbf{n}} - \sigma_T(\mathbf{I}-\hat{\mathbf{n}}\hat{\mathbf{n}})\cdot\nabla T^*\Big] \tag{3.12}$$

and the regularization function $\mathcal{R}(x)$ reads:

$$\mathcal{R}(x) = \begin{cases} -\frac{1}{(\chi\ell)^2}x^2 + \frac{2}{(\chi\ell)}x, & \text{if } 0 \le x \le \chi\ell \\ 1, & \text{if } \chi\ell < x < \ell(1-\chi) \\ -\frac{1}{(\chi\ell)^2}(\ell-x)^2 + \frac{2}{(\chi\ell)}(\ell-x), & \text{if } \ell(1-\chi) \le x \le \ell \end{cases} \tag{3.13}$$

where $0 \le \chi \le 1$ accounts for the percentage of regularized surface. For the simulations presented in CHAPTER 8, $\chi = 0.02$. Of course, when using Newtonian fluids, the viscoelastic extra stress is dropped.

The function $\mathcal{R}$ modifies the stress on a small percentage of cells located along the free surface, bringing its value on the first cell of the series (that is in contact with the solid wall) to ≈ 0. In this way, it filters out the viscous singularity of Marangoni flow. This artifice also guarantees the aforementioned continuity of the stress along the

free surface. The validity of this approach has already been shown in several studies appearing in the literature (see Ref. [181] and references therein).

3.4 Validation of the Mathematical and Numerical Framework

Before presenting the results, it is appropriate to validate each part of this complex mathematical and numerical framework. Remarkably, the results produced with the numerical framework just introduced in this chapter were compared with other results available in the literature.

More specifically, in this section the solver will be validated to prove that it is capable to predict different types of instabilities, namely (i) stationary and (ii) Hopf bifurcation for classical Rayleigh Bénard flow in Newtonian fluids, (iii) purely elastic instabilities in isothermal viscoelastic flows, (iv) overstable Rayleigh-Bénard convection in viscoelastic fluids, (v) thermovibrational instabilities in viscoelastic fluids, (vi) Hopf bifurcation for standard Marangoni flow in Newtonian liquids, and (vii) overstable Marangoni-Bénard convection in viscoelastic liquids. The results presented hereafter were published in Refs. [1–3, 6].

Let us start with the (i) point. To corroborate the accuracy in predicting the critical Rayleigh number, the present computational procedure results were compared with the linear stability analysis by Wanschura et al. [182] where the critical Rayleigh number was reported for liquid bridges heated from below with adiabatic interface and no surface-tension effects. Notably, since the first stationary bifurcation does not depend on Pr, this parameter is set to $Pr = 8$. Assuming a representative aspect ratio $AR = \text{height/diameter} = 0.68$, we have carried out different simulations for increasing values of Ra and then evaluated the disturbance growth rate ε by plotting the maximum velocity as a function of time in semi-logarithmic scale (the growth rate being given by the inclination of the straight line representing the evolution of disturbances before their amplitude is saturated). The critical Rayleigh number Ra_{cr} has finally been computed through extrapolation of the growth rate to zero. A comparison of the present Ra_{cr} with the value obtained by these authors indicates that the difference lies below 1% as reported in Table 3.1.

Table 3.1: Disturbance growth rate ε and azimuthal wavenumber m as a function of the Rayleigh number (liquid bridge of Newtonian fluid, $Pr = 8$, $AR = 0.68$, free-slip lateral boundary, mesh: 28 000 nodes, stationary bifurcation).

Ra	ε	m
1800	0.74	1
1700	0.50	1
1650	0.35	1
1570 (extrapolated)	0	1
LSA by Wansura et al. [182] $Ra_{cr} = 1560$	0	1

Table 3.2: Non-dimensional angular frequency ϖ and azimuthal wavenumber m as a function of the Rayleigh number (Newtonian fluid, $Pr = 1$, $AR = 0.34$, cylinder with adiabatic no-slip sidewall, mesh: 56 000 nodes, Hopf bifurcation).

Ra	ϖ	m
26500	47.522	3
26000	46.601	3
25500	46.159	3
24738	45.47 extr.	3
Boronska & Tuckerman [183] $Ra_{cr2} = 24738$	42.33	3

As a second step of the validation hierarchy *(ii)*, classical RB convection in a cylinder heated from below and cooled from above with adiabatic solid sidewall and aspect ratio $AR = 0.34$ has been considered. In particular, starting from the work of by Boronska & Tuckerman [183] here, the case of Newtonian fluid with $Pr = 1$ is investigated through the numerical solution of the governing non-linear equations. This benchmark corresponds to the transition from an initial steady and axisymmetric flow to a three-dimensional solution as the Rayleigh number exceeds a given threshold (Ra_{cr2}). In these circumstances, the flow is oscillatory and has azimuthal wavenumber $m = 3$. As shown in Table 3.2, the flow field non-dimensional oscillation frequency ϖ matches with a good approximation that one found by these authors.

In order to validate the viscoelastic solver with isothermal flows *(iii)*, the classical "cross-slot benchmark" has been considered. A sketch of this geometry is shown in Figure 3.1. The problem consists of a two-dimensional cross-shaped channel having characteristic width H. It is featured by two diametrically opposite inlet sections where the fluid enters the channel with a velocity $\mathcal{U}$ and two outlet sections, by which the

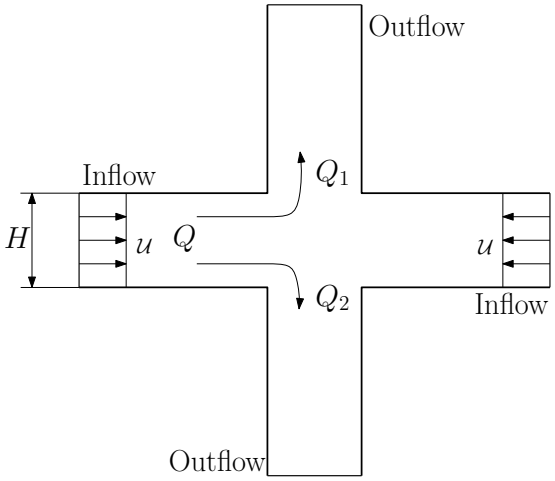

Figure 3.1: Sketch of the classical cross-slot problem.

fluid leaves the system along a direction perpendicular to that of the inflow. For this problem, the total flow rate is typically denoted by $Q = Q_1 + Q_2$, where Q_1 is the amount that goes to the top channel, and Q_2 is the fraction that goes to the bottom channel. If the fluid were Newtonian, Q_1 and Q_2 would have the same value. However, for a viscoelastic fluid, as a result of an elastic instability, a flow rate imbalance appears. It is natural to quantify the flow imbalance as:

$$\delta Q = \frac{Q_2 - Q_1}{Q} \tag{3.14}$$

To compare the results obtained with the present solver with the data available in the literature, the Weissenberg number is defined as $Wi = \lambda \mathcal{U}/H$. Moreover, for the sake of generality, the FENE-CR has been selected as a "test" model. For validation purposes, the solvent-to-total-viscosity ratio ξ is set to 0.1, the finite extensibility of the molecule $L^2 = 200$ (similarly to the rest of the present work), and the other parameters as in Rocha et al. (2009) [184] and Paulo et al. (2014) [185], i.e. the two benchmark results selected for the present validation. As evident in Table 3.3, the present results for two different values of the parameter Wi are very close to those in the literature.

The fourth step of this validation process (*iv*) has been obtained through comparison with the results of the linear stability analysis for RB convection in viscoelastic fluid layers. In particular, Table 3.4 presents the comparison with the LSA by Martínez-

Table 3.3: Comparison with the results (cross-slot benchmark) by Rocha et al. (2009) [184] and Paulo et al. (2014) [185].

Wi	Paulo et al.	Rocha et el.	δQ (present)
0.5	0.787	0.718	0.726
0.6	0.894	0.852	0.856

Table 3.4: Comparison with the linear stability analysis by Martínez-Mardones & Pérez-García [105]. (a) Non-dimensional angular frequency ϖ determined with different models as a function of the Rayleigh number, and (b) Non-dimensional angular frequency ϖ extrapolated to the critical Ra predicted by the linear stability analysis ($Ra_{\mathrm{cr}} \approx 1700$).

(a)

Ra	Oldroyd-B	FENE-CR	
		$L^2 = 10^4$	$L^2 = 10^3$
2500	15.03	15.01	15.00
2200	12.90	12.87	12.60
2000	10.90	10.90	10.90
1900	7.48	7.46	9.63
1800	5.82	5.80	7.50
1775	5.10	5.10	5.65

(b)

Approach	ϖ
FENE-CR ($L^2 = 10^3$)	4.93
FENE-CR ($L^2 = 10^4$)	4.85
Oldroyd-B	4.74
Linear Stability Analysis	4.63

Mardones & Pérez-García [105] for the onset of standard Rayleigh-Bénard convection in a layer of Oldroyd-B fluid delimited by top and bottom *solid* walls with $Pr = 10$, $\xi = 0.5$ and $\vartheta = 0.1$. The present results have been obtained using a structured mesh (2D simulation) with 4500 nodes and aspect ratio AR = width/depth = 15 with periodic boundary conditions at the lateral boundaries. The non-dimensional angular frequency of the flow oscillations ϖ has been determined. Then it has been extrapolated to the value of the critical Rayleigh number predicted by the LSA, i.e. $Ra_{\mathrm{cr}} \approx 1700$. As evident in this table, the difference between the value predicted by those authors and the present one obtained with the Oldroyd-B model is $\approx 2\%$. Moreover, to prove that the FENE-CR model converges to Oldroyd-B, the same validation was also carried out for two different values of finite extensibility parameter, namely $L^2 = 10^4$ and 10^3.

Continuing with a similar approach, given the specific topic considered in the present work, gravitationally modulated viscoelastic convection was considered (*v*). Relevant information on such a benchmark has been sourced from the study by Lyubimova &

Table 3.5: Comparison with the linear stability analysis by LYUBIMOVA & KOVALEVSKAYA [142] for $Pr = 7$, $\Omega = 26.5$, $\Gamma = 1$, $\xi = 0.1$, $\vartheta = 0.06$ ($\Sigma = 0.25$), (a) Non-dimensional amplitude of the (axial) velocity signal in the centre of the layer A_{u_y} determined with different models as a function of the Rayleigh number, and (b) Critical Rayleigh number Ra_{cr} extrapolated for $A_{u_y} = 0$.

(a)

Ra	Oldroyd-B	FENE-CR	
		$L^2 = 10^4$	$L^2 = 200$
530	6.52	6.51	6.52
560	8.31	8.31	8.31
590	11.96	11.96	11.90
620	12.99	12.94	13.07

(b)

Approach	Ra_{cr}
FENE-CR ($L^2 = 200$)	469
FENE-CR ($L^2 = 10^4$)	473
Oldroyd-B	472
Linear Stability Analysis	470

Table 3.6: Comparison with the linear stability analysis by LYUBIMOVA & KOVALEVSKAYA [142] for an Oldroyd-B fluid having $Pr = 7$, $\Omega = 26.5$, $\Gamma = 1$, $\xi = 0.1$, $\vartheta = 0.38$ ($\Sigma = 1.6$). A_{u_y} is the non-dimensional amplitude of the (axial) velocity signal in the centre of the layer.

Ra	A_{u_y}
100	4.60
110	6.45
120	7.98
130	9.28
79.5 (extrapolated)	0
84 (LSA)	0

KOVALEVSKAYA [142], where the authors applied an LSA technique to investigate the onset of Rayleigh-Bénard convection in a horizontal layer of Oldroyd-B fluid delimited by top and bottom *stress-free* walls under the effect of a time-periodic square wave acceleration (see eq. (2.74)) added to the steady gravitational acceleration.

Moreover, the *free-free* boundary condition originally used by LYUBIMOVA & KOVALEVSKAYA [142] for the top and bottom boundary can be recovered by applying the Marangoni boundary condition defined in eq. (2.50), but neglecting the thermocapillary effect, i.e. setting $\sigma_T = 0$.

For $Pr = 7, \Omega = 26.5, \Gamma = 1, \xi = 0.1, \vartheta = 0.06$, LYUBIMOVA & KOVALEVSKAYA [142] found a critical value of the Rayleigh number for the onset of buoyancy convection $Ra_{\mathrm{cr}} \approx 470$, while changing ϑ to 0.38 $Ra_{\mathrm{cr}} \approx 84$. Following the approach already un-

dertaken in step (*iv*), the computations for $\vartheta = 0.06$ have been performed using both the Oldroyd B (originally employed by these authors) and the FENE-CR assuming different values of the parameter L^2, namely, $L^2 = 10^4$ and $L^2 = 200$. It is worth recalling that the latter is a typical value used in most of the existing literature based on this model. Accordingly, it has also been employed in the present work to produce the results presented in Part II for the analysis of FENE-CR fluids. The data shown in Table 3.5 and 3.6 have been obtained using a structured mesh (2D simulation) with 4500 nodes and a domain having aspect ratio AR = width/depth = 15 with periodic boundary conditions at the lateral boundaries. In particular, in order to mimic the typical modus operandi at the basis of LSA, the non-dimensional amplitude A_{u_y} of the unsteady convective state was determined for different values of Ra (Tables 3.5a and 3.6) and then Ra_{cr} was computed through (quadratic) extrapolations of A_{u_y} to 0 (Table 3.5b). As quantitatively substantiated by these tables, the agreement between the present results and those yielded by LSA is excellent.

Interestingly, both the results for standard and modulated Rayleigh-Bénard convection demonstrate that the overall mathematical and numerical treatment underpinning the present work is *consistent*, i.e. as the finite extensibility parameter of the polymer molecule L^2 increases, the results calculated with the FENE-CR constitutive equation tend to those obtained with the Oldroyd-B (as expected).

At this point, it remains to verify the implementation of the Marangoni boundary condition for Newtonian and viscoelastic fluids. In particular, to test the validity of the regularisation strategy, a classical benchmark was considered, i.e. the Hopf bifurcation of standard Marangoni flow in a Newtonian fluid (*vi*). More specifically, the results obtained with the present approach have been assessed against those provided by a repeatedly validated in-house code, conceived to investigate similar fluid dynamics phenomena [168, 180, 181, 186–188].

The results of such an exercise (reported in Table 3.7) show a good agreement between the flow-field frequencies. Notably, hydrothermal waves (HTWs) originating from Marangoni instabilities propagate upstream. In Figure 3.2 the temporal evolution of the HTW is reported for a two-dimensional (2D) case with aspect ratio AR =

Table 3.7: Supercritical thermocapillary convection in a 2D layer of Newtonian fluid. Value of the angular frequency of the velocity signal ϖ for (a) AR = width/depth = 20, $Pr = 7$, $Ma = 10^4$ and (b) A = width/depth = 20, $Pr = 15$, $Ma = 3 \times 10^4$.

	In-house code	Present
(a)	36.2	35.3
(b)	47.1	46.1

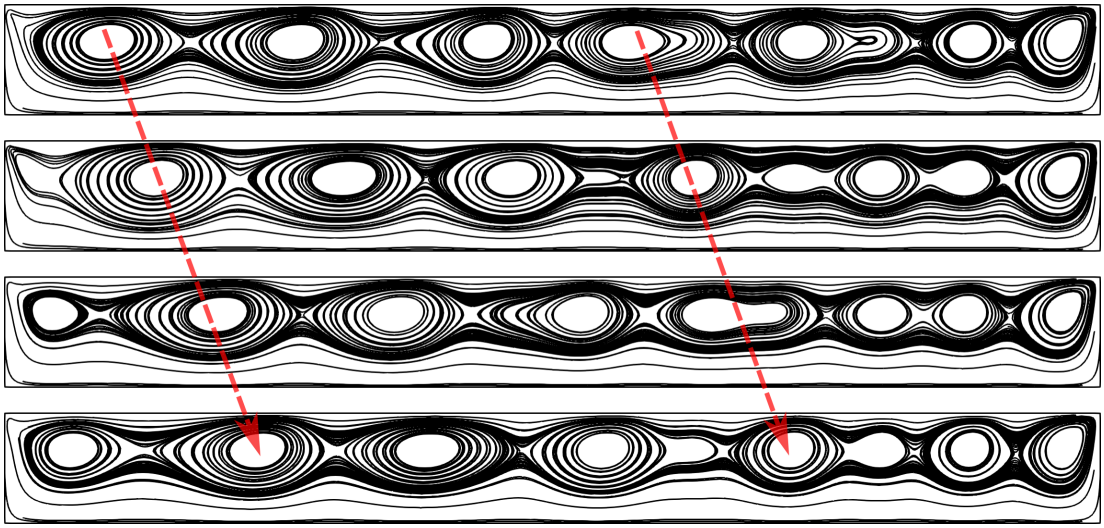

Figure 3.2: Supercritical thermocapillary convection in a 2D layer of Newtonian fluid with AR = width/depth = 20, $Pr = 15$, $Ma = 3 \times 10^4$. Four snapshots evenly spaced along the oscillation period. The red arrows follow the travelling rolls. The cavity is cooled from the left and heated from the right side. For visualization purposes, the height of the layer is not to scale (magnified by 2x).

width/depth = 20, $Pr = 15$, $Ma = 3 \times 10^4$ (to be directly compared with those reported by Lappa [186] for the same values of the governing parameters).

To verify the coherence of the viscoelastic kernel separately, the Hopf bifurcation, corresponding to the overstable behaviour of Marangoni-Bénard convection in an infinite layer, was analysed *(vii)*.

In particular for an Oldroyd-B liquid with $Pr = 200$, $\xi = 0.1$ and $\vartheta = 0.2$ the bifurcation occurs for a value of the Marangoni number $Ma_{\text{cr}} \approx 61$ if the Biot number at the free surface is 1 [128].

To determine the disturbance growth rate, we have monitored the amplitude A_{u_y} of the y component of the velocity signal provided by a numerical probe located in the centre of a 2D fluid domain having aspect ratio AR = width/depth = 7.5 (with

cyclic conditions assumed at the lateral boundaries in order to mimic a system infinitely extended along one direction). The critical Marangoni number for the onset of oscillatory convection has been obtained by extrapolating the amplitude reported in Table 3.8 to $A_{u_y} = 0$. The resulting critical value has been found to be $Ma_{\text{cr}} \approx 59$, which is in a good quantitative agreement with the data available in the work by Lebon et al. [128].

Table 3.8: Validation for Marangoni-Bénard convection in an infinite layer of Oldroyd-B fluid having $Pr = 200$, $\xi = 0.1$, $\vartheta = 0.2$, $Bi = 1$

Ma	A_{u_y}
59 (extrapolated)	0
62.5	1.40
65	2.21
67.5	2.75
70	3.23

Before moving forward with the Part II, it is worth mentioning that in addition to the validation reported in this work, the same solver was validated by other authors belonging to the James Weir Fluid Laboratory in the framework of thermogravitational and thermovibrational convection in Newtonian fluids [64, 189, 190].

Therefore, the mathematical and numerical frameworks are consistent, producing results very similar to the ones available in the literature. For this reason, the numerical model can be considered validated.

Part II

Results

Chapter 4

2D Multicellular States of Viscoelastic Thermovibrational Convection: Perpendicular Temperature Gradient and Vibrations

This chapter is based on Boaro & Lappa, 2021 'Multicellular states of viscoelastic thermovibrational convection in a square cavity' [2].

4.1 Introduction

In this chapter, using the simplified framework represented by a two-dimensional cavity, the following aspects are considered: the role played by the relative importance of (vibrationally-induced) buoyancy and viscous effects, the relationship between the emerging flow and the frequency of vibrations, the outcomes produced by an increase in the level of elasticity, and, last but not least, the onset of possible instabilities inducing a change in the dominant pattern.

Following a common practice in the previous literature about buoyancy convection in closed cavities, this chapter considers this problem in the simplified framework represented by a two-dimensional (2D) configuration with vibrations applied orthogonally to the temperature gradient. In particular, here, special emphasis is given to the triadic relationship among the three distinct temporal scales involved in these phenomena,

namely, the characteristic times related to the diffusion of heat and the relaxation of viscoelastic stresses, and the additional scale dictated by the peculiar nature of the considered flow, i.e. the frequency of "forcing". As using a simplified formulation such as that originally introduced by Gershuni might filter out the physical effects residing on small temporal scales, the overarching equations are solved in their complete non-linear and time-dependent form.

4.2 Statement of the problem

A two-dimensional (2D) square cavity having lateral no-slip and adiabatic walls ($\partial T/\partial \mathbf{n}\big|_{\text{wall}} = \mathbf{0}$) and with a fixed difference of temperature between the top and bottom no-slip walls in microgravity conditions is considered.

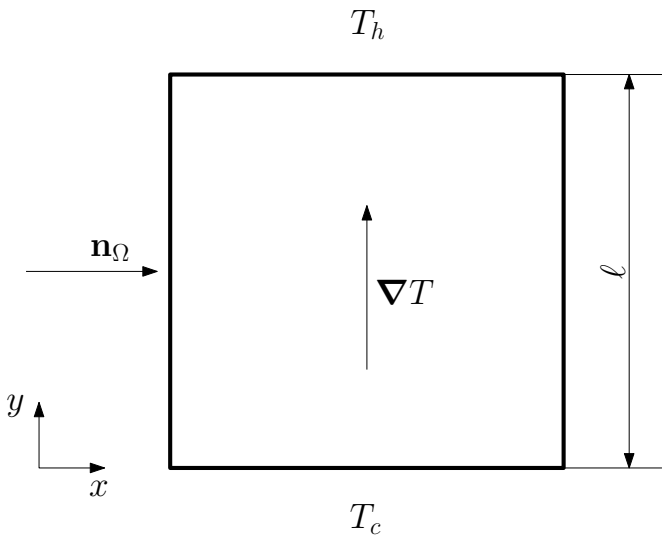

Figure 4.1: Sketch of the geometry and schematisation of the problem.

In order to disentangle the intricacies illustrated in the introduction, the analysis is performed for both Newtonian and viscoelastic fluids. This problem is summed up in Figure 4.1. The direction of the vibrations $\mathbf{n}_\Omega$ is fixed and orthogonal to the temperature gradient $\boldsymbol{\nabla} T$. Moreover, the the side of the cavity ℓ is selected as characteristic length-scale to calculate the non-dimensional quantities reported in this chapter.

The balance equations for the FENE-CR fluid (eqs. (2.69), (2.70), (2.71) and (2.72)) have been integrated over the domain using Piso method (see. the Numerical Method chapter) and the related Rhie & Chow [158] interpolation scheme, which allows the set of mixed parabolic and hyperbolic balance equation to be solved on a *co-located* grid.

Table 4.1: Mesh refinement study. Case $Pr = 10$, $Gs = 5 \times 10^2$, $\Omega = 10^2$, $Ra_\omega = 10^3$, $\vartheta = 0.1$, $\Sigma = 1.6$, viscoelastic fluid. Presented data relate to probes located in the centre of the cell $(1/2, 1/2)$, and in the point $(1/8, 7/8)$ (the "corner").

Mesh	Centre		Corner	
	A_{u_y}	Ω_{u_y}	A_{u_y}	Ω_{u_y}
20×20	0.0149	0.192	0.0032	0.194
40×40	0.0154	0.197	0.0035	0.193
60×60	0.0156	0.197	0.0031	0.195
80×80	0.0157	0.196	0.0033	0.195
100×100	0.0158	0.195	0.0031	0.195

It is worth highlighting that the steady buoyancy term $PrRaT\mathbf{i}_g$ in eq. (2.70) is set to $\mathbf{0}$ in order to mimic the absence of gravitational field.

Moreover, a standard Second-Order Upwind Difference Scheme (Souds) has been used for the spatial discretisation of the convective terms of the momentum and energy equation, while a CDS (Central Difference Scheme) stencil, yet accurate to the second-order, has been implemented for the diffusive terms. Special attention has been paid to the solution of eq. (2.72). In particular, in place of the Souds scheme, a Minmod variant has been chosen for the discretisation of the convective terms. This approach has guaranteed good performances over a wide range of parameters and good agreement with test cases. Moreover, to mitigate the numerical singularities mentioned in chapter 3, the numerical procedure was implemented through a bsd method.

4.2.1 Mesh refinement study

The balance equations have been discretised on a Cartesian grid having the same number of divisions in each direction. For the grid refinement, the amplitude (A_{u_y}) and the frequency (Ω_{u_y}) of the y component of $\mathbf{u}_{\text{mean}}$ signal measured with two virtual probes located in the centre and in the north-west corner of the cell respectively were considered as control parameters. Moreover, it was assumed a viscoelastic fluid with $Pr = 10$, $Gs = 5 \times 10^2$, $\Omega = 10^2$, $Ra_\omega = 10^3$ and $\vartheta = 0.1$ ($\Sigma = 1.6$). As witnessed by the results in Table 4.1, a mesh having 80 cells in each direction is sufficient to ensure

grid-independent solutions, which explains why this chapter used this resolution for all the cases described in Sect. 4.3.

4.3 Results

As already explained to a certain extent in Section 4.1, this study aims to carry out a parametric analysis of the thermovibrational problem in a square cavity filled with a FENE-CR fluid and compare the results with those obtained for a Newtonian liquid in the same conditions. Both the Newtonian and the viscoelastic case are analysed in microgravity environment. Towards this end, without loss of generality, it was assumed $Pr = 10$ (this value being representative of a large class of high-Pr "Boger fluids"). Obviously, for a Newtonian fluid the viscosity simply reduces to $\nu_0 = \nu$ and the Prandtl number becomes $Pr = \nu/\alpha$ since it does not have a polymeric component.

Moreover, the viscoelastic fluid considered in this chapter has $\xi = 0.5$ ($\rightarrow \zeta = (1-\xi)/\xi = 1$) and $L^2 = 200$. Due to the high-dimensional nature of the space of parameters that characterizes this problem, one parameter will be systematically varied, while the other independent non-dimensional groups are kept constant. Notably, in the absence of observational information to properly constrain the model parameters, such an approach is instrumental in revealing the "process controlling factors".

4.3.1 Preliminary analysis of the Newtonian problem

Most conveniently, in the frame of the above-mentioned step-by-step approach, let us initially analyse the effect of the Gershuni number on the pattern evolution of $\mathbf{u}_{\text{mean}}$ for a Newtonian fluid. More specifically, let us fix the value of the angular frequency to $\Omega = 10^2$ and vary Ra_ω in order to have Gs spanning the range of orders of magnitude from $O(10^2)$ to $O(10^7)$. In this regard, let us start from the observation that, in general ($Gs > O(10^2)$), the mean-field is not steady, but exhibits an oscillatory behaviour. A first example of such dynamics for the initial sub-range of Gs going from $O(10^3)$ to $O(10^4)$ is depicted in Figure 4.2.

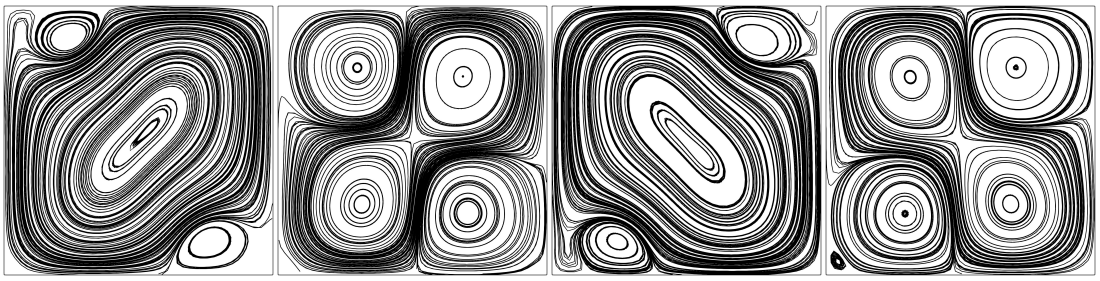

(a) **(b)** **(c)** **(d)**

Figure 4.2: Streamlines of $\mathbf{u}_{\text{mean}}$, $Pr = 10$, $Gs = 5 \times 10^2$, $\Omega = 10^2$ and $Ra_\omega = 10^3$. Thermovibrational convection in Newtonian fluid. Four snapshots equally spaced in time within the oscillation period $T_{\mathbf{u}_{\text{mean}}} \cong 30$. (a) $t_0 = 39.6$, (b) $t = t_0 + (1/4)T_{\mathbf{u}_{\text{mean}}}$, (c) $t = t_0 + (1/2)T_{\mathbf{u}_{\text{mean}}}$, (d) $t = t_0 + (3/4)T_{\mathbf{u}_{\text{mean}}}$

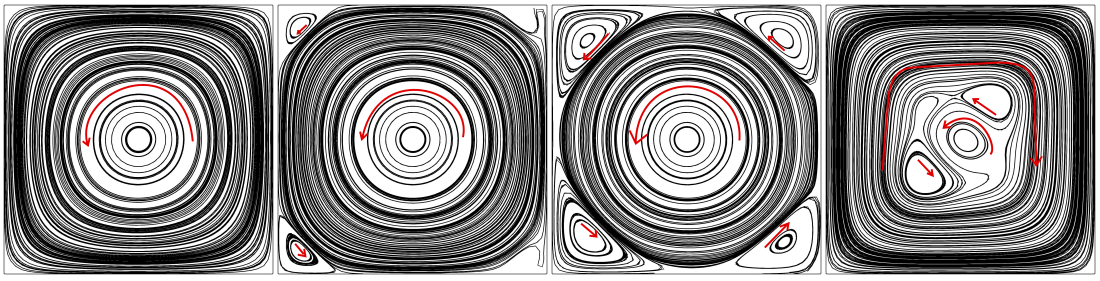

(a) **(b)** **(c)** **(d)**

Figure 4.3: Streamlines of the total velocity $\mathbf{u}$, $Pr = 10$, $Gs = 5 \times 10^2$, $\Omega = 10^2$ and $Ra_\omega = 10^3$. Thermovibrational convection in Newtonian fluid. Detail of the inversion of the central cell in the neighbourhood of $T_\Omega/4$. (a) $t = 0.28$, (b) $t = 0.2838$, (c) $t = 0.284$, (d) $t = 0.2848$.

The aforementioned inversional symmetry pattern can be distinguished there, i.e. two small cells are located in opposite corners of the cavity while a big central vortex, stretched along the diagonal of the square, occupies almost the entire domain (frame 4.2a). This diagonal direction represents a symmetry plane for the pattern. As revealed by the sequence of snapshots, however, as time passes, the eddies located in the corners keep expanding until the four cells with comparable diameter, representing the aforementioned "quadrupolar field", are formed. At this stage, a new process is enabled by which two cells of this configuration progressively undergo coalescence until a condition similar to the one represented in the initial snapshot is recovered. The cells in the corners eventually grow again until the intermediate state with the quadrupolar field

re-appears. This process is characterized by a period (hereafter denoted by $T_{\mathbf{u}_{\text{mean}}}$) much larger than the period of the forcing (i.e. $T_{\mathbf{u}_{\text{mean}}} >> T_\Omega$).

Figure 4.3 shows the corresponding total velocity field. As the reader will realize by taking a look at this sequence, the flow essentially consists of a main roll that changes periodically its sense of circulation (from the clockwise to the counterclockwise sense and vice versa within the forcing period T_Ω). In some snapshots, smaller rolls nucleating inside the main circulation can be seen.

Notably, these behaviours should be interpreted as the result of the superposition of convective modes with different symmetries. Relevant information along these lines, are reported in SUBSECTION 1.1.1 , which presents some results by Mizushima [30]. Although that analysis was entirely focused on classical Rayleigh-Bénard (RB) convection, the considerations elaborated there are relatively general and can, therefore, be applied also to the circumstances considered in the present work.

The system analysed in this chapter present a symmetry along the x axis in Figure 4.1, i.e. the symmetry with respect to the direction of the imposed vibrations, and the analogous reflection property with respect to the vertical cavity centreline, i.e. the direction of the applied temperature gradient.

Though for standard RB convection, one mode only is generally selected at the onset, it is known that the combination of different modes excited at the same time for relatively high values of the control parameter (the standard Rayleigh number) can lead to more complex patterning behaviours. As an example, Mizushima & Adachi [31] found the diagonal mode, i.e. the pattern with the central extended roll that seems to tilt to one side under the influence of the smaller vortices, to be produced as a result of the interplay of more fundamental modes (**(aa)** + **(ss)**). Similar results were also reported in the study on RB convection by Lappa [191] where a sequence of events like that depicted in Figure 4.2 was found for relatively high values of Ra ($Ra = 5 \times 10^5$ for $Pr = 15$).

This way of categorizing different solutions on the basis of the number and location of rolls is extremely useful; it is generally regarded as "a spatial perspective" for flow interpretation, an application of what is generally known as "vorticity thinking". In the

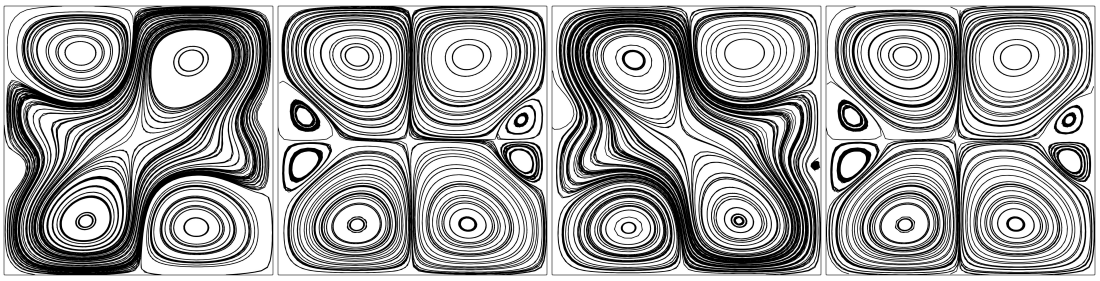

(a) **(b)** **(c)** **(d)**

Figure 4.4: Streamlines of $\mathbf{u}_{\text{mean}}$, $Pr = 10$, $Gs = 1.01 \times 10^5$, $\Omega = 10^2$ and $Ra_\omega = 1.42 \times 10^4$. Thermovibrational convection in Newtonian fluid. Four snapshots equally spaced in time within the oscillation period $T_{\mathbf{u}_{\text{mean}}} \cong 26.8$. (a) $t_0 = 40$, (b) $t = t_0 + (1/4)T_{\mathbf{u}_{\text{mean}}}$, (c) $t = t_0 + (1/2)T_{\mathbf{u}_{\text{mean}}}$, (d) $t = t_0 + (3/4)T_{\mathbf{u}_{\text{mean}}}$.

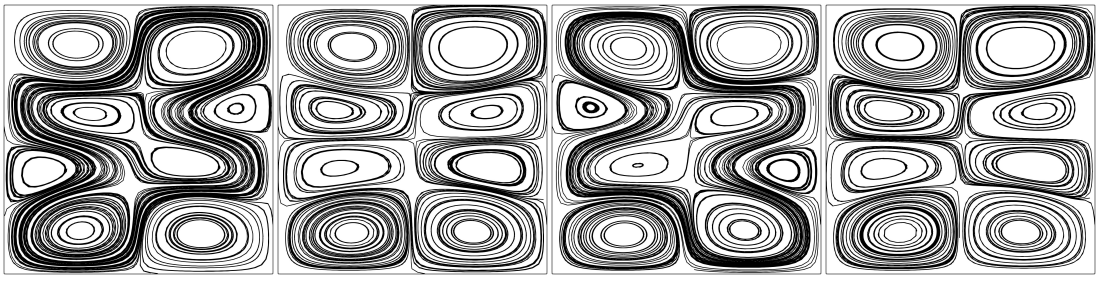

(a) **(b)** **(c)** **(d)**

Figure 4.5: Streamlines of $\mathbf{u}_{\text{mean}}$, $Pr = 10$, $Gs = 2.75 \times 10^5$, $\Omega = 10^2$ and $Ra_\omega = 2.35 \times 10^4$. Thermovibrational convection in Newtonian fluid. Four snapshots equally spaced in time within the oscillation period $T_{\mathbf{u}_{\text{mean}}} \cong 32.1$.(a) $t_0 = 40.2$, (b) $t = t_0 + (1/4)T_{\mathbf{u}_{\text{mean}}}$, (c) $t = t_0 + (1/2)T_{\mathbf{u}_{\text{mean}}}$, (d) $t = t_0 + (3/4)T_{\mathbf{u}_{\text{mean}}}$.

light of these propaedeutical arguments, the stages of evolution reported in Figure 4.2 can therefore be seen as the superposition or competition of fundamental modes of time-averaged convection with different symmetries.

As witnessed by Figure 4.4, however, an increase in Ra_ω can induce a change in the time-averaged streamlines distribution ($Gs = 1.01 \times 10^5$). Some of the features visible in the previous Figure 4.2 can still be clearly recognized; as an example, by comparing frame 4.2a and 4.4a it becomes evident that, though the considered increase of Ra_ω affects the minimum size of the smaller cells located in the corners, the diagonal directions still play the role of symmetry planes. Nevertheless, interestingly, new features show up during the evolution. These are very evident in frame 4.4b, where four small

cells pop up in proximity to the lateral adiabatic walls (two for each side). Apart from these details, however, the evolution is quite similar to the one discussed for the previous case.

As qualitatively illustrated in Figure 4.5, other morphological changes become effective on further increasing Ra_ω ($Gs = 2.75 \times 10^5$). The two opposing couples of newly formed cells adjacent the adiabatic walls have now a size that is comparable to that of the corner cells (frame 4.5b). Though the dynamics are still similar to those described for $Gs = 5 \times 10^2$, as an important distinguishing mark, the big central cell is taken over by an involved circulation system encompassing a zig-zag-shaped arrangement of (four) smaller cells (see frame 4.5a).

The spatio-temporal scenario consists essentially of the alternation of a configuration with eight distinct time-averaged rolls regularly arranged in two vertical columns and four horizontal rows, i.e. a **(ss)** configuration (Figure 4.5b and 4.5d) and two intermediate patterns where one cell of each row contributes to the formation of a zig-zag shaped circulation system pervasive throughout the cavity (Figure 4.5a and 4.5c being one the mirror image of the other). Hereafter, these patterns will be referred to as the "columnar mode of time-averaged convection".

A further increase in the vibrational Rayleigh number does not affect considerably the dynamic evolution of this mode from a qualitative point of view. However, the cells located in the centre of the cavity keep growing until configurations like those shown in Figure 4.6a and 4.6b are obtained. The cells located close to the adiabatic sides of the cavity become so large that they occupy almost the whole space of the geometry (see Figure 4.6b).

Before moving to the cases with viscoelastic fluid, as a concluding remark for this section, it is also worth highlighting that for not too high values of Ω, (as expected) the problem also sensitively depends on this parameter .

Interestingly, if Ω is increased to 1.5×10^2 keeping Gs constant, the dynamics of the system changes completely. As an example, Figure 4.7 shows the streamlines patterning behaviour of a fluid with the same value of Gs considered in Figure 4.2 ($Gs = 5 \times 10^2$) and a slightly larger value of Ω ($Ra_\omega = 1.5 \times 10^3$ and $\Omega = 1.5 \times 10^2$).

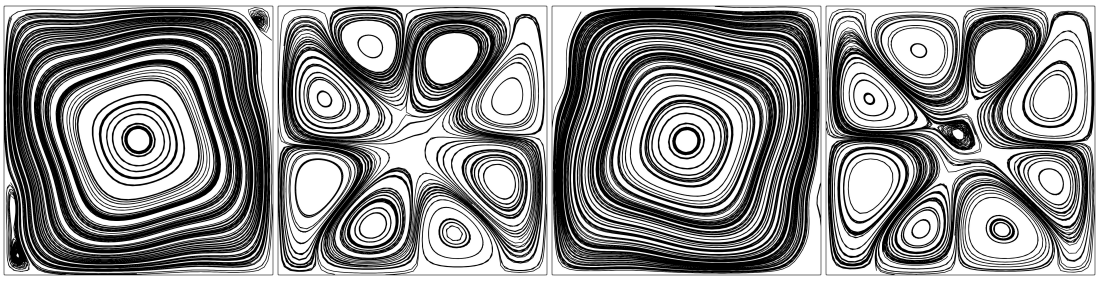

(a) **(b)** **(c)** **(d)**

Figure 4.7: Streamlines of $\mathbf{u}_{\text{mean}}$, $Pr = 10$, $Gs = 5 \times 10^2$, $\Omega = 1.5 \times 10^2$ and $Ra_\omega = 1.5 \times 10^3$. Thermovibrational convection in Newtonian fluid. Four snapshots equally spaced in time within the oscillation period $T_{\mathbf{u}_{\text{mean}}} \cong 22.3$. (a) $t_0 = 26.5$, (b) $t = t_0 + (1/4)T_{\mathbf{u}_{\text{mean}}}$, (c) $t = t_0 + (1/2)T_{\mathbf{u}_{\text{mean}}}$, (d) $t = t_0 + (3/4)T_{\mathbf{u}_{\text{mean}}}$.

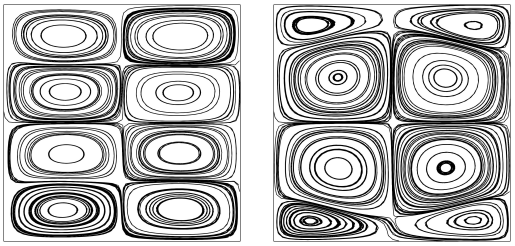

(a) **(b)**

Figure 4.6: Streamlines of $\mathbf{u}_{\text{mean}}$, $Pr = 10$, $\Omega = 10^2$. Thermovibrational convection in Newtonian fluid. Snapshots to compare to frame 4.5b. (a) $Gs = 6 \times 10^5$, $Ra_\omega = 3.46 \times 10^4$. $t = 40.8 + (1/4)T_{\mathbf{u}_{\text{mean}}}$, $T_{\mathbf{u}_{\text{mean}}} \cong 32$, (b) $Gs = 1 \times 10^7$, $Ra_\omega = 1.41 \times 10^5$. $t = 43 + (1/4)T_{\mathbf{u}_{\text{mean}}}$, $T_{\mathbf{u}_{\text{mean}}} \cong 32$

As the reader will easily realize by inspecting this figure, the scenario is different. Initially (frame 4.7a) there is a single cell with streamlines having square morphology. However, two smaller cells, located in the north-east and south-west corners, respectively, grow as time passes. Due to this phenomenon, the central cell undergoes a progressive corrugation process that breaks it into eight independent rolls.

This time, however, the time-averaged rolls are not aligned along the direction of the walls; rather they are disposed radially with respect to the centre of the cavity, i.e. they satisfy a property of centro-symmetry; therefore, this regime will be denominated "radial mode of time-averaged convection".

After some time, the central vortex pervasive throughout the cavity forms again; however, in this case, the smaller cells (the eddies) are located in the north-west and south east corners. Stripped to its basics, this specific phenomenon may therefore be

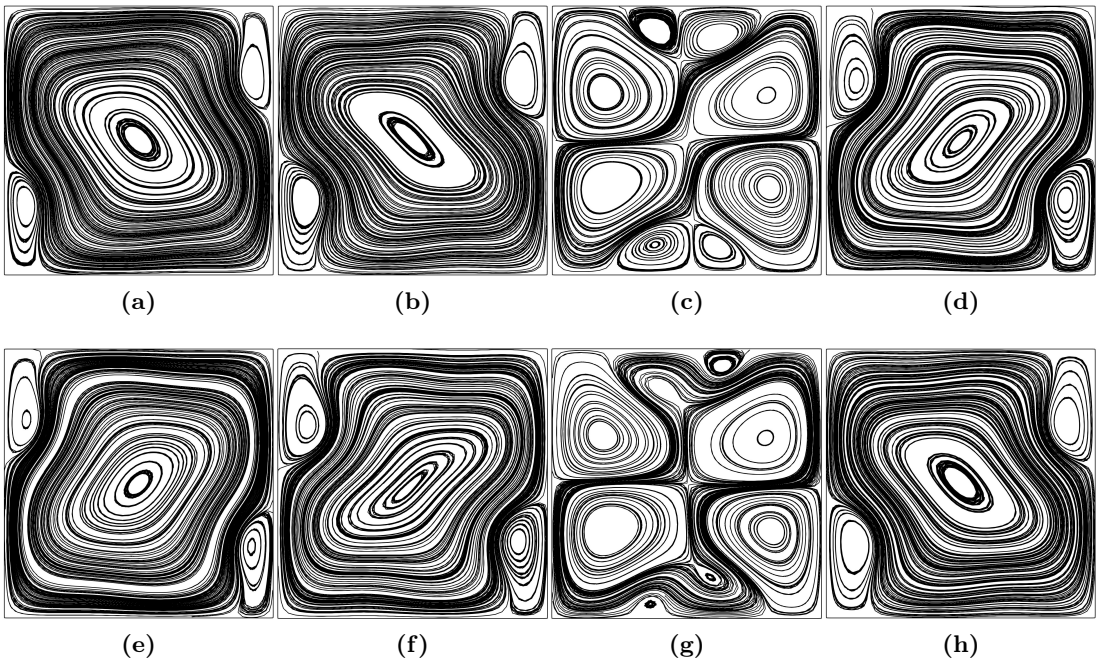

Figure 4.8: Streamlines of $\mathbf{u}_{\text{mean}}$, $Pr = 10$, $Gs = 5 \times 10^2$, $\Omega = 1.75 \times 10^2$ and $Ra_\omega = 1.75 \times 10^3$. Thermovibrational convection in Newtonian fluid. Eight snapshots equally spaced in time within the oscillation period $T_{\mathbf{u}_{\text{mean}}} \cong 18.3$. (a) $t_0 = 22$, (b) $t = t_0 + (1/8)T_{\mathbf{u}_{\text{mean}}}$, (c) $t = t_0 + (1/4)T_{\mathbf{u}_{\text{mean}}}$, (d) $t = t_0 + (3/8)T_{\mathbf{u}_{\text{mean}}}$, (e) $t = t_0 + (1/2)T_{\mathbf{u}_{\text{mean}}}$, (f) $t = t_0 + (5/8)T_{\mathbf{u}_{\text{mean}}}$, (g) $t = t_0 + (3/4)T_{\mathbf{u}_{\text{mean}}}$, (h) $t = t_0 + (7/8)T_{\mathbf{u}_{\text{mean}}}$.

interpreted as the alternation of modes with the **(aa)** and the central symmetry, respectively.

The complexity of the pattern increases as the frequency is set to $\Omega = 1.75 \times 10^2$ (as depicted in figure Figure 4.8).

In these circumstances, the initial size of the two eddies mentioned before is bigger than that found for the case with $\Omega = 1.5 \times 10^2$. Moreover, although the evolution mechanism is very similar to the previous one, at a certain stage four big rolls manifest in the centre of the cavity while other four smaller cells are located in pair close to the cold and hot walls respectively. This state may therefore be regarded as a "hybrid radial-columnar time-averaged mode of convection".

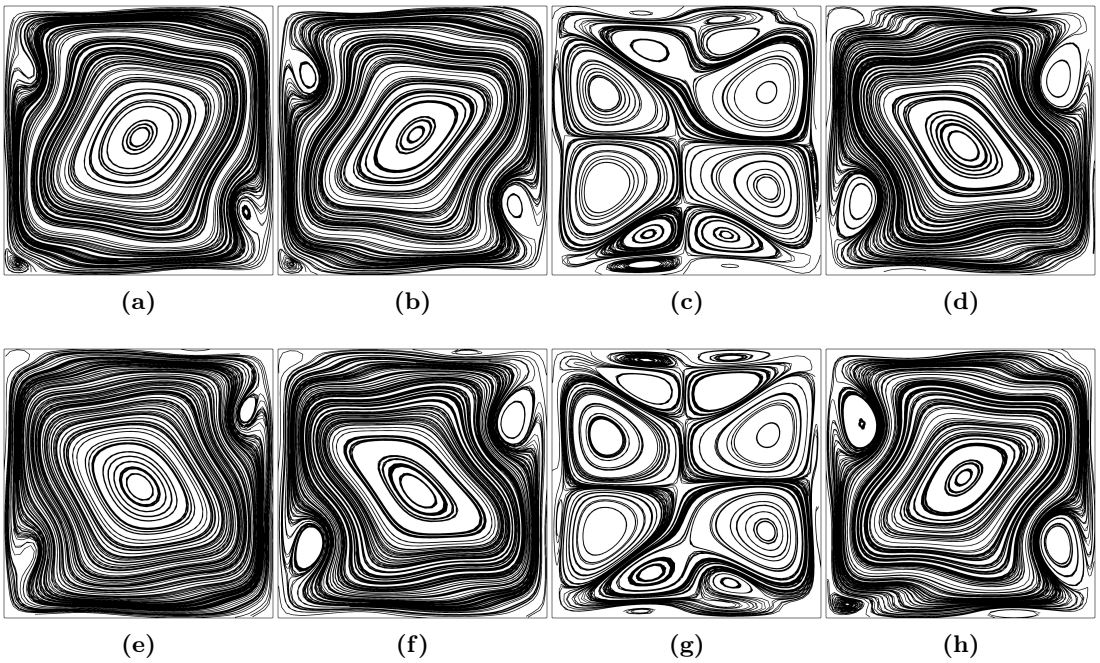

Figure 4.9: Streamlines of $\mathbf{u}_{\text{mean}}$, $Pr = 10$, $Gs = 5 \times 10^2$, $\Omega = 10^2$, $Ra_\omega = 10^3$, $\vartheta = 0.1$ and $\Sigma = 1.6$. Thermovibrational convection in viscoelastic fluid. Eight snapshots equally spaced in time within the oscillation period $T_{\mathbf{u}_{\text{mean}}} \cong 32.14$. (a) $t_0 = 39.1$, (b) $t = t_0 + (1/8)T_{\mathbf{u}_{\text{mean}}}$, (c) $t = t_0 + (1/4)T_{\mathbf{u}_{\text{mean}}}$, (d) $t = t_0 + (3/8)T_{\mathbf{u}_{\text{mean}}}$, (e) $t = t_0 + (1/2)T_{\mathbf{u}_{\text{mean}}}$, (f) $t = t_0 + (5/8)T_{\mathbf{u}_{\text{mean}}}$, (g) $t = t_0 + (3/4)T_{\mathbf{u}_{\text{mean}}}$, (h) $t = t_0 + (7/8)T_{\mathbf{u}_{\text{mean}}}$.

A further increase in Ω to 200 generates a pattern that is basically the same already illustrated in Figure 4.6a. This solution seems to take the role of preferred mode of convection even for higher values of Ω.

4.3.2 The influence of Gs for a viscoelastic fluid

Following the same approach undertaken in the previous section, specific numerical examples are conceived and presented to provide inputs for an increased understanding of the mechanisms underlying viscoelastic fluid flow . In order to do so, let us fix the frequency to $\Omega = 10^2$ and vary Ra_ω (and therefore Gs). Obviously, in this case, the set of parameters to be considered is richer as it also includes the elasticity number ϑ, which initially was set to $\vartheta = 0.1$ (the corresponding value of Σ being $\Sigma = 1.6$).

Starting again from the case $Gs = 5 \times 10^2$ (the related pattern evolution being depicted in Figure 4.9), it can be seen that the initial frames (4.9a and 4.9b) look similar to the corresponding ones in Figure 4.8 (the aforementioned mixed radial-columnar mode of time-averaged convection); although, in this case the lateral eddies nucleate in the north-west and south-east corners, they still manifest themselves in proximity to the adiabatic walls. In particular, comparison of Figure 4.8b and Figure 4.9b is instrumental in showing that when the viscoelastic fluid is considered, the streamlines of the main central vortex are more "undulated" with respect to the Newtonian case. The evolution in time is similar to that already illustrated in Figure 4.8, but the streamlines display a more complex topology. Indeed, due to the emergence of two new couples of (small) rolls along the hot and cold walls, respectively, a total of twelve cells can be distinguished. Such cells are organized in two columns aligned with the temperature gradient direction. Also in this case, the more spatially extended rolls located in the central area expand and merge until a single main vortex is established again. The second half of the period begins and evolves displaying a qualitatively similar behaviour.

In this regard, comparison of Figure 4.10 with Figure 4.3 is also extremely useful as it reveals the changes induced by viscoelastic effects in the total (instantaneous) velocity. Indeed, it can be seen that in terms of total velocity field, the number of rolls present in the latter case is always larger. This indirectly confirms the increased complexity of the time-averaged pattern shown in Figure 4.9 with respect to that reported in Figure 4.2.

For the sake of completeness, Figure 4.11 and Figure 4.12 show the evolution over the forcing period T_Ω of selected components of the viscoelastic stress tensor, i.e. the first normal stress and tangential stress, respectively (the second normal stress is not shown as it displays a configuration that appears rotated by 90 degree with respect to that of the first normal stress). Interestingly, these patterns indicate that the first (second) normal stress generally attains relatively large values in proximity to the walls perpendicular (parallel) to the imposed temperature gradient. The corresponding tangential component essentially follows the evolution of the instantaneous velocity field, i.e. it is characterized by regions of positive and negative values adjacent the solid boundaries, which periodically swap their position within the forcing period. As evident

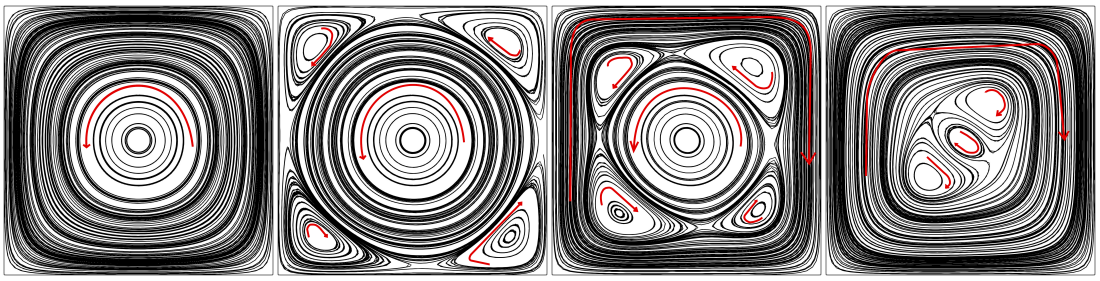

(a) (b) (c) (d)

Figure 4.10: Streamlines of the total velocity $\mathbf{u}$, $Pr = 10$, $Gs = 5 \times 10^2$, $\Omega = 10^2$, $Ra_\omega = 10^3$, $\vartheta = 0.1$ and $\Sigma = 1.6$. Thermovibrational convection in viscoelastic fluid. Detail of the inversion of the central cell in the neighbourhood of $T_\Omega/4$. (a) $t = 0.3539$, (b) 0.3557, (c) 0.3566, (d) 0.3575.

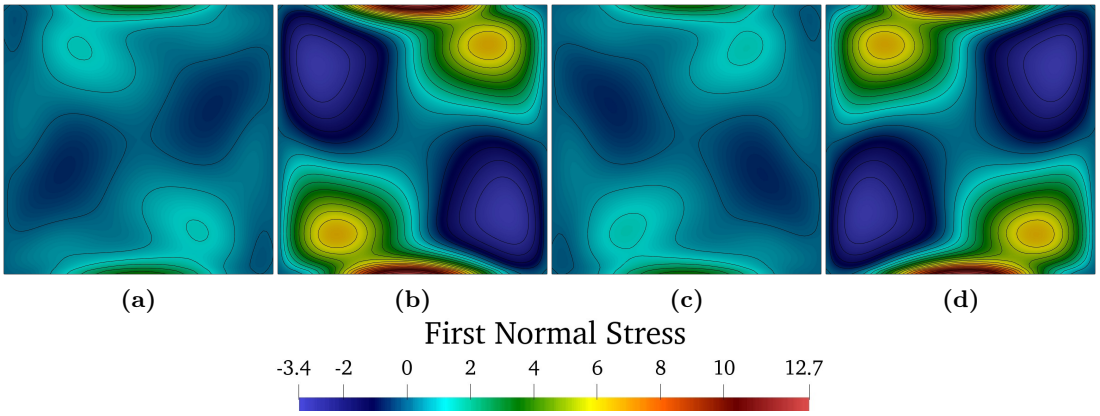

(a) (b) (c) (d)

Figure 4.11: First normal stress, $Pr = 10$, $Gs = 5 \times 10^2$, $\Omega = 10^2$, $Ra_\omega = 10^3$, $\vartheta = 0.1$ and $\Sigma = 1.6$. Thermovibrational convection in viscoelastic fluid. Four snapshot equally spaced in time within the oscillation period T_Ω. (a) $t_0 = 0.34$, (b) $t = t_0 + T_\Omega/4$, (c) $t = t_0 + T_\Omega/2$, (d) $t = t_0 + 3/4T_\Omega$.

in Figure 4.13b, if evaluated in the time-averaged space, this component gives rise to a sort of four-pole pattern displaying a weak modulation in time (not shown). In previous studies (see, e.g., Ref. [192]) one of the remarkable flow features of both Boger and shear-thinning viscoelastic fluids has been found to be vortex formation and vortex enhancement near corners and other similar geometrical features, which is in line with the present findings.

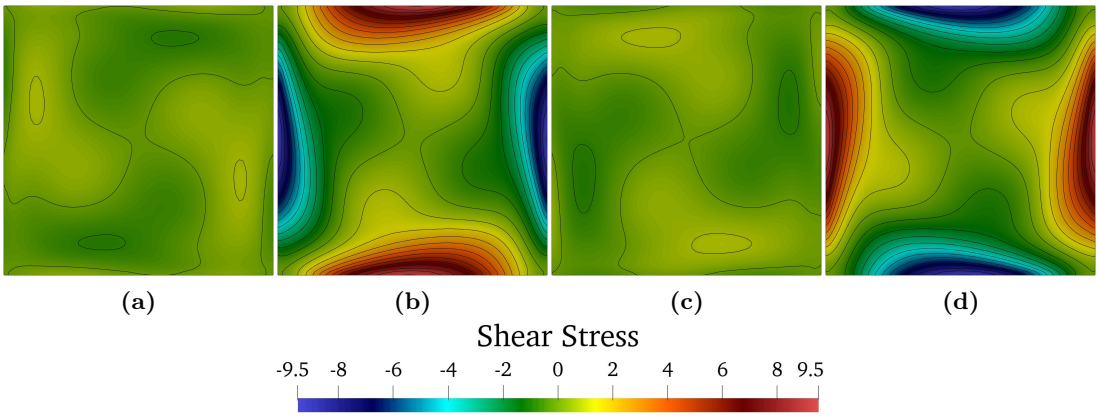

Figure 4.12: Tangential stress, $Pr = 10$, $Gs = 5 \times 10^2$, $\Omega = 10^2$, $Ra_\omega = 10^3$, $\vartheta = 0.1$ and $\Sigma = 1.6$. Thermovibrational convection in viscoelastic fluid. Four snapshot equally spaced in time within the oscillation period T_Ω. (a) $t_0 = 0.34$, (b) $t = t_0 + T_\Omega/4$, (c) $t = t_0 + T_\Omega/2$, (d) $t = t_0 + 3/4$.

The most striking effect produced by an increase in Ra_ω can be appreciated in Figure 4.14, where for $Gs = 2 \times 10^3$ a significant change in the smoothness of the time-averaged streamlines also starts to develop.

Although the dynamics are basically the same already described for smaller values of the Gershuni number, the shape of the streamlines, previously slightly undulated, exhibits an evident corrugation. The centre of the main vortex (compare frame 4.9b and 4.14b) moves from the middle of the cavity to a position closer to the corner. Figure 4.14c also reveals that the transitional multicellular structure (established in a certain sub-interval of the period $T_{\mathbf{u}_{\text{mean}}}$) is now distorted and the overall pattern is no longer *symmetric* (as it was in the previous case with respect to the vertical mid-plane). Moreover, the distortions, due to elastic effects, tend to generate smaller cells inside the four bigger central rolls (see frame 4.14c).

Quite surprisingly, as a fleeting glimpse into Figure 4.15 would confirm, a further increase in the vibrational Rayleigh number ($Ra_\omega = 2.32 \times 10^3$, $Gs = 2.7 \times 10^3$) leads to a mode of convection that is more ordered. A relatively extended central vortex is still produced; however, in this case its shape resembles an inclined cross with the branches oriented along the diagonals of the cavity. A preferred (main) diagonal, i.e. the south-west to north-east one (see e.g. frame 4.15a and 4.15b) can still be identified in certain

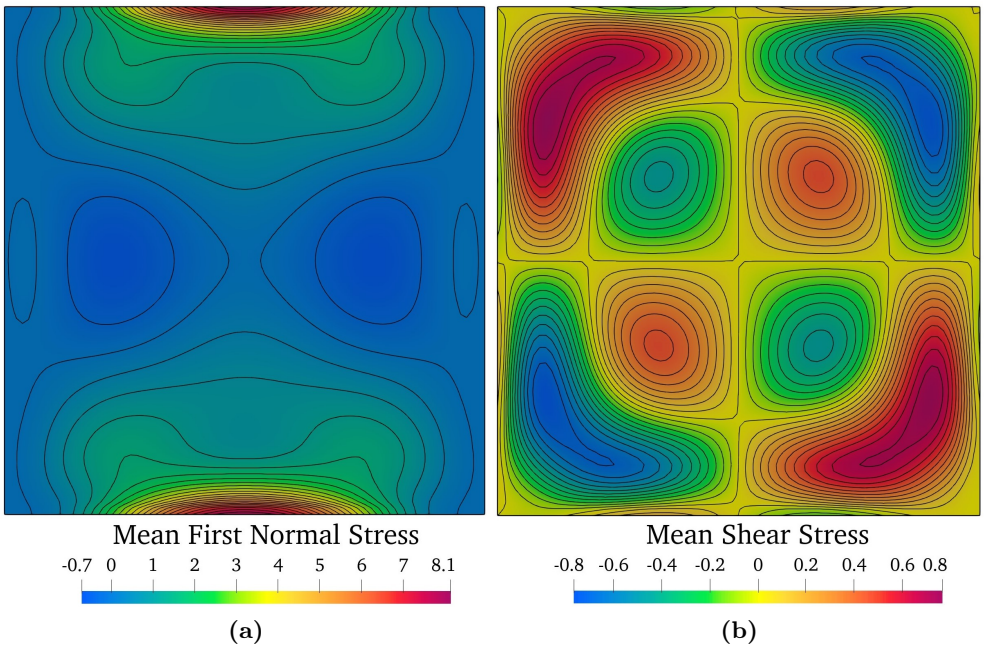

Figure 4.13: Mean stress tensor component, $Pr = 10$, $Gs = 5 \times 10^2$, $\Omega = 10^2$, $Ra_\omega = 10^3$, $\vartheta = 0.1$ and $\Sigma = 1.6$. Thermovibrational convection in viscoelastic fluid. Snapshot for $t = 39.1$. (a) Mean first normal stress, (b) mean shear stress.

stages of evolution. A switch in this preferred direction, however, occurs every half period. In the corners not occupied by the central vortex, i.e. the corners lying on the secondary diagonal, three smaller independent eddies (for each corner) appear. Notably, their size increases until they occupy a region that is approximately 1/8 of the total area of the square cavity. During this evolution, a radial distribution of the cells, resembling the aforementioned radial mode of time-averaged convection (depicted in Figure 4.7b for the Newtonian case), can be recognized. There is indeed a notable analogy between these two modes of convection. Some differences can be identified as well. The outer boundary of the cells is not smooth and displays some undulations. Besides, several smaller secondary eddies, not present in Newtonian liquids, are located in proximity to the walls. A further increase in Ra_ω has the effect to reduce the size of the small rolls located in the corners (frame 4.16b for the case of $Gs = 3.6 \times 10^3$). Furthermore, taking a look at the morphological evolution of the main central vortex, it may be concluded

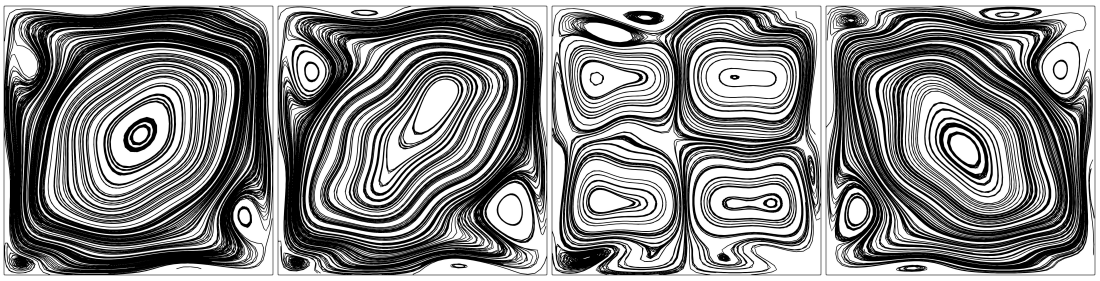

(a) **(b)** **(c)** **(d)**

Figure 4.14: Streamlines of $\mathbf{u}_{\text{mean}}$, $Pr = 10$, $Gs = 2\times10^3$, $\Omega = 10^2$, $Ra_\omega = 1.61\times10^3$, $\vartheta = 0.1$ and $\Sigma = 1.6$. Thermovibrational convection in viscoelastic fluid. Four snapshots equally spaced in time within half oscillation period $T_{\mathbf{u}_{\text{mean}}} \cong 32.1$ (the second part of the period is specular with respect the diagonal of the cavity). (a) $t_0 = 39.2$, (b) $t = t_0 + (1/8)T_{\mathbf{u}_{\text{mean}}}$, (c) $t = t_0 + (1/4)T_{\mathbf{u}_{\text{mean}}}$, (d) $t = t_0 + (3/8)T_{\mathbf{u}_{\text{mean}}}$.

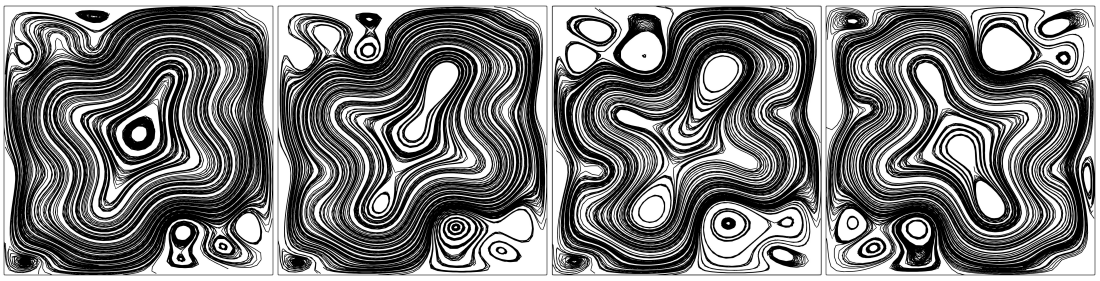

(a) **(b)** **(c)** **(d)**

Figure 4.15: Streamlines of $\mathbf{u}_{\text{mean}}$, $Pr = 10$, $Gs = 2.7\times10^3$, $\Omega = 10^2$, $Ra_\omega = 2.32\times10^3$, $\vartheta = 0.1$ and $\Sigma = 1.6$. Thermovibrational convection in viscoelastic fluid. Four snapshots equally spaced in time within half oscillation period $T_{\mathbf{u}_{\text{mean}}} \cong 33$ (the second part of the period is specular with respect the diagonal of the cavity). (a) $t_0 = 39.15$, (b) $t = t_0 + (1/8)T_{\mathbf{u}_{\text{mean}}}$, (c) $t = t_0 + (1/4)T_{\mathbf{u}_{\text{mean}}}$, (d) $t = t_0 + (3/8)T_{\mathbf{u}_{\text{mean}}}$.

that as Gs (Ra_ω) is made higher, the morphology of this cell is gradually transformed from an initially elliptic shape into a cross-like geometrical configuration.

Finally, Figure 4.17 reports the evolution of the maximum of the instantaneous and time-averaged components of the viscoelastic stress tensor as a function of the Gershuni and the vibrational Rayleigh numbers for fixed ϑ and Ω. Although morphological changes in the structure of the patterns already shown in Figure 4.11, Figure 4.12 and Figure 4.13 were not noticed over these ranges of Gs and Ra_ω, the growing behaviour of these quantities can clearly be discerned in this figure. This should be seen as a

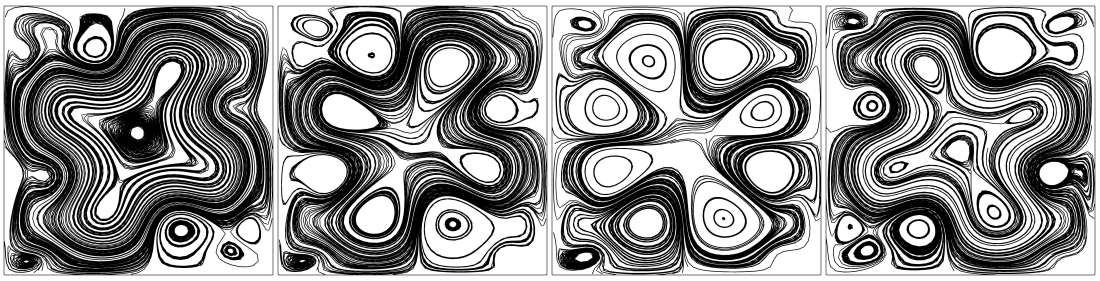

(a) **(b)** **(c)** **(d)**

Figure 4.16: Streamlines of $\mathbf{u}_{\text{mean}}$, $Pr = 10$, $Gs = 3.6 \times 10^3$, $\Omega = 10^2$, $Ra_\omega = 2.68 \times 10^3$, $\vartheta = 0.1$ and $\Sigma = 1.6$. Thermovibrational convection in viscoelastic fluid. Four snapshot equally spaced in time within half oscillation period $T_{\mathbf{u}_{\text{mean}}} \cong 33$ (the second part of the period is specular with respect the diagonal of the cavity). (a) $t_0 = 39.2$, (b) $t = t_0 + (1/8)T_{\mathbf{u}_{\text{mean}}}$, (c) $t = t_0 + (1/4)T_{\mathbf{u}_{\text{mean}}}$, (d) $t = t_0 + (3/8)T_{\mathbf{u}_{\text{mean}}}$.

justification for the increasing recognizable importance of the aforementioned "undulations" in the shape of the streamlines. Interestingly, both the fluctuating and the mean components of the viscoelastic stress tensor scale with $Ra_\omega^{1/2}$, which might be seen as a similarity with known behaviours in the Newtonian case for small forcing frequencies such as those considered in the present work (Ref. [10] and references therein).

The study of situations with $Gs > 3.6 \times 10^3$ was prevented by viscoelastic singularities, these being a well-known problem of this category of liquids (Refs. [163–167]).

4.3.3 The influence of Σ and ϑ

Having completed a sketch of the situations that can be obtained when Gs is increased for a moderate level of elasticity ($\vartheta = 0.1$ in the preceding section), let us now turn to considering the role played in all these dynamics by the triadic interplay existing among the typical characteristic time scales involved in these phenomena, namely, the reference time scale (ℓ^2/α), the fluid relaxation time and the period of vibrations.

In the non-dimensional space of parameters, these can be reduced to two characteristic numbers only, i.e. ϑ and Σ. As illustrated in the preceding sections, these two parameters can be varied independently.

Starting again with the case $\vartheta = 0.1$ ($\Sigma = 1.6$) already shown in Figure 4.9, in particular, the value of the elasticity number was varied in an interval between $\vartheta = 0.2$

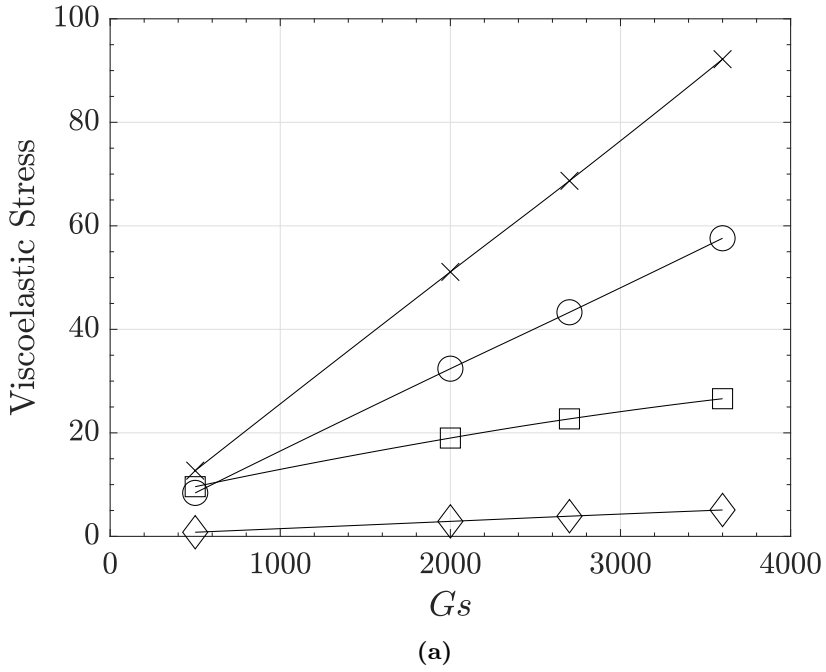

(a)

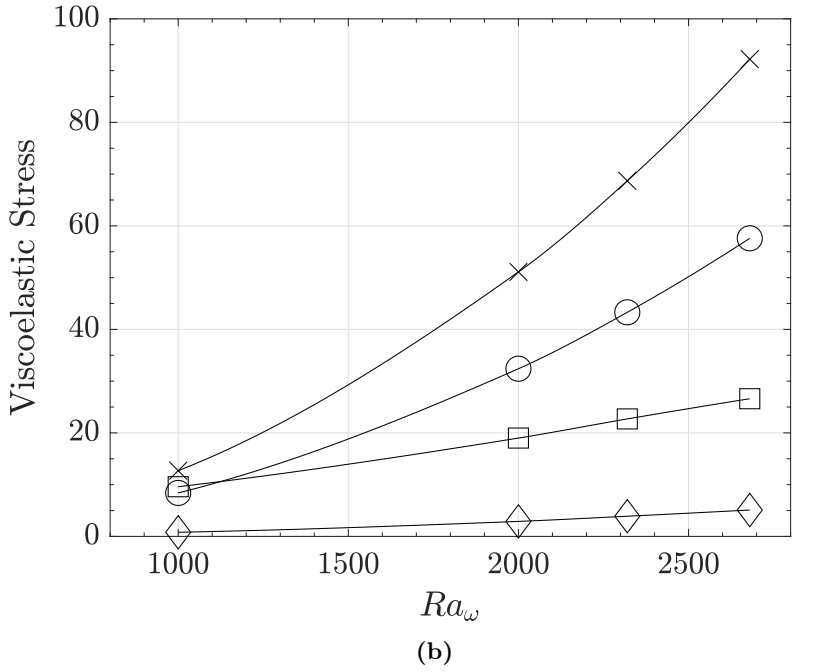

(b)

Figure 4.17: Representation of the maximum of the instantaneous first normal stress τ_{xx} ($\times$), the time-averaged first normal stress $\tau_{xx,\mathrm{mean}}$ ($\circ$), the instantaneous shear stress τ_{xy} ($\square$), the time-averaged shear stress $\tau_{xy,\mathrm{mean}}$ ($\diamond$) as a function of the control parameters. $Pr = 10$, $\Omega = 100$, $\vartheta = 0.1$. (a) Variation of the components of $\tilde{\boldsymbol{\tau}}$ and $\tilde{\boldsymbol{\tau}}_{\mathrm{mean}}$ as a function of Gs, (b) Variation of the components of $\tilde{\boldsymbol{\tau}}$ and $\tilde{\boldsymbol{\tau}}_{\mathrm{mean}}$ as a function of Ra_ω.

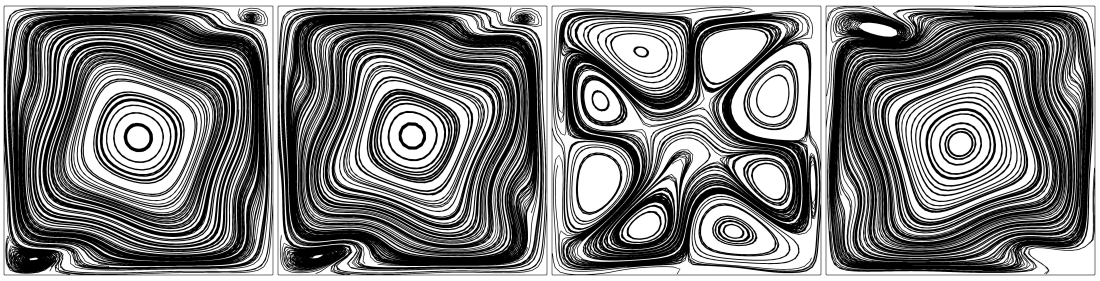

(a) **(b)** **(c)** **(d)**

Figure 4.18: Streamlines of $\mathbf{u}_{\text{mean}}$, $Pr = 10$, $Gs = 5 \times 10^2$, $\Omega = 10^2$, $Ra_\omega = 10^3$, $\vartheta = 0.5$ and $\Sigma = 8$. Thermovibrational convection in viscoelastic fluid. Four snapshots equally spaced in time within half oscillation period $T_{\mathbf{u}_{\text{mean}}} \cong 32.1$ (the second part of the period is specular with respect the diagonal of the cavity). (a) $t_0 = 38.7$, (b) $t = t_0 + (1/8)T_{\mathbf{u}_{\text{mean}}}$, (c) $t = t_0 + (1/4)T_{\mathbf{u}_{\text{mean}}}$, (d) $t = t_0 + (3/8)T_{\mathbf{u}_{\text{mean}}}$.

and $\vartheta = 0.9$ while keeping fixed Ω. Interestingly, the simulations have revealed that, in a rather unexpected way, higher values of ϑ can produce more ordered phenomena (Figure 4.18) with a sequence of stages of evolution that does not change qualitatively as ϑ grows.

The patterning behaviour looks really similar to the one already reported in Figure 4.7 for a Newtonian fluid. However, a closer look also reveals some differences. Indeed, small eddies are located close to the corners (south-west corner in 4.18a and north-west/south-east in 4.18d) and other secondary cells (similar to the ones found for $\vartheta = 0.1$) emerge in proximity to the adiabatic walls (frame 4.18c).

A simple rationale for the observed "regularization" of this pattern can be elaborated once again taking into account the influence of the viscoelastic stresses. Along these lines, the curves in Figure 4.19 are instrumental in demonstrating that, for a fixed $\Omega = 100$, the instantaneous and time-averaged components of the viscoelastic stress tensor decrease as a function of ϑ (which varies in the range between 0.1 and 0.9). Although this behaviour may look rather counter-intuitive, it is worth recalling that similar findings have been reported by other authors for a set of companion problems (Refs. [193–195]). In the present case, the related dependencies can be expressed mathematically as follows:

$$\tau_{xx} \approx 0.9\vartheta^{-1.1669} \tag{4.1}$$

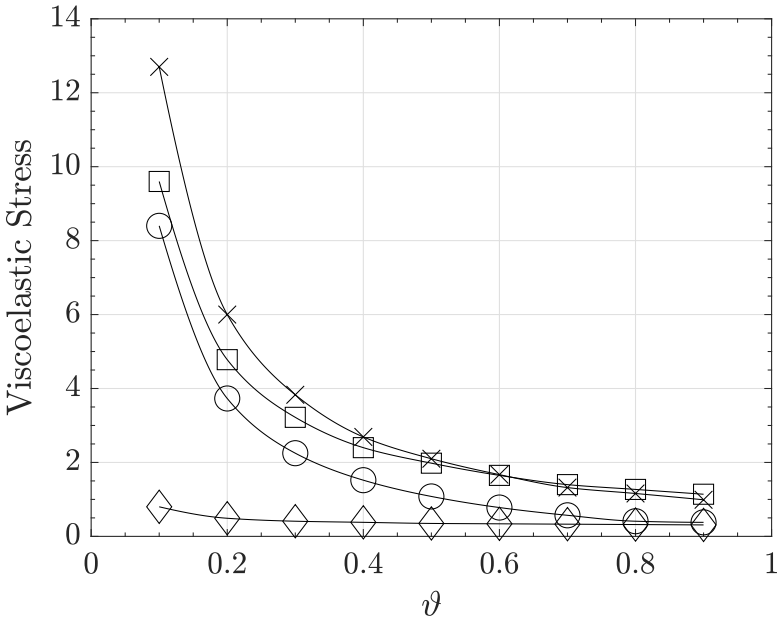

Figure 4.19: Variation of the maximum of the instantaneous first normal stress τ_{xx} ($\times$), the time-averaged first normal stress $\tau_{xx,\mathrm{mean}}$ ($\circ$), the instantaneous shear stress τ_{xy} ($\square$), the time-averaged shear stress $\tau_{xy,\mathrm{mean}}$ ($\diamond$) as a function of ϑ. $Pr = 10$, $\Omega = 100$, $Gs = 5 \times 10^2$, $Ra_\omega = 10^3$.

$$\tau_{xx,\mathrm{mean}} \approx 0.354\vartheta^{-1.4429} \tag{4.2}$$

$$\tau_{xy} \approx 1.01\vartheta^{-0.9716} \tag{4.3}$$

$$\tau_{xy,\mathrm{mean}} \approx 0.277\vartheta^{-0.403} \tag{4.4}$$

In order to complete the analysis of the different functional dependencies and gain further understanding of the observed dynamics, the sensitivity of the overall fluid-dynamic problem to the Σ number has also been assessed. In particular, as shown by eq. (2.82), for a fixed ϑ, Σ has been modified by changing Ω.

The case of $\Sigma = 1.6$ has already been analysed in Section 4.3.2. For larger values of this parameter, the simulations show that the pattern comes back to the configuration illustrated in Figure 4.2. Interestingly, on increasing Σ, for ϑ fixed to 0.1, the time-averaged viscoelastic tangential stress exhibits a growing trend, whereas its corresponding instantaneous (total) counterpart and the normal stress (both instantaneous and mean versions) become all smaller as the elasticity parameter grows (Figure 4.20).

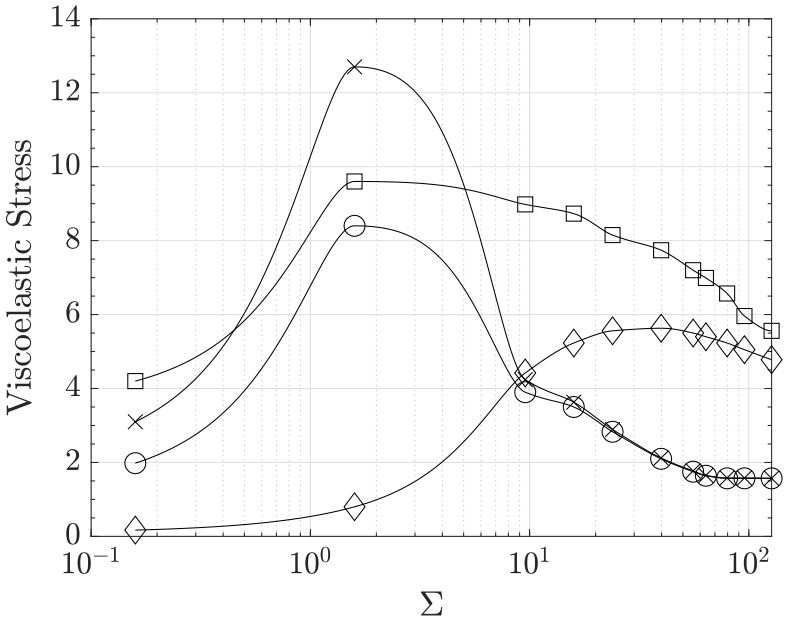

Figure 4.20: Variation of the maximum of the instantaneous first normal stress τ_{xx} ($\times$), the time-averaged first normal stress $\tau_{xx,\mathrm{mean}}$ ($\circ$), the instantaneous shear stress τ_{xy} ($\square$), the time-averaged shear stress $\tau_{xy,\mathrm{mean}}$ ($\diamond$) as a function of Σ. $Pr = 10$, $Gs = 5 \times 10^2$, $Ra_\omega = 10^3$, $\vartheta = 0.1$, $\Omega \in [10; 8 \times 10^3]$.

As qualitatively and quantitatively substantiated by Figure 4.21, however, an even more interesting scenario can be observed in terms of non-dimensional amplitude and non-dimensional angular frequency of the $\mathbf{u}_{\mathrm{mean}}$ signal, measured by a virtual probe located in the centre of the cavity.

As evident in this figure, both the curves display a series of maxima and minima. For instance, for $\Sigma = 9.6$ a minimum is attained; the resulting pattern is a quadrupolar distribution of the streamlines with a quasi-stationary behaviour. On increasing Σ to 16 the evolution previously shown in Figure 4.2 is recovered.

This non-monotonic trend obviously calls for a complementary interpretation and, perhaps the most obvious way to do so is to point out that the switching of the trajectory of a system in the space of phases among two or more concurrent attracting sets (as one of the control parameters is changed) is not a new phenomenon in fluid-dynamics, especially when viscoelastic fluids are considered. As illustrated, e.g., by Refs. [1, 135], convection in viscoelastic fluids is often characterized by the existence of

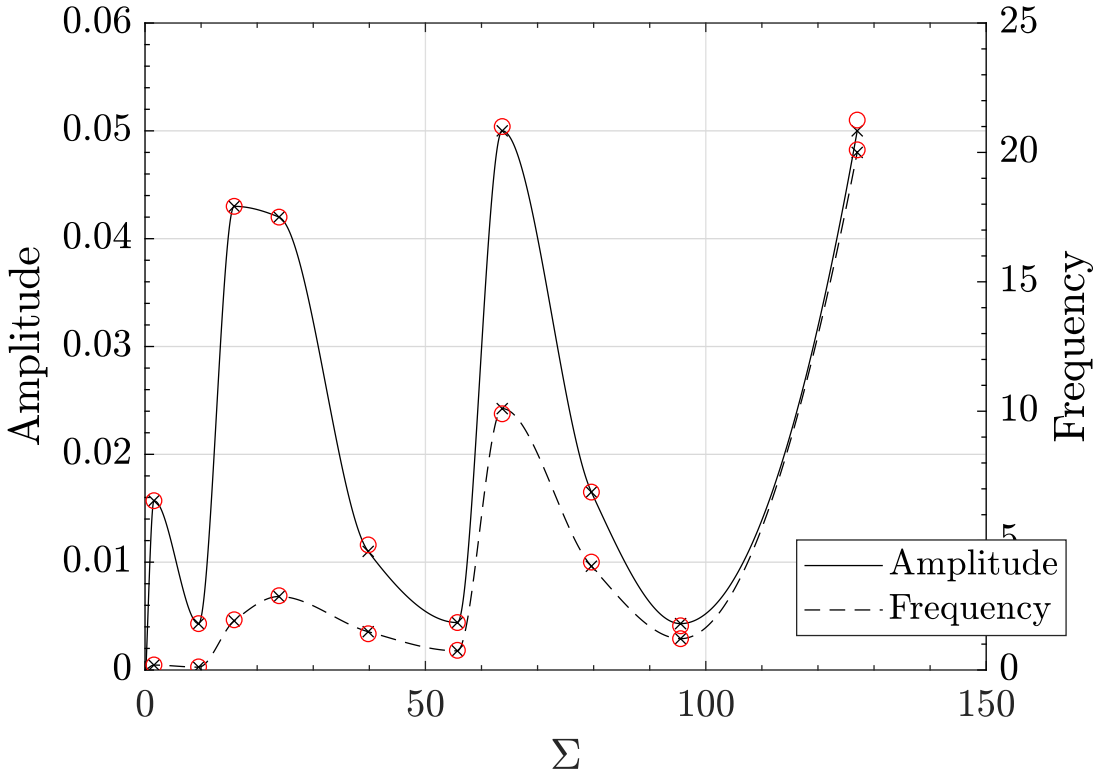

Figure 4.21: Variation of the non-dimensional amplitude and the non-dimensional angular frequency of $\mathbf{u}_{\text{mean}}$ as a function of Σ. $Pr = 10$, $Gs = 5 \times 10^2$, $\vartheta = 0.1$, $\Omega \in [10; 8 \times 10^3]$. The symbols $\times$ and $\circ$ refer to the results obtained with the FENE-CR and the Oldroyd-B, respectively.

multiple attractors, i.e. solutions which can coexist in the space of phases for a fixed set of input parameters. It is known that the presence of multiple attractors can act as an additional source of apparent randomness in a chaotic system producing sudden and repeated jumps from a branch of solutions to another branch. As an example, a chaotic attractor can reduce to a simple time-periodic flow following a chaos "crisis" similar to that observed in standard Rayleigh-Bénard convection by Paul et al. [196] (this kind of bifurcation can be viewed as a sudden change in the size of the attractor [197]). As also illustrated by Grebogi et al. [198] and Arnold et al. [199], apparently intermittent behaviours can be induced by the "collision" of a chaotic attractor with an unstable periodic orbit or its stable manifold. Such collisions can drive a system to-

wards a different scenario giving rise to non-monotonic trends similar to that displayed in Figure 4.21.

Before being carried away by this fascinating idea, however, one should reflect on the fact that, since in the present case the flow has always been found to be simply periodic, mechanisms based on the crisis of strange attractors, such as those invoked by Ref. [135], should obviously be ruled out.

While a precise clarification of the cause-and-effect relationships underlying such non-monotonic behaviour will require tools and methods which are beyond the scope of the present study, here let us limit ourselves to pointing out that additional simulations conducted using the Oldroyd-B paradigm have shown no significant departure from the trend summarized in Figure 4.21, which indirectly provides evidence that such fascinating dynamics should not be ascribed to the specific viscoelastic model employed (the FENE-CR).

4.4 Discussion

Using the observations made in the preceding section as a pre-requisite and building on some common principles on which both the Oldroyd-B and the FENE-CR rely, a potentially useful analogy between the present and other known phenomena was elaborated, based on some notable similarities between two seemingly unrelated branches of physics and engineering. Here, let us consider the evident similarity between the phenomenon reported in Figure 4.21 and another category of problems, i.e. that of mechanical systems subjected to vibrations where *viscoelastic* "components" are intentionally used to implement *vibrational mode control*.

Developing this analogy obviously requires understanding how these systems work. In practice, they generally employ a series of viscoelastic parts as connections between sub-structures [200]. From a technical standpoint, such components are used for their renowned ability to provide a good protection against vibrations through generation of deformations (by which a significant part of the available vibrational energy is *dissipated*).

In the past, these complex multi-component structures (widely used for disparate applications in engineering) have been characterized in terms of relatively simple models able to provide meaningful information on their behaviour in a relatively straightforward way. Such models have generally been built on the basis of rational physical arguments and by turning the original mechanical system into *a network of specialized functions*, each accounting for a specific physical effect.

As an example, since the above-mentioned parts are generally made of materials that have high elasticity and, at the same time, can play the role of energy-dissipating components, each of them can be considered theoretically equivalent to an assembly formed by a spring (with a certain stiffness) and a damper (with a certain energy dissipation coefficient). The simplest case is obviously that of an isolated viscoelastic mass (a single substructure) vibrating under the effect of an external forcing, which can be mimicked or modelled as a simple spring-oscillator model with a single degree of freedom (DOF). If the single spring is assembled with the damper in a side-by-side configuration, the problem can be reduced from a purely mathematical point of view to a single ordinary differential equation $m\ddot{x} + c\dot{x} + kx = f(t, \Omega)$ where m is the mass, c is the damping coefficient, k is the stiffness and $f(t, \Omega)$ represents the external forcing.

Of course, actual mechanical systems [200] used for vibrational mode control are very complicated and have large amounts of DOFs. For this reason, their mathematical characterization, in general, relies on systems of coupled equations (their number being equal to the number of involved DOFs). These sets of coupled equations have largely been studied over the years due to their ability to predict the so-called "resonances" and "anti-resonances" [200, 201]. The former simply correspond to the well-known ability of dynamical systems to produce oscillations of relatively high amplitude, not because the system has entered a particularly chaotic state, but because the frequency of the forcing has become equal to one (there might be many depending on the number of DOFs) of the frequencies of natural oscillation of the considered system. Vice versa, the latter refers to the remarkable possibility to mitigate the oscillatory behaviour induced by an external forcing by taking advantage of the intrinsic elastic response of the system itself. Put simply, this means that specific frequencies exist for which *a destructive interference*

is established between the external driving force and one of the many oscillators present in the considered multi-component structure; most remarkably, it is known that at these frequencies the oscillation amplitude can drop to almost zero.

These resonances and anti-resonances can typically be seen in the so-called amplitude-frequency characteristic curve of the considered system, i.e. a plot reporting the amplitude of oscillation and a function of the frequency of the driving force, where they correspond to peaks and valleys, respectively. These plots (see, e.g., Refs. [200, 202]) are surprisingly similar to that shown in Figure 4.21, which may indicate that the dynamics of the vibrated viscoelastic fluid considered in the present work are governed by similar principles. Along these lines and further pursuing the analogy between the present problem and the aforementioned multi-functional structures (consisting of viscoelastic parts subjected to external vibrational forcing), it is worth recalling the fundamental properties of the so-called Dumbbell paradigm on which the viscoelastic models described in Chapter 2 are based. In the framework of this paradigm, indeed, a viscoelastic fluid can be seen as a combination of a collection of fluid parcels of a solvent (masses) and molecules of polymer (springs).

The analogy set in this way might easily be extended even to the governing mathematics. Though for multi-components mechanical systems it essentially consists of sets of ordinary differential equations, whereas for a viscoelastic fluids the dynamics are governed by partial differential equations, a one-by-one relationship could be established among the related terms: namely $m\ddot{\mathbf{x}}$, $c\dot{\mathbf{x}}$, $k\mathbf{x}$ and $\mathbf{f}(t, \Omega)$ corresponding to the substantial derivative of the fluid velocity, the Laplacian of velocity (viscous effect), the divergence of the elastic (extra) stress tensor and the time-dependent buoyancy term in eq. (2.70), respectively.

To put our results in a broader perspective and create other useful links with the existing literature, the reader may also consider some other studies appearing recently about the dynamics of viscoelastic fluids in pipe systems. Actually, the idea that the response of viscoelastic fluids to external excitations can provide a new way to control a system with "dynamic modulation functions" is not new and has already been exploited to a certain extent to develop new microfluidic logical components considering the effect

of constant or impulsive forces [203]. As an other example, most recently, by applying the Oldroyd-B model to the transient response of a viscoelastic Poiseuille flow in a two-dimensional channel for different types of forcing at the inflow, Zhang et al. [204] have clearly shown that a state of resonance can be attained if a periodic square wave force is applied and its frequency matches the intrinsic frequency of oscillation of the viscoelastic, i.e. the frequency of the oscillatory flow that would be obtained by applying a force constant in time.

4.5 Conclusions

This chapter has attempted to assemble a simple, physically intuitive and reasonably self-contained discussion of pure thermovibrational convection in a viscoelastic fluid. A square cavity has been considered given its intrinsic ability to reveal the hidden symmetries of the different convective modes that can be excited in the space of parameters. As made evident by a critical comparison of Newtonian and viscoelastic cases, viscoelasticity can deeply influence the properties of this type of flow.

For Newtonian fluids, the patterning scenario (in terms of time-averaged flow) essentially consists of the alternation of a roll configuration displaying inversional symmetry and a quadrupolar roll distribution. This spatio-temporal behaviour is stable over a relatively wide range of values of the Gershuni number. For relatively high values of Gs, the transition to a different pattern occurs gradually and in an ordered way. The shape of the streamlines remains smooth and the interpretation of the time-dependent flow is relatively straightforward. The number of rolls changes from a minimum of three to a maximum of eight in the range of Gs considered in the present work. Furthermore, specific symmetry properties can be recognized in each case.

For the viscoelastic liquid, the scenario changes dramatically. The regular phenomena displayed by the Newtonian case are taken over by more involved mechanisms, which, for the lowest values of Gs reduce to the alternation between three and twelve principal time-averaged rolls plus four additional small rolls located in proximity to the adiabatic walls. Besides, hand by hand with an increase in the complexity of the pattern, the time-averaged flow displays an increasing sensitivity to Gs (or to Ra_ω for a given

value of the forcing frequency). Remarkably, changes are not limited to a qualitative modification of the flow topology. Appreciable variations also affect the magnitude of the time-averaged velocity. As an example, for $Gs = 5 \times 10^2$, $\Omega = 10^2$ and $\vartheta = 0.1$, the amplitude (A_{u_y}) of the signal of time-averaged velocity measured by a probe located in the centre of the cavity is $A_{u_y,\text{viscoelastic}} = 1.57 \times 10^{-2}$ and $A_{u_y,\text{Newt}} = 8.2 \times 10^{-3}$ for the viscoelastic and the corresponding Newtonian fluid, respectively.

The most interesting cases are those where the characteristic time of the vibrations and the relaxation time are comparable. In such conditions, complex dynamics are established due to the competition between the propensity of polymer molecules to return to a relaxed position and the external vibrations that stretch and shrink them on a regular basis. This phenomenon manifests itself with complex patterns characterized by corrugated rolls and with a non-monotonic behaviour in the amplitude-Σ plane. The latter trend exhibits a fascinating similarity with the typical behaviour of mechanical systems equipped with viscoelastic "components" for vibrational mode control. Notably, viscoelastic flows share a remarkable analogy with these systems in terms of governing equations and physical interpretation of the involved terms.

The next chapter will focus on the natural continuation of this study to assess the influence of the vibrations direction by analysing the case of a 2D square cavity vibrated along the temperature gradient direction.

Chapter 5

2D Multicellular States of Viscoelastic Thermovibrational Convection: Concurrent Temperature Gradient and Vibrations

This chapter is based on Boaro, MacDowall & Lappa, 2022 'The symmetry properties and bifurcations of viscoelastic thermovibrational convection in a square cavity' [7].

5.1 Introduction

The previous Chapter has analysed the case of a 2D square cavity, differentially heated and vibrated in a direction that is orthogonal to the temperature gradient.

Building on the intrinsic ability of this configuration to reveal the hidden symmetries of the different convective modes that can be excited in the space of parameters, it has been shown that elasticity can lead to complex dynamics driven by the competition between the propensity of polymer molecules to return to a relaxed position and the external vibrations that stretch and shrink them on a regular basis.

The natural evolution of that work is to asses how these non-linear effects can manifest in the case of concurrent temperature gradient and vibrations.

5.2 Statement of the problem

A two-dimensional (2D) square cavity having lateral no-slip and adiabatic walls ($\partial T/\partial \mathbf{n}\big|_{\text{wall}} = \mathbf{0}$) and with a fixed difference of temperature between the top and bottom no-slip walls is considered. The related reference system and the boundary conditions are reported in Figure 5.1. This figure also shows that direction of the vibrations (as uniquely defined through the related unit vector $\mathbf{n}_\Omega$) is fixed and parallel to the temperature gradient $\boldsymbol{\nabla} T$ ("parallel configuration"). Similarly to the case with vibrations orthogonal to the temperature gradient, the side of the cavity ℓ is selected as characteristic length of this problem.

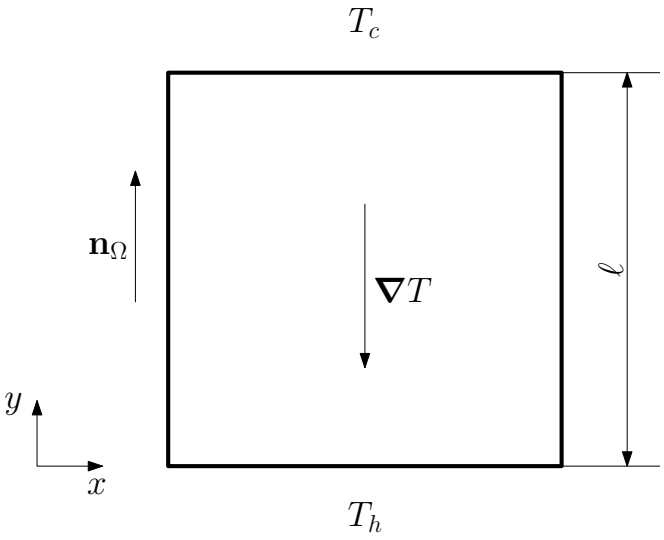

Figure 5.1: Sketch of the geometry and schematisation of the problem.

For continuity with the previous chapter, the balance equations for a FENE-CR fluid, eqs. (2.69), (2.70), (2.71) and (2.72), are solved in the framework of a segregated finite volume method (in space and time) using the computational platform OpenFOAM. Accordingly, the Piso algorithm with a collocated disposition for the primitive variables and the classical Rhie & Chow [158] interpolation scheme are employed for the time-marching procedure.

Here, the log-conformation technique is used to stabilise the viscoelastic solver while a second-order accurate backward scheme is used to discretise the equations in time, a second-order accurate central difference scheme for the spatial discretization of the diffusive terms and a third-order Cubista scheme for the analogous treatment of the convective terms. To avoid nonphysical oscillations, the Cubista scheme is implemented

Table 5.1: Mesh refinement study. Case $Pr = 10$, $\xi = 0.5$, $\Omega = 100$, $Ra_\omega = 2.8 \times 10^4$ and $\vartheta = 0.1$.

Mesh size	$\overline{Nu}$	$\overline{K}$	$\overline{EE}$	%error $\overline{Nu}$	%error $\overline{K}$	%error $\overline{EE}$
20×20	1.60	294.6	36.6			
40×40	1.79	724.0	91.9	11.88	145.76	151.09
60×60	2.014	948.0	138.0	12.51	30.94	50.16
80×80	2.04	1001	149.2	1.29	5.59	8.12
100×100	2.04	1032	155	0	3.1	3.89

through a deferred correction approach and the non-scalar quantities are handled in a component-wise way [174].

Moreover, it is worth highlighting that the steady buoyancy term $PrRaT\mathbf{i}_g$ in eq. (2.70) is set to $\mathbf{0}$ in order to mimic the absence of gravitational field.

5.2.1 Mesh refinement study

A representative case for the mesh refinement analysis is selected as follows. The Prandtl number and viscosity ratio are set to $Pr = 10$ and $\xi = 0.5$, respectively (as these are the fixed dimensionless values considered in this study); moreover, in line with the conditions considered in the results section, $\Omega = 100$ (maximum value of angular frequency), $Ra_\omega = 2.8 \times 10^4$ (close to the maximum value of the vibrational Rayleigh number) and $\vartheta = 0.1$ (value located in the centre of the range explored in this study). The corresponding variations of $\overline{Nu}$, $\overline{K}$, and $\overline{EE}$ on varying the mesh size are reported in Table 5.1. As quantitatively substantiated in this table, an increase in numerical resolution from a mesh 80×80 to 100×100, does not produce appreciable changes in the Nusselt number. The corresponding variations of kinetic and elastic energy are less than 4%, which is an acceptable compromise between accuracy ad time consumption. For these reasons, a mesh having 80 divisions along the vertical and horizontal side of the cavity is chosen for the analysis presented in Sect. 5.3.

5.3 Results

As even a cursory glimpse into the earlier chapters would immediately confirm, the considered problem is characterized by a rich set of influential parameters, which lead naturally to the need of a reasonable choice about those which have to be fixed and those to be varied (not to make the scale of the overall problem intractable). For consistency with Chapter 4, here, in particular, Pr and ξ are fixed to $Pr = 10$ and $\xi = 0.5$, respectively. The angular frequency and vibrational Rayleigh number, however are allowed to span relatively wide ranges, namely, $\Omega = 50$, 75 and 100, and $Ra_\omega \in [Ra_{\omega,\mathrm{cr}}, 3.3 \times 10^4]$, where $Ra_{\omega,\mathrm{cr}}$ is the critical vibrational Rayleigh number for the onset of thermovibrational convection. Moreover, different values of the elasticity number, $\vartheta = 0.10$, 0.15 and 0.20, are examined. Following a logical approach, each of these parameters is systematically varied while keeping constant all the others, this modus operandi being instrumental for the identification of the specific role played by each of them.

5.3.1 Neutral curves

According to the principles of the classical linear stability analysis (LSA), the basic (equilibrium) state of a dynamic system becomes (locally) unstable against a certain class of infinitesimal disturbances only if the set of parameters describing the system belongs to a region of the space of parameters where such disturbances can be amplified. Such amplification is mathematically represented (in the framework of the LSA approach) by an exponential behaviour, which, in turn can be directly put in relation with the eigenvalues of the Jacobian of the linearised equations [105].

Although the present approach does not rely on LSA, the above concepts still represent a useful basis on which the (critical) conditions for the onset of convection can be determined. Indeed, the required theoretical link is provided by the realization that the numerical approach described in Chapter 3 can provide information directly on the amplitude of disturbances and the related evolution in time. Backward extrapolation (to zero) of the disturbance growth rate on a semi-logarithm scale can be used to determine

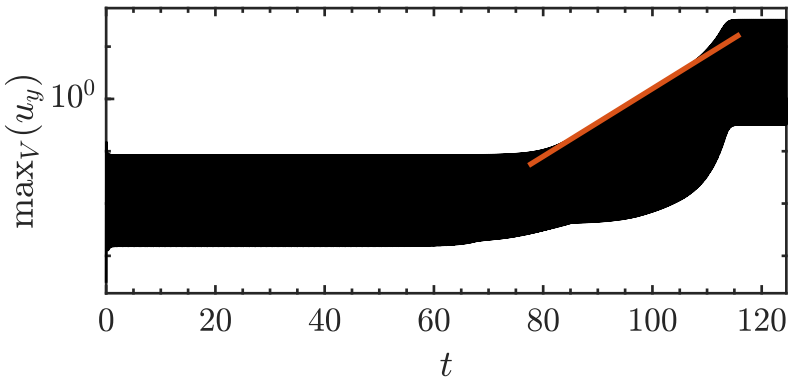

Figure 5.2: Evolution in time of the vertical velocity maximum for the case of $\Omega = 50$, $\vartheta = 0.15$ and $Ra_\omega = 8.89 \times 10^3$. Amplifying disturbances. The angular coefficient of the orange line represents the disturbance growth rate.

the same value of the critical parameter, which would be provided in principle by the LSA.

Using a diffusive state (linear distribution of the temperature in y direction and stationary fluid) as an initial condition and monitoring the global maximum of the y component of the velocity over time ($\max_V(u_y)$, V is the volume of the domain) it is easy to assess whether the disturbance is amplifying or not. Specifically, since from LSA it is known that the disturbance will grow exponentially at the onset of convection, the best way to do so is to plot $\max_V(u_y)$ in a semi-logarithmic plane (y axis having a logarithmic scale). Figure 5.2 reports an example of an amplifying disturbance. The orange line inclination (angular coefficient) represents the *growth rate* (ε) of the instability. To calculate the critical value of the vibrational Rayleigh number, it is sufficient to estimate the law $\varepsilon(Ra_\omega)$ in a region close to the critical threshold. The critical value of the vibrational Rayleigh number ($Ra_{\omega,\mathrm{cr}}$) is recovered by extrapolating ε to 0. The outcomes of this process are reported in Table 5.2, where $Ra_{\omega,\mathrm{cr}}$ is given as a function of the couple (ϑ, Ω).

Figure 5.3 provides additional insights into such dependencies by showing separately the effects of ϑ and Ω. In particular, Figure 5.3a makes evident that, in general, lower frequencies are more destabilizing than the higher ones. This result is in accordance with other studies involving Newtonian [65, 189] fluids. Indeed, in the limit $\Omega \to 0$

Table 5.2: Critical values of the vibrational Rayleigh number $Ra_{\omega,\mathrm{cr}}$ as a function of the elasticity number and angular frequency. Case $Pr = 10$, $\xi = 0.5$.

		ϑ		
		0.1	0.15	0.2
Ω	50	9280	8853	9023
	75	14061	14785	15634
	100	20432	22087	23563

the thermovibrational flow tends to the standard thermogravitational counterpart, i.e. case where the acceleration has never a stabilizing role (in the vibrational case, the acceleration tends to kill the flow in the part of the period where it is directed from the hot to the cold wall); vice versa, when Ω attains a high value, there is an increase in the critical threshold (which would theoretically become infinite in the limit as $\Omega \to \infty$, i.e. when the flow enters the aforementioned potential flow regime, see Sect. 1.2).

Although the concept of overstability discussed in Chapter 1 is still valid in the present case (as an example it was verified that no convection is produced in an equivalent Newtonian fluid with $Pr = 10$ subjected to vibrations with $\Omega = 100$ although a value of the Rayleigh number as high as $Ra_\omega = 2.5 \times 10^4$ is considered), providing a clear picture about the effect of the elasticity number is less straightforward. For relatively small values of the vibrational frequency ($\Omega = 26.5$) Boaro & Lappa [3] found that for a particular combination of parameters ($\xi = 0.1$ and $Pr = 7$) $Ra_{\omega,\mathrm{cr}}$ decreases monotonically as ϑ is increased. This result is also in accordance with the classic literature about Rayleigh-Bénard (RB) convection in viscoelastic fluid [107, 110]. Here the scenario is slightly different. For $\Omega = 50$, $Ra_{\omega,\mathrm{cr}}$ initially decreases (see Figure 5.3b). However, for a further increase of ϑ, $Ra_{\omega,\mathrm{cr}}$ raises again. Notably, $\Omega = 50$ is the only case for which this non-monotonic behaviour was found. For the two other values of the angular frequency, the trend revealed by the present numerical results is the opposite of what one would expect in standard RB viscoelastic convection, i.e. the critical threshold increases with ϑ.

Notably, this scenario is reminiscent of that reported in Chapter 4 (seeFigure 4.19 and 4.20), for the square cavity with orthogonal vibrations. As already explained to a certain extent in the introduction, it was found that, in analogy with the beha-

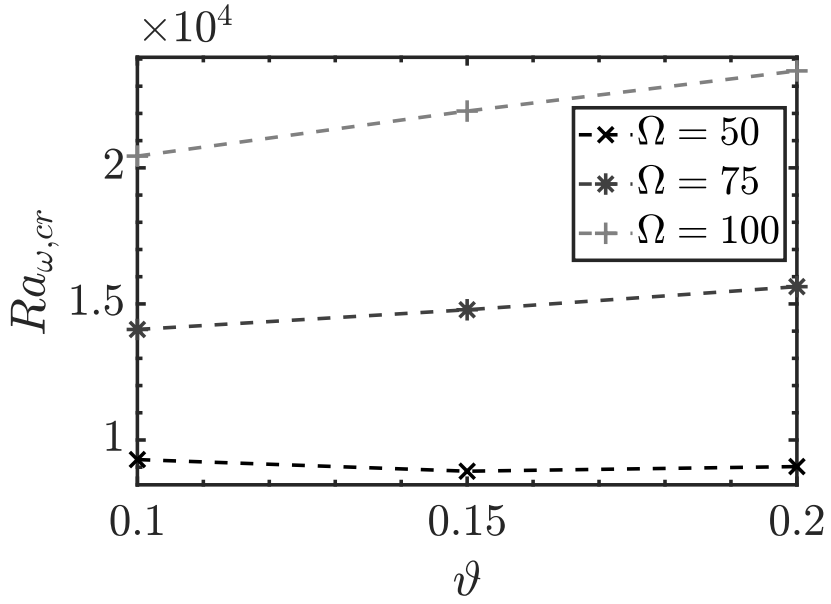

(a)

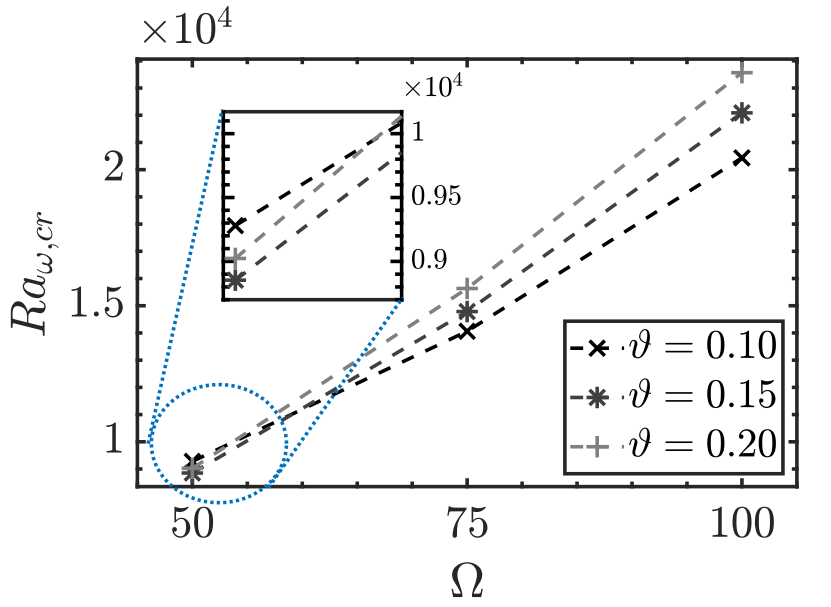

(b)

Figure 5.3: Influence of ϑ (a) and Ω (b) on the critical vibrational Rayleigh number.

viour of certain multi-component mechanical systems that undergo resonances and anti-resonances, vibrated viscoelastic systems can also display regions of variable stability. More precisely, it was observed that for values of the parameter Σ smaller than one,

Table 5.3: Different values of Σ as a function of ϑ and Ω.

		ϑ		
		0.1	0.15	0.2
Ω	50	0.79	1.19	1.59
	75	1.19	1.79	2.38
	100	1.59	2.39	3.18

where Σ is the ratio between relaxation time and period of the forcing vibrations as formally defined in eq. (2.82), the intensity of the mean and instantaneous viscoelastic stress tensor components increase with Σ, whereas, for $\Sigma > 1$ they are inversely proportional to ϑ (and therefore Σ).

The corresponding variation of the parameter Σ for the conditions considered in the present chapter can be gathered from Table 5.3, where it is reported as a function of ϑ and Ω. It can be seen there that for $\Omega = 50$, Σ varies in a relatively restricted neighbourhood of 1, which confirms that the non-monotonic evolution laws or dependencies are not an exclusive prerogative of the perpendicular case. Just like variations of Σ in a narrow range around to the value of 1 can cause non-monotonic changes in the flow amplitude in the case with vibrations perpendicular to the temperature gradient, it can produce similar variations in the critical threshold for the onset of convection in the parallel case.

As illustrated further in the next section, changing the vibrational frequency can also impact significantly the patterning behaviour.

5.3.2 Pattern selection and observed bifurcations

Similarly to what has been discussed in SUBSECTION 1.1.1 and CHAPTER 4 , the simplest way to elaborate a relevant classification of the emerging patterns in terms of symmetries and multiplicity of the related cellular structure is to rely on the approach originally implemented by MIZUSHIMA [30], see Figure 1.6.

For the considered problem, two dominant symmetries were found, namely the **(aa)** and **(sa)** . Additional insights into these modes of convection can be gathered from Figure 5.4, which quantitatively substantiate the relationship between the considered

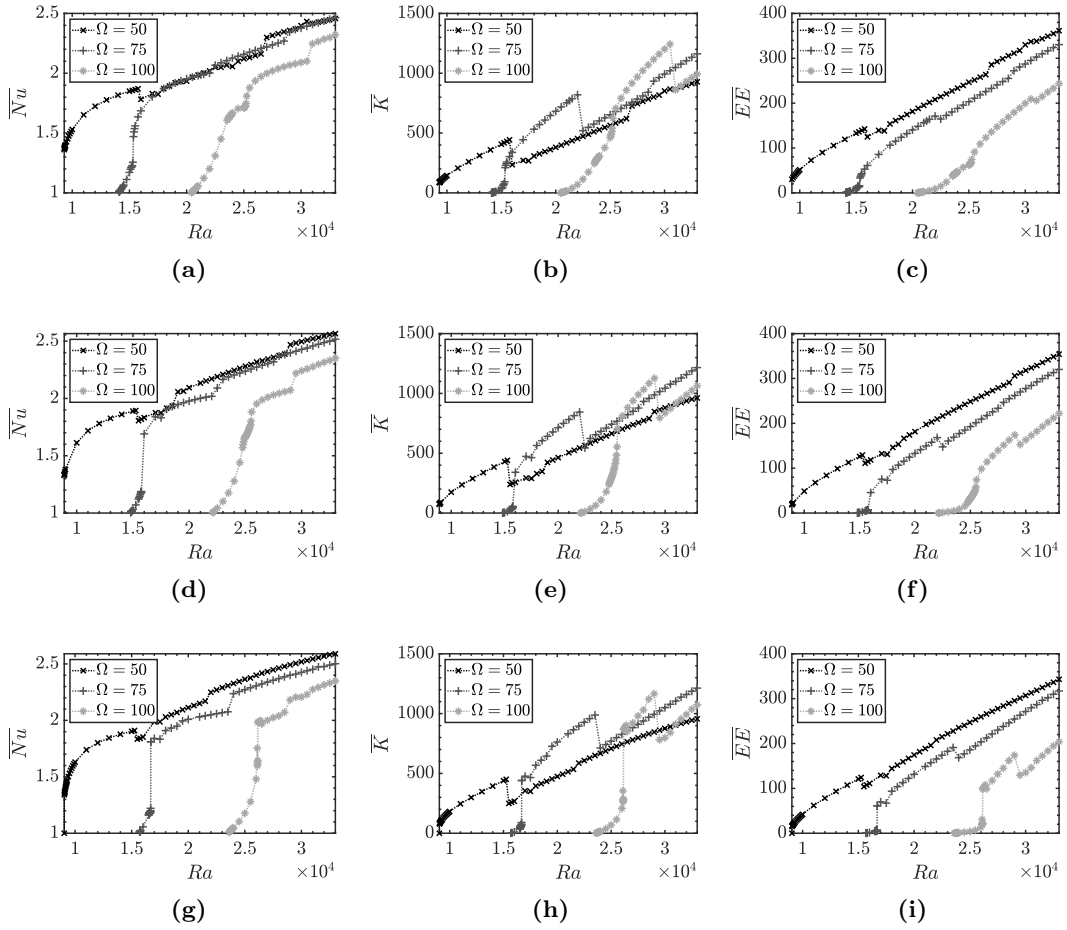

Figure 5.4: Variation of $\overline{Nu}$ (first column), $\overline{K}$ (second column), and $\overline{EE}$ (third column) for $\vartheta = 0.10$ (a)-(c), $\vartheta = 0.15$ (d)-(f), and $\vartheta = 0.20$ (g)-(i) as a function of the vibrational vibrational Rayleigh number. A bigger version of this figure is available in Appendix B.

value of the vibrational Rayleigh number $Ra_\omega \in [Ra_{\omega,\mathrm{cr}}, 3.3 \times 10^4]$ and the "global measures" defined in Sect. 5.2, i.e. $\overline{Nu}$, $\overline{K}$ and $\overline{EE}$.

Following up on the previous point, the first column of Figure 5.4 provides a first glimpse of the effect of the vibrational Rayleigh number on $\overline{Nu}$. It can be seen that while for $\Omega = 50$ the time average Nusselt number increases with a concave down parabolic law at the onset of convection, for $\Omega = 75$ and 100 the curve is concave upwards. Similar considerations can be made for the $\overline{K}$ and $\overline{EE}$ graphs. This difference is due to the fact that at $\Omega = 50$ the flow emerging from the diffusive state displays an **(aa)** symmetry. On

the contrary, for the other two values of the angular frequency, the dominant symmetry is the **(sa)** .

For $\Omega = 50$ the **(aa)** configuration is stable in the range $Ra_{\omega,\mathrm{cr}} \leq Ra_\omega \leq 1.575 \times 10^4$ for $\vartheta = 0.10$, $Ra_{\omega,\mathrm{cr}} \leq Ra_\omega \leq 1.525 \times 10^4$ for $\vartheta = 0.15$ and $Ra_{\omega,\mathrm{cr}} \leq Ra_\omega \leq 1.525 \times 10^4$ for $\vartheta = 0.20$.

Instead, for $\Omega = 75$ the **(sa)** configuration is stable in the range $Ra_{\omega,\mathrm{cr}} \leq Ra_\omega \leq 1.515 \times 10^4$ for $\vartheta = 0.10$, $Ra_{\omega,\mathrm{cr}} \leq Ra_\omega \leq 1.571 \times 10^4$ for $\vartheta = 0.15$ and $Ra_{\omega,\mathrm{cr}} \leq Ra_\omega \leq 1.652 \times 10^4$ for $\vartheta = 0.20$ while for $\Omega = 100$ the corresponding intervals are $Ra_{\omega,\mathrm{cr}} \leq Ra_\omega \leq 2.630 \times 10^4$ for $\vartheta = 0.10$, $Ra_{\omega,\mathrm{cr}} \leq Ra_\omega \leq 2.490 \times 10^4$ for $\vartheta = 0.15$ and $Ra_{\omega,\mathrm{cr}} \leq Ra_\omega \leq 2.6148 \times 10^4$ for $\vartheta = 0.20$.

By denoting by Ra_ω^I the right end of such a stability interval, Figure 5.4 is also instrumental in showing that on exceeding Ra_ω^I, a second bifurcation takes place. For $\Omega = 50$, the **(aa)** dominated solution is taken over by a **(sa)** symmetric configuration, and vice-versa, the **(sa)** configuration becomes an **(aa)** flow when $\Omega = 75$ and 100. The sudden change in the solution comes with an abrupt variation of $\overline{Nu}$, $\overline{K}$ and $\overline{EE}$. In particular, on jumping from an **(aa)** to a **(sa)** solution all these three quantities are lowered, whereas they abruptly increase when going from a **(sa)** to an **(aa)** branch (it is worth recalling here that similar phenomena have been observed in other categories of viscoelastic flows, e.g., the transition from traveling-wave to standing-wave solutions reported by Lappa & Boaro [1] for RB flow in cylindrical configurations with lateral stress-free conditions).

For $\Omega = 50$ the **(sa)** configuration is stable in the range $Ra_\omega^I < Ra_\omega \leq 3.3 \times 10^4$ for $\vartheta = 0.10$, 0.15 and 0.20. Therefore, in this case, the flow maintains the **(sa)** configuration over a relatively wide range of vibrational Rayleigh numbers.

An increase in the frequency makes the system response more involved. While for $\Omega = 75$ and $\vartheta = 0.15$, and $\Omega = 100$ and $\vartheta = 0.20$ the flow bifurcates directly from a **(sa)** to an **(aa)** modes of convection when $Ra_\omega > Ra_\omega^I$, for all the other cases there is a range of the control parameter for which the flow displays an *intermittent* response. These solutions will be analysed in detail in section 5.3.3.

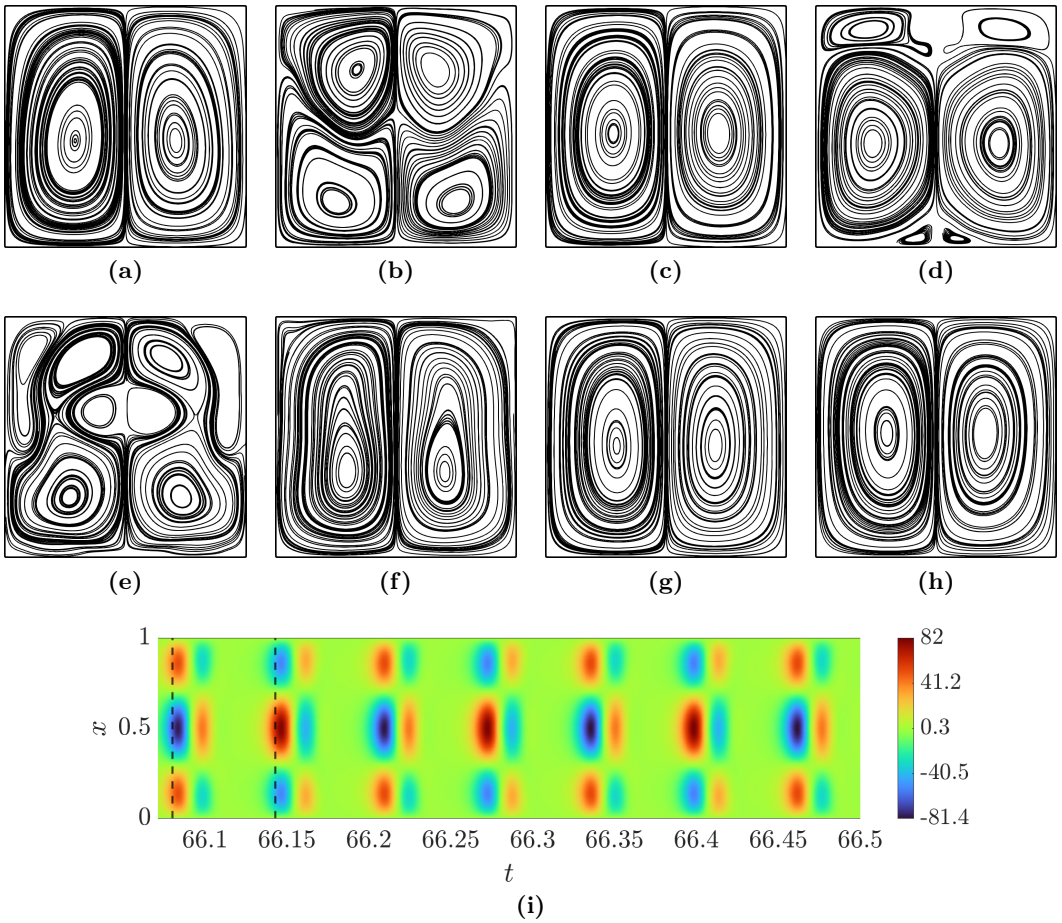

Figure 5.5: Pattern evolution for the case of $Pr = 10$, $\xi = 0.5$, $\vartheta = 0.10$, $\Omega = 100$ and $Ra_\omega = 2.355 \times 10^4$. The streamlines are sampled evenly over a period of the external vibration (half a period of the pattern dynamic evolution) (a)-(h). The spatio-temporal map (i) represent the vertical component of the velocity (u_y) over the centre-line orthogonal to the side-walls ($0 \leq x \leq 1$ and $y = 0.5$). The vertical dotted lines show the interval over where the streamlines where sampled starting at $t_0 = 66.08$. Cavity heated from below.

To summarize, for $\Omega = 75$ the **(aa)** symmetry stability range is $1.535 \times 10^4 \leq Ra_\omega \leq 2.2 \times 10^4$ for $\vartheta = 0.10$, $Ra^I_\omega < Ra_\omega <\leq 2.2 \times 10^4$ for $\vartheta = 0.15$ and $1.669 \times 10^4 \leq Ra_\omega \leq 2.35 \times 10^4$ for $\vartheta = 0.20$ while for $\Omega = 100$ the range is $2.525 \times 10^4 \leq Ra_\omega \leq 3.05 \times 10^4$ for $\vartheta = 0.10$, $2.555 \times 10^4 \leq Ra_\omega \leq 2.9 \times 10^4$ for $\vartheta = 0.15$ and $Ra^I_\omega < Ra_\omega \leq 2.9 \times 10^4$ for $\vartheta = 0.20$.

By indicating with Ra^{II}_ω the next bifurcation point for the **(aa)** symmetry stability interval related to the $\Omega = 75$ and $\Omega = 100$ branches, the symmetry of the system

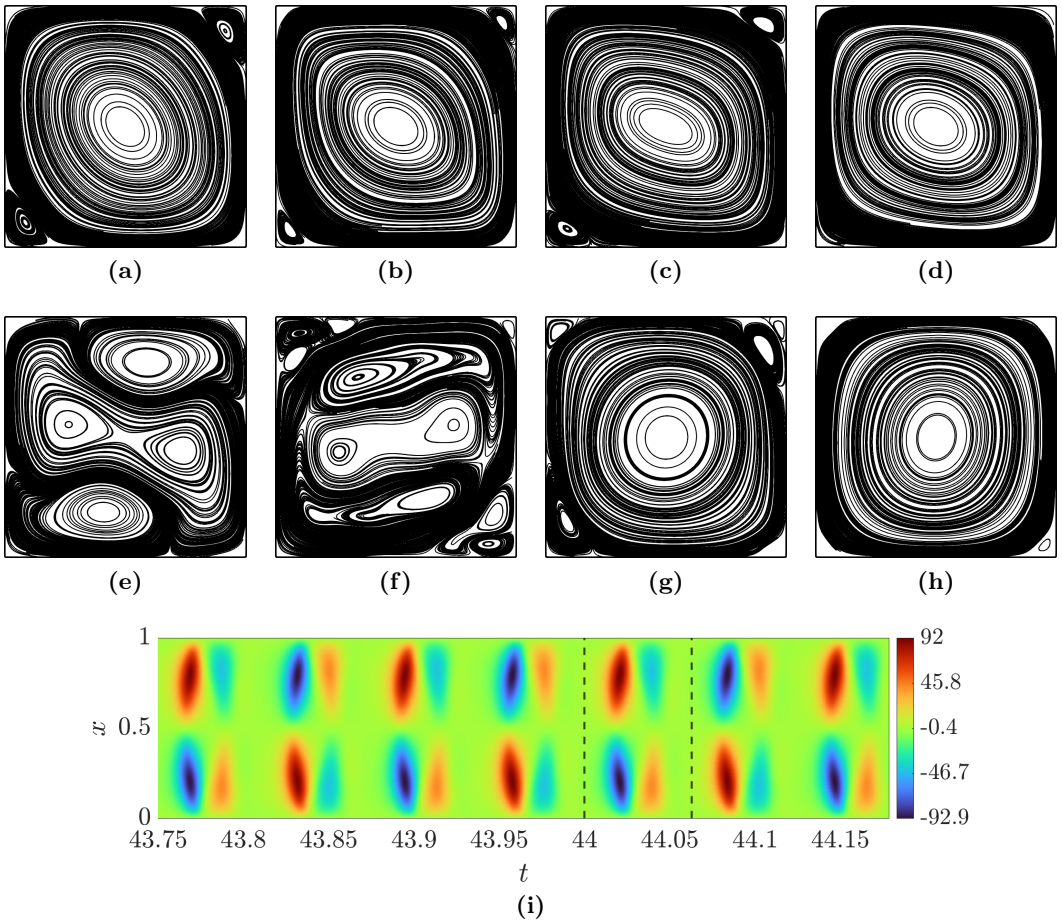

Figure 5.6: Pattern evolution for the case of $Pr = 10$, $\xi = 0.5$, $\vartheta = 0.10$, $\Omega = 100$ and $Ra_\omega = 2.55 \times 10^4$. The streamlines are sampled evenly over a period of the external vibration (half a period of the pattern dynamic evolution) (a)-(h). The spatio-temporal map (i) represent the vertical component of the velocity (u_y) over the centre-line orthogonal to the side-walls ($0 \leq x \leq 1$ and $y = 0.5$). The vertical dotted lines show the interval over where the streamlines where sampled starting at $t_0 = 44$. Cavity heated from below.

changes again as soon as it is exceeded, returning to a **(sa)** configuration. For all the considered solutions, this symmetry is stable in the interval $Ra_\omega^{II} < Ra_\omega < 3.3 \times 10^4$.

At this stage, it is also worth highlighting that, in analogy to thermovibrational convection in an infinite layer of viscoelastic fluid [3, 4], the temporal response of the system to the application of vibrations in all these cases has found to be sub-harmonic, i.e. the flow evolves in time with a frequency that is half of the forcing frequency. The related patterning behaviour is depicted for two representative cases, i.e. $\Omega = 100$,

$\vartheta = 0.10$ and $Ra = 2.355 \times 10^4$ for the **(sa)** symmetry, and $Ra = 2.55 \times 10^4$ for the **(aa)** symmetry in Figure 5.5 and Figure 5.6, respectively. For both cases, the related spatio-temporal map of the vertical component of the velocity (u_y) over a horizontal line passing through the centre of the cavity ($0 \leq x \leq 1$, $y = 0.5$) is also reported. The dashed vertical lines in the maps represent the time interval where the streamlines were sampled. These maps are a useful tool to represent in a compact way the system dynamic evolution [3, 4, 190].

A detailed interpretation of the phenomena shown in these figures can be provided as follows. For the **(sa)** case reported in Figure 5.5, at the beginning of the oscillation period (Figure 5.5a) the flow displays the typical two counter-rotating cells (compare with Figure 1.6), which occupy the whole available space and the convective cell on the left (right) rotates clockwise (anticlockwise). The sense of rotation can be directly inferred from the spatio-temporal map (Figure 5.5i). As the time progresses, two small cells, rotating in the opposite direction with respect to the initial ones, nucleate in proximity to the cold boundary (Figure 5.5b) and grow until their size becomes comparable to the cavity height, thereby suppressing the two initial cells (Figure 5.5c). The associated map is instrumental in showing that the new cells rotate in the opposite direction. In the meantime, the external vibrations have entered their "stabilising" period, as confirmed in the map by the sudden decrease in the velocity intensity (Figure 5.5d and 5.5i). However, the system never attains a motionless state (this is one of the main differences from studies dealing with Newtonian fluids [189, 190]). Rather, by leveraging the elasticity accumulated in the fluid (i.e. the energy that was stored in the polymer molecules during the destabilizing phase), the system is able to maintain the ongoing unsteady flow. This conclusion is supported by both the spatio-temporal map and the analysis of Nu, K or EE signals (omitted for the sake of brevity). Between frame 5.5e and 5.5h there are two other inversions until, at the end of the period of vibrations, the **(sa)** is recovered. However, the sense of rotation is not the same as the initial one. This is the manifestation of the aforementioned half-subharmonicity of the spatio-temporal behaviour. As evident from the map, before recovering the initial situation another period of vibrations is needed. During the second period, the evolution is mirror-symmetric with

respect to the one just analysed (for the sake of brevity, the description of the pattern evolution over the second period is omitted).

Similar considerations can be made for the evolution of the pattern with **(aa)** symmetry. Starting from the initial situation depicted in Figure 5.6a, a single cell occupying almost the whole volume of the cavity and rotating anticlockwise can be seen. Smaller eddies are located in the north-east and south-west corners. As time passes, the size of these two eddies oscillates, as visible in Figure 5.6b-5.6d until at a certain stage they start growing (Figure 5.6e), thereby compressing the main central cell and merging with it (Figure 5.6f). As a result, another central patch of fluid rotating clockwise is formed Figure 5.6g. In the meantime, the direction of the vibrations has become stabilizing for the flow. However, since the intensity of convection is now stronger (see Figure 5.4a), this indirectly confirms that the fluid has stored more energy with respect the previous case (see Figure 5.4b and 5.4c). At the end of the first period of vibrations, the residual elastic energy allows the fluid to move clockwise inside the cell. Even in this case, the half-subharmonicity is evident from the map.

By cross comparison of Figs. 5.5i and 5.6i, at this stage the reader will have realized that the two symmetries produce different behaviours in the spatio-temporal maps. Indeed, while for the **(sa)** symmetry the maps display three streaks, this number is reduced to two only for the **(aa)** symmetry.This observation will be analysed better in the next section. As a concluding remark for this section, let us discuss another effect related to the average energies reported in Figure 5.4.

In particular, let us highlight that, while for the elastic energy, regardless the value of ϑ, the inequality $\overline{EE}_{100} < \overline{EE}_{75} < \overline{EE}_{50}$ holds, a similar relationship cannot be easily deduced for $\overline{Nu}$ and (especially) for $\overline{K}$. Indeed, while at the onset of convection the inequality is true for all the averaged quantities, for $\vartheta = 0.1$, $\overline{Nu}_{75} > \overline{Nu}_{50}$ in a certain sub-range of Ra_ω, while $\overline{Nu}_{100} < \overline{Nu}_{75}$ and $\overline{Nu}_{50}$, regardless of the considered value of Ra_ω. Similar results were also reported by Crewdson & Lappa [189] for Newtonian fluids in the range of small frequencies (see Fig. 10 and 11 in Ref. [189]). Although those authors analysed the evolution of the maximum of the Nusselt number (here, it is the time-averaged value), trends similar to that reported in the present study were

obtained (which may be regarded as a possible hint for the existence of universality class in thermovibrational convection when it is considered in square cavities at low frequencies).

For what concerns the average kinetic energy, producing inequalities similar to the $\overline{EE}$ and $\overline{Nu}$ ones is not as straightforward as one would imagine. Indeed, this parameter is particularly affected when the bifurcation takes place. Moreover, since for every combination of (ϑ, Ω), the transition to a new solution occurs in different ranges of Ra_ω, abrupt jumps and intersecting lines are present in the graph in the central column of Figure 5.4, which make such an attempt almost impossible. To elucidate further the significance of this observation, one should keep in mind that $\overline{K}$ accounts for the overall fluid field behaviour, while $\overline{Nu}$ and $\overline{EE}$ consider only a sub range of the component of temperature gradient and extra stress tensor respectively. Owing to this "component filtering", $\overline{Nu}$ and $\overline{EE}$ do not represent all the non-linear effects that naturally emerge in the fluid. Interestingly, similar concepts were proven experimentally in the context of RB convection in elasto-viscoplastic gels [127] where it was shown that, while the calculated Nu generally displays small (almost negligible) oscillations, K can closely captures the ongoing microphysical mechanism responsible for the flow bifurcation. Similar insights can be inferred from the numerical study for RB convection in viscoelastic fluids by Zheng et al. [205], which here is used to support the increased complexity observed in the trends of the K parameter.

5.3.3 Dynamic evolution of intermittent states

This subsection is finally devoted to the "intermittent" response, which, as mentioned earlier, was detected for $(\vartheta, \Omega) = (0.10, 75)$, $(0.20, 75)$, $(0.10, 100)$ and $(0.15, 100)$. In order to do so, let us analyse the signal of the velocity vertical component (u_y) probed in the centre of the cavity $(x, y) = (0.5, 0.5)$ for the characteristic case of $\Omega = 100$, $\vartheta = 0.10$ and $Ra_\omega = 2.4 \times 10^4$ reported in Figure 5.7. Such a figure is useful as it clearly shows that, in addition to the half-subharmonic variation of the signal, another long-period disturbance is affecting the flow evolution. The corresponding spatio-temporal map over the long period is reported in figure Figure 5.8. Building on such plots and

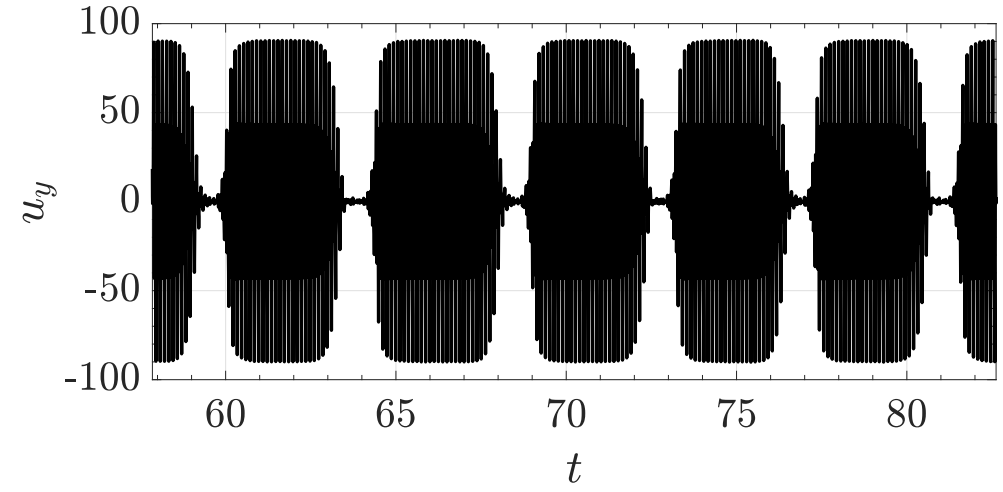

Figure 5.7: Vertical component of the velocity probed in the centre of the cavity for $\Omega = 100$, $\vartheta = 0.10$ and $Ra_\omega = 2.4 \times 10^4$.

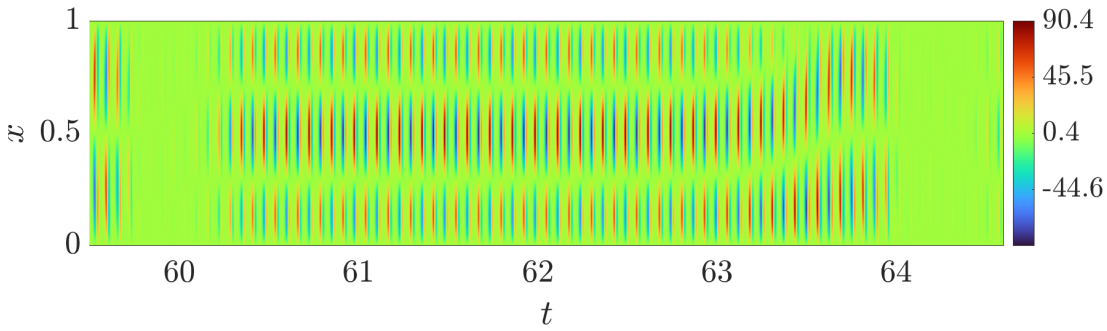

Figure 5.8: Spatio-temporal map of the vertical component of the velocity (u_y) over the centre-line orthogonal to the side-walls ($0 \leq x \leq 1$ and $y = 0.5$) for $\Omega = 100$, $\vartheta = 0.10$ and $Ra_\omega = 2.4 \times 10^4$.

the observations about the patterning behaviour for the two different convective modes made in Sect. 5.3.2, it can be inferred that, during the long period of oscillation (hereafter simply called secondary oscillation) the flow *intermittently* displays both a **(sa)** and **(aa)** symmetry. The period of time in which a single mode is stable depends on the control parameters. Moreover, between each secondary oscillation, the flow becomes diffusive and stationary, i.e. the convective instabilities are temporally suppressed.

Most interestingly, the (angular) frequency ϖ of the secondary oscillation changes as a function of the vibrational Rayleigh number. This is shown in Figure 5.9 where the variation of the angular frequency of the secondary oscillation is presented as a func-

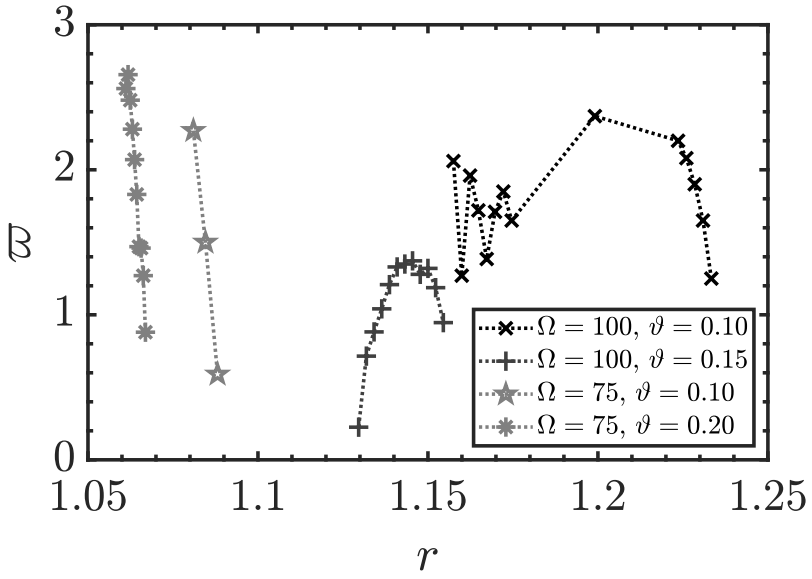

Figure 5.9: Angular frequency ϖ of the secondary oscillation as a function of the reduced vibrational Rayleigh number $r = Ra_\omega / Ra_{\omega,\mathrm{cr}}$.

tion of the reduced vibrational Rayleigh number $r(\vartheta, \Omega) = Ra_\omega / Ra_{\omega,\mathrm{cr}}(\vartheta, \Omega)$, where $Ra_{\omega,\mathrm{cr}}(\vartheta, \Omega)$ is the critical vibrational Rayleigh number for the onset of thermovibrational convection reported in Table 5.2 (used to represent all the four combination of (ϑ, Ω) in the same plot).

For $\Omega = 75$, the smallest frequency of the signal behaves as a linear function of r, or equivalently Ra_ω. Increasing the vibrational frequency to 100 has the effect of producing a non-monotonic law for the secondary oscillation frequency. Moreover, while for $\Omega = 75$ the intermittent behaviour was observe only over a small range of Ra_ω, this fascinating mechanism is stable over a wider interval of the control parameter for $\Omega = 100$.

Furthermore, a particular phenomenon shows up for the specific combination $(\vartheta, \Omega) = (0.20, 75)$, more specifically between the region of stability of the solution with the **(sa)** symmetry and the intermittent dynamics. A range of Ra_ω exists where the **(aa)** symmetry is stable. However, inspection of the related case depicted in Figure 5.10, and its comparison with the "standard" symmetric **(aa)** state, lead to the conclusion that the centre of rotation of the main cell oscillates horizontally with a low frequency. This state can be interpreted as a precursor of the state with intermittent evolution. Indeed,

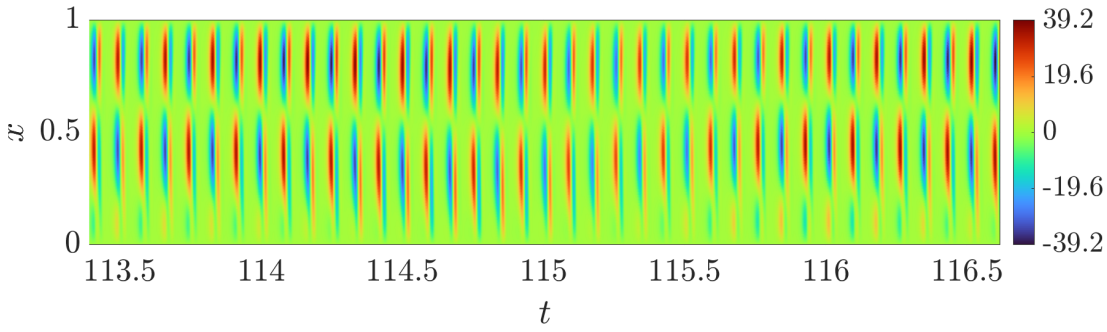

Figure 5.10: Spatio-temporal map of the vertical component of the velocity (u_y) over the centre-line orthogonal to the side-walls ($0 \leq x \leq 1$ and $y = 0.5$) for $\Omega = 75$, $\vartheta = 0.20$ and $Ra_\omega = 1.657 \times 10^4$.

a relatively weak cell can be seen in the proximity of the left side ($x = 0$), which is periodically suppressed by the bigger and stronger central vortex. This solution is stable for $1.653 \times 10^4 \leq Ra_\omega \leq 1.658 \times 10^4$.

In order to gain additional insights into the intermittent state, some simulations have been repeated by initializing them with the **(sa)** and **(aa)** solutions in place of the diffusive conditions. Remarkably, these additional computations have clarified that the unique regime in which the intermittent behaviour occurs does not depend on the initial conditions or the specific path of evolution followed by the system. This apparent innocuous observation is instrumental in filtering out chaos-related aspects as possible root causes for the interpretation of this regime. Thermal flows in the "parallel" case are particularly prone to develop "multiple solutions", i.e. different states that can be entered for a fixed value of the control parameter depending on the initial conditions [10, 206]. Generalized consensus exists in the literature that the competition among these attractors (existing in parallel in the space of parameters) can cause multi-frequency states and ensuing transition to chaos. Behaviours of such a kind become even more frequent when viscoelastic fluids are considered, relevant examples in the case of of RB and MB convection being the works by Lappa & Boaro [1] and Lappa & Ferialdi [135].

Building on the the insensitivity of the "intermittent" state to the initial conditions and the fact that, on further increasing the control parameter a more regular behaviour is recovered, however, it can be inferred that this peculiar regime should be regarded as a

meta-stable (quasi-periodic) condition in which the system continuously jump from one mode of convection to the other. In this regard, the same analogy already developed by Boaro & Lappa [3] with the resonant modes of convection identified by Rogers et al. [207] could be applied. Such peculiar mode of convection is driven by the coexistence of two distinct category of disturbances (each displaying a different temporal dependence), which are allowed to interact in a resonant way (Figure 5.7).

5.4 Conclusions

Thermovibrational convection in the considered square cavity with vibrations parallel to the imposed temperature gradient is enabled as a threshold is exceeded in terms of Rayleigh number, which depends to a significant extent on the considered value of the elasticity number and the frequency of the forcing (the vibrations). While an increase in the frequency generally leads to a larger value of this critical parameter, a variation of the fluid elasticity can produce various trends depending on the considered frequency. The frequency also determines the emerging symmetry; in particular, two main categories of concurrent disturbances are at play in the considered region of the space of parameters.

On increasing the Rayleigh number, a unique hierarchy of bifurcations is produced where the initial symmetry displayed by the flow can be taken over by the concurrent one over a certain interval of the vibrational Rayleigh number. However, as a second threshold is exceeded the flow returns to its original symmetry.

Although this scenario applies to most of the situations considered, a subregion of the space of parameters exists where the competition of the two convective modes with different symmetries can give rise to an intermittent spatio-temporal behaviour before a state with one or the other symmetry is recovered.

In the following chapter the direction of the vibrations will remain fixed in the parallel configuration. However, the flow will be allowed to emerge in laterally unbounded (infinite) 3D shallow layer.

Chapter 6

On the Competition of Overstability and Stabilizing Effects in Vibrated 3D Viscoelastic Layers

This chapter is based on Boaro & Lappa, 2021 'Competition of overstability and stabilizing effects in viscoelastic thermovibrational flow' [3].

6.1 Introduction

As the reader might have realised from the arguments presented in Chapter 1, most of the pioneering studies in the field of thermally-driven flow were dealing with simple geometrical configurations. Previous chapters investigated the case of square laterally bounded geometries. However, the archetype that certainly has enjoyed the most popularity is the infinite layer. Indeed, under simplifying assumptions (mostly related to the top and bottom boundary condition) this model admits analytical solution for a wide variety of convective flows.

Let us recall that in the context of viscoelastic thermovibrational flows, Yang [141], and Lyubimova & Kovalevskaya [142] investigated the infinite layer of viscoelastic liquid simultaneously subjected to a steady and a time-varying acceleration (the steady and oscillatory components having similar amplitude). Although interesting new physical mechanisms were identified, the dynamics driving these types of solutions are still largely unknown. In particular, these two studies, using an LSA approach, do not consider physical (no-slip) boundary conditions. Moreover, they do not tackle the problem of "pure" thermovibrational flow, but only its hybrid version.

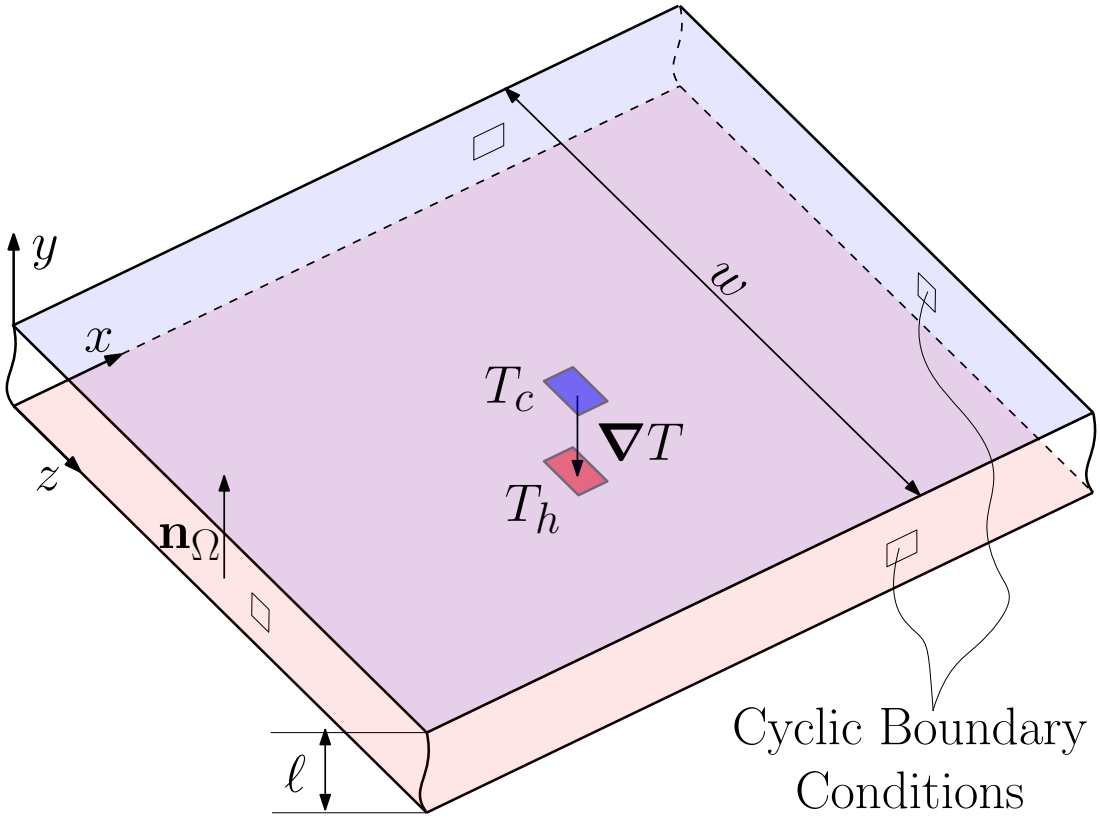

Figure 6.1: Sketch of the geometry and scheme of the problem.

This automatically results in two important issues or questions, which need to be pinpointed suitably here: is the overstability concept still applicable to pure thermovibrational convection? Moreover, it is unknown whether the mechanisms supposed to be operative in the case of Newtonian fluids still play a role in this case or not. Beyond the mere motivation to bridge the abovementioned gap, this chapter is also specifically interested in pushing forward viscoelastic thermovibrational convection in a shallow cavity as a new archetypal problem to improve our fundamental understanding of some of the processes discussed in Part I. Moreover, the constraint of two-dimensional flow assumed in the two earlier chapters is removed, i.e. the flow is allowed to develop a fully three-dimensional response.

6.2 Statement of the problem

As discussed in the introduction, the problem is to determine how a relatively high level of elasticity can interfere with the low-frequency branch of thermovibrational convection when vibrations are parallel to the imposed temperature gradient.

From a mathematical point of view, for simplicity, this problem can be modelled as a parallelepipedic shallow domain having a square symmetry (same size along the x and z directions) and aspect-ratio $AR = w/\ell = 15$ (where w represents the side of the bases and ℓ is the related distance along the y axis which represents the problem's characteristic length). The top and bottom boundaries are considered as solid no-slip walls (*solid-solid* configuration) having fixed temperature (Dirichlet boundary condition) in such a way that the difference of temperature $\Delta T = T_h - T_c$ is maintained constant. Moreover, in order to mimic the behaviour of and *infinite* layer, *cyclic* boundary conditions are implemented at the sides. A sketch of this configuration is shown in Figure 6.1. The external vibrations are assumed to have a fixed direction that is parallel to the temperature gradient $\boldsymbol{\nabla} T$, as sketched in Figure 6.1.

The balance equations for the Oldroyd-B fluid (eqs. (2.69),(2.70), (2.71) and (2.65)) have been integrated over the domain using Piso method (see. the Numerical Method chapter) and the related Rhie & Chow [158] interpolation scheme, which allows the set of mixed parabolic and hyperbolic balance equation to be solved on a *co-located* grid.

For the practical implementation of the Piso approach, the diffusive and convective terms appearing in the different equations have been discretised here using a CDS (Central Difference) scheme accurate to the second-order. However, the CDS has been replaced with the Minmod variant for the specific solution of eq. (2.70). This "work-around" has been introduced to mitigate some of the known numerical difficulties related to viscoelastic fluids, and ensure stability of the numerical procedure over a wide range of parameters. Nonetheless, to further improve the algorithm stability and mitigate the numerical singularities mentioned in chapter 3, the numerical procedure was implemented through a bsd technique, as described in Section 3.2.

Table 6.1: Mesh refinement study. Case $Pr = 7$, $\Omega = 26.5$, $Ra_\omega = 1170$, $\vartheta = 0.38$, $\Sigma = 1.6$, viscoelastic fluid. 2D simulation.

Mesh	A_{u_y}	$\overline{Nu}$
150×30	24.46	1.13
150×35	24.73	1.14
200×30	26.67	1.15
200×35	27.15	1.15
300×35	29.52	1.18
410×35	31.23	1.21
450×40	31.87	1.22

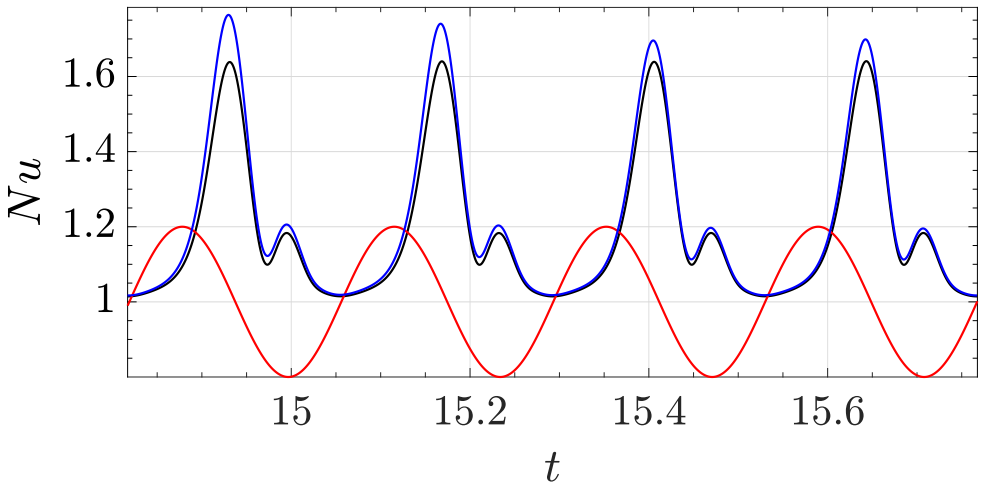

Figure 6.2: Time evolution of the Nusselt number for 2 different densities of the mesh, in black (—) $200 \times 35 \times 200$, in blue (—) $300 \times 35 \times 300$, in red (—) the qualitative evolution of the acceleration. 3D simulations.

Moreover, it is worth highlighting that the steady buoyancy term $PrRaT\mathbf{i}_g$ in eq. (2.70) is set to $\mathbf{0}$ in order to mimic the absence of gravitational field.

6.2.1 Mesh refinement study

The present chapter considers a 3D geometry. Since conducting a grid independence-study would be extremely expensive from a computational point of view, following a common practice in the literature, here the mesh refinement study has been (initially) limited to the equivalent 2D configuration (assumed to have infinite extension along the third direction z). Such a modus operandi relies on the realization that since the

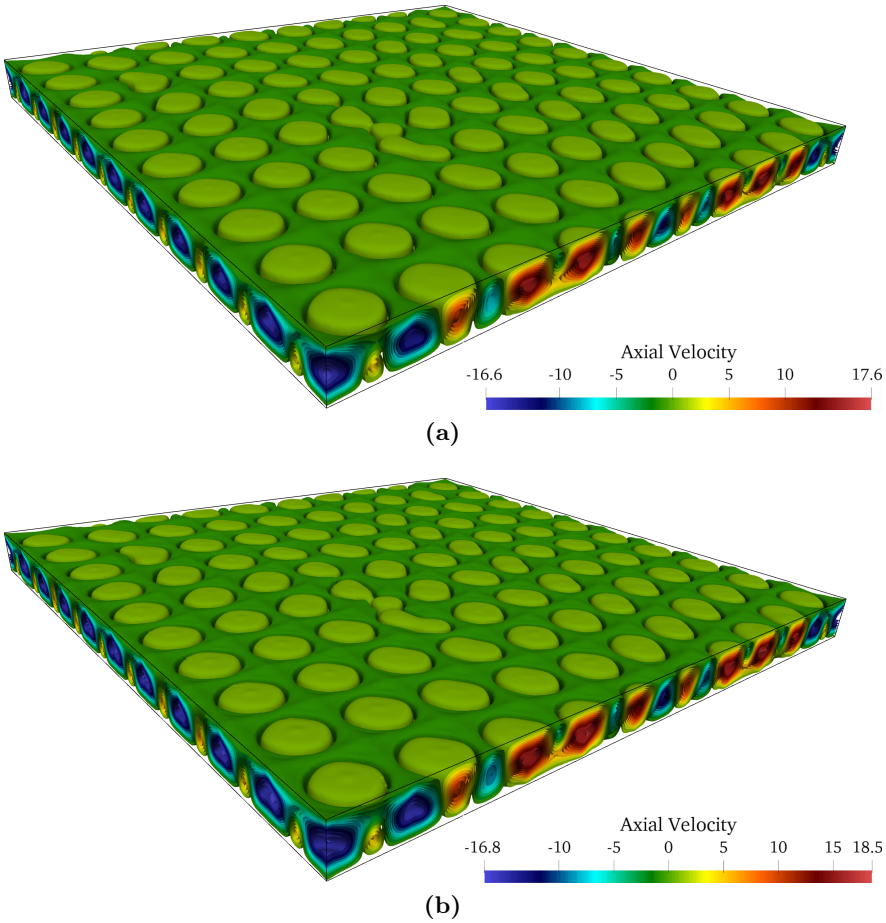

Figure 6.3: 3D isosurfaces of the axial velocity for the case with $Pr = 7$, $\Omega = 26.5$, $Ra_\omega = 1170$, $\xi = 0.1$, $\vartheta = 0.38$, $t = t_0$, (a) mesh $200 \times 35 \times 200$, (b) mesh $300 \times 35 \times 300$.

considered 3D problem is isotropic with respect to the horizontal direction (i.e. no preferred direction exists in the xz plane), the required grid resolution for the x direction can also be applied to the perpendicular direction z.

As sensitive quantities for such investigation, this study analyses the amplitude (A_{u_y}) of the y component of the **u** signal measured with a virtual probe located in the centre of the layer, and the time averaged value of the Nusselt number (defined by eq.(2.84)) for the following set of representative parameters: viscoelastic fluid with $Pr = 7$, $\Omega = 26.5$, $Ra_\omega = 1170$, $\vartheta = 0.38$ and $\Sigma = 1.6$. As quantitatively substantiated by the data reported in Table 6.1, a mesh with 300×35 cells can provide a reasonable level of grid independence. Indeed, when the number of points in the horizontal direction

exceeds 300, the solution becomes essentially independent from the mesh (the percentage variations for a variation of 100 points being 5% only for the instantaneous velocity and less than 3% for the average Nusselt number, a reasonable approximation from an engineering standpoint).

In order to verify the applicability of these findings to the complete (original) problem, the study has also been repeated considering a 3D parallelepipedic shallow domain having a square symmetry (yet referring to both the velocity signal and the Nusselt number). As witnessed by Figure 6.2, apart from a small vertical shift in the position of the curves, a change in the mesh has no impact on the system temporal response. The same conclusion also stems from Figure 6.3 where the 3D pattern (system behaviour in space) is shown for the same conditions of Figure 6.2.

Taking into account the main implications of Figure 6.2 and 6.3, in the present work most of simulations have been conducted using a grid with $200 \times 35 \times 200$ cells (a reasonable compromise between accuracy and the required simulation time).

6.3 Results

As assessing 3D effects through comparison with numerical simulations conducted under the constraint of two-dimensionality is always beneficial (actually the history of thermal convection is full of examples where focused comparisons of such a kind were instrumental in clarifying the nature of the dominant disturbances and possibles regimes of motion), this section initially discusses some simulations carried out neglecting the z direction (see subsection 6.3.1; the third dimension is re-introduced later in subsection 6.3.2, which is entirely dedicated to the presentation and critical analysis of the related results).

On the one hand, this modus operandi is intentionally implemented to discern the ability of the flow to develop 3D components of velocity when the disturbances saturate their amplitude, on the other hand it fits into a more "practical" strategy where 2D simulations are used to determine the critical threshold for the onset of fluid motion (known to be driven by two-dimensional disturbances) with notable computational savings.

Table 6.2: Extrapolation of the critical vibrational Rayleigh number $Ra_{\omega,\mathrm{cr}}$ for a layer of viscoelastic fluid delimited by differentially heated *solid-solid* walls with $Pr = 7$, $\Omega = 26.5$, $\xi = 0.1$. The present results have been obtained using 2D simulation and a domain having $AR = 15$ with cyclic boundary conditions at the lateral boundaries.

ϑ	$Ra_{\omega,\mathrm{cr}}$
Newtonian	16070
0.06	3245
0.24	1207
0.38	956

In particular, this chapter considers a layer of an Oldroyd-B liquid having $Pr = 7$ and $\xi = 0.1$ subjected to external vibrations with a frequency $\Omega = 26.5$ (low frequencies regime). Three different level of elasticity are examined, i.e. $\vartheta = 0.06$, 0.24 and 0.38 corresponding to a value of $\Sigma = 0.25$, 1.01 and 1.6 respectively.

6.3.1 2D results and critical convective threshold

This section is dedicated to the aforementioned 2D study, by which the value of the *critical* vibrational Rayleigh number $Ra_{\omega,\mathrm{cr}}$ is computed for any considered value of the elasticity number ϑ. In particular, in order to mimic the typical approach envisaged by LSA (as already done in section 3.4 to support the validation of the present solver), the needed threshold values are determined by extrapolating the amplitude A of probe signals to 0. For this purpose, a grid with 410×35 nodes is used. The ensuing results are presented in Table 6.2.

As quantitatively substantiated by this table, the critical threshold for the onset of convection strongly depends on the level of elasticity (ϑ). As expected, and in accordance with other studies on Rayleigh-Bénard (RB), Marangoni-Bénard (MB) and Marangoni or thermocapillary (TC) convection in viscoelastic liquids [105, 107, 110, 111, 117, 128], the bifurcation occurs at lower values of the governing parameter (in this case $Ra_{\omega,\mathrm{cr}}$) for more elastic fluids. Interestingly, there is a shift of one order of magnitude if the results for Newtonian and viscoelastic fluids are compared (i.e. from $O(10^4)$ to $O(10^3)$).

In order to compare our results for different values of ϑ (the simulations with Newtonian fluid may be seen as the limit of $\vartheta \to 0$), a new parameter $r = Ra_\omega / Ra_{\omega,\mathrm{cr}}$

can be defined, i.e. the ratio between the effective Ra_ω used for the numerical simulation and the corresponding critical value (the one determined through extrapolation, reported in Table 6.2). To fix the ideas, throughout the present study, this ratio is set to $r \approx 1.2$ (in other words, all the presented results exceed the critical threshold by a similar percentage).

Specific characterization of all these states is provided through the introduction of suitable quantities used to assess the "response" of the system from both fluid-dynamic and thermal points of view. More precisely, this work considers an axial velocity signal (the probe being located in the centre of the cavity) and the time evolution of the *Nusselt number* $Nu(t)$ calculated on the hot plate and defined by eq (2.83). In addition, the *time average Nusselt number* $\overline{Nu}$ defined in eq. (2.84) was also employed.

Following a logical approach, let us conveniently start from the analysis of the velocity signals. Moreover, the Newtonian case is considered first (expected to be simpler in comparison to the cases where overstability enters the dynamics).

This is shown in Figure 6.4a where the typical behaviour with the fluid oscillating continuously between a quiescent state and convective motion can be recognized. This is in agreement with known solutions for square cavities (see e.g. [65, 189]). These peculiar dynamics are due to the continuous transition from stabilising (heating from above) to destabilising (heating from below) effects as the external dynamic force (resulting from the application of vibrations) changes its sign. As witnessed by the velocity signal spectrum (Figure 6.5a), this periodic alternation has the same frequency of the external vibrations Ω. Therefore, the state shown in this figure can be categorised as a Synchronous-Periodic (SP) one ([65, 189]). Further confirmation for this interpretation stems from the evolution in time of the Nusselt number $Nu(t)$ (Figure 6.6a). When the fluid is in quiescent conditions, thermally diffusive conditions are established, and, accordingly, $Nu(t) = 1$.

The situation dramatically changes when the viscoelastic conditions are considered (see Figures 6.4b, 6.4c and 6.4d). As the reader will easily realize by inspecting these figures, no time interval exists where quiescent conditions are attained (Figure 6.4 and

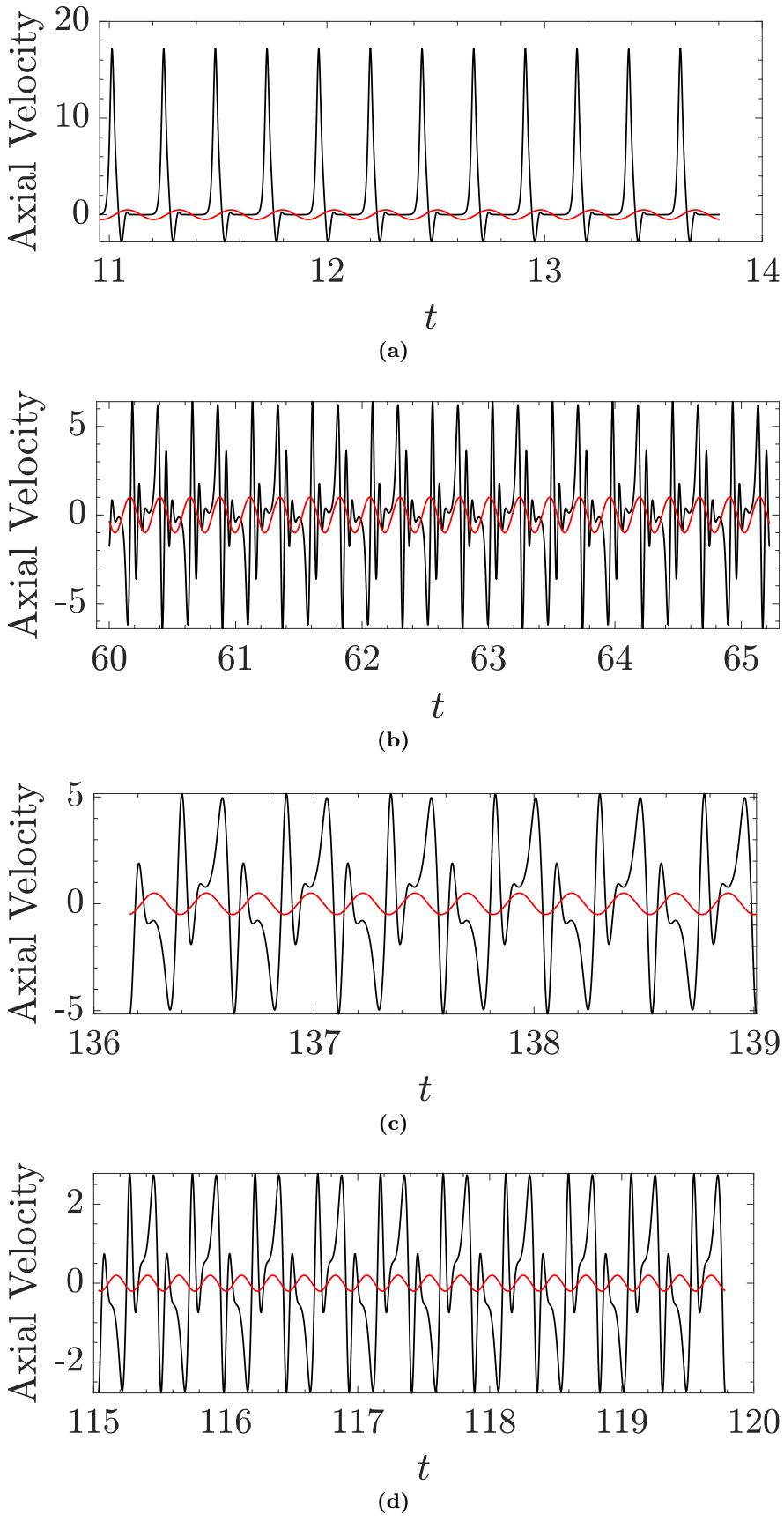

Figure 6.4: Time evolution of the Axial velocity signal. The probe is located in the centre of the layer. Numerical simulation with $AR = 15$,$Pr = 7$, $\Omega = 26.5$, $\xi = 0.1$ (a) Newtonian fluid, $Ra_\omega = 19750$, (b) $\vartheta = 0.06$, $Ra_\omega = 3500$, (c) $\vartheta = 0.24$, $Ra_\omega = 1475$, (d) $\vartheta = 0.38$, $Ra_\omega = 1170$. In black (—) is represented the signal, in red (—) the evolution of $\mathbf{a}_\Omega$.

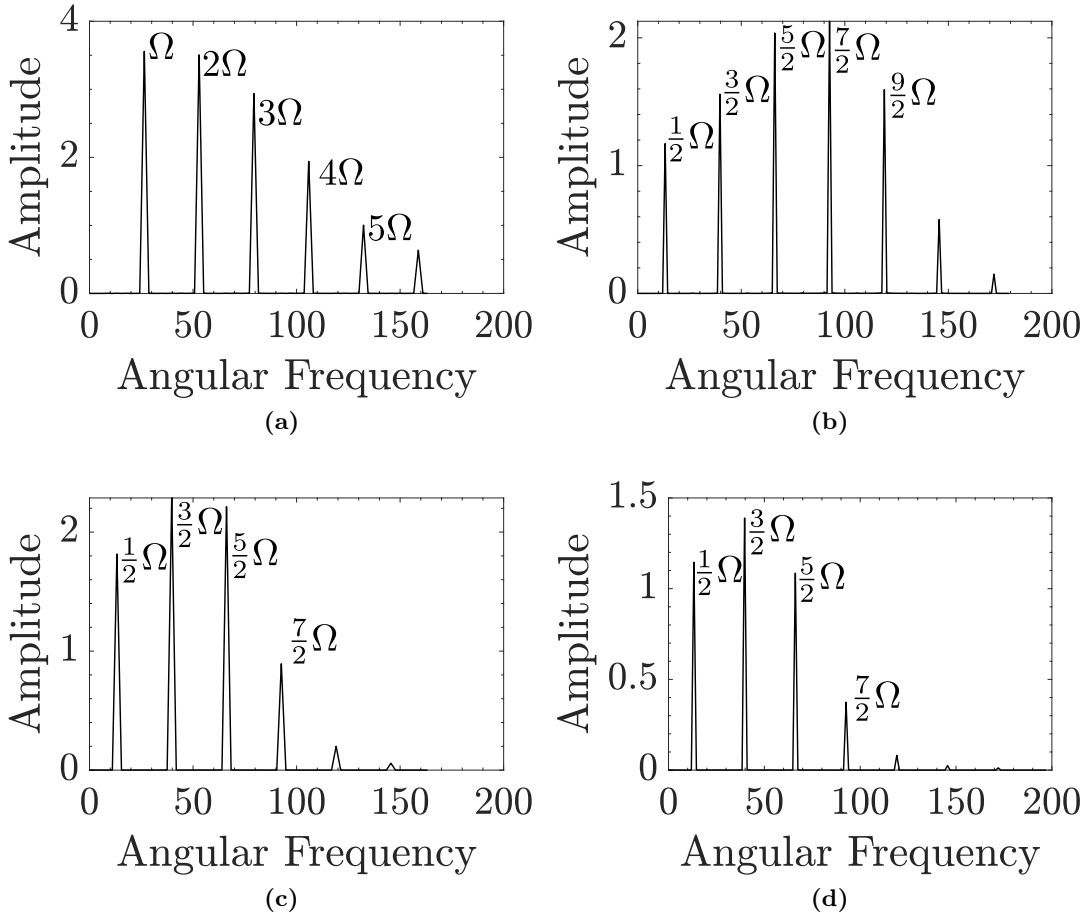

Figure 6.5: Angular frequency of the Axial velocity signal. The probe is located in the centre of the layer. Numerical simulation with $AR = 15$,$Pr = 7$, $\Omega = 26.5$, $\xi = 0.1$ (a) Newtonian fluid, $Ra_\omega = 19750$, (b) $\vartheta = 0.06$, $Ra_\omega = 3500$, (c) $\vartheta = 0.24$, $Ra_\omega = 1475$, (d) $\vartheta = 0.38$, $Ra_\omega = 1170$.

6.6). Moreover, as one would expect in the light of the arguments provided before, for $\vartheta = 0.24$ and 0.38, $Nu(t)$ is always higher than one.

Another notable modification in the dynamics concerns the frequency spectrum. The simple correspondence between the forcing frequency and the frequency of the induced velocity field is no longer a feature of these solutions. As evident in Figure 6.5, the flow displays frequencies that are smaller than the frequency of the imposed force (e.g., $\Omega/2$). The behaviour can therefore be classified as half-subharmonic (SU) ([189] and references therein).

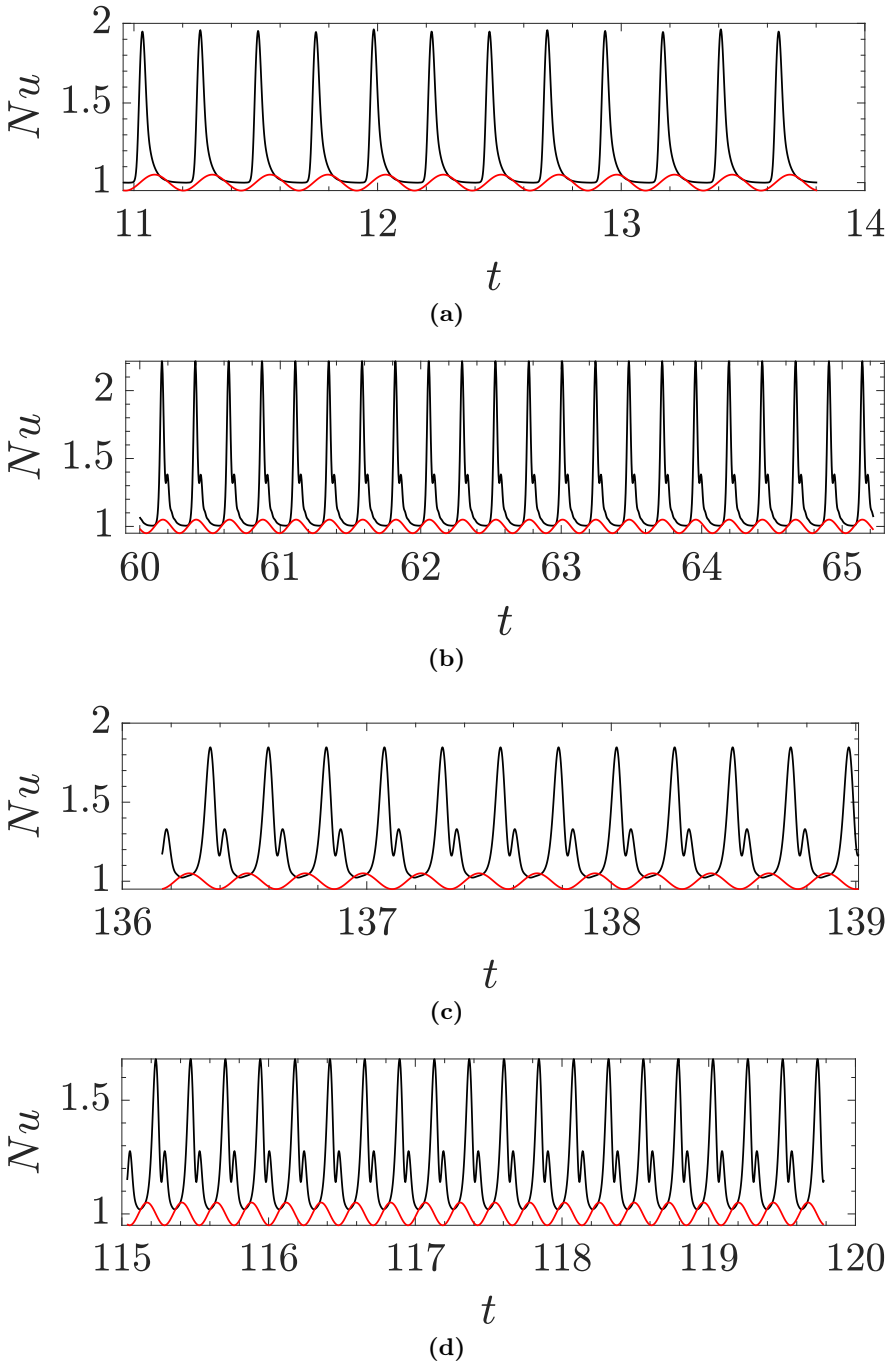

Figure 6.6: Time evolution of $Nu(t)$.Numerical simulation with $AR = 15$, $Pr = 7$, $\Omega = 26.5$, $\xi = 0.1$ (a) Newtonian fluid, $Ra_\omega = 19750$, $\overline{Nu} = 1.16$, (b) $\vartheta = 0.06$, $Ra_\omega = 3500$, $\overline{Nu} = 1.22$, (c) $\vartheta = 0.24$, $Ra_\omega = 1475$, $\overline{Nu} = 1.24$, (d) $\vartheta = 0.38$, $Ra_\omega = 1170$, $\overline{Nu} = 1.21$. In black (—) is represented $Nu(t)$, in red (—) the evolution of $\mathbf{a}_\Omega$.

Interestingly, even if the velocity spectrum is different for the two types of fluid, the Nusselt number spectrum, for the sake of brevity not reported, indicates that $Nu(t)$ exhibits a SP evolution in all the cases analyzed (which indicates that the SU components of the temperature gradient at the wall reciprocally compensate when they are integrated).

The time average Nusselt Number $\overline{Nu}$ also provides meaningful information. For the Newtonian fluid, $\overline{Nu} = 1.16$; it however increases to $\overline{Nu} = 1.22$ for $\vartheta = 0.06$ and $\overline{Nu} = 1.24$ for $\vartheta = 0.24$. Further increasing ϑ has the effect of making $\overline{Nu}$ smaller ($\overline{Nu}|_{\vartheta=0.38} = 1.21$).

It can therefore be concluded that, for a viscoelastic fluid, the heat exchange due to convective phenomena is more effective ($\overline{Nu}_{\text{Newt}} < \overline{Nu}_{\text{visc}}$). An explanation/justification for this trend can be elaborated in its simplest form on the basis of the argument that when overstability takes place, there are no transitional stages where the fluid is quiescent or thermal diffusive conditions are established.

As viscoelastic fluids are characterised by intrinsic 3D patterning behaviour when the disturbances saturate their amplitude (see e.g. [1]), the next section is entirely dedicated to the presentation of the related 3D non-linear simulations.

6.3.2 3D pattering behaviour and evolution

A simple rationale for the expected 3D nature of the emerging flow when the constraint of two-dimensionality is removed can be gathered from the companion problem related to the Rayleigh-Bénard convection in a viscoelastic fluid. While in the Newtonian case, it is well known that the dominant flow structure in an infinite layer (or a sufficiently shallow enclosure) is simply given by a set of perfectly parallel rolls, convection in viscoelastic fluids is generally 3D even if relatively small values of the Rayleigh number are considered. As an example, Lappa and Boaro [1] have shown that the patterning behaviour consists of parallel convective rolls that continuously break and re-assemble in a direction orthogonal to the initial one (this mechanism being periodic in time, see Figure 1.19).

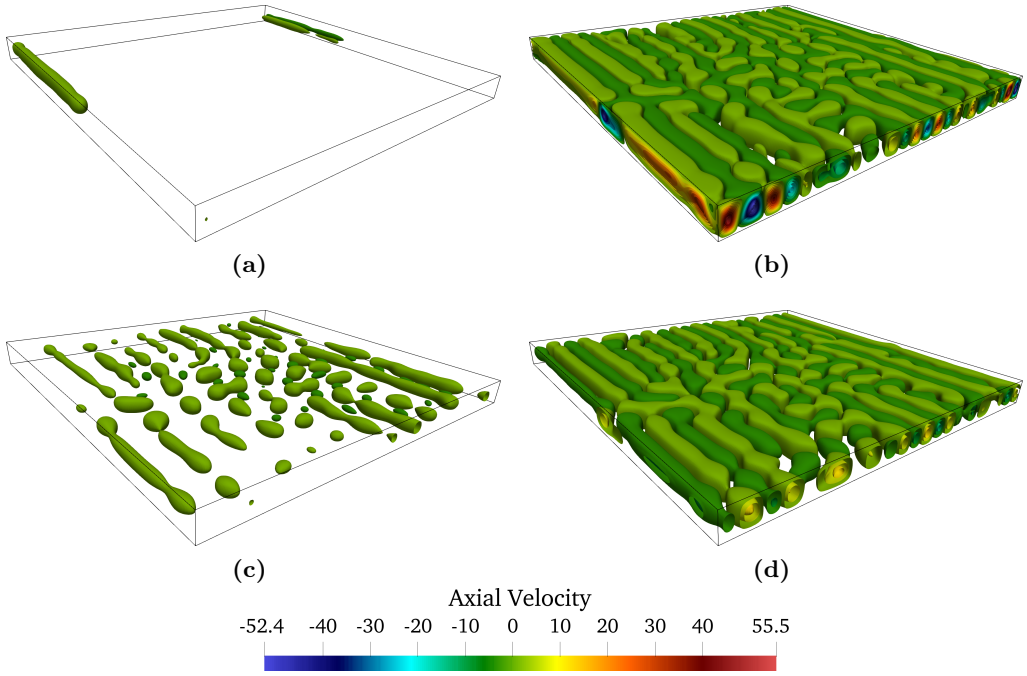

Figure 6.7: Thermovibrational convection in a layer of Newtonian fluid delimited by differentially heated solid walls (snapshots of the isosurfaces of the y component of velocity evenly distributed over the first half period T_Ω). $Pr = 7$, $\Omega = 26.5$, $Ra_\omega = 19750$.

Following the same approach undertaken in subsection 6.3.1, however, let us firstly consider the limiting condition of $\vartheta \to 0$, that is the Newtonian liquid. In this regard, it is also worth remarking that in the present study all the 3D simulations (for both Newtonian and Oldroyd-B fluids) have been conveniently initialised by remapping the 2D solutions in the equivalent 3D geometry. Obviously, this approach relies on the crucial information provided by earlier LSA studies, i.e. that the disturbances are 2D at the onset of convection and then they progressively become 3D as they saturate their amplitude (a concept which applies to buoyancy flow in both Newtonian and viscoelastic fluids [142]).

The first figure of the sequence related to the 3D results (Figure 6.7) shows the time-evolution of the Newtonian fluid over half of the period of oscillation $T_\Omega/2$ (the second half of the period is not represented as it simply corresponds to a motionless state).

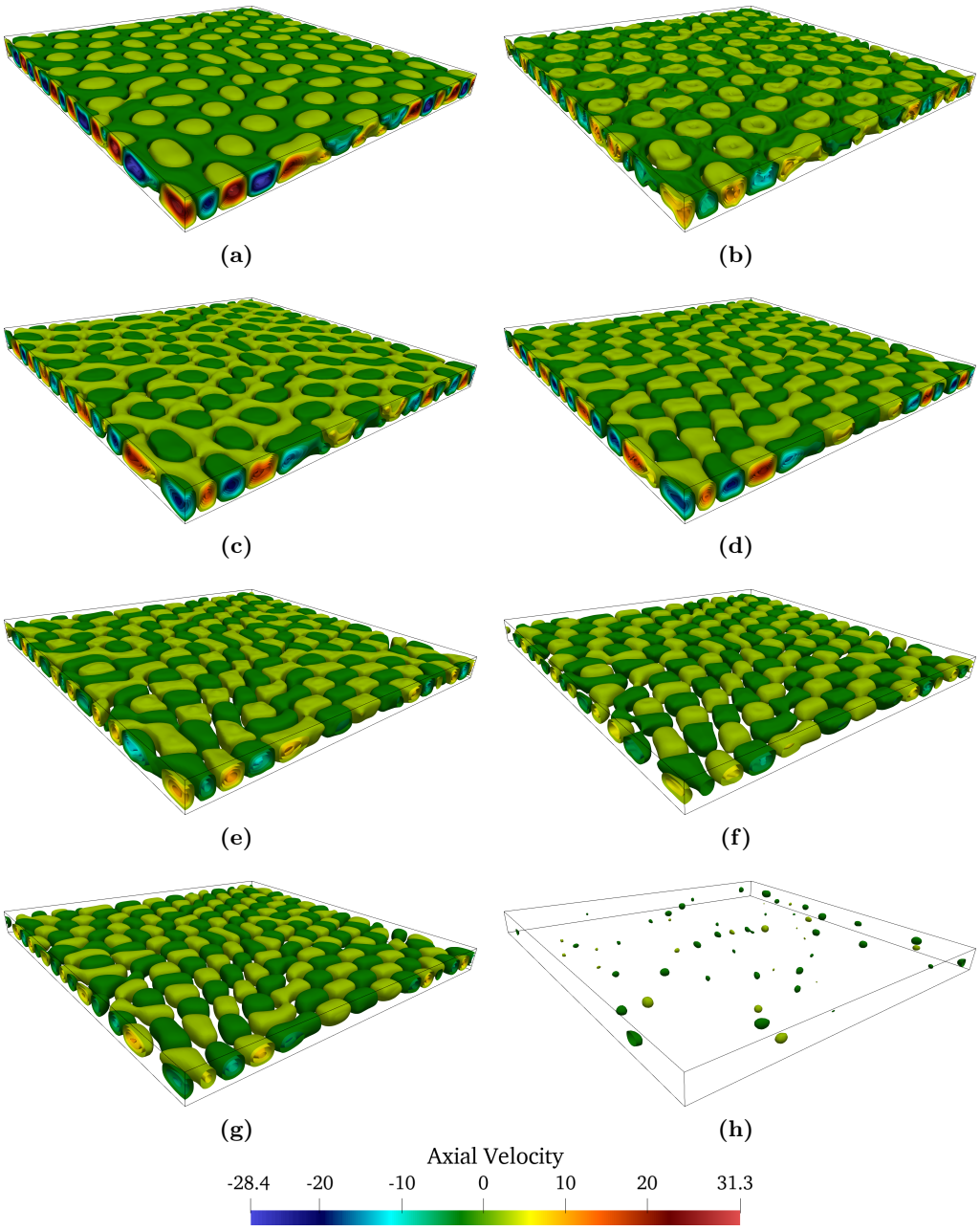

Figure 6.8: Thermovibrational convection in a layer of Oldroyd-B fluid delimited by differentially heated solid walls (snapshots of the isosurfaces of the vertical component of velocity evenly distributed over the interval $\mathcal{I}_1$). $Pr = 7$, $\Omega = 26.5$, $Ra_\omega = 3500$, $\xi = 0.1$, $\vartheta = 0.06$.

A kind of pulsation occurs in the thermal and velocity fields. In particular, it can be seen that the initial diffusive state (Figure 6.7a) is destabilised by the vibrations, which promote the onset of convection. Quasi-longitudinal rolls arise and grow until they reach a certain (maximum) dimension and intensity (Figure 6.7b). At this stage, a pulsating behaviour is enabled, as witnessed by Figure 6.7c, where a decrease in the strength of convection can be noticed. The rolls then re-emerge with the same arrangement that they were displaying in Figure 6.7b but with a different sense of rotation (Figure 6.7d). However, in this transitional state, the velocity field does not reach the same intensity seen in the first part or the pulsation. This is due to the stabilizing effect of the vibrations, which in the meantime have changed direction, thereby tending to promote a new diffusive (quiescent) state.

This behaviour has a one-to-one correspondence with the velocity signal. Put simply, both for the 2D (see Figure 6.4a) and the 3D case (not reported here due to the similarity with the 2D data) a negative spike can be detected in the velocity signal. It corresponds to the aforementioned pulsation mechanism supported by a switch in the role of the dominant acceleration (from destabilizing to stabilizing).

As expected, this simple pulsating mechanism, which in the literature is also referred to as *standing wave*, becomes more involved when the Newtonian fluid is replaced by the equivalent viscoelastic liquid (same Pr and r, see Figures 6.8–6.15).

Given the complexity of the overall scenario, recalling briefly the trends already identified in the framework of the propaedeutical 2D analysis (subsection 6.3.1) is also beneficial.

As explained in that section, the convective phenomena that arise when ϑ is not zero can display a SU response to the harmonic action of the buoyancy force, i.e. the angular frequency of the thermal and fluid-dynamic fields can be $\Omega/2$.

To fully understand the physical implications of this type of behaviour, for instance, one may consider the velocity field $\mathbf{u}(t)$. By denoting with t_0 the time at which flow sampling is started, and recalling that $T_\Omega = 2\pi/\Omega$ is the period of the external vibrations, a SU behaviour may be considered equivalent to stating that $\mathbf{u}(t_0) = \mathbf{u}(t_0 + 2T_\Omega)$. In order to fully characterize or describe the system response in this case, therefore, it

is convenient to split ideally the oscillation period of the flow in four identical sub-intervals. In the following these will be referred as $\mathcal{I}_1 = [t_0, T_\Omega/2]$, $\mathcal{I}_2 = [T_\Omega/2, T_\Omega]$, $\mathcal{I}_3 = [T_\Omega, 3/2T_\Omega]$ and $\mathcal{I}_4 = [3/2T_\Omega, 2T_\Omega]$.

Along these lines, Figure 6.8 illustrates the evolution of the axial velocity (isosurfaces) in $\mathcal{I}_1$ for $\vartheta = 0.06$ in the 3D case. It can be immediately seen that, interestingly, parallel rolls are no longer an emerging property of the flow. The parallel-roll-based structure is indeed taken over (Figure 6.8a) by a different (lattice-like) organization. While cold fluid moves from the cold plate towards the hot one, it is interrupted by localized islands of rising (hot) fluid. The isosurfaces of positive and negative axial velocity form two lattices of cold and hot fluid, perfectly entangled with one another.

As time passes, the aforementioned islands tend to split (Figure 6.8b). A careful analysis of this mechanism (for the sake of brevity not illustrated in this study), has revealed that this phenomenon is caused by the nucleation of cold plumes in proximity to the cold plate. The currents of hot fluid eventually merge together and form a lattice mirror symmetric with respect to the one described at the beginning of the evolution (Figure 6.8c).

In this regard, an analogy might be established with the earlier findings of Chapter 4. Although obtained under the constraint of two-dimensionality (FENE-CR fluids evolving in a vibrated square cavity), those results revealed the nucleation of plumes or eddies close to the solid boundaries, which therefore should not be regarded as an exclusive prerogative of the dynamics reported here.

This pulsating-like behaviour is retained throughout $\mathcal{I}_1$; however, as the aforementioned stabilizing phase is approached, the intensity of the velocity field reduces progressively, until, at the end of the interval (Figure 6.8h) an almost diffusive state is attained. Another key observation concerns the lattice structure seen in Figure 6.8c, which with time is taken over by a *checkerboard-like* pattern.

Figure 6.9 refers to the next sub-interval ($\mathcal{I}_2$). This figure is useful as it reveals that the flow field keeps pulsating (Figures 6.9a and 6.9b), until, at the end of this second phase, the intensity of the velocity field starts to increase again (Figure 6.9d). In this part of the time-advancement it is evident that the layer displays a diffusive behaviour

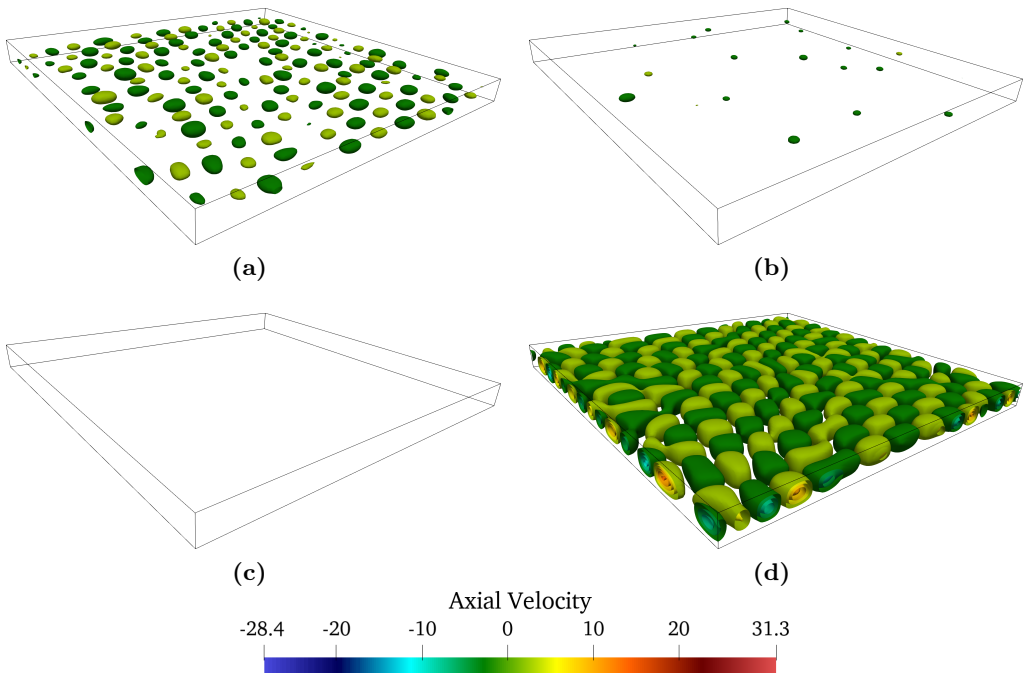

Figure 6.9: Thermovibrational convection in a layer of Oldroyd-B fluid delimited by differentially heated solid walls (snapshots of the isosurfaces of the vertical component of velocity evenly distributed over the interval $\mathcal{I}_2$). $Pr = 7$, $\Omega = 26.5$, $Ra_\omega = 3500$, $\xi = 0.1$, $\vartheta = 0.06$.

in a subset of the interval (revealed by both the patterning behaviour (Figure 6.9c and the evolution of $Nu(t)$, not reported here for the 3D case due to the similarity with the 2D data of Figure 6.6).

The next figure of the sequence (Figure 6.10) illustrates what happens when the third sub-interval is entered. As a fleeting glimpse into this figure would confirm, the pattern evolution is similar in $\mathcal{I}_1$ and $\mathcal{I}_3$. Eventually, in the interval $\mathcal{I}_4$ the evolution repeats itself in a similar way to $\mathcal{I}_2$ and, for sake of brevity, it is omitted here.

An increase in the elasticity parameter ($\vartheta = 0.24$) does not lead to substantial changes in the dynamics. By inspecting Figure 6.11a, however, a new feature can be highlighted: the interconnection between the different islands of hot fluid tends to become more evident (they form a kind of "net"). Moreover, the morphology of the islands is slightly different (their inner boundary is no longer circular and resembles the shape of a "heart"). The evolutionary progress in time is still similar to that described before,

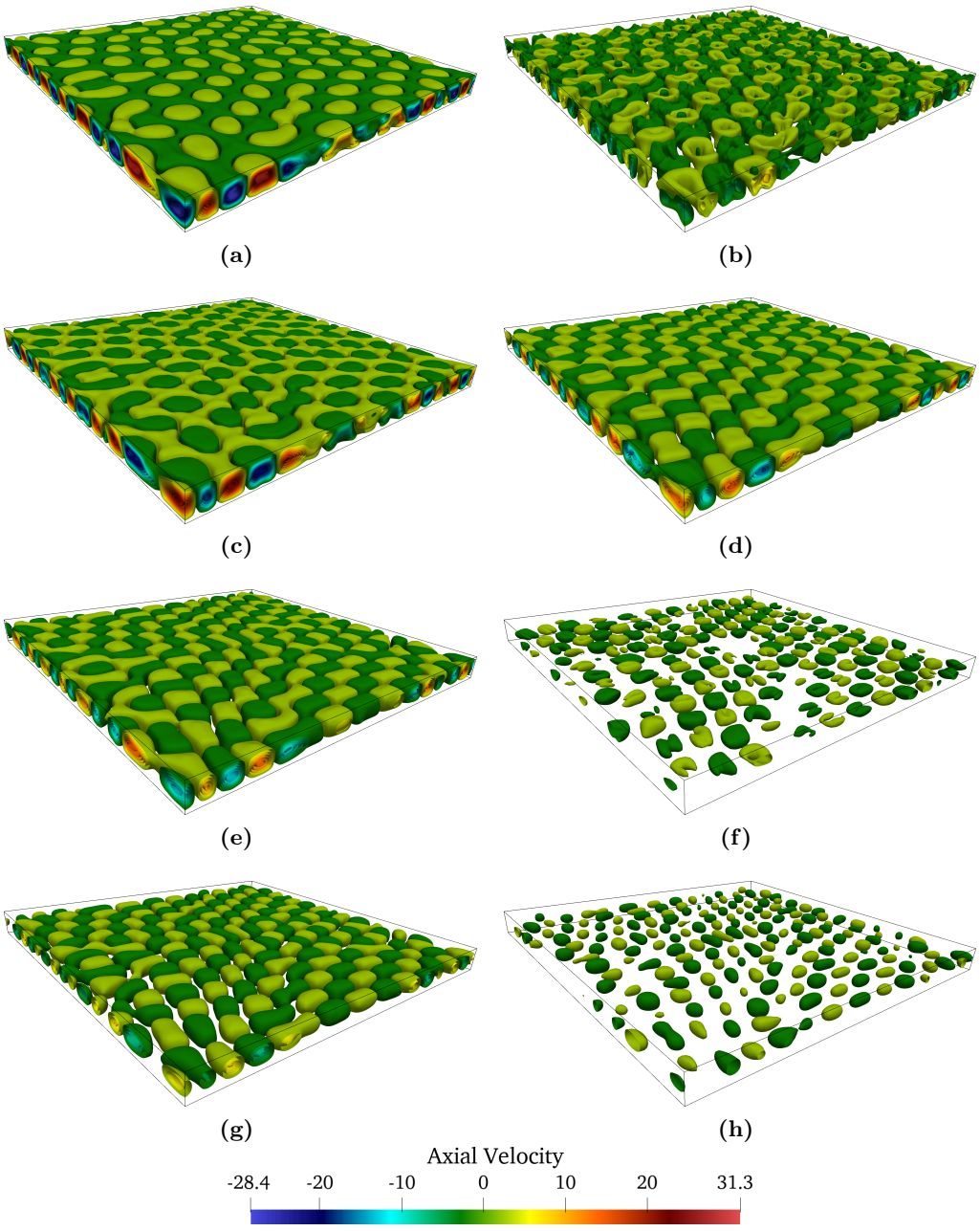

Figure 6.10: Thermovibrational convection in a layer of Oldroyd-B fluid delimited by differentially heated solid walls (snapshots of the isosurfaces of the vertical component of velocity evenly distributed over the interval $\mathcal{I}_3$). $Pr = 7$, $\Omega = 26.5$, $Ra_\omega = 3500$, $\xi = 0.1$, $\vartheta = 0.06$.

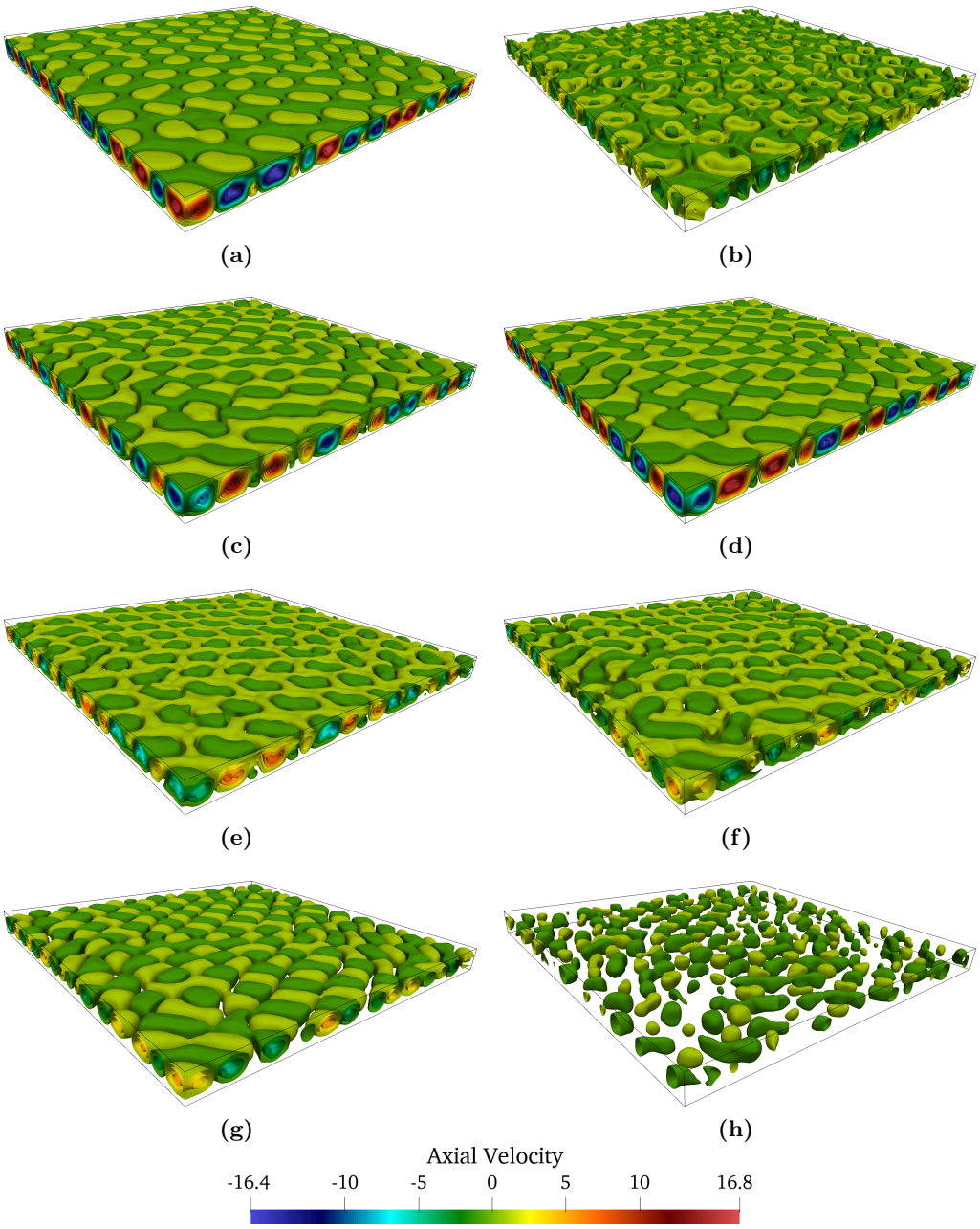

Figure 6.11: Thermovibrational convection in a layer of Oldroyd-B fluid delimited by differentially heated solid walls (snapshots of the isosurfaces of the vertical component of velocity evenly distributed over the interval $\mathcal{I}_1$). $Pr = 7$, $\Omega = 26.5$, $Ra_\omega = 1475$, $\xi = 0.1$, $\vartheta = 0.24$.

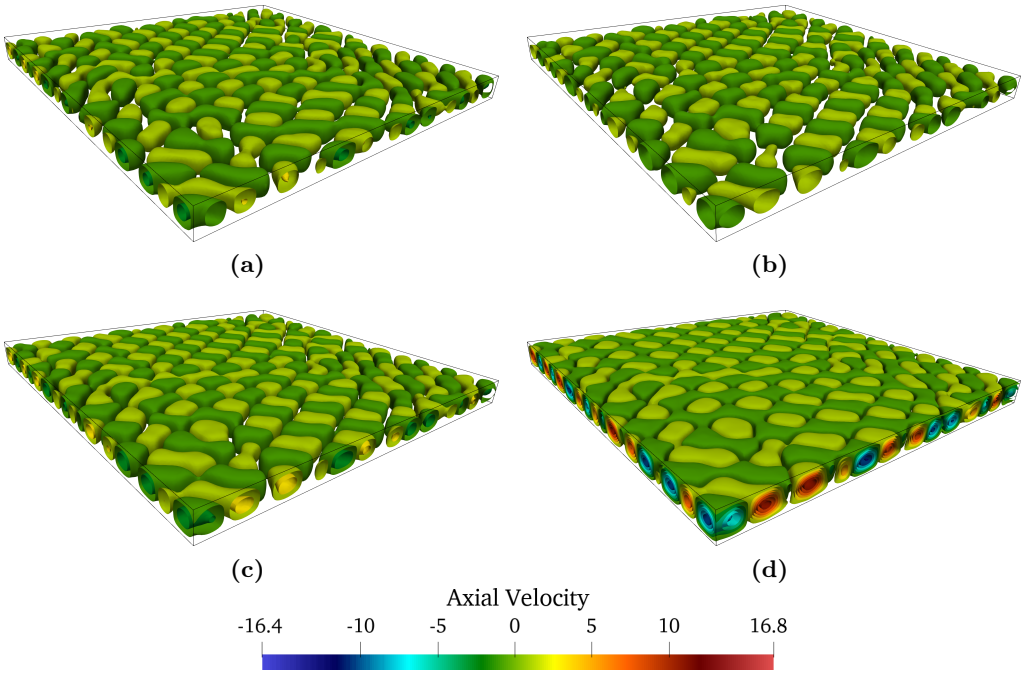

Figure 6.12: Thermovibrational convection in a layer of Oldroyd-B fluid delimited by differentially heated solid walls (snapshots of the isosurfaces of the vertical component of velocity evenly distributed over the interval $\mathcal{I}_2$). $Pr = 7$, $\Omega = 26.5$, $Ra_\omega = 1475$, $\xi = 0.1$, $\vartheta = 0.24$.

e.g. in Figure 6.11b the small rolls of cold fluid in proximity to the cold wall are visible. The intensity of the velocity still undergoes a decrease after some time, but less than in the previous case.

Eventually, in Figure 6.11c the inversion of the flow axial direction takes place. At this stage, however, things become more complex. Indeed, the hot fluid plumes that are now detached one from each other, start merging in proximity to the cold boundary, pushing the cold fluid to the hot plate (and vice-versa) (see Figure 6.11d and 6.11e). The hot fluid close to the cold wall is therefore cooled, the intensity of the velocity field becomes smaller and new cold plumes tend to be formed again.

Other two "inversions" take place between Figures 6.11e–6.11h; however, approaching the time interval $\mathcal{I}_2$ the intensity of $\mathbf{u}$ diminishes. It is also worth observing that now, at the end of $\mathcal{I}_1$ the flow-field still displays convective structures.

This means that, unlike the case with $\vartheta = 0.06$, convection is not suppressed (Figure 6.12). In particular, in $\mathcal{I}_2$ small pulsations of the rolls are still present. However, this oscillatory mechanism is limited to a weak modulation of the intensity of the velocity field, which never changes its sign. Put differently, the modulation is not strong enough to cause the inversion of the velocity. At the end of $\mathcal{I}_2$ a situation similar to the one described in the previous case is attained ($\mathbf{u}(t_0, \mathbf{x}) = \mathbf{u}(t_0 + T_\Omega, \mathbf{x} + \mathbf{a})$). Therefore, for the sake of brevity, the second part of the oscillation period is glossed over here (i.e. the evolution of the pattern in $\mathcal{I}_3$ and $\mathcal{I}_4$ for $\vartheta = 0.24$).

As a final case, let us analyse $\vartheta = 0.38$ (Figure 6.13). Surprisingly, the structure of the lattice is now perfectly ordered (the related convective features are evenly distributed in space, Figure 6.13a). The increase in the elasticity parameter has the effect to give to cold plumes a well defined and rounded shape. This kind of self organised structure is reminiscent of the so called *complex order* structures originally reported by Rogers and coworkers [207–210] for modulated gravitational convection in Newtonian fluids (see Figure 6.14). Even for this case the entanglement between cold and hot fluid lattices can be clearly observed.

The dynamics are similar to that analysed for lower values of ϑ, i.e. the formation of colder fluid eddies (Figure 6.13b, the visible part is actually the imprint of the small eddies on the main structures) is followed by the weakening of the velocity field intensity that leads to an inversion of the plume configuration (Figure 6.13d). In particular, it can observed that smaller blobs of hot fluid moving toward the centre of the main plumes.

As evident in Figure 6.13d, a checkerboard distribution is eventually established. Blobs of hot and cold fluid occupy the whole vertical space, i.e. there is not interconnection and stratification of the plumes (as it was, e.g., in Figure 6.13a). Now the isolated plumes (see e.g. the ones representing the rising fluid) tend to merge together (Figure 6.13e) in such a way that all the blobs are interconnected and the stratification is established once more.

Later on, new cold eddies (not visible) start forming again. This mechanism leads to the fascinating convective structure depicted in Figure 6.13f. It is reminiscent of the

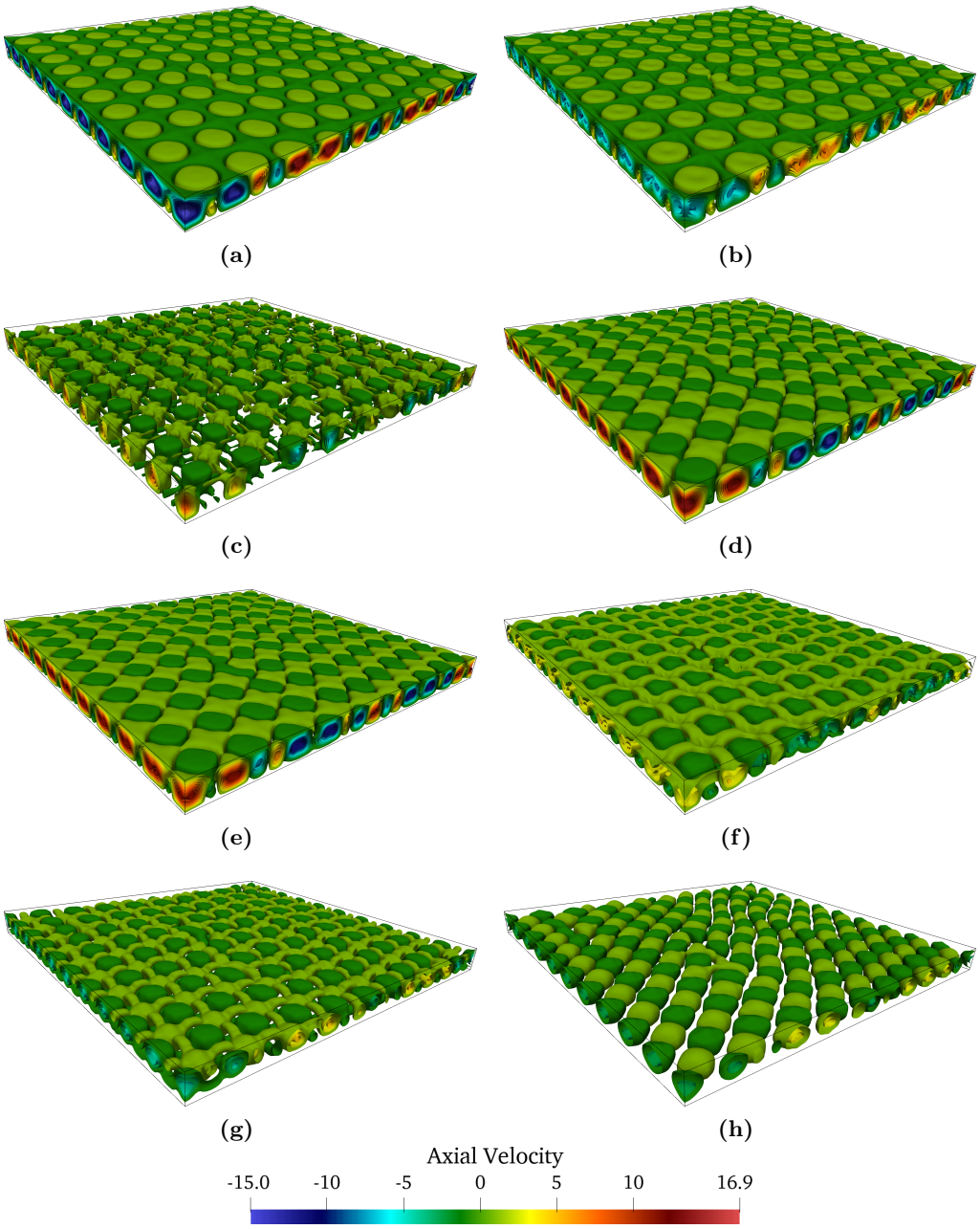

Figure 6.13: Thermovibrational convection in a layer of Oldroyd-B fluid delimited by differentially heated solid walls (snapshots of the isosurfaces of the vertical component of velocity evenly distributed over the interval $\mathcal{I}_1$). $Pr = 7$, $\Omega = 26.5$, $Ra_\omega = 1170$, $\xi = 0.1$, $\vartheta = 0.38$.

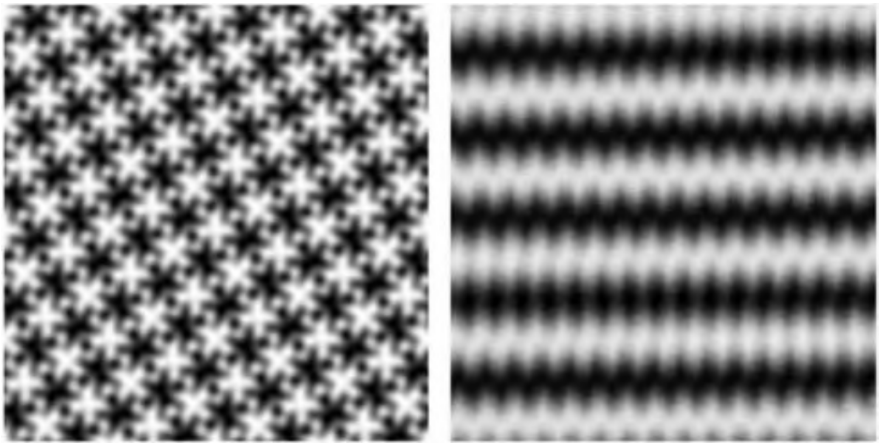

(a) (b)

Figure 6.14: Complex ordered patterns observed for $Pr = 0.930$ and $\Omega = 98$: square superlattice (a) at $Ra = 4750$, $Fr = 3.75 \times 10^{-4}$; roll superlattice (b) at $Ra = 4795$, $Fr = 3.732 \times 10^{-4}$, Fr is the Froude number defined as $Fr = \Gamma/\Omega^2$. After Rogers et al [208].

so called *bimodal convection* observed in Newtonian fluids (see, e.g., Figure 1.5a and Refs. [27, 211, 212]).

A direct comparison of Figures 6.8h and 6.11h and 6.13h finally reveals that the higher the elasticity of the fluid, the larger intensity of velocity field at the end of $\mathcal{I}_1$.

For the sake of completeness, the pattern evolution in $t \in \mathcal{I}_2$ is represented in Figure 6.15. While, on the one hand, this figure shows that the dominant mechanism essentially resembles that already described for $\vartheta = 0.24$, on the other hand, it qualitatively supports the realization that in these circumstances the rolls have accumulated enough energy to invert their sense of rotation.

6.4 Discussion

As a relevant means to provide additional insights into the dynamics described in section 6.3, Figure 6.16 provides an alternate representation of the flow (for the different conditions considered in the present work) by revealing the evolution of the axial velocity (perpendicular to the plates) along a fixed line parallel to the x direction (belonging to

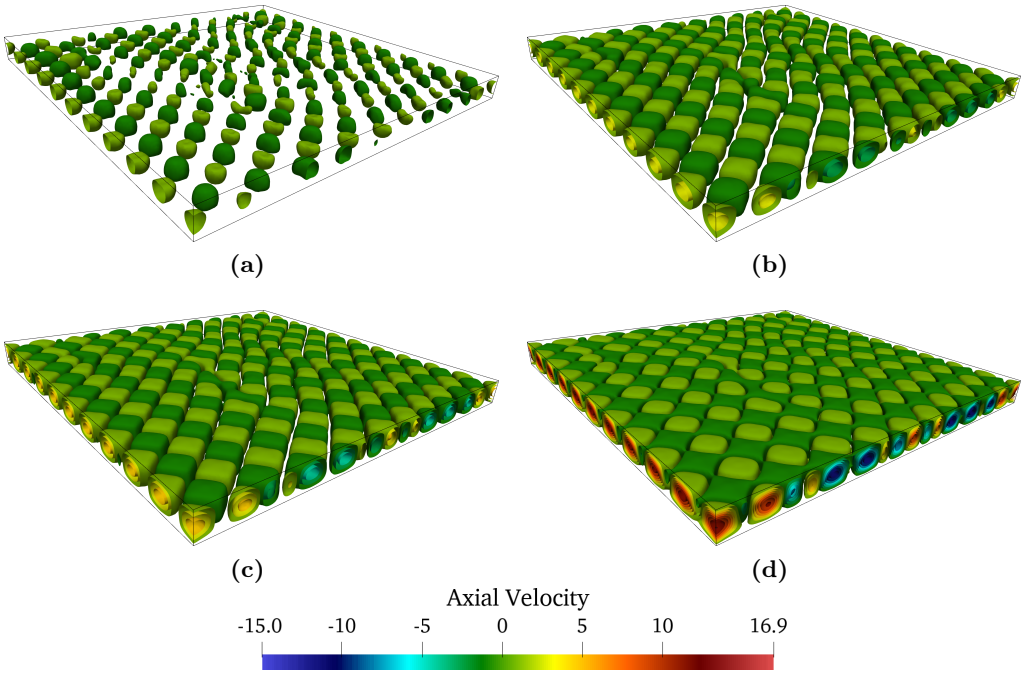

Figure 6.15: Thermovibrational convection in a layer of Oldroyd-B fluid delimited by differentially heated solid walls (snapshots of the isosurfaces of the vertical component of velocity evenly distributed over the interval $\mathcal{I}_2$). $Pr = 7$, $\Omega = 26.5$, $Ra_\omega = 1170$, $\xi = 0.1$, $\vartheta = 0.38$.

the mid-height plane, i.e. $0 < x < 15$, $y = 0.5$ and $z = 7.5$) as a function of time (over the interval $2T_\Omega$).

This figure is instrumental in showing synthetically the various flow weakening and strengthening effects reported in section 6.3 as a function of the elasticity parameter. Along these lines, examination of another quantity, i.e. $\mathrm{tr}(\tilde{\boldsymbol{\tau}})$, is even more useful. Indeed, this parameter is known for its ability to represent (be proportional to) the local *elastic energy* stored in the fluid (see e.g. Ref. [213]; owing to this relationship, in the following it will simply refer to as "elastic energy"). These data (Figure 6.17) obviously serve as another source of information for the interpretation of the fascinating mechanisms described before.

In particular, the significance of this additional figure resides in its ability to make evident that the elastic energy accumulated by the flow in the transitional stages of

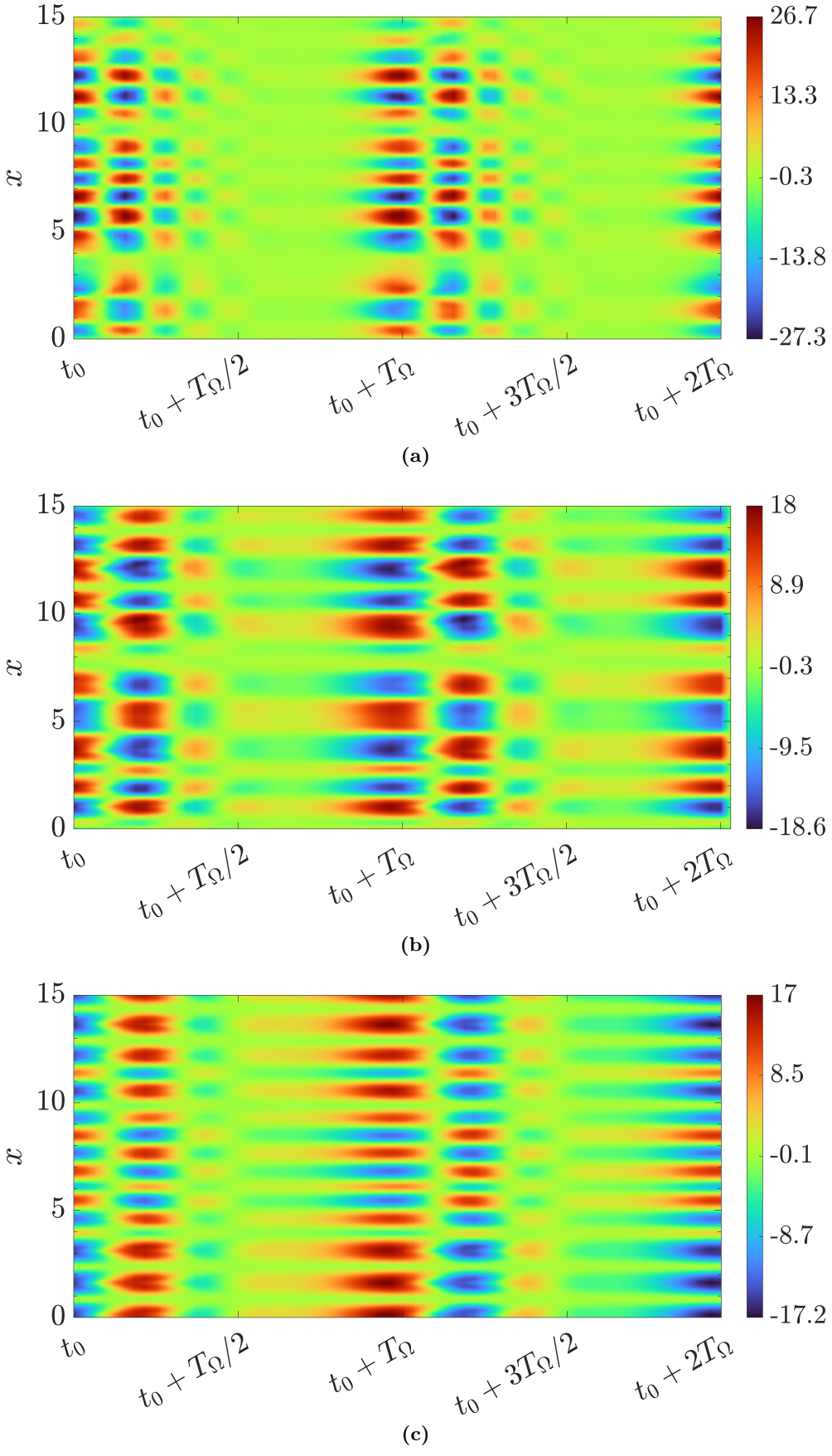

Figure 6.16: Color field of axial velocity (y component of $\mathbf{u}$) as a function of the time and the x coordinate in the centre of the cavity. $0 < x < 15$, $y = 0.5$, $z = 7.5$. (a) $\vartheta = 0.06$, (b) $\vartheta = 0.24$, (c) $\vartheta = 0.38$.

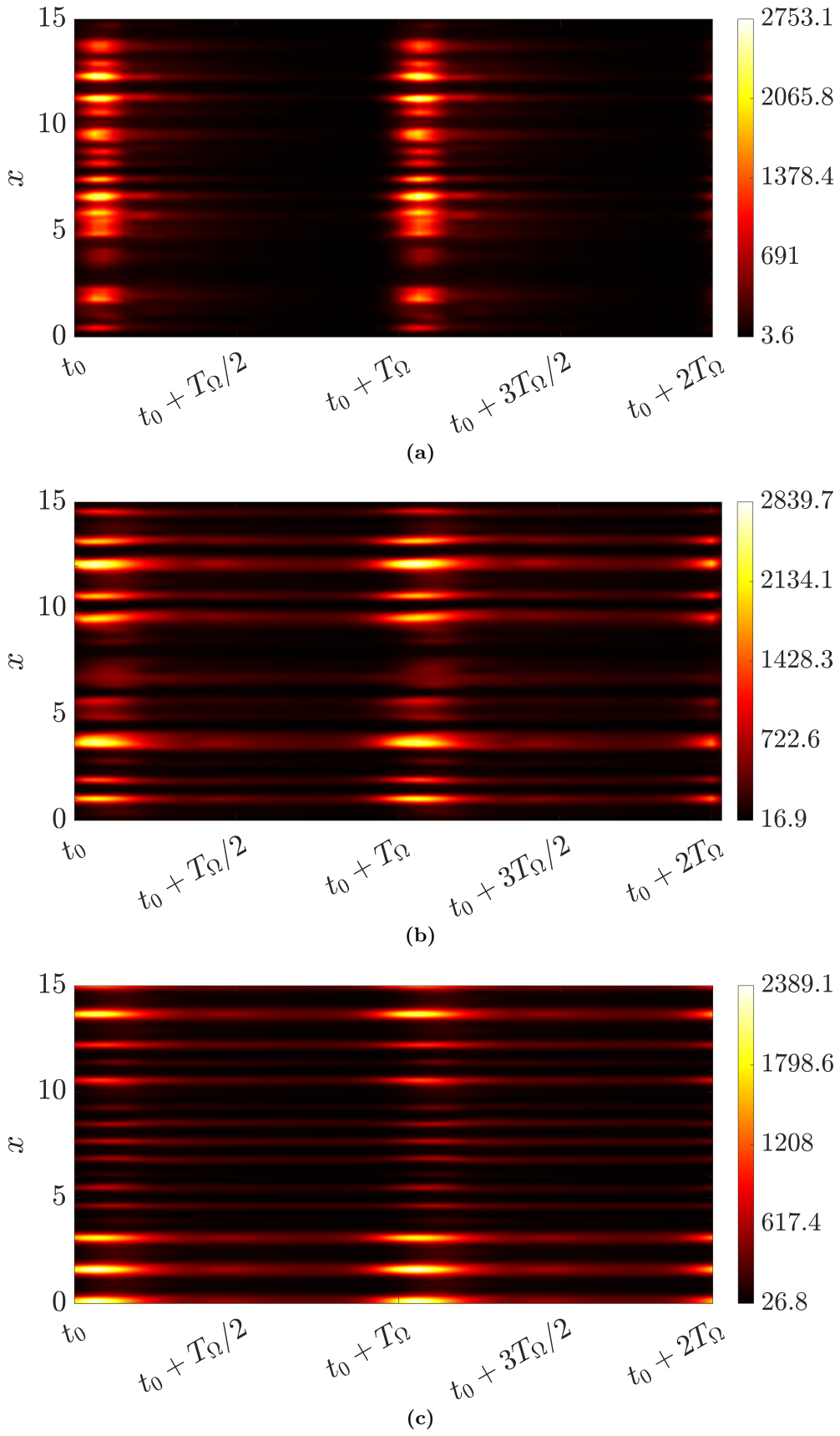

Figure 6.17: Color field of $\mathrm{tr}(\tilde{\boldsymbol{\tau}})$ as a function of the time and the x coordinate in the centre of the cavity. $0 < x < 15$, $y = 0.5$, $z = 7.5$. (a) $\vartheta = 0.06$, (b) $\vartheta = 0.24$, (c) $\vartheta = 0.38$.

evolution where the acceleration is destabilizing is released more gradually (when the acceleration changes sign) for larger values of ϑ (compare Figure 6.17a, b and c).

In this regard, it is also worth recalling the parameter Σ, i.e. the ratio between the relaxation time λ and the period of external vibration T_ω, formally defined in section 2.3. In the present work, since the vibrations frequency is constant, Σ is a linear function of ϑ. In particular, its values are $\Sigma = 0.25$, 1.01 and 1.6 for $\vartheta = 0.06$, 0.24 and 0.38, respectively. One may therefore argue that when $\vartheta = 0.06$ the polymer molecule has sufficient time to relax to the initial position before the cycle of external vibration is finished. Obviously, similar considerations can be used to interpret the other two cases for which the molecules relaxation time and the vibration cycle coincide (for $\vartheta = 0.24$) or for which the polymer molecule cannot relax completely within the oscillation period (for $\vartheta = 0.38$).

These facts can directly be connected to the ability of the polymeric liquid to retain and store elastic energy and, to sustain specific convective states along the oscillation period.

The next figure (Figure 6.18) provides the spatial distribution of this energy at the two characteristic times $t = t_0$ and $t = t_0 + T_\Omega/2$, which paves the way to a brief excursus on the analogies or affinities between this kind of dynamics and the very similar ones previously identified by Rogers et al. [207–210] for modulated Rayleigh-Bénard convection in Newtonian fluids.

As spontaneous symmetry breaking and pattern formation are universal phenomena observed in a wide variety of non-equilibrium systems, here this realization can be used as an opportunity to develop an analogy which may help the reader to glean hints and draw inferences about what factors may facilitate the formation of patterns like those reported in the present work.

Along these lines, it is worth recalling that canonical planforms such as those formed by Rayleigh-Bénard (RB) or Marangoni-Bénard (MB) convection display relatively simple basic structures, generally consisting of stripes (rolls) or hexagons. It is also known that, in some circumstances, such structures tend to be distorted on long scales, that is, the pattern might have disordered local orientations, and/or contains defects

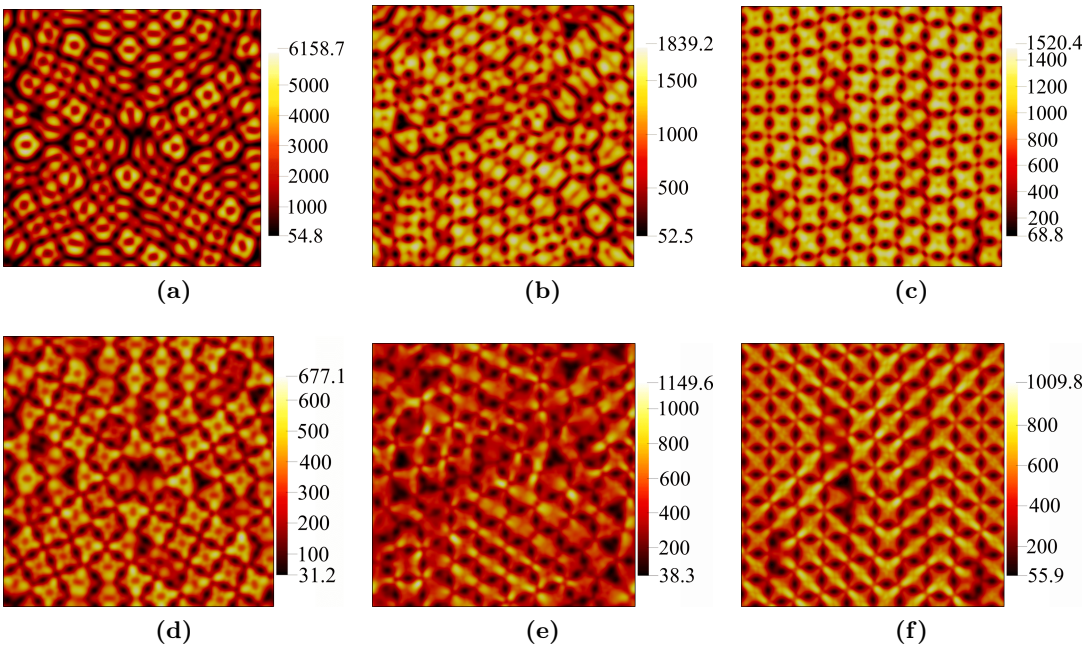

Figure 6.18: Distribution of $\mathrm{tr}(\tilde{\boldsymbol{\tau}})$ on the xz plane at $y = 1$ (cold plate). (a)-(c) $\vartheta = 0.06$, 0.24 and 0.38 respectively, $t = t_0$. (d)-(f) $\vartheta = 0.06$, 0.24 and 0.38 respectively, $t = t_0 + T_\Omega/2$.

of various types such as domain walls, dislocations or disclinations. These geometrical features can make the flow slightly more complex than the perfect planforms expected for the idealized infinite layer case and/or for conditions very close to the critical ones. Another known (although rarer) kind of complexity is represented by "complex order", namely, a structure where order manifests itself in a nontrivial way. Exemplars pertaining to this class of patterns are "quasi-crystalline states"; their distinguishing mark is the ability to develop a complicated spatial structure that never repeats itself, but is well ordered in the Fourier space.

Relevant theoretical background for this category of phenomena can be found in the earlier work by Pismen & Rubinstein [214] where the concept of complex order was introduced on a set of rigorous bases. Towards the end to interpret the present results, here let us limit ourselves to discussing the most fundamental underlying idea, that is, the relationship between complex order and the initial isotropy of the considered system.

Put simply such a notion can be expressed as follows: transitions to non-symmetric states in isotropic systems generally imply a preferred wavelength but no preferred direction; as a natural consequence of this property, an indefinite number of modes can be excited in principle at the same time, with the related wave vectors having the same absolute value but being directed in arbitrary directions. In such a process, in some special conditions, crystalline structure can be developed due to nonlinear interactions among these modes as they grow and saturate their amplitude.

Additional insights into these concepts (these being beyond the scope of the present section) can be found in the study by Lifshitz [215] where these phenomena have been further split in quasi-periodic crystals and superlattices depending on certain properties of the involved modes and their spatial relationships.

Coming back to the original problem of interest in the present study, i.e. vertically-oscillated layer, it is worth re-emphasizing that such a system preserves the original isotropy of the classical RB and MB systems. The analogy with the systems investigated by Rogers and coworkers can be pursued further considering that, as illustrated in section 6.3, the present layer has displayed the ability to develop both harmonic (H) and subharmonic (S) temporal responses when viscoelasticty enters the dynamics even though conditions very close to the critical ones are considered ($r = 1.2$).

Rogers and coworkers [207–210] had considered RB convection in a Newtonian fluid ($Pr = 0.93$) under the effect of vibrations. In such conditions (and in analogy with the dynamics reported in section 6.3) they found both (H) and (S) responses and even circumstances where both behaviours were present (in a sub-region of the space of parameters originating from a "bicritical" point). Over a parameter range where the mechanisms (H) and (S) have comparable influence, the spatial scales associated with both responses were found to coexist and lead to "resonant states" resulting in complex, highly ordered patterns.

These phenomena and related conditions may be considered formally similar to those examined in the present work where superlattice-like structures have been observed in combination with the existence of two distinct spatial scales, each displaying a different temporal dependence (the reader being referred again to the information reported in

section 6.3). In the framework of the analogy proposed here, one may argue that while in Newtonian fluids the existence of disturbances with different temporal scales does require concurrent mechanisms driving the flow (gravity and vibrations in the case of Rogers and coworkers), in the present problem these are naturally present as a results of the ability of viscoelasticity to cause the coexistence of harmonic and subharmonic modes with distinct critical wavenumbers. Put simply, the presence of a second driving force is not needed as viscoelasticity provides the fluid with natural capacity to develop disturbances with various wavelengths (this being through the ability of the molecules of dispersed polymer to stretch and deform under the effect of a primary flow and exert a back influence on the flow which generated the deformation, thereby leading to the emergence of a "secondary" flow).

6.5 Conclusions

Thermovibrational flow in a layer of viscoelastic fluid with imposed vibrations parallel to the temperature gradient has been investigated.

This study has opened a new path to a much better understanding of this attractive system, which has many interesting aspects. In particular, concepts from disparate and segregated research areas were combined to provide better knowledge of viscoelastic thermovibrational convection in specific sub-regions of the space of parameters where a Newtonian fluid would display relatively simple (canonical) behaviours.

It has been proven that the onset of thermovibrational convection in Oldroyd-B fluids occurs for values of the control parameter (Ra_ω), which are one order of magnitude smaller than the equivalent threshold to be exceeded in the companion Newtonian case, thereby lending evidence to the applicability of the concept of "overstability" to these circumstances.

It has been shown that the relatively obvious dynamics typical of slightly supercritical states in Newtonian fluids, where the flow is characterized by the existence of parallel rolls that periodically disappear and re-emerge with different sense of rotation are taken over for viscoelastic fluids by a kind of complex order driven by the interplay

of the time-varying (stabilizing/destabilizing) role of the vibration induced acceleration and the ability of the fluid to store and release elastic energy.

The stored energy allows the viscoelastic medium to sustain a convective flow even in the stages where the external force plays a stabilizing role (i.e. it tends to suppress fluid motion). In this specific phases, the intensity of the flow field is directly related to the quantity of energy that the fluid could store in the preceding stage. In turn, such a quantity is directly related to the elasticity number (and in turn to the Weissenberg number), i.e. the fluid elasticity level, and to the ratio between elastic and dynamic oscillation characteristic times (i.e. the parameter Σ).

In the attempt to interpret the peculiar nature of the observed 3D planforms and the overall related scenario it was emphasized on some prior investigations that can be linked to the general problem relating to the emergence of superlattices in isotropic systems. Building on these works, this chapter introduced an interesting analogy and some new observations, both general and system-specific, which will require additional attention in the future.

The following chapter will be devoted to assess how the shape of the vibrations impacts the patterning configuration and its dynamics in an infinite layer of FENE-CR fluid.

Chapter 7

Sinusoidal and Pulse (Square) Waves in Viscoelastic fluids: Analogies and Differences

This chapter is based on Lappa & Boaro, 2021 'Viscoelastic Thermovibrational Flow Driven by Sinusoidal and Pulse (Square) Waves' [4].

7.1 Introduction

Chapter 6 revealed that complex order can be excited in microgravity if an infinite layer of viscoelastic fluid is sinusoidally shaken along the direction of the temperature gradient.

Moreover let us recall that the other few works dealing with modulated Rayleigh-Bénard convection in microgravity (Refs. [141, 142]) employed pulse (or square) waves as external and time dependent force. Interestingly, the influence of the shape of the vibrations has not often been assessed.

In such a context, the present study aims to probe the role of an influential factor heretofore scarcely considered, that is, the specific (temporal) shape of the forcing used to produce thermovibrational convection. The main objective of the present numerical investigation is the assessment of the modifications induced in the patterning behaviour of a viscoelastic fluid when classical sinusoidal vibrations are replaced with a "square wave". This can be seen as a non-sinusoidal (yet periodic) forcing where the amplitude alternates (yet at a constant frequency) between fixed minimum and maximum values, with the same duration at minimum and maximum and instantaneous transitions

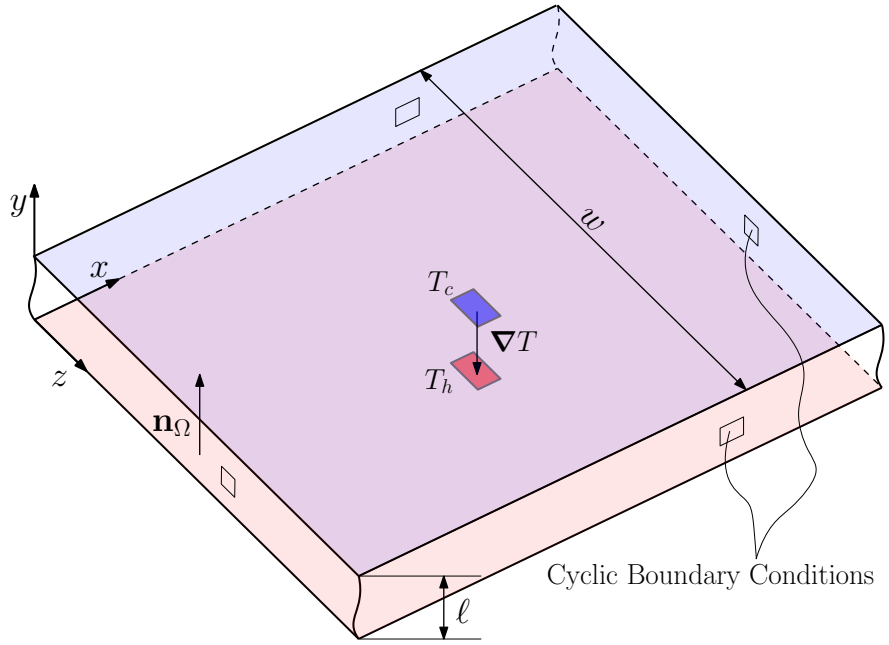

Figure 7.1: Sketch of the geometry and scheme of the problem.

between such extrema (also known as pulse waves). Such a change in the waveform is expected to have a remarkable impact on the dynamics of viscoelastic.

Moreover, the control parameters will be set in such a way to be comparable with the results presented by Lappa & Boaro [1], see also Figure 1.19.

7.2 Statement of the problem

Following the same rationale at the basis of chapter 6, a shallow infinite layer of aspect ratio $AR = w/\ell = 15$ is considered, where w represents the extension in the x and z directions (square basis), and ℓ accounts for the depth of the layer and is used in this chapter as characteristic length scale to calculate the non-dimensional quantities. To mimic an infinite domain, cyclic (or periodic) boundary conditions are applied along the sides of the layer, while no slip walls play the role of top and bottom boundaries. Such solid walls are differentially heated in such a way that a temperature gradient is established within the domain. The related difference of temperature reads $\Delta T = T_h - T_c$, where the subscripts h and c denote the *"hot"* and *"cold"* sides respectively. A scheme of the domain is depicted in Figure 7.1.

In this chapter, two different types of vibrations will be employed, i.e. sinusoidal and square shaped. Moreover, a FENE-CR model having $L^2 = 200$ has been chosen for the closure of the balance equations. Therefore, eqs. (eqs. (2.69),(2.70), (2.71) and (2.72) have been discretised over a uniform Cartesian grid having $200 \times 35 \times 200$ cells (see subsection 6.2.1 for the complete grid independence analysis). Eqs. (2.73) and (2.74) are used to model the sinusoidal and square waves respectively (the dimensional version of the acceleration waves are defined in eqs. (2.46) and (2.47)). Additionally, the steady buoyancy term $PrRaT\mathbf{i}_g$ in eq. (2.70) is set to $\mathbf{0}$ in order to mimic the absence of gravitational field.

All the diffusive and convective terms have been evaluated though a second order accurate central difference scheme (CDS) with the exception of the convective term of eq. (2.72), where the Minmod scheme has been used to improve the algorithm accuracy. In addition, the simulation was stabilised using a BSD technique (see Section 3.2).

Moreover, since the mesh study carried out in chapter 6 still holds, the study presented in this study employed a mesh with $200 \times 35 \times 200$ cells.

7.3 Results

This chapter focuses on a layer of viscoelastic (FENE–CR) fluid with $Pr = 8$, $\xi = 0.5$, and $\vartheta = 0.1$ subjected to either sinusoidal or square vibrations having frequency $\Omega = 25$. For both cases, the resulting vibrational Rayleigh number is $Ra_\omega = 4000$. Furthermore, the model parameter L^2 is set to 200 as in the previous chapters and in Ref [1]. Let us recall that the FENE-CR can adequately represent highly elastic solutions known as "Boger fluids" (see, e.g., Ref [107]), able to retain an essentially constant viscosity over a wide range of shear rates. Relevant examples are represented by a class of water-based polymer dilute solutions at ambient or moderate temperatures, e.g., water between 25 °C and 50 °C with limited amount of a polymer such a PAM, PEG, PEO, PVP, Xanthan Gum, etc, for which the Prandtl number would be similar to that considered in the present work ($Pr \cong 8$) and $\xi < 1$. The rheological parameters (Pr and ξ) considered here are almost identical to those examined by Li & Khayat [107] , who assumed a Boger fluid with $Pr \cong 7$ (and ξ varying in the range between 0 and

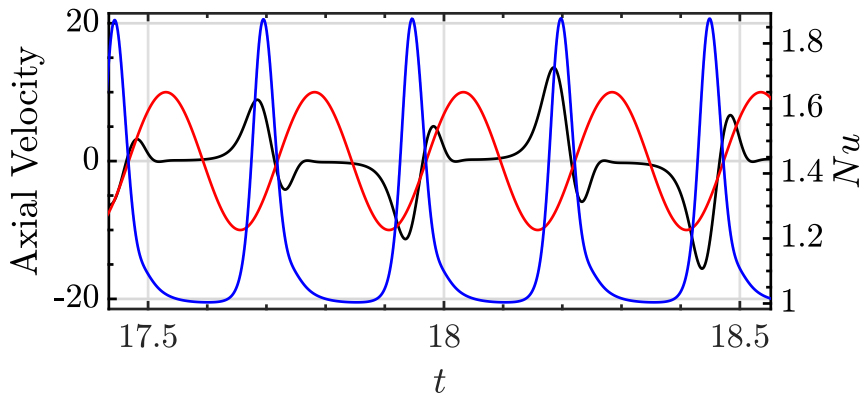

(a)

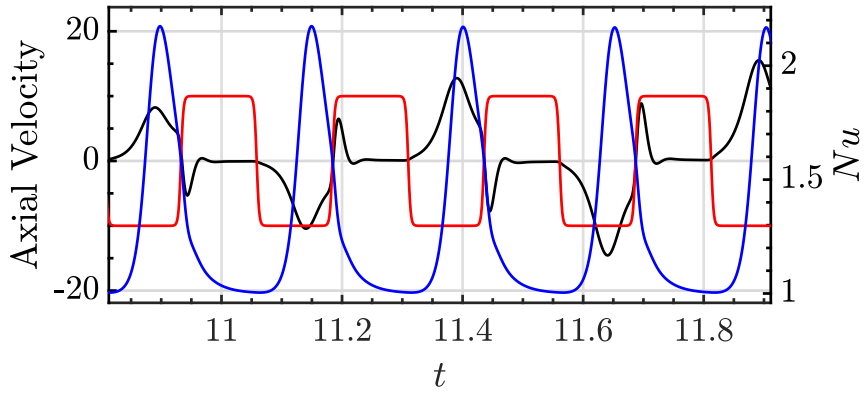

(b)

Figure 7.2: Time evolution of the Axial velocity (probe being located in the centre of the layer), and Nusselt number. Numerical simulation with $AR = 15$, $Pr = 8$, $\Omega = 25$, $\xi = 0.5$, $\vartheta = 0.1$, and $Ra_\omega = 4000$. (a) Sinusoidal and (b) Pulse waves. In black (—) is represented the axial velocity, in blue (—) $Nu(t)$, and in red (—) the *qualitative* evolution of $\mathbf{a}_\Omega(t)$. An alternative representation of this figure is depicted in Appendix C.

0.79). Assuming $\lambda \cong 10^{-3}\, s$ (a typical realistic value for small polymer concentrations) and thermal diffusivity $\alpha \cong 1.5 \times 10^{-7}\, m^2/s$ over this range of temperatures, these values would correspond to $\vartheta = 0.1$ setting $0.04\, mm$ as the distance between the plates.

7.3.1 Forcing and related system response

Given the complexity of the considered subject, before starting to deal with the structure and evolution of the fluid dynamic field, for the convenience of the reader, in

this subsection the system response is initially assessed in terms of "localized" or "global" parameters (by which drawing initial conclusions on the behaviour of the system is relatively straightforward).

In particular, in order to highlight differences and similarities between the two "shapes" of the acceleration signal, this study concentrates on the time evolution of two representative quantities, namely, the axial fluid velocity (the velocity component perpendicular to the solid walls) recorded by a virtual probe located in the centre of the layer, i.e. $(7.5, 0.5, 7.5)$, and an integral quantity, that is the *Nusselt* number calculated on the hot (bottom) plate with eq. (2.83).

Along these lines, Figure 7.2 provides the evolution in time of the two aforementioned characteristic thermal and fluid dynamic quantities together with the forcing. It can be seen that, when the external force (in red) $\mathbf{a}_\Omega > 0$ the acceleration has a positive direction (with respect to the unit vector $\mathbf{n}_\Omega$, see Figure 7.1), the effect of the vibration is *stabilizing*, i.e. the vibrations act as a damper for the convective instability. On the contrary, when the external force $\mathbf{a}_\Omega < 0$, the vibrations act in a way that is similar to the steady gravitational acceleration in the classical problem of Rayleigh-Bénard convection. Therefore, in this time interval vibrations are *destabilizing*, i.e. they promote convective motion. These simple arguments also clarify the reason why the Nusselt number and the forcing are out of phase. The Nusselt number is largely increased in the stage where vibrations play a destablizing role and tends to the unit value (corresponding to quiescent conditions) as their effect is reverted.

Given this premise, it is easy to realize that, due the peculiar shape of the forcing, the switch between stabilizing and destabilizing phases can happen in different ways: the smooth transition, typical of the sinusoidal wave is taken over by an abrupt change in the acceleration direction for the case with the pulse wave. Moreover, as a result of the different shape of the forcing signal, the pulse wave might be expected to exert a stronger influence on the fluid.

In order to prove the last statement, it is worth comparing $Nu(t)$ for the two cases. As quantitatively substantiated by the data, the maximum and the time average value (see eq.(2.84)) of the Nusselt number are lower for the case with sinusoidal acceleration

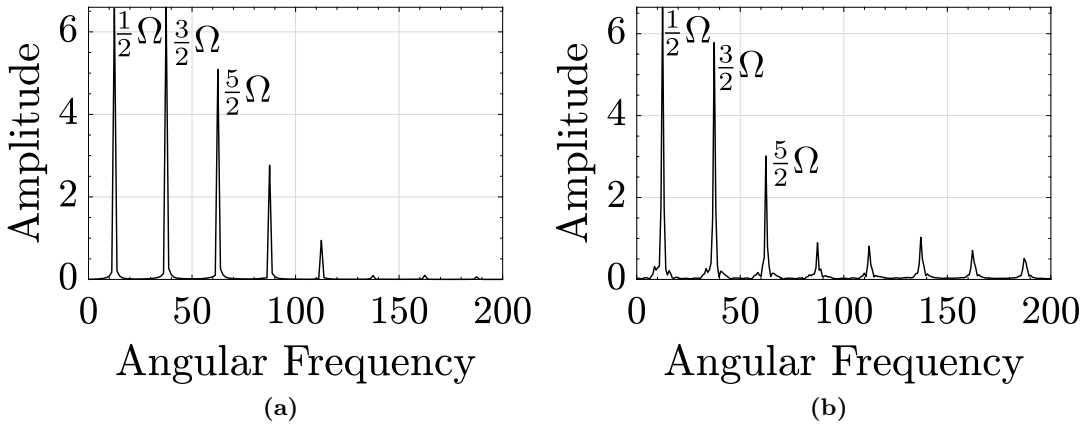

Figure 7.3: Angular frequency of the Axial velocity signal (probe being located in the centre of the layer). Numerical simulation with $AR = 15$, $Pr = 8$, $\Omega = 25$, $\xi = 0.5$, $\vartheta = 0.1$, and $Ra_\omega = 4000$. (a) Sinusoidal and (b) Pulse waves.

($Nu_{\max} = 1.88$, $\overline{Nu} = 1.18$) and bigger for the pulse one ($Nu_{\max} = 2.17$, $\overline{Nu} = 1.30$). A justification for this trend can be elaborated in its simplest form on the basis of the argument that while the sinusoidal acceleration attains its maximum intensity for a single instant in time, the square acceleration maintains a constant maximum intensity for half of the period of oscillations.

The axial velocity signal can also be used to get useful insights into these dynamics. Interestingly, in the stabilizing semi-period both signals (hereafter $v_S(t)$ and $v_P(t)$ for the sinusoidal and pulse waves respectively) reach a zero value at certain time. However, a careful analysis of their shape reveals that while $v_P(t)$ is stabilized to a null value in a certain interval of the stabilizing period, $v_S(t)$ changes continuously in this interval, i.e. $dv_S/dt \neq 0$ in every time sub-interval (while it can locally reach 0).

In the light of these initial findings, the reader may expect that when the the fluid is excited by pulse waves it will display a more involved behaviour in the destabilizing phase if compared with the case of sinusoidal forcing for the same value of Ra_ω (more detail about this interesting concept later will be provided later).

As a concluding task for this initial analysis, the frequency of the $Nu(t)$ and $u_y(t)$ signals were also calculated. In agreement with the results of Chapter 6 and the earlier results by Lyubimova & Kovalevskaya [142], obtained with a non-linear nu-

merical approach and linear stability analysis, respectively, the flow field exhibits a half-subharmonic response to both types of wave, i.e. the frequency of $u_y(t)$ is half of the frequency of the acceleration, that is $\Omega/2$ (interestingly as shown in Figure 7.3, the related frequency spectrum displays three dominant frequencies, namely $\Omega/2$, $\Omega + \Omega/2 = 3\Omega/2$ and $2\Omega + \Omega/2 = 5\Omega/2$, where the second and the third components are produced by the obvious non-linear interference between the flow sub-harmonic response and the forcing). Yet in accordance with the results of Chapter 6, $Nu(t)$ shows a simple harmonic response (its frequency is exactly Ω).

Before moving to the next section, taking into account the periodicity of the flow field ($\mathbf{u}(t_0) = \mathbf{u}(t_0 + 2T_\Omega)$, $T_\Omega = 2\pi/\Omega$) four sub-intervals of time were conveniently defined: $\mathcal{I}_1 = [t_0, T_\Omega/2]$, $\mathcal{I}_2 = [T_\Omega/2, T_\Omega]$, $\mathcal{I}_3 = [T_\Omega, 3/2T_\Omega]$ and $\mathcal{I}_4 = [3/2T_\Omega, 2T_\Omega]$, where t_0 is a convenient instant of time. Here, t_0 was selected as $t_0 = 17.94$ for the case of sinusoidal acceleration, and $t_0 = 11.14$ for the pulse acceleration (see Figure 7.2). Similarly to the previous chapters, let us define the parameter Σ. Since in this chapter both ϑ and Ω are fixed, $\Sigma = 0.4$.

7.3.2 Patterning behaviour and 3D evolution

In this section (entirely dedicated to the analysis of the 3D behaviour of the considered flows), first let us examine the 3D isosurfaces of the axial velocity for the case of sinusoidal shaking for $t \in \mathcal{I}_1$, see Figure 7.4.

At the time t_0 (Figure 7.4a) the flow displays an ordered convective structure consisting of groups of parallel rolls each oriented along a given preferential direction. The evolution of this pattern is quite simple. As time progresses, the intensity of the axial velocity becomes smaller (Figure 7.4b) until the rolls change their sense of rotation (Figure 7.4c). This pulsation of the velocity field is a common solution for Rayleigh-Bénard systems and it is generally referred to in the literature as *standing wave* (see Ref [10] and reference therein).

Although after the inversion of the sense of rotation the intensity of the axial velocity tends to increase, it never reaches again the same value that it had at $t = t_0$ (Figure 7.4d). Indeed, the acceleration is changing direction, and therefore the stabiliz-

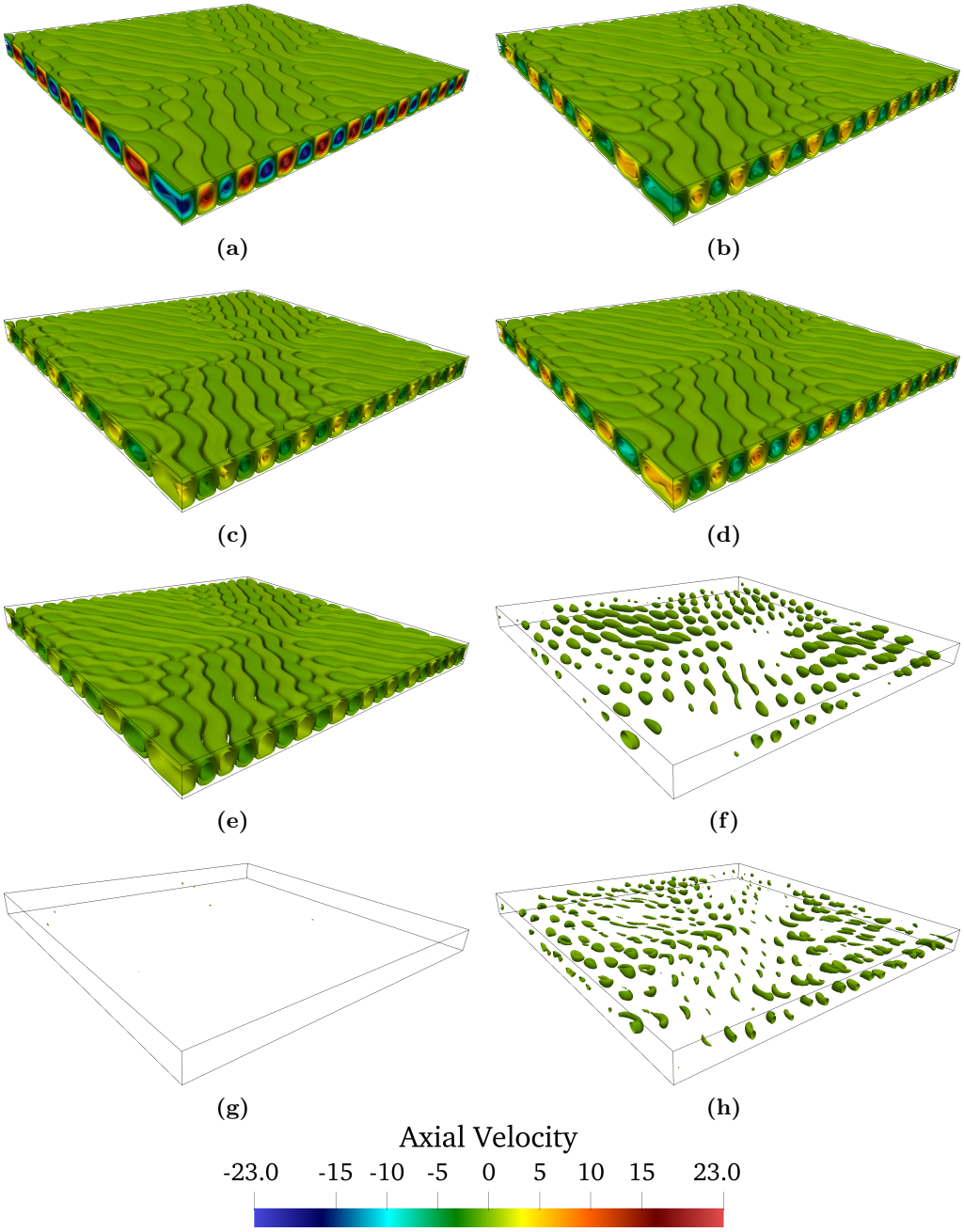

Figure 7.4: Thermovibrational convection in a layer of FENE–CR fluid delimited by differentially heated solid walls (snapshots of the isosurfaces of the vertical component of velocity evenly distributed over the interval $\mathcal{I}_1$). $Pr = 8$, $\Omega = 25$, $Ra_\omega = 4000$, $\xi = 0.5$, $\vartheta = 0.1$, sinusoidal acceleration.

ing effect of the vibrations starts to influence the amplitude of convection. As evident in Figures 7.4e-7.4h, interestingly, the rolls keep pulsating. However, this pulsation is no longer a result of a variation in the direction of the buoyancy force, rather it is driven by the residual *elastic energy* stored in the polymer molecules. This concept will be discussed afterwards.

Here, let us limit ourselves to pointing out that, from a phenomenological point of view, in the initial part of the interval $\mathcal{I}_2$, Figure 7.5a, even if the acceleration is in its stabilizing phase, the intensity of the rolls increases again: the rolls, initially disperse in the domain, start to grow in intensity until they merge together (Figures 7.5a-7.5d).

It is also worth noticing that after the last inversion of sense, visible in Figures 7.4a-7.4d, the rolls have not changed again their sense of rotation. However, since now the fluid motion is sustained only by the elastic energy stored in the fluid in the preceding destabilizing phase and not by the buoyancy force, the intensity of the velocity field becomes smaller as the elastic energy is dissipated through viscosity effects (compare Figures 7.4d and 7.5d).

As the flow evolves, the acceleration changes it sign and starts to play again a destabilizing role, thereby promoting the rise of the velocity field (see Figures 7.5f-7.5g). Now, the buoyancy force that drives the fluid motion, along with the elastic energy, leads to a situation similar to the initial one ($t = t_0$), both for intensity and shape of the rolls, but with a different sense of rotation as evident in Figure 7.5h.

The second part of the oscillation period ($\mathcal{I}_3$ and $\mathcal{I}_4$) evolves in similar way to the one just described, and for the sake of brevity, it is not describe it in detail.

Rather, let us concentrate on the companion case, that is the situation with the pulse acceleration (see Figure 7.6 for the behaviour over the interval $\mathcal{I}_1$). Remarkably, it can be seen that the rolls are no longer aligned along a particular direction. Instead, they form randomly organised structures. The elongated shape that characterizes the case with sinusoidal vibration is now replaced by a mix between short longitudinal and rounded rolls as depicted in frame 7.6a.

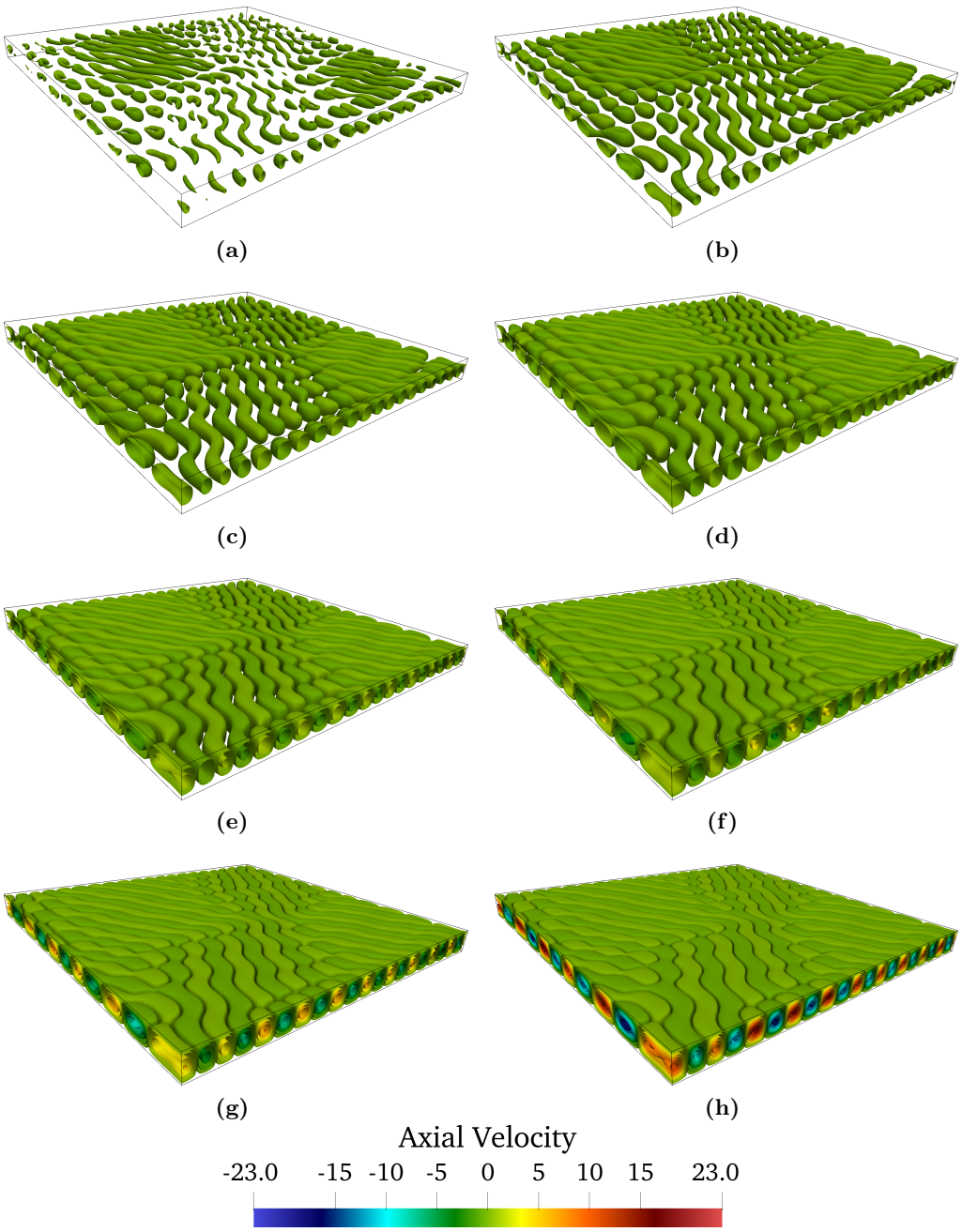

Figure 7.5: Thermovibrational convection in a layer of FENE–CR fluid delimited by differentially heated solid walls (snapshots of the isosurfaces of the vertical component of velocity evenly distributed over the interval $\mathcal{I}_2$). $Pr = 8$, $\Omega = 25$, $Ra_\omega = 4000$, $\xi = 0.5$, $\vartheta = 0.1$, sinusoidal acceleration.

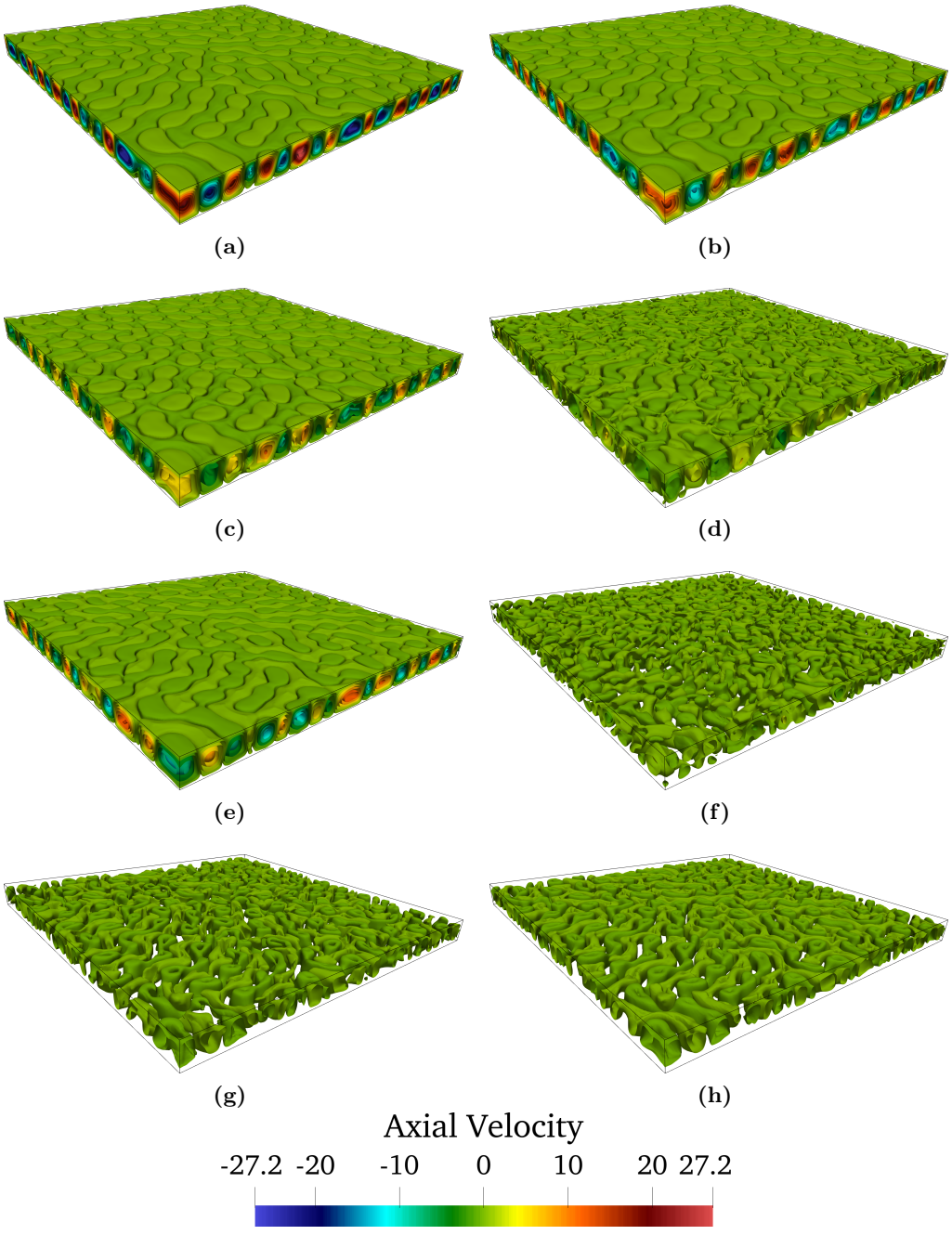

Figure 7.6: Thermovibrational convection in a layer of FENE–CR fluid delimited by differentially heated solid walls (snapshots of the isosurfaces of the vertical component of velocity evenly distributed over the interval $\mathcal{I}_1$). $Pr = 8$, $\Omega = 25$, $Ra_\omega = 4000$, $\xi = 0.5$, $\vartheta = 0.1$, pulse wave acceleration.

Recalling the concepts introduced in the earlier subsection, this scenario might be seen as a realization of the increased complexity of the flow expected when the acceleration follows a pulse wave time evolution.

Although the spatio-temporal behaviour differs in the two cases under analysis, however the leading mechanism of evolution remains basically the same, namely a standing wave. Indeed, the velocity field initially undergoes a shrinkage in intensity (Figures 7.6b-7.6c) until eventually the fluid changes its sense of rotation (Figures 7.6d-7.6e). It is worth observing that also in this case the overall intensity of the velocity field after the first inversion is smaller than that in the initial frame (compare Figures 7.6a-7.6e).

Despite these similarities, however, a closer look at the first part of the pattern evolution (frames 7.6a-7.6c) reveals that a secondary mechanism is at play in this case, namely, a *breaking roll* mode of convection [1, 168]. This specific behaviour has been already observed as a typical mode of convection in classical Rayleigh-Bénard viscoelastic flows. Its dynamics basically consists of convective rolls that break and reform but in a direction that is perpendicular to the original one. To visualize this process, as an example, the reader may consider the first roll in the corner of the layer in frame 7.6a. It is easy to observe that, as the pattern evolves, this rolls tends to merge with the closest roll of the same sign (frames 7.6b and 7.6c).

Nonetheless, this peculiar mechanism is mediated by the predominant standing wave and by the fact that in the meantime the vibrations became stabilizing for the flow field (and therefore, the fluid motion is no longer driven by buoyancy but only by the elastic energy stored by the polymer molecules).

When the vibrations become stabilizing, the standing wave is still the dominant solution. In this case the fluid has stored enough energy to continue pulsating and to invert the sense of rotation two other times (Figures 7.6e-7.6f and 7.6f-7.6g).

As the interval $\mathcal{I}_2$ is entered, the vibrations are more or less at half of their stabilizing phase. In this stage the acceleration has a constant value (as opposed to a sinusoidal acceleration, which changes continuously in time). This constant stabilizing acceleration has the effect to dampen and almost annihilate the convective structures. This

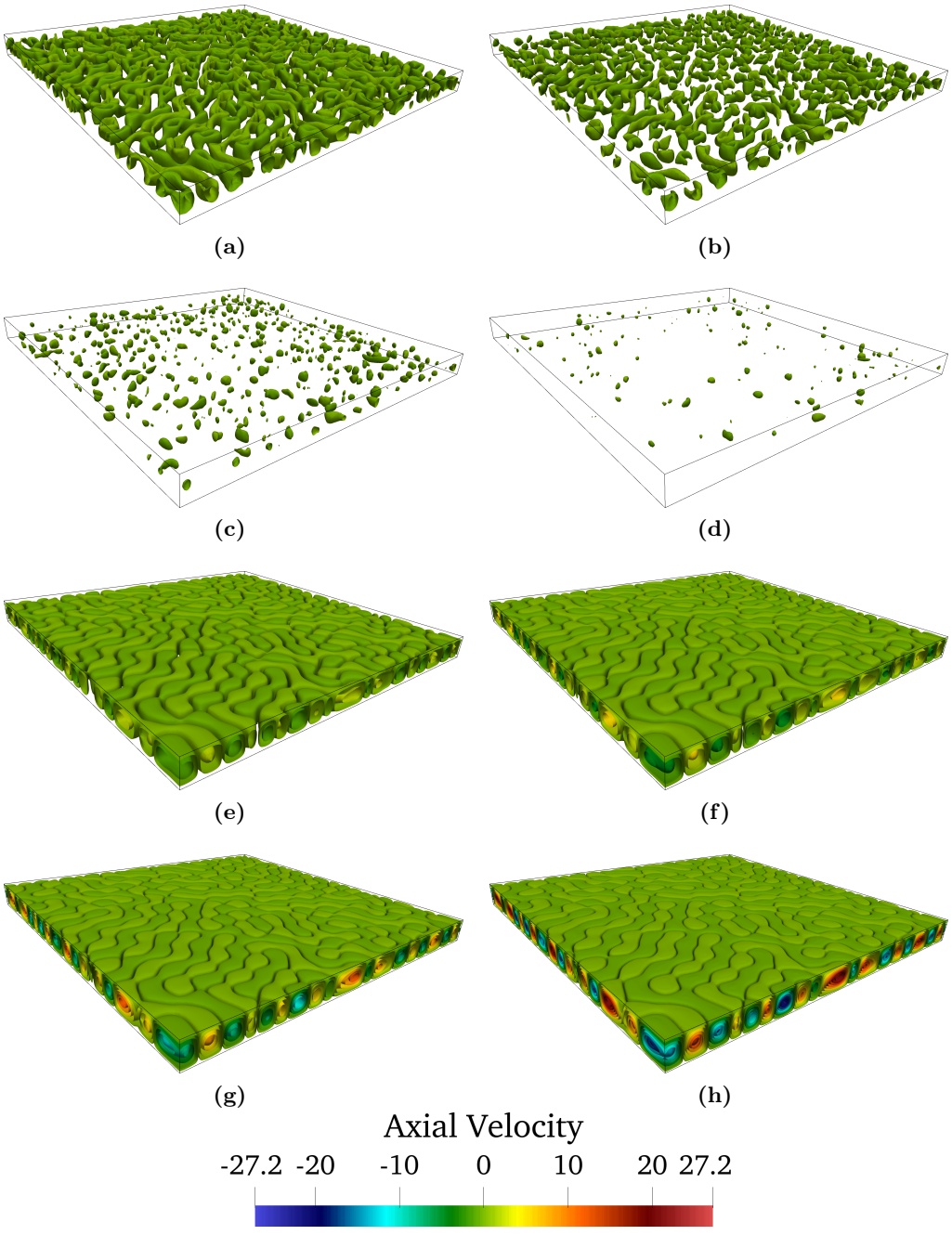

Figure 7.7: Thermovibrational convection in a layer of FENE–CR fluid delimited by differentially heated solid walls (snapshots of the isosurfaces of the vertical component of velocity evenly distributed over the interval $\mathcal{I}_2$). $Pr = 8$, $\Omega = 25$, $Ra_\omega = 4000$, $\xi = 0.5$, $\vartheta = 0.1$, pulse wave acceleration.

becomes more evident when the patterning behaviours for sinusoidal and pulse forcing are compared in $\mathcal{I}_2$ (compare Figure 7.5 and 7.7).

As the system enters the second part of $\mathcal{I}_2$, the acceleration suddenly changes its direction. As a result, convective instabilities are newly excited and the velocity field starts increasing its intensity. The spatial arrangement of the rolls is the same as at the beginning of $\mathcal{I}_1$ but with an inversion of the sense of rotation (as depicted in Figure 7.7e-7.7h).

The dynamics in $\mathcal{I}_3$ and in $\mathcal{I}_4$ are relatively similar to the one just described and, for this reason, its description is omitted. However it is worth highlighting that the breaking rolls mechanism is still effective over $\mathcal{I}_3$.

As a concluding remark for this subsection, one last point should be clarified. As illustrated on the basis of a purely heuristic approach in this subsection, a key factor driving the fascinating dynamics of the systems under analysis is its ability to retain *elastic energy* and release it when the external time dependent forcing does not play a destabilizing role. A classical way to estimate the local elastic energy in a viscoelastic fluid is to calculate the trace of the extra-stress tensor $\mathrm{tr}(\tilde{\boldsymbol{\tau}})$ (this quantity being *proportional* to the local elastic energy) [213].

Figure 7.8 reports the evolution of $\mathrm{tr}(\tilde{\boldsymbol{\tau}})$, hereafter simply called "elastic energy", along a fixed line parallel to the x direction (belonging to the mid-height plane, i.e. $0 < x < 15$, $y = 0.5$ and $z = 7.5$) as a function of time (over the interval $2T_\Omega$). On this basis, it is easy to see that moving from a sinusoidal to a pulse wave acceleration increases the amount of elastic energy stored by the polymer molecules. It is also worth noting that the elastic energy field exhibits a harmonic response to the periodic forcing, regardless of its shape (waveform).

7.4 Discussion and Conclusions

The results presented in this study should be regarded as an extension of previous work of the present authors on these subjects. On one hand, this chapter have considered conditions close to those examined in Chapter 6, i.e. thermovibrational convection in an infinite layer of viscoelastic fluid having $Pr = O(1)$, and with a similar frequency of

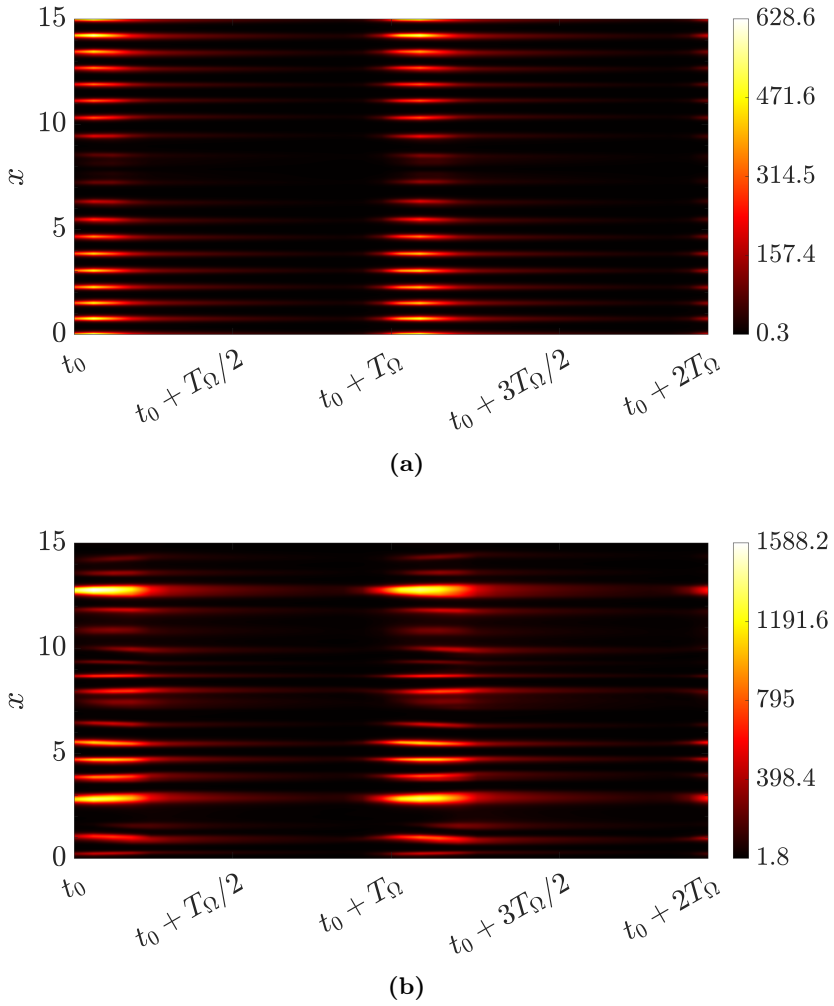

Figure 7.8: Color field of $\mathrm{tr}(\tilde{\boldsymbol{\tau}})$ as a function of the time and the x coordinate in the centre of the cavity. $0 < x < 15$, $y = 0.5$, $z = 7.5$. Numerical simulation with $AR = 15$, $Pr = 8$, $\Omega = 25$, $\xi = 0.5$, $\vartheta = 0.1$, and $Ra_\omega = 4000$. (a) Sinusoidal and (b) Pulse waves.

the external forcing (set as sinusoidal wave in the previous chapter). On the other hand, a FENE–CR fluid with $L^2 = 200$ having $Pr = 8$, $\xi = 0.5$ and $\vartheta = 0.1$ has been assumed (as in Lappa & Boaro [1], where attention was paid to classical Rayleigh-Bénard convection, i.e the case with acceleration constant in time and space).

In the present work, the parameter Σ (ratio between relaxation time and period of the external forcing) has been fixed to $0.4 < 1$, which implies that in a period of vibrations, the polymer molecules are potentially able to relax and go back to their

initial configuration. This is the feature allowing the system to release elastic energy when it enters the stabilizing phase of the vibrations (where such energy is progressively dissipated by viscous effects, similarly to what happens in an harmonic oscillator, see Figure 7.8).

As illustrated in the results section, in the case of sinusoidal forcing, the periodic excitation and dampening of convective modes (mediated by the accumulation and release of elastic energy) can generate *complex-ordered* structures.

Following the classification made by Rogers and coworkers to categorise complex ordered structures arising from modulated Rayleigh-Bénard convection in Newtonian fluids [207–210], here, the observed patterns might be classified as *roll superlattices*. The roll superlattice is a *subharmonic* pattern emerging in states that are slightly supercritical. Once the Rayleigh number is increased and exceeds a certain threshold (which, in turn, depends on the amplitude of vibrations), these planforms can undergo a transition to a *square superlattice* (SQS) state [208].

Given these premises, it is interesting to compare the results of the present study ($\vartheta = 0.1$), with the one reported in Chapter 6 (considering in particular the cases with $\vartheta = 0.06$ and 0.24). In that work, "more" supercritical solutions were examined and the obtained superlattice-like structures were akin to the SQS observed in the modulated Rayleigh-Bénard problem. This indicates that the general conclusion that an increase in the critical parameter can turn a roll superlattice into an SQS also holds for thermovibrational convection in a viscoelastic fluid.

Moving forward to the case with pulse wave acceleration, it can be concluded that the ordered patterns seen for the sinusoidal forcing are taken over by a distribution of rolls that is more similar to the one observed in classical RB convection in viscoelastic fluids. In particular, the initial distribution of the rolls is reminiscent of the flow pattern that arises in a shallow viscoelastic liquid bridge (see Ref. [1] $AR = 0.17$, $Ra = 2000$, $\vartheta = 0.1$, where AR = height/diameter and Ra represent the classical Rayleigh number). In Ref. [1] the flow was found to display a peculiar breaking-roll evolution (see Figure 1.19). In the present case, this mechanism (sustained by buoyancy forces), vanishes as soon as the system enters its stabilizing phase (the differences between the two systems can

obviously be found in the different cause-and-effect relationships enabled by steady and time-varying accelerations).

The following chapter will put aside thermovibrational flow to concentrate on another class of thermally driven flow that can arise in microgravity, i.e. Marangoni flow in finite layers of Oldroyd-B fluid.

Chapter 8

Marangoni Flow in Viscoelastic Layers

This chapter is based on Boaro & Lappa, 2022 'On the competition of transverse and longitudinal modes of Marangoni convection in a three-dimensional layer of viscoelastic fluid' [6].

8.1 Introduction

Thermocapillarity can be defined as the tendency or ability of liquids to develop surface flow in the presence of temperature gradients.

These effects are omnipresent in nature and technology; inorganic and organic material solidification, crystal growth from the melt, soldering, film processing are just examples of the myriad technological processes where a liquid is exposed to a gas in the presence of temperature gradients with various orientations.

These systems have gained considerable momentum in the recent years owing to the rising tide of new studies aiming to deeply investigate them after filtering out the concurrent influence of gravitational effects (this being made possible by sounding rockets of various types and the advent of space platforms such as the International Space Station [216]). They have also been addressed extensively through numerical approaches of various kinds (see Refs [217–219] just to cite some relatively recent contributions). Despite the remarkable efforts of research groups with various backgrounds and objectives, and the different directions from which the problem has been tackled, however, as the reader might have gathered from Chapter 1, the physical understanding of surface-tension-driven flows is far less advanced than of buoyancy-driven convection.

If in place of Newtonian fluids, viscoelastic liquid are analysed, the understanding of these systems is even less structured and developed. Focusing on the object of this chapter, i.e., Marangoni flow (the temperature gradient acts in a direction parallel to the surface tension), some guidance is provided by the investigations by Hu et al. [136–138] Patne et al. [139, 140] that have considered unbounded layers of fluid. It is worth highlighting that these works do not solve the equation in their non-linear and time dependent form, but rather use an LSA approach.

Although these studies have opened up a new perspective on the subject, a development of the subject has not received yet a continuation with non-linear approaches. In particular, an open question is whether the modes of convection that have been specifically identified through LSA can be excited at the same time and eventually result in multiple solutions and ensuing peculiar convective states. The present study may be regarded as an attempt along these lines. In short, it follows and integrates the line of inquiry started by Lappa & Ferialdi [135] about the non-linear analysis of Marangoni-Bénard flow in viscoelastic fluids, by considering the equivalent problem in a finite layer of liquid with parallel temperature gradient.

The problem is tackled in the framework of direct numerical solution of the governing non-linear equations and results are provided for different levels of elasticity and distance from the critical conditions. In addition, relevant theoretical links are also explored with respect to recent literature (not necessarily related to surface-tension-driven flows) where the general interconnections between ordinary (inertial) and elastic turbulence have been considered.

8.2 Statement of the problem

A finite 3D layer of viscoelastic fluid is considered. The layer is delimited at the sides and at the bottom by no-slip walls, while the top boundary is modelled as an adiabatic and non-deformable free surface. Such a geometry can be characterized synthetically through its (dimensional) depth h (which is also used as characteristic length scale to calculate the non-dimensional quantities) and the aspect ratios $AR_x = \ell/h = 20$ and $AR_z = w/h = 10$ for the x and z directions respectively. Obviously, the associated

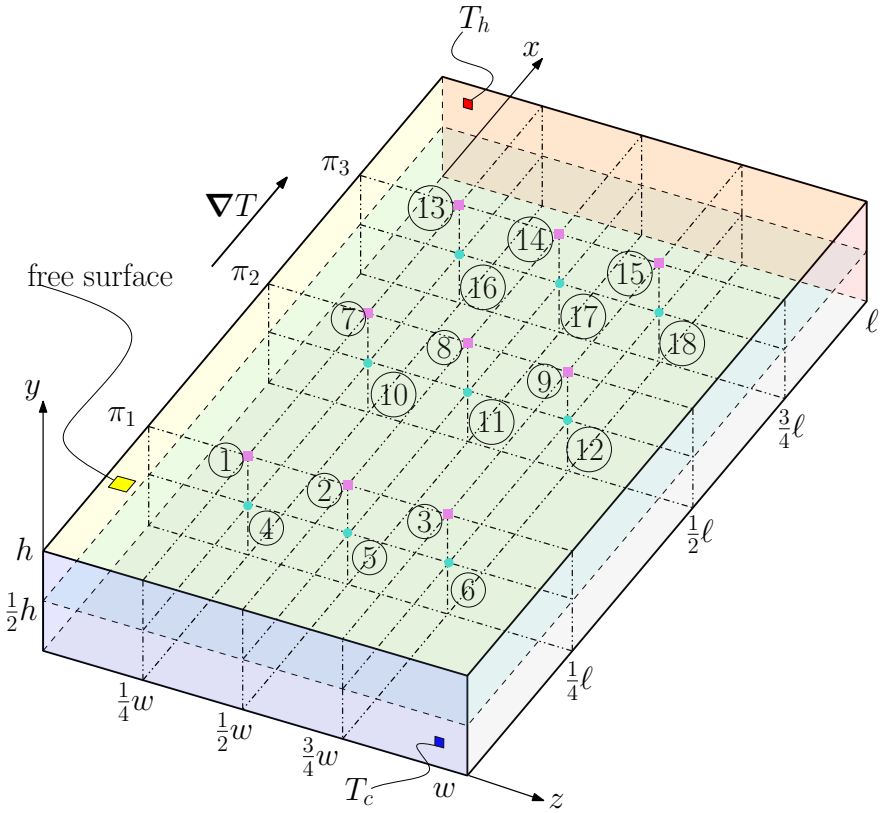

Figure 8.1: Schematization of the problem and locations where numerical probes have been placed to study the time-dependent behaviour of the flow

dimensional problem also requires that the fluid type and the applied temperature gradient ($\boldsymbol{\nabla} T$) are specified.

The OpenFOAM computational platform has been used to solve the overall set of governing equations for an Oldroyd-B fluid with "active" free surface (eqs. (2.69),(2.70), (2.71) and (2.65) with eq. (2.75) as boundary condition). More specifically, the equations have been discretised in space and integrated in time using a control volume method through a segregated time-marching procedure. Similarly to the previous chapters, the Piso algorithm with a collocated disposition for the primitive variables and the e Rhie & Chow [158] interpolation scheme was employed.

Using a log-conformation approach to guarantee stability of the solution over a vast range of elasticity and Marangoni numbers, the equations are discretised with second order accurate backward scheme in time, while a second order accurate central difference

scheme is used for the spatial discretization of the diffusive terms and a third order Cubista scheme for the analogous treatment of the convective terms. As pointed out in chapter 5, to avoid non-physical oscillations, the Cubista scheme is implemented though a deferred correction approach and the non scalar quantities are handled in a component-wise way [174].

Last but not least, the Marangoni boundary condition is regularised in order to filter out unphysical singularities in proximity to the corners between heated boundaries and free surface (see section 3.3 for more detail about the implementation.

Moreover, it is worth highlighting that the steady buoyancy term $PrRaT\mathbf{i}_g$ in eq. (2.70) is set to $\mathbf{0}$ in order to mimic the absence of gravitational field.

8.2.1 Mesh refinement study

Selecting a relevant mesh is a non-trivial task stemming from the opposite needs to achieve grid-independent results and minimize the computational cost as much as possible. This is generally achieved with ab-initio coarse-grained numerical simulations for a representative case, followed by a progressive increase in the used numerical resolution (typically achieved by using more computational points) until the sensitivity of the results on the grid drops below a given (pre-fixed) threshold. There are therefore two levels of difficulties intrinsically embedded in such an exercise, one being the intrinsic computational 'overheads' of the considered problem (which determine the effective computational cost), another one being the issue of discerning what can really be considered "representative" in terms of convergence.

For what concerns the first aspect, some of the typical computational drawbacks of this category of flows have already been illustrated in Chapter 3, where the relevant countermeasures were discussed (to be typically implemented together with a choice of the time integration step much smaller than that required in the equivalent Newtonian fluid situation). The second aspect (the selection of a relevant case for the mesh sensitivity assessment) brings problems of its own, these being the problem "dimensionality" (i.e. two dimensions or three dimensions?), the flow regime (steady, oscillatory or tur-

bulent) and, last but not least, the quantity or process to be monitored to draw some relevant conclusions.

As in the present work (as it will be illustrated in detail in section 8.3), the flow displays a marked tendency to produce three-dimensional (3D) states that differ significantly from the equivalent 2D counterparts, a quite obvious choice should be a fully 3D case. Since, as it will be yet illustrated in detail in section 8.3, the flow is also able to produce turbulent states for relatively small values of the Marangoni and elasticity numbers (and these states constitute integral part of our study), a representative case should therefore contain these elements too, i.e. be chaotic. This specific aspect, in turn, connects to the last of the issues mentioned above, i.e. the identification of relevant local or global parameters or trends to be checked as the numerical resolution is increased.

In order to satisfy the requirement about a flow that is at the same time 3D and chaotic, the case $Pr = 7$, $Ma = 500$ and $\vartheta = 0.2$ has been selected. Accordingly (with the objective in mind of making the properties of the emerging solution somehow "quantifiable"), for each solution it was determined the related velocity power spectral density (PSD).

In particular, the spectra have been calculated for two different velocity (u_y) signals, one located in the center of the layer (probe 11 in Figure 8.1) and one closer to the solid boundary (probe 12). Figure 8.2 shows such spectra for four different meshes. The related legend displays the used number of points along x, y and z, respectively. In order to assess the overall level of convergence, let us also calculate a "global measure", i.e. the integral $\mathcal{I}$ of the PSD in the sub-range that follows the elastic turbulence decay law. This quantity is related to the total power carried in such a sub-range. These values are summarized in Table 8.1.

As the Reader will realize by inspecting these data, moving from a mesh having $300 \times 30 \times 150$ elements to one having $350 \times 30 \times 175$ has a negligible effect on both the scaling law (more precise about the implications of this observation will be provided later), the PSD amplitude, and the overall power carried in the spectra. For these reasons, a mesh with $300 \times 30 \times 150$ elements has been adopted for the present analysis

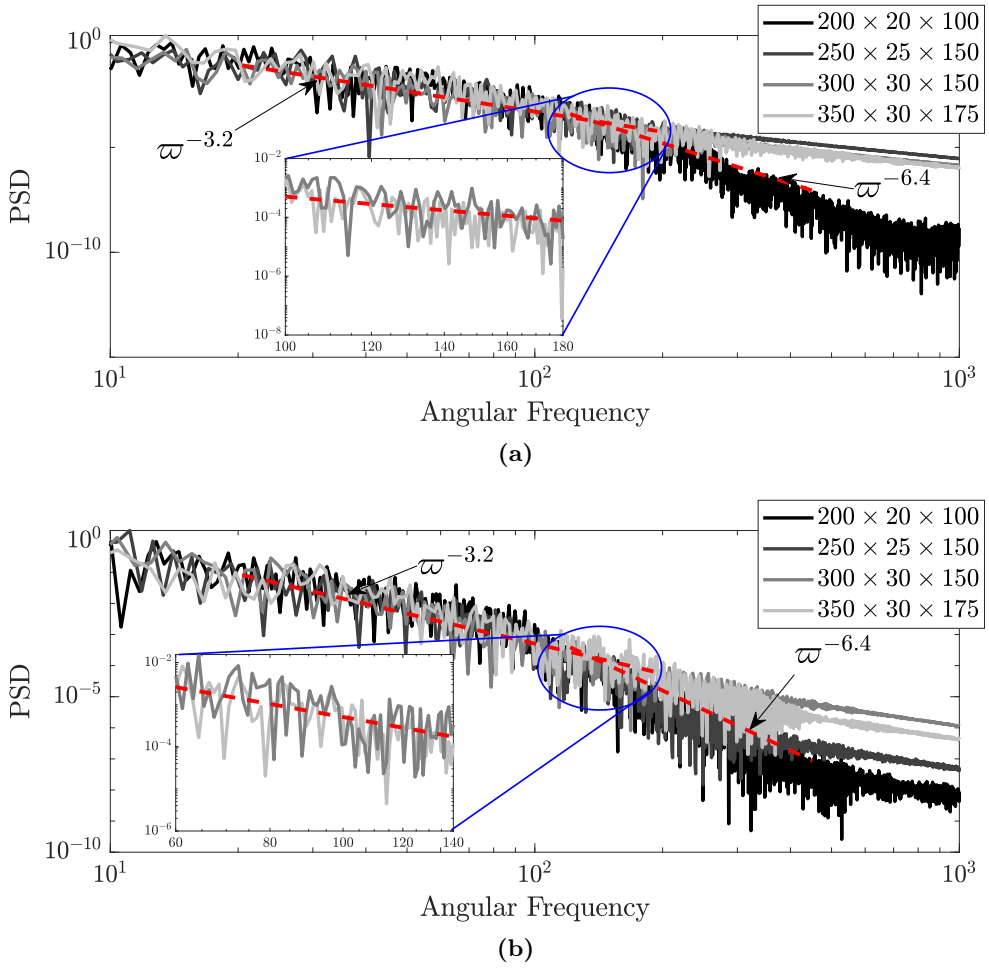

Figure 8.2: 3D viscoelastic thermocapillary flow, spectra of the y component of the velocity signal probed in (a) the centre of the layer (probe 11) and (b) closer to the wall (probe 12). Mesh refinement study with $Ma = 500$ and $\vartheta = 0.2$.

(able to guarantee reasonable grid-independence while limiting the otherwise excessive computational time).

8.3 RESULTS

All the cases presented hereafter relate to an Oldroyd-B fluid having $Pr = 7$ and $\xi = 0.1$ while the Marangoni (Ma) and the elasticity (ϑ) numbers are allowed to span relatively wide ranges ($Ma = 500$, $\vartheta \in [0.03, 0.2]$ and $Ma = 2500$, $\vartheta \in [0.01, 0.65]$).

Given the well-known ability of Marangoni flow to produce transverse or longitudinal modes of convection in Newtonian fluids depending on the value of the Prandtl number

Table 8.1: Integral of the PSD over the sub-range of elastic turbulence ($\mathcal{I}$) for four different meshes.

mesh	$\mathcal{I}$	
	probe 11	probe 12
$200 \times 20 \times 100$	4.43	3.25
$250 \times 25 \times 125$	3.18	1.5
$300 \times 30 \times 150$	2	1.58
$350 \times 30 \times 175$	2	1.54

([88–90]), as well as in viscoelastic fluids ([136–138]), a precise analysis hierarchy is implemented in the remainder of this work, by which these two categories of disturbances are partially separated.

In this regard, let us recall that, unlike the LSA approach, where the spatial structure of disturbances can be fixed "a priori", this is not possible when an approach like that implemented in the present study is used. Indeed, when the problem is solved in its nonlinear form, the disturbances are naturally produced and selected out of the full possible spectrum of allowed perturbations according to their growth rate, i.e. on a "most-dangerous disturbance" basis. A possible way to concentrate on a specific category of disturbances, therefore, simply consists of preventing the system from developing certain perturbations by forcing it to retain certain symmetries in space, e.g. by obliging it to maintain a two-dimensional behaviour (2D simulations).

This approach is intentionally used here to distinguish 2D (transverse) disturbances from the more complex spectrum potentially excited when the flow is allowed to develop along all the spatial dimensions (3D simulations).

8.3.1 2D disturbances

Although, as it will be clearly shown in section 8.3.2, the modes of convection that spontaneously arise in viscoelastic thermocapillary convection are essentially 3D, in line with the theoretical predictions of available LSA studies ([136–138]), disturbances that are essentially 2D in nature can also be expected for high-Pr fluids if Ma and ϑ are located in a certain subregion of the space of parameters. As outlined before, these can be captured and studied in great detail if the problem is investigated numerically under

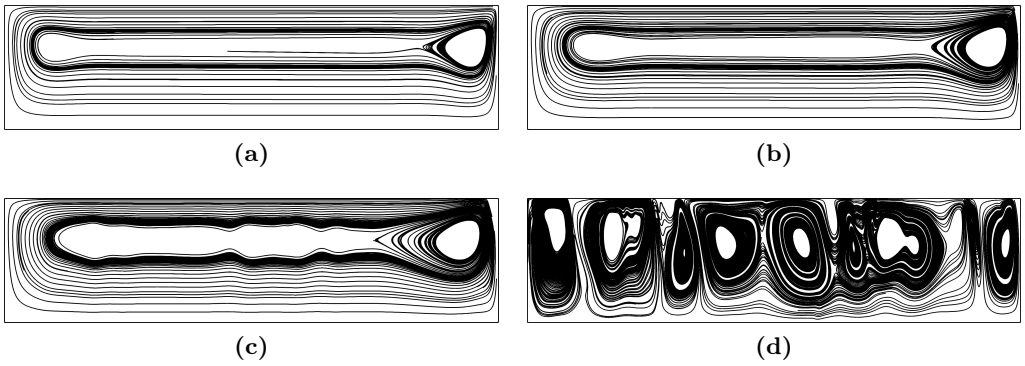

Figure 8.3: 2D viscoelastic thermocapillary flow, Streamlines for the case of $Ma = 500$, (a) $\vartheta = 0.1$, (b) $\vartheta = 0.15$, (c) $\vartheta = 0.2$, (d) $\vartheta = 0.4$. The cavity is cooled from the left and heated from the right side. For visualisation purposes, the height of the layer is magnified 5x. (a)-(c) depict the final stationary state, (d) reports the streamlines distribution at $t = 64.13$.

the constraint of two-dimensionality. Obviously, with 2D simulations, 3D perturbations are naturally filtered out thereby leaving the ground to transverse waves or other effects which develop along the direction of the interface.

Given such premises, it is also worth recalling (see again the arguments provided in Chapter 1) that, in general, no threshold in terms Ma must be exceeded in order to produce fluid motion. This is a typical feature of thermocapillary convection. For Newtonian fluids, if a temperature gradient is applied along the free surface, no matter how small, a single stationary circulation system is established inside the cavity in the form of a horizontally elongated roll.

This is still true in a viscoelastic fluid provided both the Marangoni number and the elasticity number are sufficiently small. In particular, according to the present results, for the Marangoni number in the range $500 \leq Ma \leq 2500$, a steady state is attained only if the elasticity number is smaller than a given ϑ_{cr} (which depends on the considered value of the Marangoni number), whereas more complex phenomena are enabled as soon ϑ is increased beyond this limit.

Following a logical approach where situations of increasing complexity are presented as the discussion progresses, most conveniently, let us start from the description of the results obtained for the branch of solutions corresponding to $Ma = 500$. In this case,

according to the numerical simulations the value of the threshold corresponds to $\vartheta_{\mathrm{cr}} = 0.15$ (as a low frequency disturbance arises and a wave becomes visible for this value of the elasticity parameter). This may be regarded as a metastable condition because the wave survives only for a limited period of time (after this time, an asymptotic state with the classical elongated single cell is recovered). For slightly larger values of the elasticity number, however, this disturbance is turned into a permanent wave traveling in the downstream direction and manifesting as a weak corrugation in the shape of the streamlines (Figure 8.3c). This perturbation has clearly an elastic nature as witnessed by its connection to the elasticity number and its direction of propagation (as opposed to the classical hydrothermal disturbances in Marangoni flow, which, as described in chapter 1 and shown in Figure 3.2) propagates upstream).

Notably, and in a quite unexpected way, a further increase in ϑ leads to a completely different situation where, although a disturbance traveling in the same direction of the surface flow can still be recognized, (Figure 8.3d at $t = 46.88$ for $\vartheta = 0.4$), its effects are not limited to a corrugation of the streamlines of the main Marangoni cell. Rather the original single-roll circulation system is taken over by a multicellular structure consisting of a train of cells, which spread continuously in the downstream direction while randomly merging each other or, vice versa, being split into smaller eddies.

This remarkable change in the patterning behaviour is reflected by an analogous modification visible in the velocity PSD (power spectral density $\mathcal{P}$) distribution obtained for a signal probed in the centre of the layer (see Figure 8.4). As qualitatively and quantitatively substantiated by this plot, the spectrum displays the typical properties of a turbulent flow, namely, a broad continuous power-law-decay region spanning more than two orders of magnitude in terms of frequency.

Another key observation concerns the tide displayed by such a distribution of amplitudes for $\varpi > 10$. Notably, it does not follow the classical Kolmogorov scaling law, i.e. $\mathcal{P}(\varpi) \propto \varpi^{-5/3}$, where ϖ is the angular frequency. Rather the exponent is ≈ -3.2 in the intermediate range of frequencies and -6.4 in the high-frequency interval, which indicates that the considered chaotic state is not inertial in nature (the discussion will return to this very important concept later).

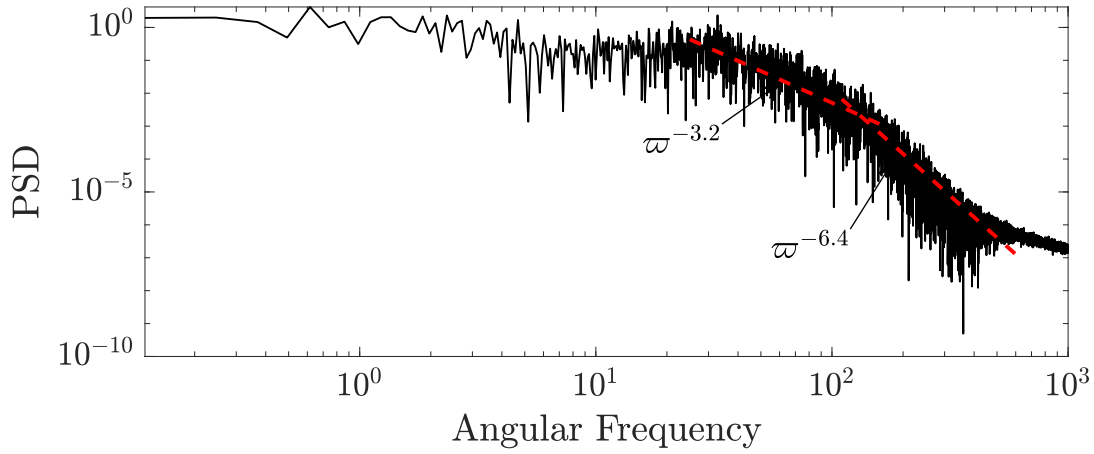

Figure 8.4: Power spectral density as a function of the angular frequency for the case of $Ma = 500$ and $\vartheta = 0.4$ in a logarithmic plane. The dashed red lines indicate the overall descending law of the spectrum.

A larger Marangoni number ($Ma = 2500$) increases the range of values of the elasticity number in which a stable elastic wave can be obtained. The elastic disturbance still travels downstream, however, it can be obtained for a value of ϑ as low as 0.045, basically one order of magnitude smaller than that found for $Ma = 500$.

The different stages of evolution taken by the flow in one period of oscillation for this value of ϑ can be seen in Figure 8.5. Comparing this figure with the chaotic state reported in Figure 8.3d, it becomes evident that the morphology and the number of the rolls is different. The angular frequency is $\varpi = 91.6$ and, interestingly, a small increase in the elasticity number has the effect of causing a decrease in such a value. Moreover, at $\vartheta = 4.575 \times 10^{-2}$ new frequencies start to populate the spectrum, thereby making the identification of a predominant frequency in the flow relatively difficult or meaningless.

The significance of the next two figures of the sequence (Figure 8.6 and Figure 8.7) resides in their ability to reveal the progressive transitions undergone by the signals and the related spectrum, respectively, as the elasticity parameter is increased.

For $\vartheta = 4.5 \times 10^{-2}$ the signal exhibits a relatively regular behaviour, and this is reflected by its spectrum (plotted on a logarithmic plane in Figure 8.7a) where the aforementioned dominant frequency can be clearly recognized ($\varpi = 91.6$ together with its harmonics, i.e. higher order multiples). A small increase in ϑ leads to a more involved

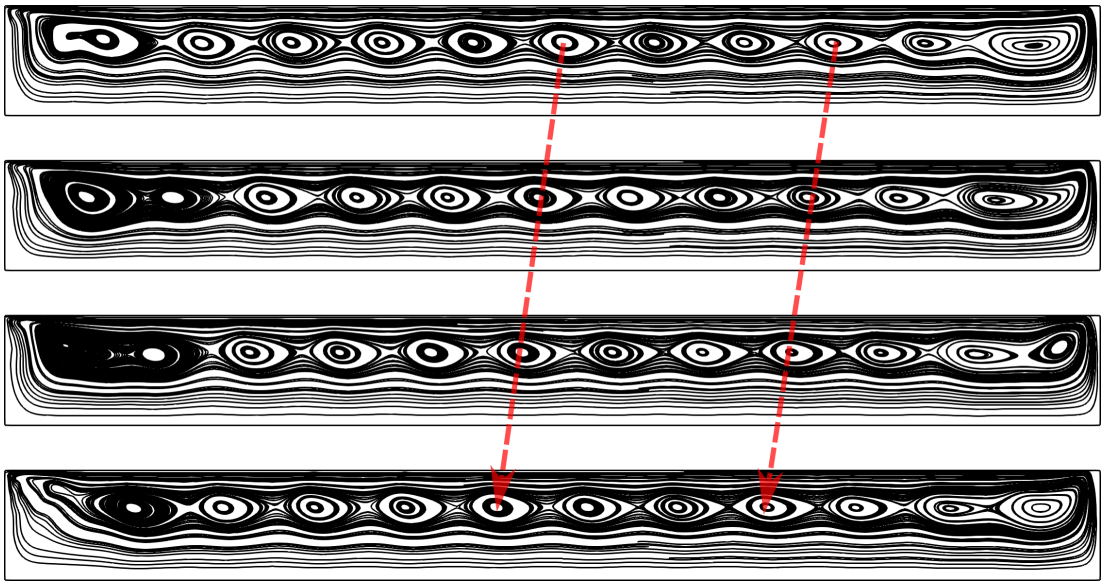

Figure 8.5: Elastic wave traveling downstream for the case of $Ma = 2500$ and $\vartheta = 0.045$. Four snapshots evenly spaced along the oscillation period. The red arrow follows one of the travelling rolls. The cavity is cooled from the left and heated from the right side. For visualization purposes, the height of the layer is not to scale (magnified by 2x).

flow. Indeed, for $\vartheta = 4.575 \times 10^{-2}$ the signal displays in some intervals a regular and periodic behaviour, alternated to small periods of chaotic busts. Finally, for $\vartheta = 6.5 \times 10^{-2}$, a completely turbulent signal is produced and the same scaling already identified for $Ma = 500$ and $\vartheta = 0.4$ can be recognized, namely, the "$-3.2/-6.4$" law.

To complement this scenario with additional relevant data, Figure 8.8 reports the frequency corresponding to the highest amplitude in the spectrum as a function of ϑ. The graph is terminated at $\vartheta \gtrsim 0.064$ as beyond this point distinguishing clearly such a frequency is no longer possible. Such a plot is useful as the non-monotonic behaviour evident there indicates that disturbances with different wavenumber (and therefore frequency) can be excited for the considered value of the Marangoni number and therefore compete to become the most energetic mode of convection in the flow. There is a continuous switch from one dominant mode to another and back to the original mode as the elasticity parameter is increased, which indicates that a discrete set of modes exist which are in competition. In this regard an analogy might be drawn

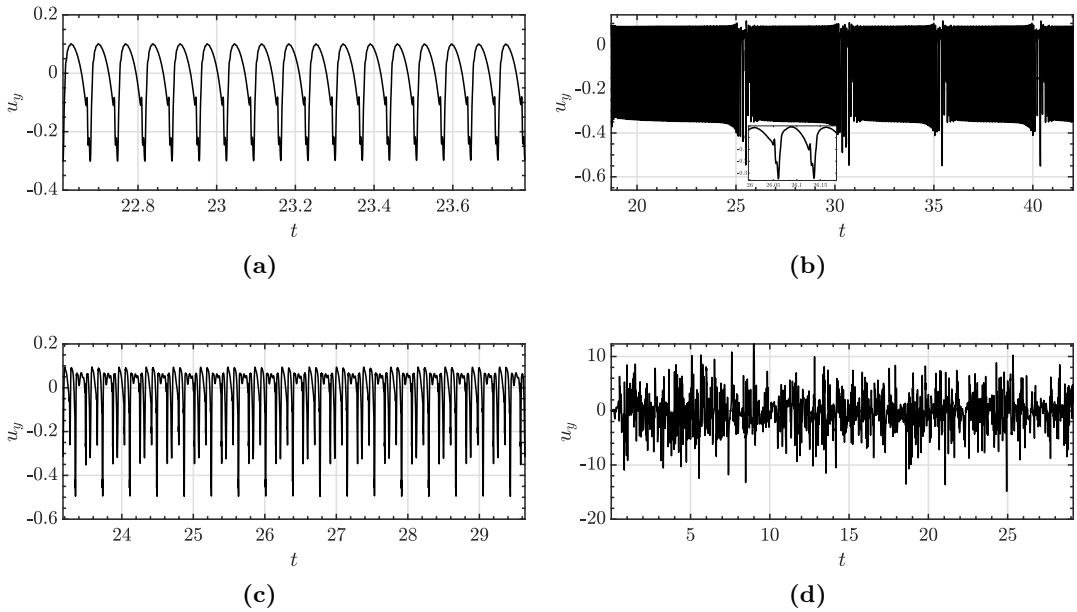

Figure 8.6: 2D viscoelastic thermocapillary flow, y component of the velocity signal probed in the centre of the layer for $Ma = 2500$, (a) $\vartheta = 4.5 \times 10^{-2}$, (b) $\vartheta = 4.575 \times 10^{-2}$, (c) $\vartheta = 5 \times 10^{-2}$, (d) $\vartheta = 6.5 \times 10^{-2}$.

with other viscoelastic phenomena where multiple solutions are known to be the rule rather than an exception [1, 135].

Interestingly, in Figure 8.8 the curves seem to tend to an asymptotic state with $\varpi \approx 52$, which indicates that the energy tends to reside on a smaller frequency as a completely chaotic state is approached. An explanation/justification for this trend can be elaborated in its simplest form on the basis of the two-fold argument that 1) the total energy of the system is fixed (let us recall that all these transitions are produced as a result of an increase in ϑ, not Ma, which is fixed to 2500) and 2) the system can take advantage of a larger set of scales to distribute its energy as the number of coexisting modes is increased (rather than requiring an increase in the frequency of the disturbances as one should expect for transitions produced by an increase in the Marangoni number).

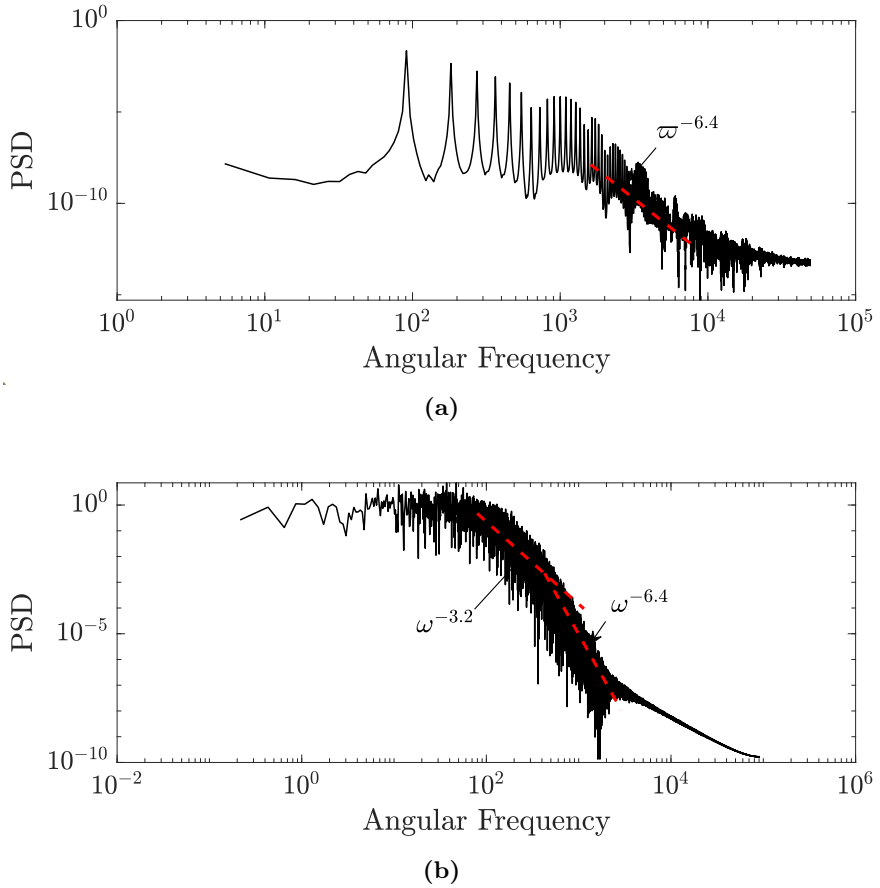

Figure 8.7: 2D viscoelastic thermocapillary flow, spectra of the y component of the velocity signal probed in the centre of the layer for $Ma = 2500$, (a) $\vartheta = 4.5 \times 10^{-2}$, (b) $\vartheta = 6.5 \times 10^{-2}$.

8.3.2 3D disturbances

After considering the problem in the simplified framework represented by a two-dimensional (2D) configuration, let us now turn to interpreting the equivalent dynamics emerging when such a constraint is removed. This specific modus operandi obeys the logic illustrated at the beginning of section 8.3, i.e. the precise intention to discern intrinsically 3D effects through critical comparison of the results provided by 3D simulations with the "equivalent" 2D ones (i.e. conducted for the same set of parameters). As it will be illustrated in detail in this section, a strategy based on the progression from 2D to 3D simulations is indeed instrumental in revealing the role played by the dimensionality of the problem (that is the number of space dimensions involved) and

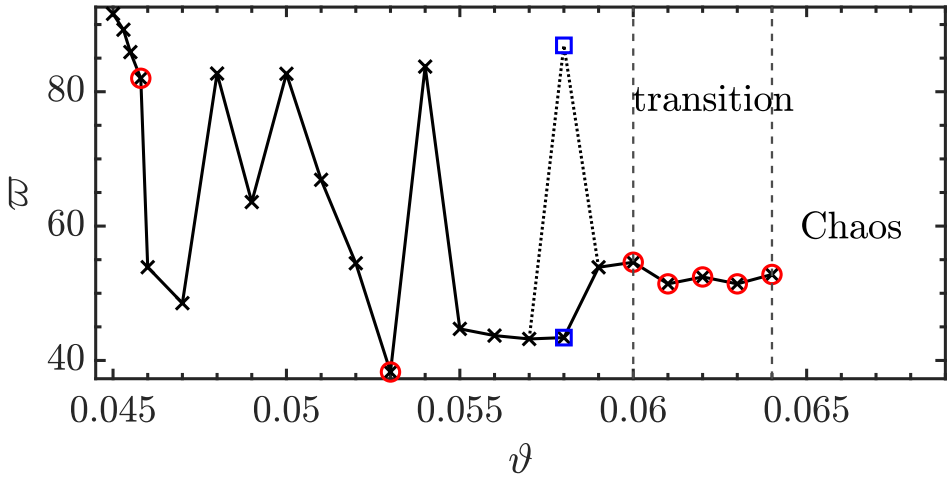

Figure 8.8: 2D viscoelastic thermocapillary flow at $Ma = 2500$. Angular frequency (ϖ) with the higher PSD as a function of the elasticity number ϑ. The $\times$ simply marks the points in the (ϑ, ϖ) plane, $\circ$ marks the cases that display a spectrum that is more chaotic than the majority of the other points and $\square$ denotes a case where two frequencies have the same PSD.

the different level of "criticality" of disturbances that break or do not break certain symmetries of the considered system.

For consistency with the 2D results presented earlier, such analysis is implemented starting from the lower end of the considered interval of Ma, namely, $Ma = 500$. The main outcomes of the related 3D explorative simulations are shown in Figure 8.9, Figure 8.10 and Figure 8.11 for values of the elasticity number which decrease from a ϑ larger than that needed to produce time-dependence in 2D ($\vartheta_{\mathrm{cr2D}} = 0.15$) to a value as small as 0.03 (namely, $\vartheta = 0.2$, 0.15, 0.05, and 0.03 are considered).

The most striking outcome of these simulations is the evidence they provide about the ability of the effective problem dimensionality to cause a departure from idealized solutions (such as the elongated single transverse roll typical of stable Marangoni flow) even if relatively small values of ϑ are considered.

As a fleeting glimpse into Figure 8.9 for $\vartheta = 0.03$ would immediately confirm, if the processes that depend on the details of the third direction are not excluded, longitudinal rolls are formed, i.e. a new class of disturbances is enabled. Besides their different spatial structure (the axes of the rolls being essentially aligned with the x

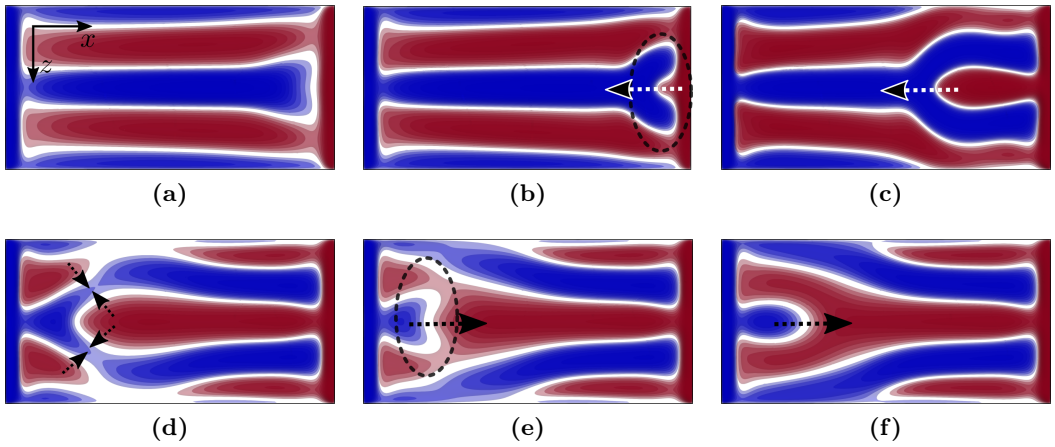

Figure 8.9: Thermocapillary convection in viscoelastic fluid, $Ma = 500$ and $\vartheta = 0.03$. Isosurfaces of the y component of the velocity. The red and blue isosurfaces represent positive and negative value of u_y respectively. The layer is cooled from the left and heated from the right. (a) $t = 4.59$, (b) $t = 5.5$, (c) $t = 11.22$, (d) $t = 19.13$, (e) $t = 20.28$, and (f) $t = 21.30$.

direction), these modes of convection also differ significantly from the waves typical of 2D flow due to their temporal behaviour. A good impression of the overall unsteady three-dimensional motion associated with this kind of disturbances can be inferred from the different snapshots reported in this figure (Figure 8.9) at different times.

Four initial parallel rolls can be spotted in Figure 8.9a. These rolls maintain their position until a variation in their topology is produced in proximity to the heated boundary (Figure 8.9b). Warmer fluid starts to rise inside the region initially occupied by colder and descending liquid. As a result of this effect, the colder region is split in two parts, thereby giving rise to a fork-like shape in the roll distribution (with a central jet of hot fluid surrounded by two parallel strips of cold fluid, (Figure 8.9c).

Interestingly, this variation in the topological configuration of the rolls is not stationary, rather, in an initial stage this "defect" travels in the downstream direction (i.e. from the hot side towards the cold one, from left to right in the figure), thus taking a behaviour formally similar to that observed for the elastic waves in the 2D case. The dislocation travels along the whole length of the cavity until it reaches the cold boundary (Figure 8.9d). Here, as a result of its interaction with this wall, a new fork-like localized feature is created that is mirror symmetric with respect to the original one

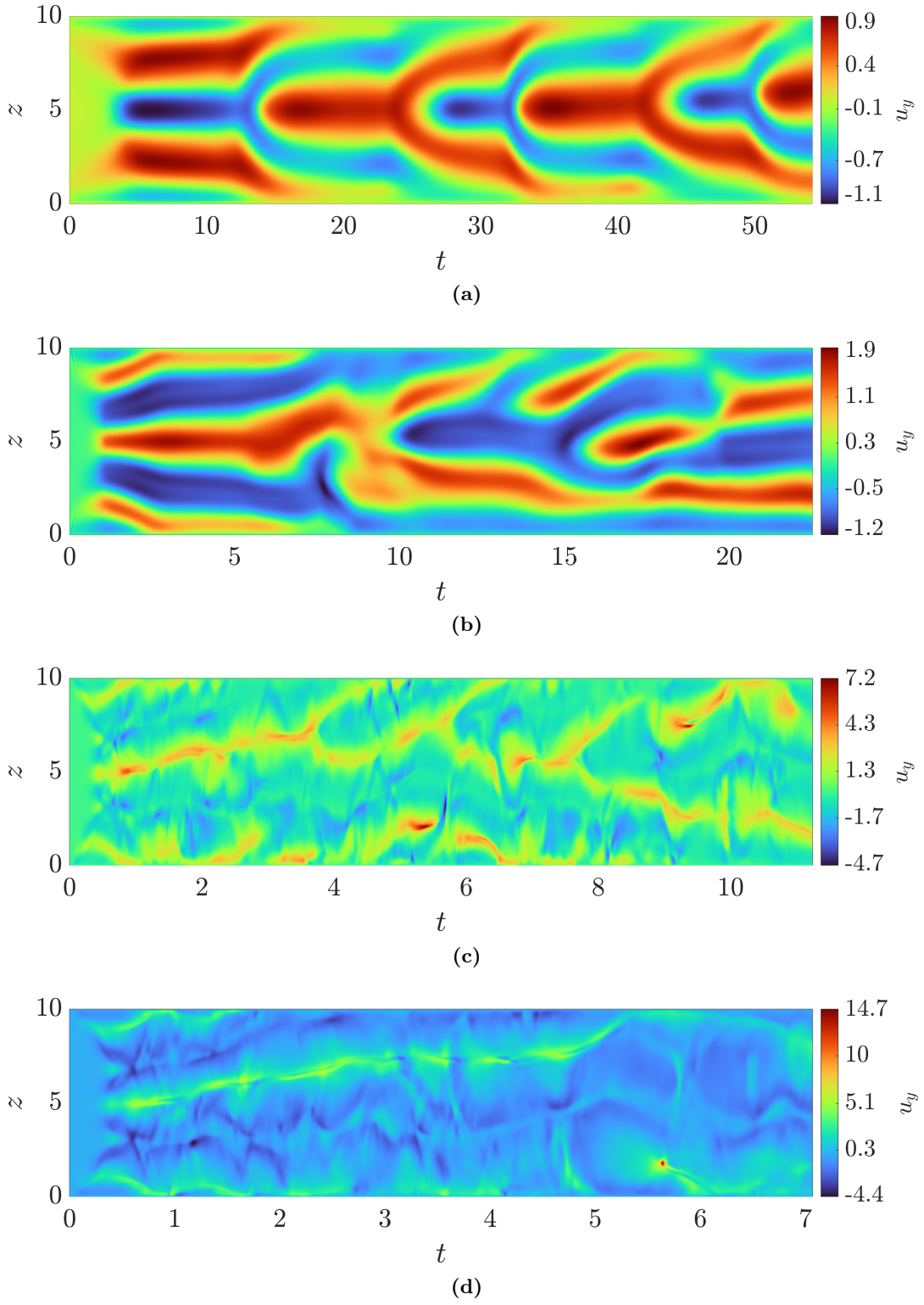

Figure 8.10: Color field of y component of $\mathbf{u}$ as a function of the time and z component in the centre of the layer, with $x = 10$, $y = 0.5$, and $0 \leq z \leq 10$ the for $Ma = 500$, (a) $\vartheta = 0.03$, (b) $\vartheta = 0.05$, (c) $\vartheta = 0.15$, (d) $\vartheta = 0.2$.

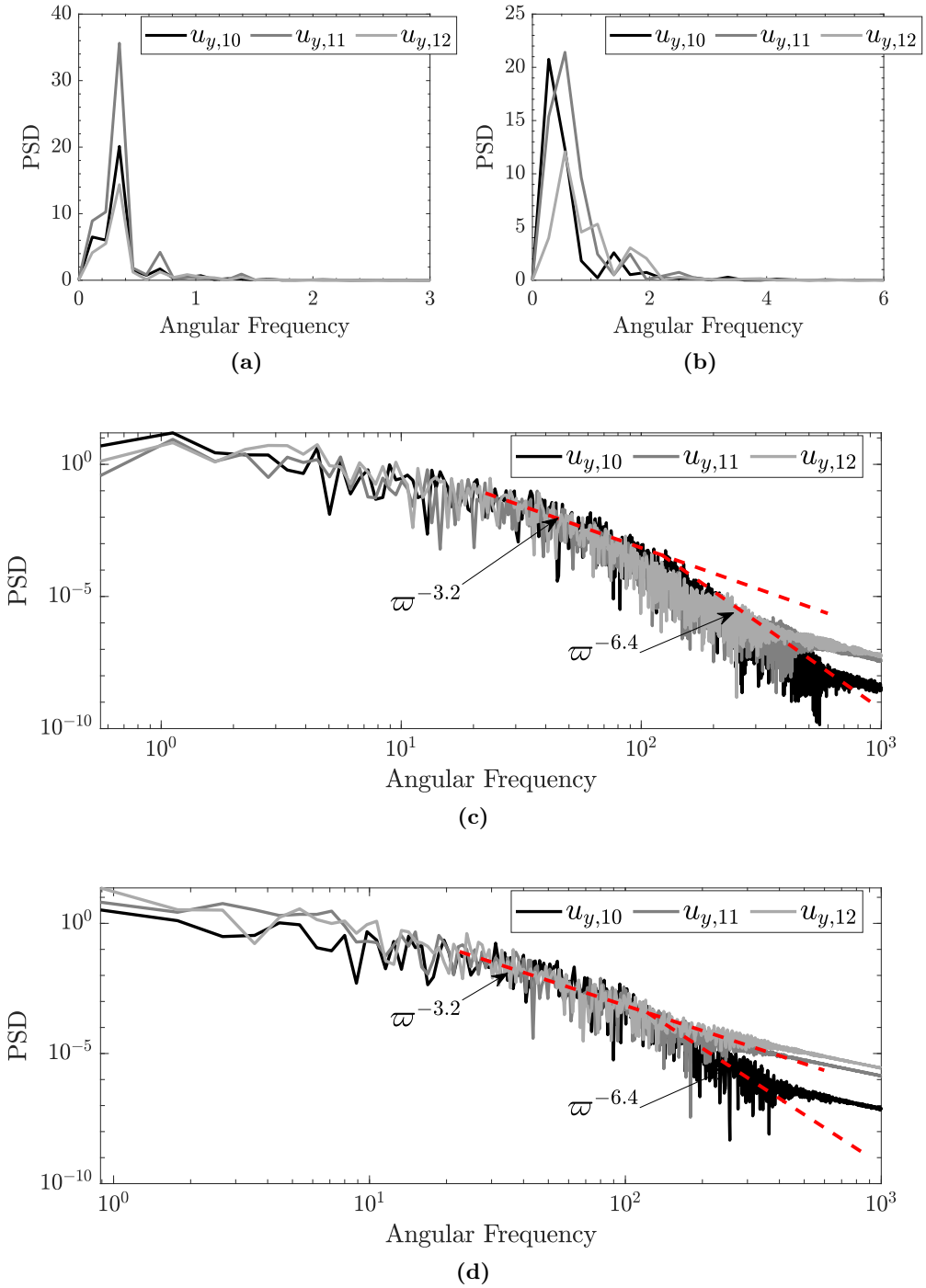

Figure 8.11: 3D viscoelastic thermocapillary flow, spectra of the y component of the velocity signal probed in the centre of the layer($x = 10$, $y = 0.5$) at $z = 2.5$ ($u_{y,10}$), 5 ($u_{y,11}$) and 7.5 ($u_{y,12}$) for $Ma = 500$, (a) $\vartheta = 0.03$, (b) $\vartheta = 0.05$, (c) $\vartheta = 0.15$, (d) $\vartheta = 0.2$.

(this time a central jet of cold fluid surrounded by two parallel strips of hot fluid can be distinguished, Figure 8.9e). At this stage, the feature carrying the colder fluid starts to travel in the upstream direction (thereby formally resembling the behaviour of a classical hydro-thermal wave, Figure 8.9f).

These findings are naturally complemented by those reported in Figure 8.10a where the spatio-temporal map of the vertical component of the velocity (u_y) along a fixed line in the spanwise direction passing through the centre of the layer is shown (i.e. $x = 10$, $y = 0.5$, and $0 \leq z \leq 10$). This map is particularly useful as it allows the derivation of additional properties of the pattern which would otherwise be hidden or less evident ([3, 190]). In particular, it reveals that the propagation in the upstream motion is faster than the downstream counterpart. The phenomenon repeats itself periodically over time with an angular frequency $\varpi = 0.35$ (Figure 8.11a).

A variation of the elasticty number can produce interesting changes. While, a decrease in ϑ to 0.02 leads to a simple steady solution with a single transverse roll (that for the sake of brevity is omitted from the discussion), vice versa, increasing it to 0.05 has just the opposite effect. A first sign of this increased complexity can be gathered from the spatio-temporal map (Figure 8.10b). As a distinguishing mark with respect to earlier behaviour seen in Figure 8.10a, the mirror symmetry with respect to the mid-plane $z = 5$ is broken. The same information can also be inferred from the spectra reported in Figure 8.11b. These relate to the velocity signals provided by probes located at different positions along the spanwise direction (points 10, 11, and 12 shown in Figure 8.1, i.e. three points located in the centre of the layer and evenly spaced along z). The related frequencies are clearly different; while $\varpi_{10} = 0.28$, $\varpi_{11} = \varpi_{12} = 0.556$.

A further increase in ϑ has the remarkable effect of producing smaller scale details in the spatio-temporal pattern (Figure 8.10c and Figure 8.10d), i.e. features that correspond to higher values of the wavenumber in space and, accordingly, higher frequencies in time (Figure 8.11c and Figure 8.11d).

As a final look at Figure 8.11d would indicate, moreover, signals probed at different locations follow slightly different laws, indeed, while the signal related to probe 10 scales as the 2D cases analyzed in the preceding section ($-3.2/-6.4$ law), the other two signals

(11 and 12) do not change the inclination (they obey a $\varpi^{-3.2}$ scaling). Most importantly, the corresponding spatio-temporal map (Figure 8.11d) also illustrates that in this case the 3D disturbances have a predominant tendency to travel in the downstream direction (the important implications of this apparently cursory observation will be considered in section 8.4).

The remainder of this section is finally devoted to the analysis of the other branch of solutions, i.e. the cases with $Ma = 2500$. In particular, three values of ϑ are considered, namely 0.01, 0.02 and 0.05 (in this regard, it is worth recalling that the companion 2D simulations carried out for $\vartheta = 0.01$ and 0.02 revealed the trivial steady solution with a single cell occupying the entire length of the cavity, while the elastic wave travelling downstream was found for $\vartheta = 0.05$).

Once again, as witnessed by the outcomes of the 3D simulations, consideration of the spanwise direction can cause a dramatic departure from the dynamics obtained under the constraint of 2D flow. In particular, unlike the corresponding stationary or periodic 2D counterparts, all these cases exhibit a chaotic behaviour (not shown for the sake of brevity).

8.4 Discussion

As made evident by the descriptions reported in the earlier section, the problem of transition in a viscoelastic fluid layer supporting Marangoni stresses is rich, and several issues contribute to make it more involved. In the present section an attempt is made to shed some additional light on these dynamics through an interesting analogy with other phenomena and adequate consideration of the dominant theories available in the literature for the interpretation of fluid phenomena with elasticity.

In particular, in the endeavour to meet these objectives, the discussion is articulated along two different threads, namely, first, the interconnections between the dimensionality of the disturbances and the observed sequence of bifurcations will be considered and, second, how their specific nature also contributes to determine the progression towards chaos will be analysed.

8.4.1 Spatial and Physical Nature of the observed disturbances

In this subsection, the details of "how" and "when" disturbances which are intrinsically 2D or 3D in nature are excited, compete and eventually cause the onset of turbulence, are the main subject of discussion. In order to do so, let us initially transcend the specific nature of the mechanisms causing instability and focus on purely spatial aspects, i.e. the different orientation of the recognizable multi-cellular structures produced in both 2D and 3D as the elasticity parameter is increased. In this regard, let us rely on a "similarity approach", that is, some arguments are developed in the light of the similar dynamics which have been observed in a companion category of phenomena, namely, the instabilities of buoyancy (gravitational convection) in differentially heated (along the horizontal direction) liquid metals. This subject, also known as the Hadley flow problem, has attracted much attention over the last decades, resulting in a variety of well-established results.

For relatively small values of the temperature difference, the Hadley flow displays a basic state that is very similar to that of Marangoni convection, i.e. a horizontally elongated single circulation extending between the hot and cold sides of the fluid container. As the control parameter is increased, it can support disturbances with transverse and/or longitudinal orientation just like those described in section 8.3.

In other words, an effort is made here towards the identification of classes of "universality" that do not depend on the inertial or viscoelastic nature of the considered problem, which however may help to explain the present findings or provide useful hints or clues. This is the reason why in the following some relevant historical details about this specific category of buoyant flow are briefly recalled (see also section 1.1.2).

In this regard it is certainly worth starting from the simple remark that Hart [38] was the first to assess the response of differentially heated liquid metals to fluid-dynamic disturbances having a transverse or longitudinal orientation. Later, Gill [40] examined in more detail the second category of disturbances. Taken together, these initial investigations provided relevant information about the expected patterning behaviour and the mechanisms responsible for the excitation of these perturbations. It was shown that

while in the first case (transverse disturbances) 2D circulations appear close to the inflection point of the basic velocity profile (such perturbation rolls therefore develop in a direction perpendicular to the basic flow), in the latter case, the axes of the rolls emerging as a result of the instability are parallel to the basic flow.

Put simply, the longitudinal rolls emerging in liquid metals combine with the basic unicellular flow typical of the Hadley convection thereby forcing the fluid parcels to describe helical paths in space. For the sake of completeness, it is also worth mentioning that, as yet shown by these landmark studies, while the instability leading to transverse rolls is driven by the mean shear stress (this is the reason why it is often referred to as "shear instability" and the related disturbances as hydrodynamic), the longitudinal rolls are made possible by the dynamical coupling between the mean shear stress and the buoyancy force, i.e. thermal effects directly contribute to the instability mechanism, from which the denomination of "hydrothermal disturbances".

Subsequent instructive efforts appearing in the literature have clarified that these modes of convection are not mutually exclusive, nor are they progressive and that the development of turbulence via a hierarchy of instabilities can involve a rich variety of concurrent paths or lines of evolution. Although a plethora of studies have been conducted on these specific aspects, here it is convenient referring to the works by Lappa & Ferialdi, because in those analyses the dynamics for a small value of the Prandtl number ($Pr = 0.01$) were investigated with and without the constraint of 2D flow, Refs. [220] and [221] respectively (thereby following an approach similar to that undertaken in the present work).

Given these premises, the sought similitude with the phenomena presented in section 8.3 can therefore be introduced as follows: 1) in Ref. [220] 2D disturbances were manifesting as waves traveling in the fluid from the hot side towards the cold one, 2) 3D disturbances spontaneously produced by the numerical simulations [221] were causing a sudden transition to relatively chaotic fully three-dimensional states for values of the controlling parameter (the Rayleigh number) smaller than those needed to excite regular (time-periodic) streamwise waves in the 2D case. The latter perturbations were clearly displaying a 3D nature as witnessed by the presence of recognizable velocity

peaks along the third direction and spatially extended vortices along the spanwise direction. Through numerical experiments based on the use of different initial conditions, it was concluded that in 3D the spatially pervasive presence of one mode of convection does not prevent the system from developing in parallel disturbances pertaining to the other category and vice versa, thereby leading to "hybrid states", which can deeply influence the path of progression towards chaos [221].

Using this knowledge as an interpretation key, it is easy to recognize that the phenomena described in section 8.3 obey very similar dynamics. In facts, critical comparison of Figure 8.9 with the equivalent 2D findings clearly indicates that the longitudinal modes enabled in the viscoelastic Marangoni flow have a critical threshold much smaller than the companion 2D elastic waves (as witnessed by the lack of these in Figure 8.9 and the stable unicellular flow obtained for similar conditions in 2D). A critical analysis of Figure 8.10 is also extremely instructive as it leads to the remarkable conclusion that as soon as a value of the elasticity number close to the ϑ_{cr} predicted through the 2D analysis is exceeded, a sudden variation can be noticed in the 3D results. This change is qualitatively and quantitatively substantiated by the increased number of recognizable features along the streamwise direction in Figure 8.10c and 8.10d. These can be ascribed to the emergence of a train of corrugations or transverse rolls like those visible in Figure 8.3c and 8.3d, respectively (which means that 2D disturbances have been excited and they coexist with the longitudinal ones). The increased spatial complexity of the pattern obviously stems from the helical paths that result from the superposition of transverse and longitudinal convective features.

The increasing role played by the transverse (elastic) waves as the elasticity parameter grows, however, can also be inferred from the temporal behaviour of the dominant disturbance, which (as explained at the end of section 8.3) displays an increased tendency to travel in the downstream (streamwise) direction for larger values of ϑ (Figure 8.10d).

As one may infer yet by building on the companion buoyant phenomena in liquid metals, the coexistence of the two classes of disturbances in viscoelastic Marangoni flow is not limited to purely spatial effects. It has also a remarkable impact on the

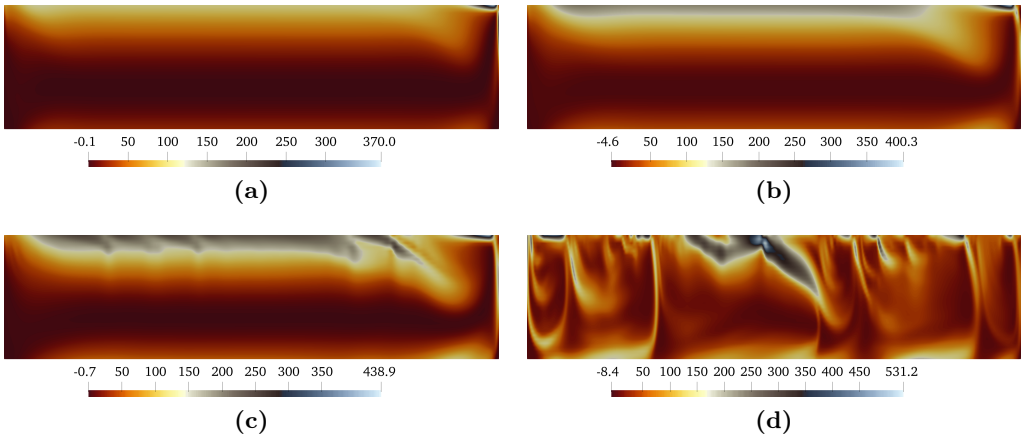

Figure 8.12: 2D viscoelastic thermocapillary flow, trace of the viscoelastic stress tensor $\mathrm{tr}(\tilde{\boldsymbol{\tau}})$ for the case of $Ma = 500$, (a) $\vartheta = 0.1$, (b) $\vartheta = 0.15$, (c) $\vartheta = 0.2$, (d) $\vartheta = 0.4$. The layer is cooled from the left and heated from the right side. For visualisation purposes, the height of the layer is magnified 5x. (a)-(c) depict the final stationary state, (d) reports $\mathrm{tr}(\tilde{\boldsymbol{\tau}})$ at $t = 64.13$.

mechanisms that lead to turbulence; this is clearly witnessed by the smaller value of the elasticity number required in 3D to get an involved frequency spectrum (like those shown in Figure 8.11c and 8.11d). Using arguments analogous to those elaborated by Lappa & Ferialdi [221], a simple way to think about this trend lies in considering the non-linear interplay between perturbations that pertain to different categories.

In other words, just like the collision of two or more limit cycles can lead to the emergence of a strange attractor for the dynamics of buoyant liquid metal flow, independent disturbances (multiple solutions), having frequencies that are not commensurate, can produce a chaotic frequency spectrum in viscoelastic Marangoni flow for relatively small values of the Marangoni and elasticity numbers [135] (refer to section 8.4.2 for additional arguments about the turbulence observed in the present study).

Remarkably, the classes of universality identifiable through this analogy can be pursued even further. Additional comparison of the dynamics investigated in Refs. [220, 221] and the present ones, indeed, indicates that in both cases the 2D disturbances do not depend on the properties of the temperature field. The latter serves only as a driver to produce the physical effect required to put the fluid in motion (the buoyancy force for

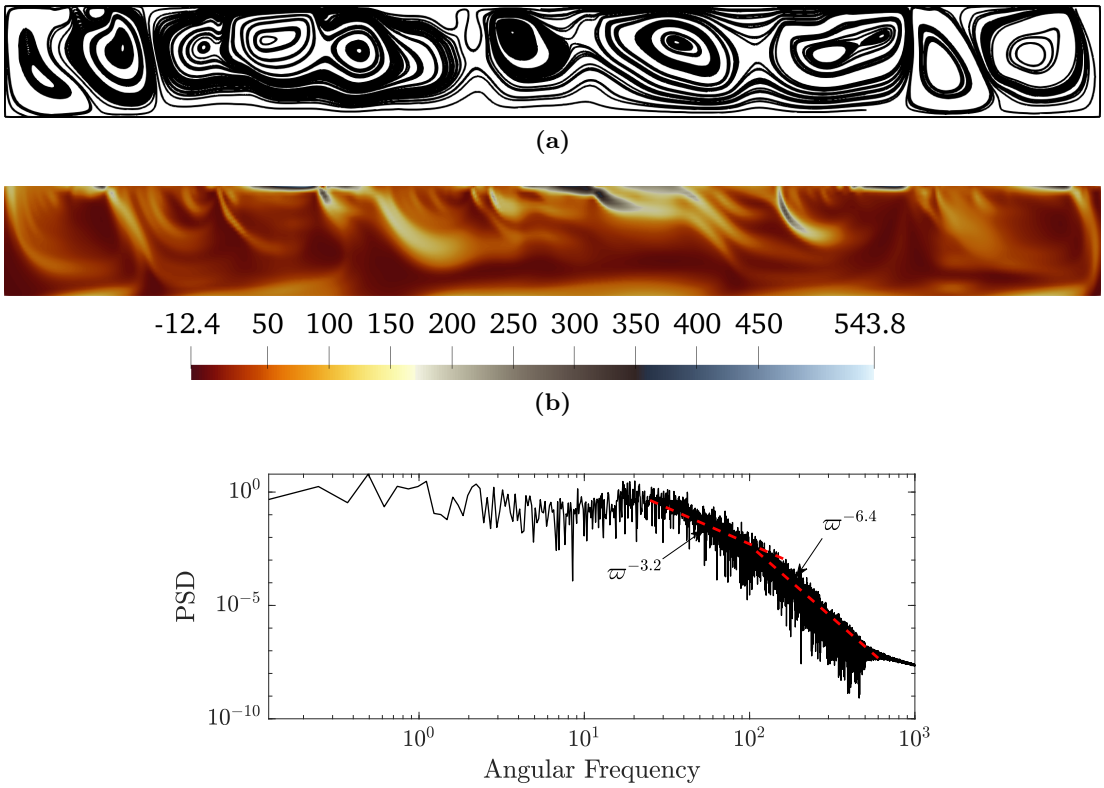

Figure 8.13: 2D viscoelastic thermocapillary flow forming for a frozen (decoupled) temperature field. Viscoelastic fluid with $Ma = 500$ and $\vartheta = 0.4$. (a) Streamlines and (b) trace of the viscoelastic stress tensor $\mathrm{tr}(\tilde{\boldsymbol{\tau}})$ at $t = 38.26$, and (c) spectrum of the y component of the velocity signal probed in the centre of the layer. The layer is cooled from the left and heated from the right side. For visualisation purposes, the height of the layer is not to scale (magnified by 2x).

the liquid metals and the thermocapillary stresses in the present case). In other words, thermal effects do not play an active role in the instability mechanism.

As witnessed by the distribution of elastic energy in Figure 8.12, the main physical process underpinning the instability in the present case is the interaction between the streamline curvature and the elastic stresses due to the stretching of polymer molecules.

The purely elastic nature of the hierarchy of bifurcations responsible for the onset of chaos in these cases is also indirectly demonstrated by the additional results obtained by repeating the 2D simulations after freezing the temperature field in a configuration corresponding to the basic steady state. In this regard, Figure 8.13 clearly shows, that although thermal disturbances are filtered out, instabilities can still occur and produce

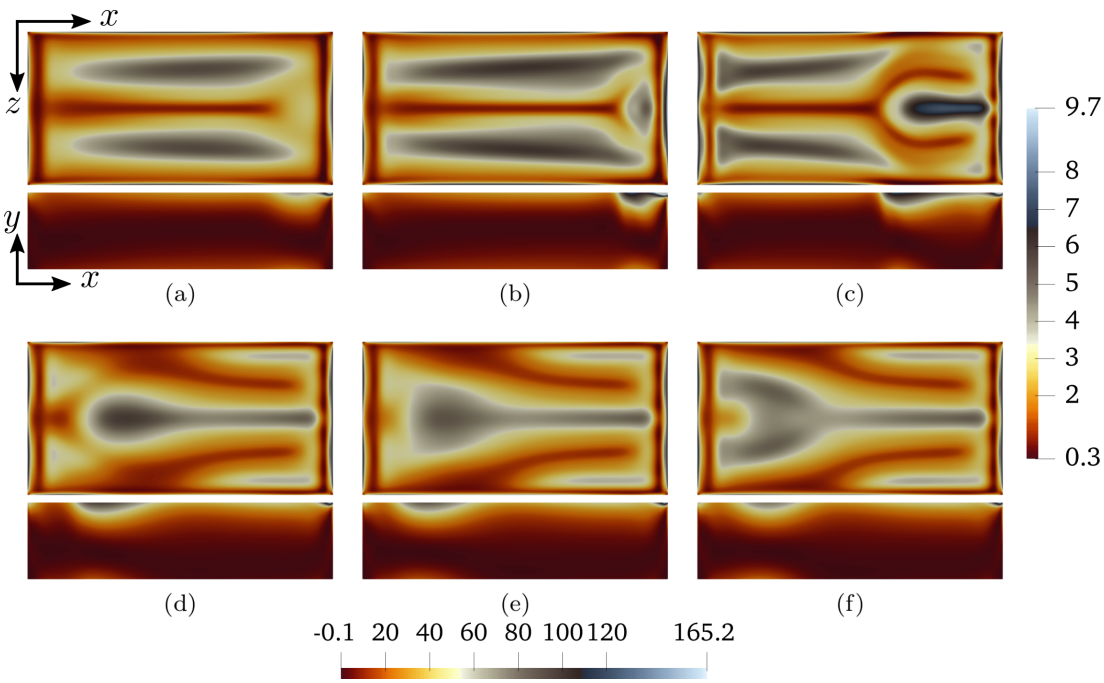

Figure 8.14: Thermocapillary convection in viscoelastic fluid, $Ma = 500$ and $\vartheta = 0.03$. Contour plot of trace of the viscoelastic stress tensor $\mathrm{tr}(\tilde{\boldsymbol{\tau}})$ at $y = 0.5$ for the xz-plane (vertical color-bar) and $z = 5$ for the xy-plane (horizontal color-bar). For visualisation purposes, the height of the layer (y direction) is not to scale (magnified 5x). The layer is cooled from the left and heated from the right. (a) $t = 4.59$, (b) $t = 5.5$, (c) $t = 11.22$, (d) $t = 19.13$, (e) $t = 20.28$, and (f) $t = 21.30$.

a chaotic state with properties similar to those obtained in the fully coupled case. Remarkably, this may be regarded as an additional feature supporting the parallelism between the 2D hydrodynamic and elastic disturbances developed here.

Additional insights into the affinity between the two distinct categories of flows stem naturally from a comparison of Figure 8.12 and Figure 8.14.

Unlike the two-dimensional ones, the longitudinal disturbances emerging in viscoelastic Marangoni flow draw energy from thermal effects, as made evident by the spatial correlation of the elastic energy with the temperature field in the xz-plane (and with the surface stresses in the xy-plane). A more rigorous verification of this physical connection can be gained once again by decoupling the velocity and temperature fields, the reader being referred to the outcomes of the related 3D simulations shown in Figure 8.15. The two-dimensional nature of the emerging flow and its structure (a single slightly corrugated cell) is instrumental in proving that, like the longitudinal

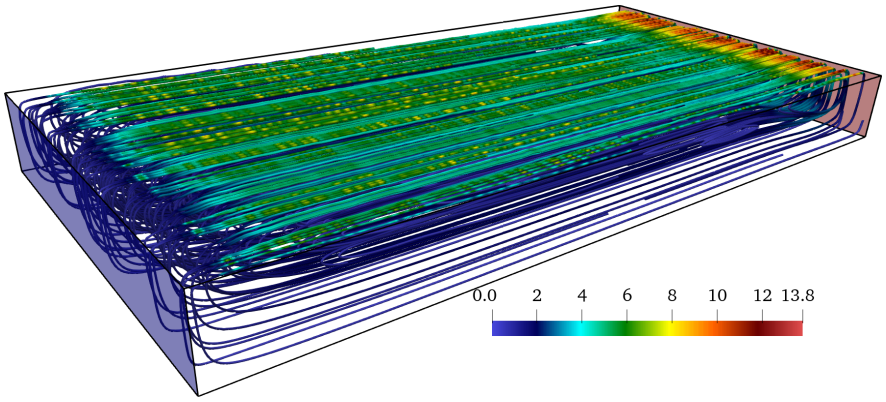

Figure 8.15: 3D single cell in viscoelastic thermocapillary flow forming for a frozen (decoupled) temperature field. Viscoelastic fluid with $Ma = 500$ and $\vartheta = 0.2$. The streamlines are colored with the magnitude of the velocity field. The layer is cooled from the left and heated from the right.

modes of buoyancy convection in liquid metals require a dynamical coupling between the mean shear stress and the buoyancy force (a dynamical balance between the inertial and gravitational forces that makes the role played by the thermal effects significant in the instability mechanism), the equivalent longitudinal modes in viscoelastic Marangoni flow rely on a similar coupling between the elastic and the thermocapillary forces.

8.4.2 Elastic turbulence

Still pursuing the parallelism introduced in section 8.4.1, let us now concentrate on the differences, i.e on those aspects which set elastic turbulence apart from the corresponding phenomena obtained when the fluid has no elastic properties.

In particular, in order to clarify the distinguishing marks, first let us consider again the case of turbulence in buoyant liquid metals (Newtonian fluids for which the concepts related to the so-called inertial turbulence apply), and then move to the viscoelastic case, still invoking the relevant literature and introducing additional levels of complexity as required.

As developed in the following, the interpretations for these two types of turbulence involve two types of relations, namely that between inertial and dissipation effects in Newtonian fluids and that between polymer molecule deformation and fluid flow in viscoelastic fluids. The former is well-known and, indeed, the underlying theory dates

back to the seminal works by Kolmogorov, who theorized the existence of a hierarchy of scales through which the kinetic energy flowing in the system per unit time is balanced precisely by the amount of energy dissipated per unit time (while energy cascades at a constant dissipation rate from macroscopic phenomena towards smaller scales [222, 223]).

Using these concepts, this author elaborated a very interesting picture of turbulence by arguing that in the chaotic scale-reduction mechanism, at a certain distance from the largest scale, the macroscopic directional biases are lost allowing therefore turbulence to become homogeneous and isotropic, i.e. direction-independent. This is equivalent to stating that in the chaotic scale-reduction mechanism, at a certain stage the flux of the cascading quantity across any scale becomes a function only of dynamic variables on that scale, which allows the energy spectrum to take a universal behaviour (this being $\mathcal{P}(\varpi) \propto \varpi^{-5/3}$ in the case of inertial turbulence, where the fixed exponent $-5/3$ accounts for the universal dependence of the energy on the "local", i.e. scale-dependent, wavenumber or frequency, [224]).

Although these concepts have been found to describe properly the known properties of turbulence on relatively small scales (in the so-called "inertial range") for several Newtonian flows (including the liquid metals discussed before and examined by Ref. [221] for the case of competing transverse and longitudinal disturbances), however, they cannot be used to describe elastic turbulence in viscoelastic fluids (see, e.g., Refs. [103, 225–228]).

As also confirmed by the present results for Marangoni flow, elastic turbulence does not depend on the Reynolds number or on equivalent non-dimensional groups. Rather chaos is enabled on increasing the elasticity (non-dimensional) parameter, which in turn is directly proportional to the relaxation time λ. The latter accounts for the ability of viscoelastic stresses to survive (unlike viscous stresses) in the limit as the fluid approaches a motionless state. This is actually the mechanism by which initial disturbances can lead to the onset of turbulence. These can produce polymer molecules stretching, the deformation of the molecules can cause secondary flows which further stretch the mo-

lecules, thereby allowing the amplification of an initial small disturbance through an iterative cause-and-effect coupling mechanism [226, 229].

As implicitly revealed by these arguments, one should therefore expect the evolution of turbulence not to be determined by the assumption of local balance between small scale (in the inertial range) energy production and dissipation, rather to be somehow controlled by the alternate equilibrium between kinetic energy and elastic energy (the energy cascading from the injection scale and dissipating due to polymer relaxation). This is indeed the rationale of various theories elaborated more recently, where, using these arguments, it has been found (see, e.g. Ref [230, 231]) that the velocity spectrum $\mathcal{P}(\varpi)$ should decay faster than ϖ^{-3} (which is in agreement with available experiments [229] and the present results).

In order to put the present results for viscoelastic flow in perspective, it is therefore worth referring to this category of studies and, in particular, the very recent work by Gupta et al. [232], where although the analysis was conducted under the constraint of two-dimensionality, a kind of flow that displays a remarkable affinity with Marangoni convection was considered, i.e. fluid motion inside a lid driven cavity.

For a fluid Prandtl number equal to that considered in the present work, Gupta et al. [232] observed an interesting dependence of the fitted values of the power-law exponent on the considered Reynolds number. Indeed, the exponent was found to be -3.18 in many situations. It is also worth recalling that the so-called elasto-inertial turbulence is expected to display a $-14/3$ scaling, which is far from the Kolmogorov scaling of $-5/3$ typical of inertial turbulence, but relatively close to the -3.5 scaling observed for purely elastic turbulence (see, e.g., Refs. [124, 151, 233–236]).

Although in the frame of the present study turbulence satisfying the $-14/3$ scaling was not observed, as a concluding remark, it is worth highlighting that, apparently, regions exist in the considered fluid layer where the typical behaviour of inertial turbulence is recovered. In particular, as evident in Figure 8.16, this happens in proximity to the free surface where the driving force is located and velocity attains its highest magnitude.

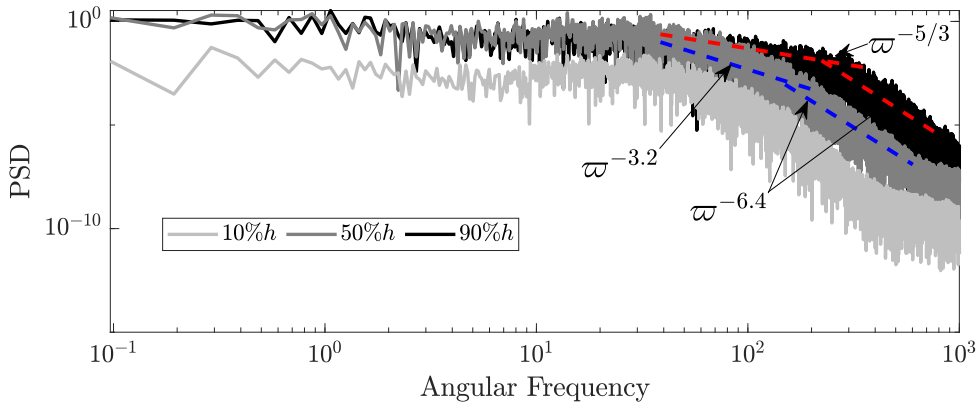

(a)

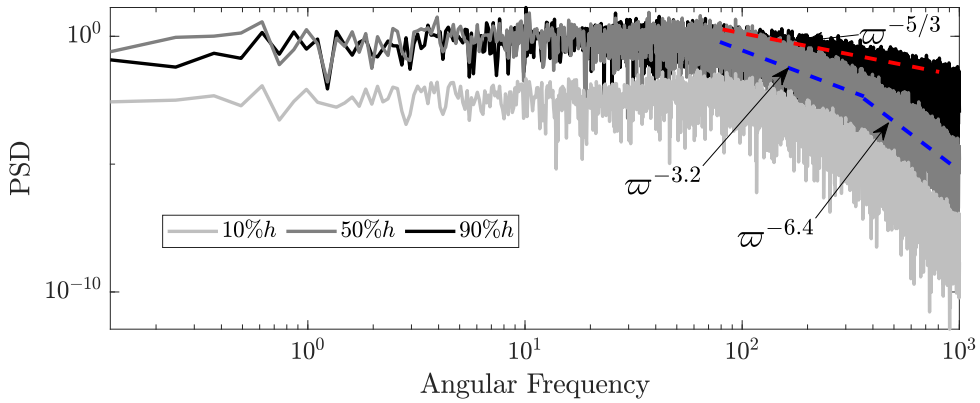

(b)

Figure 8.16: 2D viscoelastic thermocapillary flow, spectra of the y component of the velocity signal probed in the proximity to the free surface for (a) $Ma = 500$ and $\vartheta = 0.4$, (b) $Ma = 2500$ and $\vartheta = 6.5 \times 10^{-2}$.

As one may expect on the basis of simple ("heuristic") considerations, the interval of frequencies over which the behaviour is well described by the Kolmogorov exponent grows in the situation with the larger value of the Marangoni number. In both cases, however, the Kolmogorov scaling shows up only over a distance (starting from the free surface) corresponding to approximately one quarter of the total fluid layer depth. More precisely, while for $Ma = 500$ the change in the exponent (from the ≈ -3.2 typical of the bulk to $-5/3$) occurs at 20%, for $Ma = 2500$ a more complex behaviour is obtained with the exponent taking the values ≈ -3.2 for $y \leq 0.75$, ≈ -2.5 for $y = 0.8$, $\approx -5/3$ for $y = 0.85$ and ≈ -1.1 for $y = 1$.

8.5 Conclusions

The emerging properties of Marangoni convection in a layer of viscoelastic fluid have been investigated numerically to draw some general conclusions about the behaviour of this category of flows in the non-linear regime (i.e. after the disturbances have saturated their amplitude). It has been found that the elasticity of the fluid causes a remarkable decrease in the value of the Marangoni number required to excite oscillatory flow (i.e. a Hopf bifurcation) regardless of the problem dimensionality (i.e. regardless of whether the flow is constrained to retain a two-dimensional behaviour or not). This is reminiscent of the corresponding "overstable" phenomena in the companion category of Marangoni-Bénard flows.

The patterning behaviour in the fully 3D case is driven by the interplay of two distinct categories of perturbations, which can be distinguished according to the space orientation of the emerging convective structures and the nature of the mechanisms feeding them. These can be classified accordingly as transverse or longitudinal modes of convection. The former show up as transverse waves that travel in the same direction of the imposed temperature difference (in the downstream direction, as opposed to the upstream propagation sense of classical hydrothermal waves) and owe their existence to a purely elastic instability induced by the curvature of the streamlines. By contrast, the latter rely on the coupling between the temperature field and elastic effects established through the balance of stresses at the free interface. These manifest themselves as longitudinal rolls that combine with the basic unicellular flow typical of the Marangoni convection, thereby forcing the fluid parcels to describe helical paths in space.

Building on an interesting parallelism between the typical hierarchy of bifurcations of buoyant convection (the Hadley flow) in liquid metals and that of Marangoni flow in viscoelastic liquids, it has been shown that in both cases, on increasing the magnitude of the driving force, longitudinal disturbances are selected first and then transverse perturbations are excited and coexist with the longitudinal ones. This results in a set of independent convective modes that can produced turbulence through non-linear interaction.

Entering the turbulent regime, however, does not require necessarily an increase in the intensity of the driving force (the Marangoni number). For a fixed magnitude of the driving force, chaos can also be excited by increasing the level of elasticity. Accordingly, the emerging non-linear states display the typical properties of elastic turbulence as witnessed by the scaling laws and the related exponent ≈ -3.2 recognizable in the frequency spectrum (as opposed to the $-5/3$ exponent typical of inertial turbulence).

As shown by the present simulations, however, these two forms of turbulence are not mutually exclusive. These can coexists and cause a gradual transition in the aforementioned exponent along a direction perpendicular to the free interface, which indicates that the dichotomy often drawn between the related physical mechanisms should not be taken in a strict sense when dealing with viscoelastic Marangoni flow in non creeping conditions.

In the following conclusive chapter, the author will recall the fundamental discoveries of this PhD project and will propose exciting future developments of the subject.

Chapter 9

Conclusions & Future Work

In this conclusive chapter, let us retrace the outcomes of this thesis before giving some exciting ideas for the future development of this project.

Chapter 4 studied the problem of a 2D square cavity differentially heated, vibrated in a direction orthogonal to the temperature gradient, and placed in microgravity. There, the main differences between Newtonian and viscoelastic thermovibrational flow were highlighted. For the Newtonian case, the set of possible solutions is relatively simple. Indeed, the flow "jumps" from an inversional to a quadrupolar pattern for a wide range of the control parameter. By increasing the Gershuni number, the number of convective rolls increases up to a total of 8. Nonetheless, the flow remains symmetric.

The situation is considerably different in the case of viscoelastic liquids, where a zoo of possible convection modes manifests itself over a relatively small range of Gs. These modes progressively lose their symmetry as Gs is raised, revealing complex and not straightforward multicellular states. Notably, the complexity in the patterning behaviour is accompanied by a non-monotonic response of the flow field's amplitude and frequency when the elasticity of the fluid is increased. This behaviour is reminiscent of the interplay between vibrations and the natural resonances and anti-resonances that typically affect elastic systems.

An exciting prospect for the future is to investigate the corresponding dynamics for the case where the constraint of two-dimensionality is removed. While for standard (constant gravity) buoyancy convection in the Newtonian case (Refs. [237–240]), 3D effects have been shown to be limited to viscosity-induced phenomena in thin regions located in proximity to the side-walls perpendicular to the spanwise direction, there is no guarantee that a similar concept would apply to the viscoelastic case.

Continuing with the analysis of thermovibrational convection in finite cavities, Chapter 5 studied the companion parallel configuration, where the vibrations act along the direction of the temperature gradient. Here, it was shown that the critical threshold for the onset of convection does not necessarily decrease when a more elastic fluid is considered , which might still be ascribed to the non-linear interactions between the elasticity of the fluid and the vibrations and related resonances and anti-resonances effects. The flow that emerges after the first bifurcation has subharmonic spatio-temporal dynamics, while the frequency of the vibrations selects the principal patterning configuration. Interestingly, for a sub-range of the space of the parameters, and intermittent state, in which a long period disturbance interacts with the sub-harmonic dynamics was found.

The physical constraint represented by the sidewalls of the cavity have been removed in the next chapter (Chapter 6) where, in place of a compact geometry, an infinite layer has been considered. It has been shown that although the domain is physically unbounded and 3D disturbances are allowed, viscoelastic effects still play a fundamental role in influencing the emerging dynamics with respect to the companion Newtonian fluid case . It was proven that convective flows could be exited in a range of the control parameter (the vibrational Rayleigh number) that is one order of magnitude smaller when compared to a non-elastic fluid. When this critical threshold is crossed, the flow field exhibits synchronous response if the medium is Newtonian, while the dynamics become half-subharmonic in the viscoelastic case. Most interestingly, an increase in the elasticity of the fluid lead to the onset of superlattice structures typical of complex order. It has shown that the elastic energy stored in the molecule during the destabilising period of vibrations plays a fundamental role in forming these patterns.

Although this study employed sinusoidal waves, all the results available in the literature are LSA employing pulse (or square) vibrational waves. Therefore, as a natural continuation of this chapter, the case where the imposed forcing does not follow a sinusoidal law has been considered.

Regardless of the shape of the vibrations, a subharmonic pattern emerges. For sinusoidal vibration, superlattice patterns in the form of *roll superlattices* are the main

convective modes. Instead, when pulse waves excite the layer, a coexistence between the breaking-roll mechanism (typical of viscoelastic Rayleigh-Bénard convection) and less ordered structures will manifest as the preferred convective mechanism.

For what concerns the study of the pulse waves, an exciting prospect for the future is also to investigate the vibrationally modulated problem for additional (non-unit) values of the parameter Σ, for which the relaxation time of the polymer molecules is smaller or larger than the period of the forcing. This factor is also expected to contribute significantly to the number of modes that can be excited in the fluid and alter the mechanisms depicted earlier, thereby influencing the emerging patterning behaviour.

Eventually, Chapter 8 analysed Marangoni convection in a 3D finite layer of Oldroyd-B fluid. Similarly to the case of classical Rayleigh-Bénard and Marangoni-Bénard convection, and in analogy with the work presented so far in the framework of thermovibrational flows, even for the case of Marangoni flow, the initial unicellular convective roll undergoes a Hopf bifurcation for values of the Marangoni number that are smaller than the ones for Newtonian fluids. Similarly to the cases analysed in the framework of thermovibrational convection, this can be seen as a manifestation of overstability.

More interestingly, if the flow is allowed to develop in the third dimension, in accordance with the prediction of the LSA, transverse (mainly driven by the fluid's elasticity) and longitudinal (driven by hydrothermal disturbances) modes emerge. The fluid's elasticity enables these modes to coexist and interact, creating unforeseen and fascinating dynamics. It has also been shown that the coexistence of these two modes can excite chaotic motion in certain regions of the space of parameters. Interestingly, the emerging chaos is excited by increasing the elasticity of the fluid, and accordingly, the energy spectrum of the flow field does not follow the Kolmogorov scale (that characterises inertial turbulence), but instead, it displays dynamics that are typical of elastic turbulence.

An exciting prospect for the future is the generalisation of these findings to other configurations, which have enjoyed widespread use in the literature to investigate the

fundamental properties of Marangoni convection, such as the liquid bridge or the classical annular pool used to mimic the CZ crystal growth process.

As a concluding remark for this thesis, it is worth recalling, that apart from filling a gap in the literature (results for thermovibrational flow and Marangoni convection in viscoelastic fluids are very rare or do not exist), all the findings presented in this thesis have been produced to support the lines of inquiry represented by the so-called T-Paola [47–49, 241] and jeremi (Japanese European Research Experiments on Marangoni Instabilities) [242–245] space projects, supported by both ESA and the UK Space Agency. These projects deal with thermovibrational flows and Marangoni convection in Newtonian liquids with dispersed solid particles. It is known that the interaction of such solid particles with time-dependent vibrational or Marangoni flow can produce fascinating particle self-organisation phenomena. An exciting prospect for the future is a continuation or extension of such a research by considering fluids that display a viscoelastic behaviour. The increased variety of flow bifurcations and possible patterning behaviours may indeed lead to the identification of new mechanisms for particle self-assembly and stimulate a new line of research for the elaboration of adequate mathematical models. Current models for solid particle tracking in fluid flow are indeed limited to the case of Newtonian fluids. Although some authors have started to deal with this problem, see e.g., Ref [246], which by coupling rheoTool with a DEM (Discrete Element Method) package called LIGGGHTS in the framework of the open-source project *CFDEMcoupling* and using an immersed boundary technique found promising results, much work is still required in this specific area.

Apart from the interest in multi-face flows that naturally arise in the context of the T-Paola project, this author would like to propose another promising application of microgravity experiments in the context of viscoelastic convection.

In Chapter 1 the experiment by Kolodner was presented as one of the few works dealing with thermogravitational convection. However, in the scientific community, there is still disagreement about the nature of the convective flow found in that experimental study. Indeed, recalling that, in general, viscoelastic fluids are binary solutions, some scientists wonder whether the so-called Soret effect could have played an important

role in the migration of the chain of DNA employed in the experiment [127]. In this regard, an experiment in microgravity would allow disentangling convective and diffusive effects, giving closure to a problem that has divided the scientific community for almost two decades. Here, it is worth mentioning the work by Shevtsova et al. [247, 248], where, through another experiment onboard the ISS, they assessed the influence of vibrations on the thermodiffusion process. Starting from these premisses, a new and exciting space-based investigation involving fluids that display a viscoelastic behaviour could be developed.

To conclude, the field of viscoelastic thermally-driven flows in microgravity is still at an early stage. This work should be regarded as a first attempt to discover new fascinating phenomena that this class of flows can exhibit, but also as an inspiration to answer new (and old) questions about a category of complex fluids that has not been extensively investigated yet.

Part III

Appendices

Appendix A

Microscopic Derivation of the Oldroyd-B Model

To derive the equations for the *Oldroyd–B* model a linear spring is considered. The stiffness of a molecule can be evaluated on the basis of thermodynamic forces as [147]:

$$\kappa = \frac{3k_BT}{a^2} \tag{A.1}$$

where k_B is the *Boltzmann constant*. This quantity is directly related to the entropy of the polymeric chain. Therefore, accounting for eq. (2.58), eq. (2.62) becomes:

$$\tilde{\boldsymbol{\tau}}(t) = -\frac{3k_BT}{a^2}\sum_{i=1}^{N_p}\langle \mathbf{q}_j\mathbf{q}_j\delta(\mathbf{x}-\mathbf{x}_{\mathrm{cm},j})\rangle \tag{A.2}$$

It is straightforward to observe that the polymeric stress changes in time and depends not only on the velocity of the surrounding solvent, but also on the average level of deformation of the springs dispersed in the Newtonian fluid matrix. Therefore, tracking the global rate of change in polymeric deformation level seems necessary. This operation will lead to an additional equation that will be solved along with the balance equations introduced for Newtonian fluids.

Let us start by observing that the inertial forces can be neglected since the dimension of the dumbbell and its speed are small ($m_i\frac{d^2\mathbf{x}_i(t)}{dt^2} = \mathbf{0}$). Furthermore, in first approximation, the term accounting for the Brownian motion $\mathbf{F}_{B,i}$ can be neglected from eq. (2.55).

Considering eqs. (2.56), (2.58), and (A.1), the balance of force (Newton's second law) for the i-th bead of the dumbbell reads:

$$\pm\frac{3k_BT}{a^2}\mathbf{q}(t) + 6\pi\eta_s a\left[\mathbf{u}(\mathbf{x}_i(t)) - \frac{d\mathbf{x}_i(t)}{dt}\right] = \mathbf{0} \tag{A.3}$$

which implies that the velocity of the i-th bead can be calculated as:

$$\frac{d\mathbf{x}_i(t)}{dt} = \pm\frac{k_BT}{2\pi\eta_s a^3}\mathbf{q}(t) + \mathbf{u}(\mathbf{x}_i(t)) \tag{A.4}$$

Moreover, assuming that if $i = 1$, the elastic force is considered to be positive, the velocity of the first bead is:

$$\frac{d\mathbf{x}_1(t)}{dt} = \frac{k_BT}{2\pi\eta_s a^3}\mathbf{q}(t) + \mathbf{u}(\mathbf{x}_1(t)) \tag{A.5}$$

while, considering that $\mathbf{x}_2 = \mathbf{x}_1 + \mathbf{q}$, and that if $i = 2$, the elastic force is considered to be negative, the velocity of the second bead can be written as

$$\frac{d\mathbf{x}_2(t)}{dt} = \frac{d\mathbf{x}_1(t)}{dt} + \frac{d\mathbf{q}(t)}{dt} = -\frac{k_BT}{2\pi\eta_s a^3}\mathbf{q}(t) + \mathbf{u}[\mathbf{x}_1(t) + \mathbf{q}(t)] \tag{A.6}$$

Subtracting eq. (A.5) from eq. (A.6), the rate of change of molecule deformation reads:

$$\frac{d\mathbf{q}(t)}{dt} = -\frac{k_BT}{\pi\eta_s a^3}\mathbf{q}(t) + \mathbf{u}[\mathbf{x}_1(t) + \mathbf{q}(t)] - \mathbf{u}(\mathbf{x}_1(t)) \tag{A.7}$$

Let us observe that $\mathbf{q}(t)$ and $\mathbf{u}(\mathbf{x}_1)$, change over two different scales, namely microscopic and macroscopic scales respectively. Therefore, $\mathbf{u}[\mathbf{x}_1(t) + \mathbf{q}(t)]$ can be developed in a Taylor-Maclaurin series. Considering only the first order terms, the rate of change of $\mathbf{q}(t)$ reads:

$$\frac{d\mathbf{q}(t)}{dt} = -\frac{k_BT}{\pi\eta_s a^3}\mathbf{q}(t) + \boldsymbol{\nabla}\mathbf{u}(\mathbf{x}_1(t)) \cdot \mathbf{q}(t) \tag{A.8}$$

We can now define a new quantity, that is the *relaxation time* λ as:

$$\lambda = \frac{\pi\eta_s a^3}{2k_bT} \tag{A.9}$$

The relaxation time represents the characteristic time of the spring interlinking the beads. Eq. (A.8) simplifies to:

$$\frac{d\mathbf{q}(t)}{dt} = -\frac{1}{2\lambda}\mathbf{q}(t) + \boldsymbol{\nabla}\mathbf{u}(\mathbf{x}_1(t)) \cdot \mathbf{q}(t)) \tag{A.10}$$

and adding back the 3D Brownian motion, eq. (A.10) becomes:

$$d\mathbf{q}(t) = \left[-\frac{1}{2\lambda}\mathbf{q}(t) + \boldsymbol{\nabla}\mathbf{u}(\mathbf{x}_1(t)) \cdot \mathbf{q}(t)) \right] dt + \frac{1}{\sqrt{\lambda}} d\mathbf{B}(t) \tag{A.11}$$

where the constant $\lambda^{-1/2}$ was chosen as coefficient of the Brownian motion since it leads to a dumbbell with a unitary length in stationary conditions.

Let us consider a new quantity, related to $\tilde{\boldsymbol{\tau}}(t)$, that is the so-called *conformation tensor*[104]:

$$\mathbf{A}(\mathbf{x}, t) := \frac{1}{q_{\text{eq}}^2} \left\langle \sum_{j=1}^{N_p} \mathbf{q}_j \mathbf{q}_j \right\rangle \tag{A.12}$$

where $q_{\text{eq}}^2 = \left\langle \sum_{j=1}^{N_p} \mathbf{q}_j \mathbf{q}_j \right\rangle_{\text{eq}}$ and "eq" indicates that the quantity is considered at the equilibrium (no external force is applied to the dumbbell) implying that, $\mathbf{A} = \mathbf{I}$ when the molecule is relaxed.

Notably, as reported by BIRD et al [147] and remarked by HAMEDUDDIN et al. [149], the conformation tensor is a second-order positive definite tensor that accounts for the polymer deformation history. It is worth highlighting that the positive definitiveness of this tensor is at the root of several numerical techniques for the solution of the viscoelastic balance equations, as will be discussed in CHAPTER 3.

The extra-stress tensor is related to the conformation tensor through the well-known Kramers correlation [150], that for an Oldroyd-B fluid reads:

$$\tilde{\boldsymbol{\tau}}(t) = \frac{\eta_p}{\lambda}(\mathbf{A}(\mathbf{x}, t) - \mathbf{I}) \tag{A.13}$$

Let us differentiate in space and time $\mathbf{A}$, or in other words, let us consider it at $\mathbf{x}+d\mathbf{x}$ and $t+dt$:

$$\mathbf{A}(\mathbf{x}+d\mathbf{x},t+dt)=\frac{1}{q_{\text{eq}}^2}\left\langle\sum_{j=1}^{N_p}(\mathbf{q}_j+d\mathbf{q}_j)(\mathbf{q}_j+d\mathbf{q}_j)\right\rangle \tag{A.14}$$

Using eq. (A.11) it is easy to proof that:

$$\mathbf{A}(\mathbf{x}+d\mathbf{x},t+dt)=\mathbf{A}(\mathbf{x},t)-\frac{1}{\lambda}(\mathbf{A}(\mathbf{x},t)+\mathbf{I})+\mathbf{A}(\mathbf{x},t)\cdot\boldsymbol{\nabla}\mathbf{u}+(\boldsymbol{\nabla}\mathbf{u})^{\intercal}\cdot\mathbf{A}(\mathbf{x},t) \tag{A.15}$$

Moreover, considering that $\mathbf{x}+d\mathbf{x}=\mathbf{x}+\mathbf{u}dt$ the following expansion remains valid:

$$\begin{aligned}\mathbf{A}(\mathbf{x}+d\mathbf{x},t+dt)&=\mathbf{A}(\mathbf{x},t+dt)+\frac{d}{d\mathbf{x}}\mathbf{A}(\mathbf{x},t+dt)d\mathbf{x}\\&=\mathbf{A}(\mathbf{x},t)+\frac{\partial}{\partial t}\mathbf{A}(\mathbf{x},t)dt+\frac{d}{d\mathbf{x}}\mathbf{A}(\mathbf{x},t)d\mathbf{x}+\frac{\partial}{\partial t}(\frac{d}{d\mathbf{x}}\mathbf{A}(\mathbf{x},t))d\mathbf{x}dt\\&=\mathbf{A}(\mathbf{x},t)+\frac{\partial}{\partial t}\mathbf{A}(\mathbf{x},t)dt+\mathbf{u}\cdot\boldsymbol{\nabla}\mathbf{A}(\mathbf{x},t)dt+\cancel{\frac{\partial}{\partial t}(\frac{d}{d\mathbf{x}}\mathbf{A}(\mathbf{x},t))\mathbf{u}(dt)^2}\\&=\mathbf{A}(\mathbf{x},t)+\frac{\partial}{\partial t}\mathbf{A}(\mathbf{x},t)dt+\mathbf{u}\cdot\boldsymbol{\nabla}\mathbf{A}(\mathbf{x},t)dt\end{aligned} \tag{A.16}$$

Therefore, matching eq. (A.15) and eq. (A.16):

$$\frac{\partial}{\partial t}\mathbf{A}(\mathbf{x},t)+\mathbf{u}\cdot\boldsymbol{\nabla}\mathbf{A}(\mathbf{x},t)+\frac{1}{\lambda}(\mathbf{A}(\mathbf{x},t)+\mathbf{I})=\mathbf{A}(\mathbf{x},t)\cdot\boldsymbol{\nabla}\mathbf{u}+(\boldsymbol{\nabla}\mathbf{u})^{\intercal}\cdot\mathbf{A}(\mathbf{x},t) \tag{A.17}$$

This equation describes the evolution in time of $\mathbf{A}(\mathbf{x},t)$.

The balance equation for $\tilde{\boldsymbol{\tau}}(t)$ is simply obtained plugging eq. (A.13) in eq. (A.17), obtaining:

$$\lambda\left(\frac{\partial\tilde{\boldsymbol{\tau}}^*}{\partial t}+\mathbf{u}^*\cdot\boldsymbol{\nabla}\tilde{\boldsymbol{\tau}}^*\right)+\tilde{\boldsymbol{\tau}}^*=\eta_p\Big(\boldsymbol{\nabla}\mathbf{u}^*+(\boldsymbol{\nabla}\mathbf{u}^*)^{\intercal}\Big)+\lambda\Big(\tilde{\boldsymbol{\tau}}^*\cdot\boldsymbol{\nabla}\mathbf{u}^*+(\boldsymbol{\nabla}\mathbf{u}^*)^{\intercal}\cdot\tilde{\boldsymbol{\tau}}^*\Big) \tag{A.18}$$

Along with eqs. (2.14), (2.54) and (2.39), eq. (A.18) can properly describe convective flows in viscoelastic fluid with constant viscosity (Boger fluids).

Appendix B

Enlarged Figures

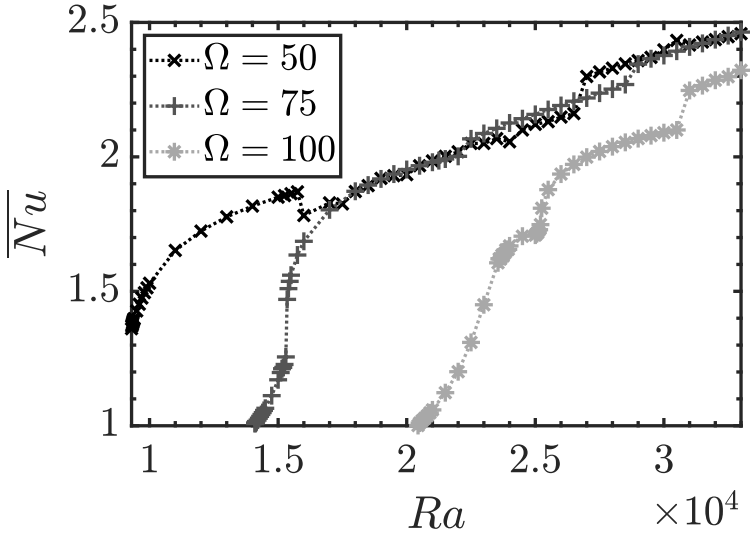
2.5
2
1.5
1
$\overline{Nu}$
$\Omega = 50$
$\Omega = 75$
$\Omega = 100$
1
1.5
2
2.5
3
Ra
$\times 10^4$

(a)

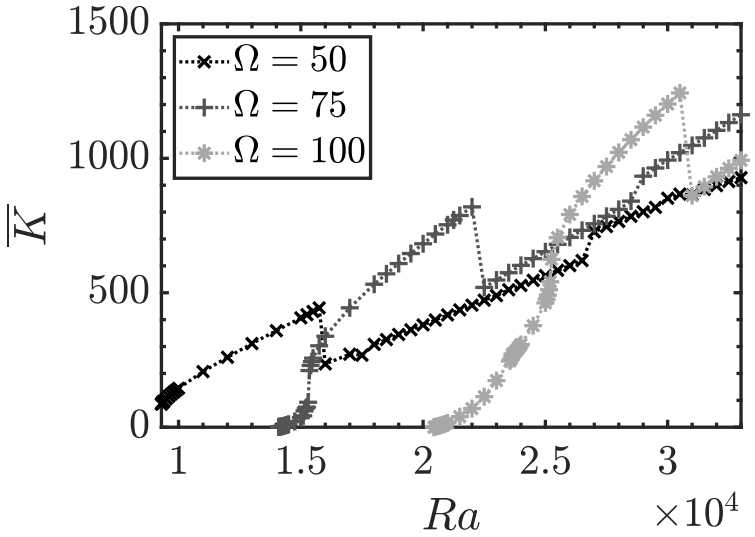
1500
1000
500
0
$\overline{K}$
$\Omega = 50$
$\Omega = 75$
$\Omega = 100$
1
1.5
2
2.5
3
Ra
$\times 10^4$

(b)

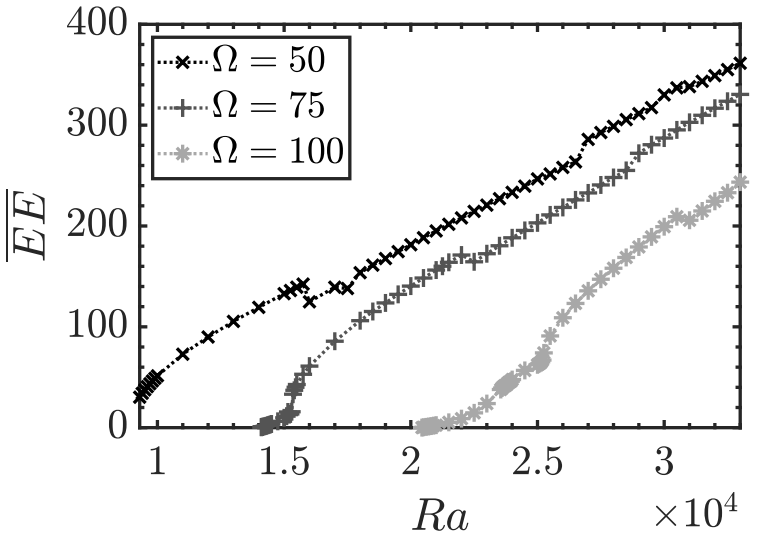
400
300
200
100
0
$\overline{EE}$
$\Omega = 50$
$\Omega = 75$
$\Omega = 100$
1
1.5
2
2.5
3
Ra
$\times 10^4$

(c)

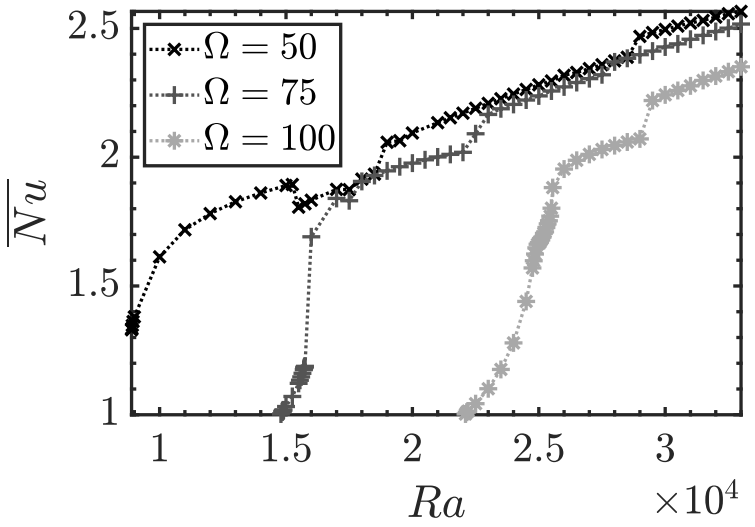
2.5
2
1.5
1
$\overline{Nu}$
$\Omega = 50$
$\Omega = 75$
$\Omega = 100$
1
1.5
2
2.5
3
Ra
$\times 10^4$

(d)

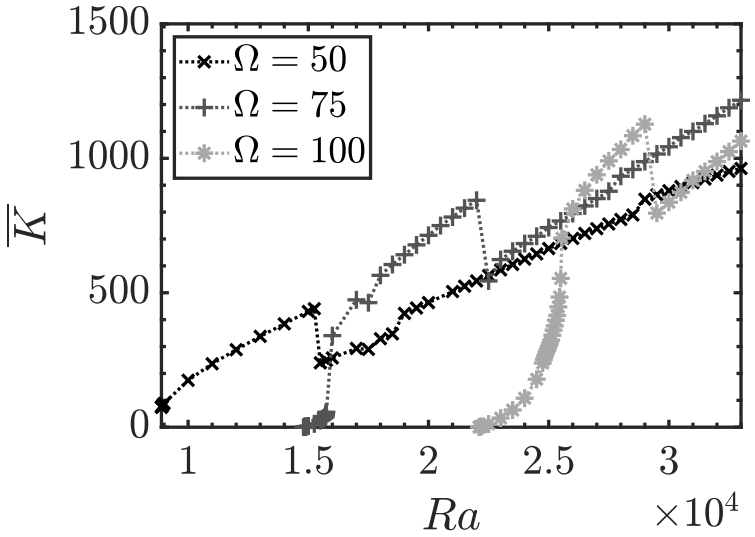
1500
1000
500
0
$\overline{K}$
$\Omega = 50$
$\Omega = 75$
$\Omega = 100$
1
1.5
2
2.5
3
Ra
$\times 10^4$

(e)

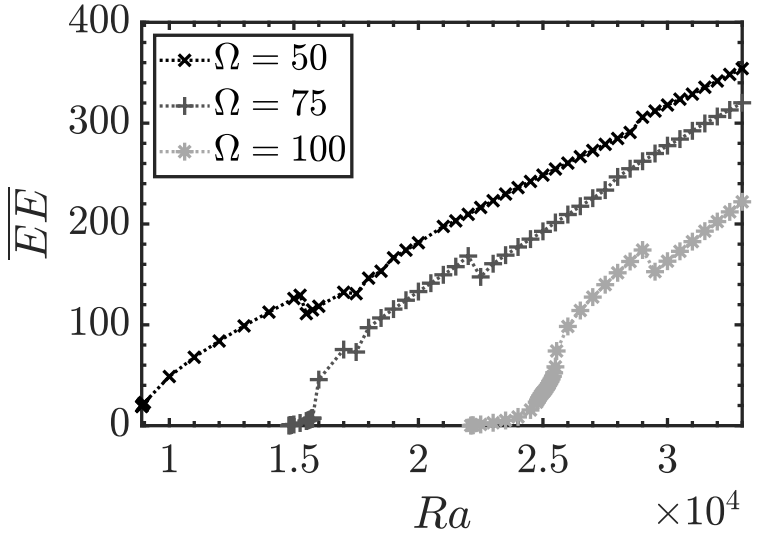
400
300
200
100
0
$\overline{EE}$
$\Omega = 50$
$\Omega = 75$
$\Omega = 100$
1
1.5
2
2.5
3
Ra
$\times 10^4$

(f)

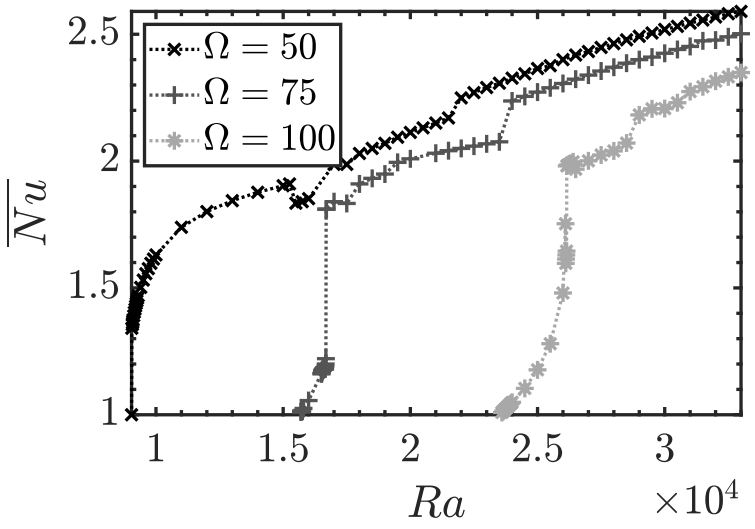

(g)

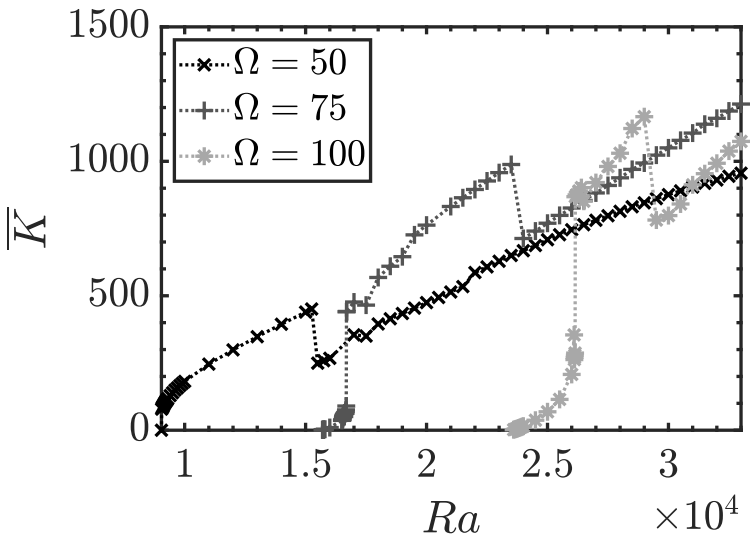

(h)

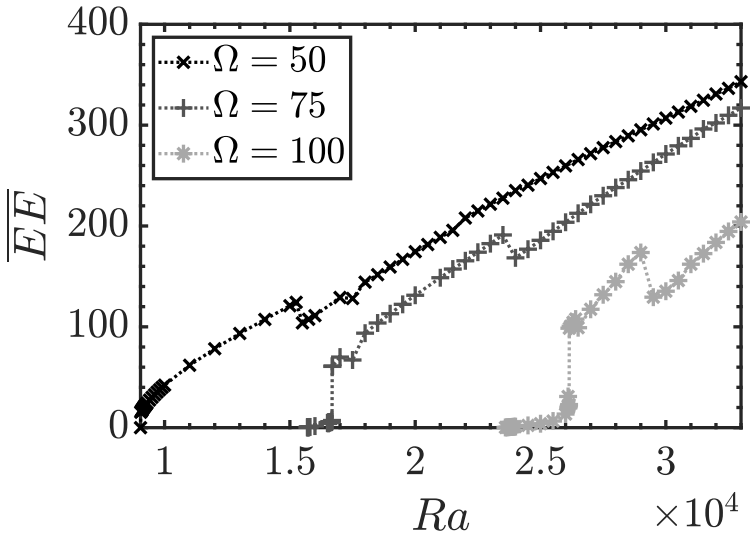

(i)

Figure B.1: Enlarged version of Figure 5.4.

Appendix C

Variation of Figure 7.2

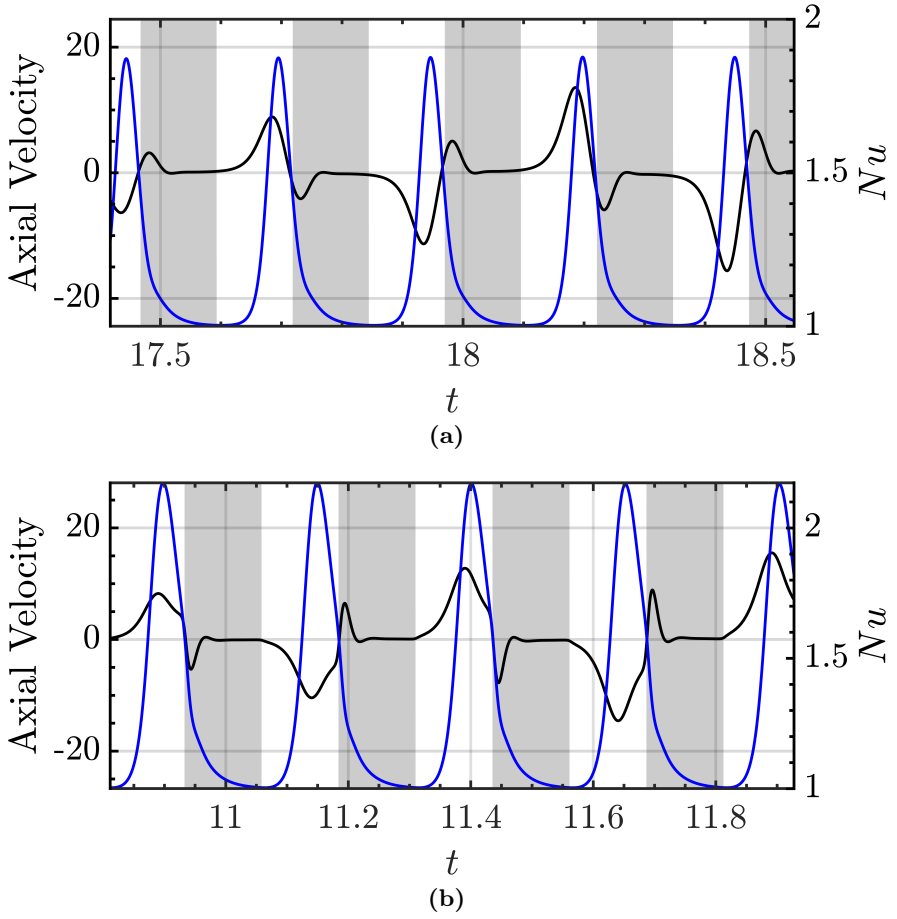

Figure C.1: Time evolution of the Axial velocity (probe being located in the centre of the layer), and Nusselt number. Numerical simulation with $AR = 15$, $Pr = 8$, $\Omega = 25$, $\xi = 0.5$, $\vartheta = 0.1$, and $Ra_\omega = 4000$. (a) Sinusoidal and (b) Pulse waves. The axial velocity is represented in black (—), while $Nu(t)$ is depicted in blue (—). The faded areas represent the interval in which $\mathbf{a}_\Omega(t) > 0$.

Bibliography

[1] Lappa, M. & Boaro, A. 'Rayleigh–Bénard convection in viscoelastic liquid bridges'. In: *Journal of Fluid Mechanics* 904 (2020), A2. doi: 10.1017/jfm.2020.608 (cit. on pp. iii, 27–29, 68, 97, 113, 121, 134, 155, 156, 165, 168, 169, 182).

[2] Boaro, A. & Lappa, M. 'Multicellular states of viscoelastic thermovibrational convection in a square cavity'. In: *Physics of Fluids* 33.3 (2021), p. 033105. doi: 10.1063/5.0041226. eprint: https://doi.org/10.1063/5.0041226. url: https://doi.org/10.1063/5.0041226 (cit. on pp. iii, 68, 77).

[3] Boaro, A. & Lappa, M. 'Competition of overstability and stabilizing effects in viscoelastic thermovibrational flow'. In: *Phys. Rev. E* 104 (2 Aug. 2021), p. 025102. doi: 10.1103/PhysRevE.104.025102. url: https://link.aps.org/doi/10.1103/PhysRevE.104.025102 (cit. on pp. iii, 68, 109, 115, 116, 122, 123, 188).

[4] Lappa, M. & Boaro, A. 'Viscoelastic Thermovibrational Flow Driven by Sinusoidal and Pulse (Square) Waves'. In: *Fluids* 6.9 (2021). issn: 2311-5521. doi: 10.3390/fluids6090311. url: https://www.mdpi.com/2311-5521/6/9/311 (cit. on pp. iii, 115, 116, 154).

[5] Lappa, M., Burel, T., Kerr, M., Crewdson, G., Boaro, A., Capobianchi, P., Bonnieu, S. V., Murphy, L., Randall, P. & Hens, S. 'Particle Vibration, an Instrument to Study Particle Accumulation Structures On Board the International Space Station'. In: *Microgravity Science and Technology* 34.3 (May 2022). doi: 10.1007/s12217-022-09939-2 (cit. on pp. iii, xxxvii).

[6] Boaro, A. & Lappa, M. 'On the competition of transverse and longitudinal modes of Marangoni convection in a three-dimensional layer of viscoelastic fluid'. In: *Physics of Fluids* 34.12 (Dec. 2022), p. 123103. doi: 10.1063/5.0131461 (cit. on pp. iii, 68, 171).

[7] Boaro, A., MacDowall, G. & Lappa, M. 'The symmetry properties and bifurcations of viscoelastic thermovibrational convection in a square cavity'. In: Ready for submission (2022) (cit. on pp. iv, 104).

[8] Crewdson, G., Boaro, A., Kerr, M. & Lappa, M. 'Supporting an ISS experiment as PhD students: a case study of the PARTICLE VIBRATION project'. In: *Proceedings of the 4th Symposium on Space Educational Activities*. Symposium on Space Educational Activities. 4th

Symposium on Space Educational Activities, SSEA 2022 ; Conference date: 27-04-2022 Through 29-04-2022. SSEA, May 2022. DOI: 10.5821/conference-9788419184405.017 (cit. on pp. iv, xxxvii).

[9] Porter, J., Salgado Sánchez, P., Shevtsova, V. & Yasnou, V. 'A review of fluid instabilities and control strategies with applications in microgravity'. In: *Math. Model. Nat. Phenom.* 16 (2021), p. 24. DOI: 10.1051/mmnp/2021020. URL: https://doi.org/10.1051/mmnp/2021020 (cit. on p. xxxiv).

[10] Lappa, M. *Thermal Convection: Patterns, Evolution and Stability*. Vol. 30. John Wiley & Sons, Ltd (2009, Chichester, England), Dec. 2009. ISBN: 978-0-470-69994-2. DOI: 10.1002/9780470749982 (cit. on pp. xxxiv, 3, 12, 16, 34, 93, 121, 160).

[11] Link, S., Huang, X., Fernandez-Pello, C., Olson, S. & Ferkul, P. 'The Effect of Gravity on Flame Spread over PMMA Cylinders'. In: *Scientific Reports* 8.1 (Jan. 2018), p. 120. ISSN: 2045-2322. DOI: 10.1038/s41598-017-18398-4. URL: https://doi.org/10.1038/s41598-017-18398-4 (cit. on p. xxxv).

[12] Nelson, E. S. *An examination of anticipated g-jitter on Space Station and its effects on materials processes*. Tech. rep. NASA, 1994. URL: https://ntrs.nasa.gov/citations/19950006290 (cit. on p. xxxvi).

[13] Rayleigh, L. 'On convection currents in a horizontal layer of fluid, when the higher temperature is on the under side'. In: *The London, Edinburgh, and Dublin Philosophical Magazine and Journal of Science* 32.192 (Dec. 1916), pp. 529–546. DOI: 10.1080/14786441608635602 (cit. on pp. 3, 4).

[14] Bénard, H. 'Les tourbillons cellulaires dans une nappe liquide'. In: *Rev. Gen. Sci. Pures Appl.* 11 (1900), pp. 1261–1271 (cit. on pp. 3, 19–21).

[15] Bénard, H. *Les tourbillons cellulaires dans une nappe liquide propageant de la chaleur par convection en régime permanent*. Vol. 23. Gauthier-Villars, 1901, pp. 62–144 (cit. on pp. 3, 19, 21).

[16] Mutabazi, I., Wesfreid, J. E. & Guyon, E., eds. *Dynamics of Spatio-Temporal Cellular Structures*. Springer New York, 2006. DOI: 10.1007/b106790 (cit. on p. 3).

[17] Lorenz, E. N. 'Deterministic Nonperiodic Flow'. In: *Journal of the Atmospheric Sciences* 20.2 (Mar. 1963), pp. 130–141. DOI: 10.1175/1520-0469(1963)020<0130:dnf>2.0.co;2 (cit. on p. 3).

[18] Jeffreys, H. 'The stability of a layer of fluid heated below'. In: *The London, Edinburgh, and Dublin Philosophical Magazine and Journal of Science* 2.10 (1926), pp. 833–844. DOI: 10.1080/14786442608564114 (cit. on p. 5).

[19] Jeffreys, H. 'Some cases of instability in fluid motion'. In: *Proceedings of the Royal Society of London. Series A, Containing Papers of a Mathematical and Physical Character* 118.779 (1928), pp. 195–208. doi: 10.1098/rspa.1928.0045. eprint: https://royalsocietypublishing.org/doi/pdf/10.1098/rspa.1928.0045. url: https://royalsocietypublishing.org/doi/abs/10.1098/rspa.1928.0045 (cit. on p. 5).

[20] Reid, W. H. & Harris, D. L. 'Some Further Results on the Bénard Problem'. In: *The Physics of Fluids* 1.2 (1958), pp. 102–110. doi: 10.1063/1.1705871. eprint: https://aip.scitation.org/doi/pdf/10.1063/1.1705871. url: https://aip.scitation.org/doi/abs/10.1063/1.1705871 (cit. on p. 5).

[21] Malkus, W. V. R. & Veronis, G. 'Finite amplitude cellular convection'. In: *Journal of Fluid Mechanics* 4.3 (1958), pp. 225–260. doi: 10.1017/S0022112058000410 (cit. on p. 5).

[22] Schlüter, A., Lortz, D. & Busse, F. 'On the stability of steady finite amplitude convection'. In: *Journal of Fluid Mechanics* 23.1 (1965), pp. 129–144. doi: 10.1017/S0022112065001271 (cit. on p. 5).

[23] Cakmur, R. V., Egolf, D. A., Plapp, B. B. & Bodenschatz, E. 'Bistability and Competition of Spatiotemporal Chaotic and Fixed Point Attractors in Rayleigh-Bénard Convection'. In: *Phys. Rev. Lett.* 79 (10 Sept. 1997), pp. 1853–1856. doi: 10.1103/PhysRevLett.79.1853. url: https://link.aps.org/doi/10.1103/PhysRevLett.79.1853 (cit. on p. 6).

[24] Busse, F. H. & Whitehead, J. A. 'Instabilities of convection rolls in a high Prandtl number fluid'. In: *Journal of Fluid Mechanics* 47.2 (1971), pp. 305–320. doi: 10.1017/S0022112071001071 (cit. on p. 7).

[25] Busse, F. H. & Clever, R. M. 'Instabilities of convection rolls in a fluid of moderate Prandtl number'. In: *Journal of Fluid Mechanics* 91.2 (1979), pp. 319–335. doi: 10.1017/S002211207900015X (cit. on p. 7).

[26] Busse, F. H. 'Non-linear properties of thermal convection'. In: *Reports on Progress in Physics* 41.12 (Dec. 1978), pp. 1929–1967. doi: 10.1088/0034-4885/41/12/003. url: https://doi.org/10.1088/0034-4885/41/12/003 (cit. on p. 7).

[27] Busse, F. H. & Whitehead, J. A. 'Oscillatory and collective instabilities in large Prandtl number convection'. In: *Journal of Fluid Mechanics* 66.1 (1974), pp. 67–79. doi: 10.1017/S0022112074000061 (cit. on pp. 8, 145).

[28] Kurzweg, U. H. 'Convective instability of a hydromagnetic fluid within a rectangular cavity'. In: *International Journal of Heat and Mass Transfer* 8.1 (1965), pp. 35–41. issn: 0017-9310. doi: https://doi.org/10.1016/0017-9310(65)90095-5. url: https://www.sciencedirect.com/science/article/pii/0017931065900955 (cit. on p. 9).

[29] Luijkx, J. M. & Platten, J. K. 'On the Onset of Free Convection in a Rectangular Channel'. In: *J.Non-Equilib.Thermodyn.* 6.3 (1981), pp. 141–158. doi: doi:10.1515/jnet.1981.6.3.141. url: https://doi.org/10.1515/jnet.1981.6.3.141 (cit. on p. 9).

[30] Mizushima, J. 'Onset of the Thermal Convection in a Finite Two-Dimensional Box'. In: *Journal of the Physical Society of Japan* 64.7 (1995), pp. 2420–2432. doi: 10.1143/JPSJ.64.2420. eprint: https://doi.org/10.1143/JPSJ.64.2420. url: https://doi.org/10.1143/JPSJ.64.2420 (cit. on pp. 9, 10, 82, 111).

[31] Mizushima, J. & Adachi, T. 'Sequential Transitions of the Thermal Convection in a Square Cavity'. In: *Journal of the Physical Society of Japan* 66.1 (1997), pp. 79–90. doi: 10.1143/JPSJ.66.79. eprint: https://doi.org/10.1143/JPSJ.66.79. url: https://doi.org/10.1143/JPSJ.66.79 (cit. on pp. 11, 82).

[32] Hadley, G. 'VI. Concerning the cause of the general trade-winds'. In: *Philosophical Transactions of the Royal Society of London* 39.437 (1735), pp. 58–62. doi: 10.1098/rstl.1735.0014. eprint: https://royalsocietypublishing.org/doi/pdf/10.1098/rstl.1735.0014. url: https://royalsocietypublishing.org/doi/abs/10.1098/rstl.1735.0014 (cit. on p. 11).

[33] Lappa, M. *Rotating Thermal Flows in Natural and Industrial Processes.* John Wiley & Sons, Ltd, 2012. isbn: 9781119960799. doi: 10.1002/9781118342411 (cit. on p. 12).

[34] Thevenard, D., Rouzand, A., Coméra, J. & Favier, J. 'Influence of convective thermal oscillations on a solidification interface in Bridgman growth'. In: *Journal of Crystal Growth* 108.3 (1991), pp. 572–582. issn: 0022-0248. doi: https://doi.org/10.1016/0022-0248(91)90236-X. url: https://www.sciencedirect.com/science/article/pii/002202489190236X (cit. on p. 12).

[35] Le Quéré, P. 'Transition to unsteady natural convection in a tall water-filled cavity'. In: *Physics of Fluids A: Fluid Dynamics* 2.4 (1990), pp. 503–515. doi: 10.1063/1.857750. eprint: https://doi.org/10.1063/1.857750. url: https://doi.org/10.1063/1.857750 (cit. on p. 12).

[36] Hurle, D. T. J. 'Temperature oscillations in molten metals and their relationship to growth striae in melt-grown crystals'. In: *The Philosophical Magazine: A Journal of Theoretical Experimental and Applied Physics* 13.122 (1966), pp. 305–310. doi: 10.1080/14786436608212608. eprint: https://doi.org/10.1080/14786436608212608. url: https://doi.org/10.1080/14786436608212608 (cit. on p. 12).

[37] Hurle, D. T. J., Jakeman, E. & Johnson, C. P. 'Convective temperature oscillations in molten gallium'. In: *Journal of Fluid Mechanics* 64.3 (1974), pp. 565–576. doi: 10.1017/S0022112074002540 (cit. on p. 12).

[38] Hart, J. E. 'Stability of Thin Non-Rotating Hadley Circulations'. In: *Journal of Atmospheric Sciences* 29.4 (1972), pp. 687–697. doi: 10.1175/1520-0469(1972)029<0687:SOTNRH>2.0.CO;2. url: https://journals.ametsoc.org/view/journals/atsc/29/4/1520-0469_1972_029_0687_sotnrh_2_0_co_2.xml (cit. on pp. 12, 190).

[39] Hart, J. 'A note on the stability of low-Prandtl-number Hadley circulations'. In: *Journal of Fluid Mechanics* 132 (1983), pp. 271–281. doi: 10.1017/S0022112083001603 (cit. on p. 12).

[40] Gill, A. E. 'A theory of thermal oscillations in liquid metals'. In: *Journal of Fluid Mechanics* 64.3 (1974), pp. 577–588. doi: 10.1017/S0022112074002552 (cit. on pp. 12, 190).

[41] Kuo, H. P. & Korpela, S. A. 'Stability and finite amplitude natural convection in a shallow cavity with insulated top and bottom and heated from a side'. In: *The Physics of Fluids* 31.1 (1988), pp. 33–42. doi: 10.1063/1.866574. eprint: https://aip.scitation.org/doi/pdf/10.1063/1.866574. url: https://aip.scitation.org/doi/abs/10.1063/1.866574 (cit. on p. 13).

[42] Gershuni, G., Laure, P., Myznikov, V., Roux, B. & Zhukhovitsky, E. 'On stability of plane parallel advective flows in long horizontal layer'. In: *Microgravity quarterly: MGQ* 3 (Jan. 1992), pp. 141–152 (cit. on p. 13).

[43] Xin, S. & Le Quéré, P. 'Linear stability analyses of natural convection flows in a differentially heated square cavity with conducting horizontal walls'. In: *Physics of Fluids* 13.9 (2001), pp. 2529–2542. doi: 10.1063/1.1388054. eprint: https://doi.org/10.1063/1.1388054. url: https://doi.org/10.1063/1.1388054 (cit. on p. 14).

[44] Monti, R., Langbein, D. & Favier, J. J. 'Influence of Residual Accelerations on Fluid Physics and Materials Science Experiments'. In: *Fluid Sciences and Materials Science in Space: A European Perspective*. Ed. by H. U. Walter. Berlin, Heidelberg: Springer Berlin Heidelberg, 1987, pp. 637–680. isbn: 978-3-642-46613-7. doi: 10.1007/978-3-642-46613-7_18. url: https://doi.org/10.1007/978-3-642-46613-7_18 (cit. on pp. 14, 15).

[45] Monti, R., Savino, R. & Lappa, M. 'Microgravity sensitivity of typical fluid physics experiment'. In: *The 17 th Microgravity Measurements Group Meeting, Cleveland, Ohio, 24-26 March 1998*. Vol. 23. 17th International Microgravity Measurements Group (MGMG) meeting , 1998, MGMG 1998 ; Conference date: 24-03-1998 Through 26-03-1998. July 1998, pp. 1–15 (cit. on p. 14).

[46] Savino, R. & Lappa, M. 'Assessment of Thermovibrational Theory: Application to G -Jitter on the Space Station'. In: *Journal of Spacecraft and Rockets* 40.2 (2003), pp. 201–210. doi: 10.2514/2.3954. eprint: https://doi.org/10.2514/2.3954. url: https://doi.org/10.2514/2.3954 (cit. on pp. 14, 15).

[47] Lappa, M. 'The patterning behaviour and accumulation of spherical particles in a vibrated non-isothermal liquid'. In: *Physics of Fluids* 26.9 (2014), p. 093301. doi: 10.1063/1.4893078. eprint: https://doi.org/10.1063/1.4893078. url: https://doi.org/10.1063/1.4893078 (cit. on pp. 15, 205).

[48] Lappa, M. 'Numerical study into the morphology and formation mechanisms of threedimensional particle structures in vibrated cylindrical cavities with various heating conditions'. In: *Physical Review Fluids* 1 (6 Oct. 2016), p. 064203. doi: 10.1103/PhysRevFluids.1.064203. url: https://link.aps.org/doi/10.1103/PhysRevFluids.1.064203 (cit. on pp. 15, 205).

[49] Lappa, M. 'On the multiplicity and symmetry of particle attractors in confined non-isothermal fluids subjected to inclined vibrations'. In: *International Journal of Multiphase Flow* 93 (2017), pp. 71–83. issn: 0301-9322. doi: https://doi.org/10.1016/j.ijmultiphaseflow.2017.03.015. url: http://www.sciencedirect.com/science/article/pii/S0301932216307121 (cit. on pp. 15, 205).

[50] Lappa, M. 'On the formation and morphology of coherent particulate structures in non-isothermal enclosures subjected to rotating g-jitters'. In: *Physics of Fluids* 31.7 (2019), p. 073303. doi: 10.1063/1.5098438. eprint: https://doi.org/10.1063/1.5098438. url: https://doi.org/10.1063/1.5098438 (cit. on p. 15).

[51] Alexander, J. I. D. 'Low-gravity experiment sensitivity to residual acceleration - A review'. In: *Microgravity Science and Technology* 3 (1990), pp. 52–68 (cit. on p. 15).

[52] Simonenko, I. B. & Zen'kovskaya, S. 'On the effect of high frequency vibrations on the origin of convection'. In: *Izv. Akad. Nauk SSSR Ser. Mech. Zhidk. Gaza* 5 (1966), pp. 51–55 (cit. on p. 15).

[53] Simonenko, I. B. 'A justification of the averaging method for a problem of convection in a field of rapidly oscillating forces and for other parabolic equations'. In: *Mathematics of the USSR-Sbornik* 16.2 (Feb. 1972), pp. 245–263. doi: 10.1070/sm1972v016n02abeh001424. url: https://doi.org/10.1070/sm1972v016n02abeh001424 (cit. on p. 15).

[54] Gershuni, G. Z. & Zhukhovitskii, E. M. 'Free thermal convection in a vibrational field under conditions of weightlessness'. In: *Soviet Physics Doklady* 24 (Nov. 1979), pp. 894–896 (cit. on p. 15).

[55] Gershuni, G. Z. & Zhukhovitskii, E. M. 'Vibrational thermal convection in zero gravity'. In: *Fluid. Mech. Sov. Res.* 15 (Jan. 1986) (cit. on p. 15).

[56] Gershuni, G. Z., Zhukhovitskii, E. M. & Yurkov, Y. S. 'Vibrational thermal convection in a rectangular cavity'. In: *Fluid Dynamics* 17.4 (July 1982), pp. 565–569. issn: 1573-8507. doi: 10.1007/BF01090025. url: https://doi.org/10.1007/BF01090025 (cit. on p. 15).

[57] Gershuni, G. Z. & Zhukhovitskii, E. M. 'Convective instability of a fluid in a vibration field under conditions of weightlessness'. In: *Fluid Dynamics* 16.4 (1982), pp. 498–504. doi: 10.1007/bf01094590 (cit. on pp. 15, 16).

[58] Khallouf, H., Gershuni, G. Z. & Mojtabi, A. 'Numerical study of two-dimensional thermovibrational convection in rectangular cavities'. In: *Numerical Heat Transfer, Part A: Applications* 27.3 (1995), pp. 297–305. doi: 10.1080/10407789508913701. eprint: https://doi.org/10.1080/10407789508913701. url: https://doi.org/10.1080/10407789508913701 (cit. on p. 17).

[59] Bouarab, S., Mokhtari, F., Kaddeche, S., Henry, D., Botton, V. & Medelfef, A. 'Theoretical and numerical study on high frequency vibrational convection: Influence of the vibration direction on the flow structure'. In: *Physics of Fluids* 31.4 (2019), p. 043605. doi: 10.1063/1.5090264. eprint: https://doi.org/10.1063/1.5090264. url: https://doi.org/10.1063/1.5090264 (cit. on p. 17).

[60] Mokhtari, F., Kaddeche, S., Henry, D., Bouarab, S., Medelfef, A. & Botton, V. 'Three-dimensional effect of high frequency vibration on convection in silicon melt'. In: *Phys. Rev. Fluids* 5 (12 Dec. 2020), p. 123501. doi: 10.1103/PhysRevFluids.5.123501. url: https://link.aps.org/doi/10.1103/PhysRevFluids.5.123501 (cit. on p. 17).

[61] Shevtsova, V., Ryzhkov, I. I., Melnikov, D. E., Gaponenko, Y. & Mialdun, A. 'Experimental and theoretical study of vibration-induced thermal convection in low gravity'. In: *Journal of Fluid Mechanics* 648 (Apr. 2010), pp. 53–82. doi: 10.1017/S0022112009993442 (cit. on p. 17).

[62] Mialdun, A., Ryzhkov, I. I., Melnikov, D. E. & Shevtsova, V. 'Experimental Evidence of Thermal Vibrational Convection in a Nonuniformly Heated Fluid in a Reduced Gravity Environment'. In: *Phys. Rev. Lett.* 101 (8 Aug. 2008), p. 084501. doi: 10.1103/PhysRevLett.101.084501. url: https://link.aps.org/doi/10.1103/PhysRevLett.101.084501 (cit. on p. 17).

[63] Mialdun, A., Ryzhkov, I. I., Melnikov, D. E. & Shevtsova, V. 'Experimental evidence of thermovibrational convection in reduced gravity'. In: *Space Research Today* 171 (2008), pp. 4–6. issn: 1752-9298. doi: https://doi.org/10.1016/S1752-9298(08)80004-7. url: http://www.sciencedirect.com/science/article/pii/S1752929808800047 (cit. on p. 17).

[64] Crewdson, G. & Lappa, L. 'Thermally-driven flows and turbulence in vibrated liquids'. In: *International Journal of Thermofluids* 11 (2021), p. 100102. issn: 2666-2027. doi: https://doi.org/10.1016/j.ijft.2021.100102. url: https://www.sciencedirect.com/science/article/pii/S2666202721000409 (cit. on pp. 18, 19, 75).

[65] Hirata, K., Sasaki, T. & Tanigawa, H. 'Vibrational effects on convection in a square cavity at zero gravity'. In: *Journal of Fluid Mechanics* 445 (Oct. 2001), pp. 327–344. doi: 10.1017/S0022112001005651 (cit. on pp. 18, 33, 108, 130).

[66] Birikh, R. V., Briskman, V. A., Chernatynski, V. I. & Roux, B. 'Control of thermocapillary convection in a liquid bridge by high frequency vibrations'. In: *Microgravity Q* 3 (1993), pp. 23–28 (cit. on p. 19).

[67] Lappa, M. 'Control of Convection Patterning and Intensity in Shallow Cavities by Harmonic Vibrations'. In: *Microgravity Science and Technology* 28.1 (Apr. 2016), pp. 29–39. issn: 1875-0494. doi: 10.1007/s12217-015-9467-4. url: https://doi.org/10.1007/s12217-015-9467-4 (cit. on p. 19).

[68] Napolitano, L. G. 'Thermodynamics and dynamics of surface phases'. In: *Acta Astronautica* 6.9 (1979), pp. 1093–1112. issn: 0094-5765. doi: https://doi.org/10.1016/0094-5765(79)90058-4. url: https://www.sciencedirect.com/science/article/pii/0094576579900584 (cit. on p. 19).

[69] Marangoni, C. 'Ueber die Ausbreitung der Tropfen einer Flüssigkeit auf der Oberfläche einer anderen'. In: *Annalen der Physik* 219.7 (1871), pp. 337–354. doi: https://doi.org/10.1002/andp.18712190702. eprint: https://onlinelibrary.wiley.com/doi/pdf/10.1002/andp.18712190702. url: https://onlinelibrary.wiley.com/doi/abs/10.1002/andp.18712190702 (cit. on p. 19).

[70] Scriven, L. E. & Sternling, C. V. 'The Marangoni Effects'. In: *Nature* 187.4733 (July 1960), pp. 186–188. issn: 1476-4687. doi: 10.1038/187186a0. url: https://doi.org/10.1038/187186a0 (cit. on p. 19).

[71] Block, M. J. 'Surface Tension as the Cause of Bénard Cells and Surface Deformation in a Liquid Film'. In: *Nature* 178.4534 (Sept. 1956), pp. 650–651. issn: 1476-4687. doi: 10.1038/178650a0. url: https://doi.org/10.1038/178650a0 (cit. on pp. 20, 22).

[72] Pearson, J. R. A. 'On convection cells induced by surface tension'. In: *Journal of Fluid Mechanics* 4.5 (Sept. 1958), pp. 489–500. doi: 10.1017/s0022112058000616 (cit. on pp. 20, 21).

[73] Scanlon, J. W. & Segel, L. A. 'Finite amplitude cellular convection induced by surface tension'. In: *Journal of Fluid Mechanics* 30.1 (Oct. 1967), pp. 149–162. doi: 10.1017/s002211206700134x (cit. on p. 21).

[74] Cloot, A. & Lebon, G. 'A nonlinear stability analysis of the Bénard–Marangoni problem'. In: *Journal of Fluid Mechanics* 145.-1 (Aug. 1984), p. 447. doi: 10.1017/s0022112084003013 (cit. on p. 21).

[75] Bragard, J. & Lebon, G. 'Non-Linear Marangoni Convection in a Layer of Finite Depth'. In: *Europhysics Letters (EPL)* 21.8 (Mar. 1993), pp. 831–836. doi: 10.1209/0295-5075/21/8/007 (cit. on p. 21).

[76] Thess, A. & Bestehorn, M. 'Planform selection in Bénard-Marangoni convection: l hexagons versus g hexagons'. In: *Phys. Rev. E* 52 (6 Oct. 1995), pp. 6358–6367. doi: 10.1103/PhysRevE.52.6358. url: https://link.aps.org/doi/10.1103/PhysRevE.52.6358 (cit. on p. 22).

[77] Parmentier, P. M., Regnier, V. C., Lebon, G. & Legros, J. C. 'Nonlinear analysis of coupled gravitational and capillary thermoconvention in thin fluid layers'. In: *Phys. Rev. E* 54 (1 July 1996), pp. 411–423. doi: 10.1103/PhysRevE.54.411. url: https://link.aps.org/doi/10.1103/PhysRevE.54.411 (cit. on pp. 22, 26).

[78] Thess, A. & Orszag, S. A. 'Temperature Spectrum in Surface Tension Driven Bénard Convection'. In: *Phys. Rev. Lett.* 73 (4 July 1994), pp. 541–544. doi: 10.1103/PhysRevLett.73.541. url: https://link.aps.org/doi/10.1103/PhysRevLett.73.541 (cit. on p. 22).

[79] Thess, A. & Orszag, S. A. 'Surface-tension-driven Bénard convention at infinite Prandtl number'. In: *Journal of Fluid Mechanics* 283 (1995), pp. 201–230. issn: 0022-1120. doi: 10.1017/S002211209500228X. url: https://doi.org/10.1017/S002211209500228X (cit. on p. 22).

[80] Thess, A., Spirn, D. & Jüttner, B. 'Viscous Flow at Infinite Marangoni Number'. In: *Phys. Rev. Lett.* 75 (25 Oct. 1995), pp. 4614–4617. doi: 10.1103/PhysRevLett.75.4614. url: https://link.aps.org/doi/10.1103/PhysRevLett.75.4614 (cit. on p. 22).

[81] Bestehorn, M. 'Square Patterns in Bénard-Marangoni Convection'. In: *Phys. Rev. Lett.* 76 (1 Jan. 1996), pp. 46–49. doi: 10.1103/PhysRevLett.76.46. url: https://link.aps.org/doi/10.1103/PhysRevLett.76.46 (cit. on p. 22).

[82] Eckert, K., Bestehorn, M. & Thess, A. 'Square cells in surface-tension-driven Bénard convection: experiment and theory'. In: *Journal of Fluid Mechanics* 356 (1998), pp. 155–197. issn: 0022-1120. doi: 10.1017/S0022112097007842. url: https://doi.org/10.1017/S0022112097007842 (cit. on p. 22).

[83] Colinet, P., Legros, J. C. & Velarde, M. *Nonlinear Dynamics of Surface-Tension-Driven Instabilities*. John Wiley & Sons, Ltd, 2001, p. 512. isbn: 9783527603114. doi: 10.1002/3527603115 (cit. on p. 22).

[84] Yih, C.-S. 'Fluid Motion Induced by Surface-Tension Variation'. In: *Physics of Fluids* 11.3 (1968), p. 477. doi: 10.1063/1.1691941 (cit. on p. 22).

[85] Strani, M., Piva, R. & Graziani, G. 'Thermocapillary convection in a rectangular cavity: asymptotic theory and numerical simulation'. In: *Journal of Fluid Mechanics* 130.-1 (May 1983), p. 347. doi: 10.1017/s0022112083001123 (cit. on p. 22).

[86] Mercier, J.-F. & Normand, C. 'Influence of the Prandtl number on the location of recirculation eddies in thermocapillary flows'. In: *International Journal of Heat and Mass Transfer* 45.4 (Feb. 2002), pp. 793–801. doi: 10.1016/s0017-9310(01)00185-5 (cit. on p. 22).

[87] Priede, J. & Gerbeth, G. 'Hydrothermal wave instability of thermocapillary-driven convection in a coplanar magnetic field'. In: *Journal of Fluid Mechanics* 347 (Sept. 1997), pp. 141–169. doi: 10.1017/s0022112097006459 (cit. on pp. 22, 23).

[88] Smith, M. K. & Davis, S. H. 'Instabilities of dynamic thermocapillary liquid layers. Part 1. Convective instabilities'. In: *Journal of Fluid Mechanics* 132 (1983), pp. 119–144. issn: 0022-1120. doi: 10.1017/S0022112083001512. url: https://doi.org/10.1017/S0022112083001512 (cit. on pp. 22, 177).

[89] Smith, M. K. 'Instability mechanisms in dynamic thermocapillary liquid layers'. In: *The Physics of Fluids* 29.10 (1986), pp. 3182–3186. doi: 10.1063/1.865836. eprint: https://aip.scitation.org/doi/pdf/10.1063/1.865836. url: https://aip.scitation.org/doi/abs/10.1063/1.865836 (cit. on pp. 22, 177).

[90] Peltier, L. J. & Biringen, S. 'Time-dependent thermocapillary convection in a rectangular cavity: numerical results for a moderate Prandtl number fluid'. In: *Journal of Fluid Mechanics* 257 (1993), pp. 339–357. issn: 0022-1120. doi: 10.1017/S0022112093003106. url: https://doi.org/10.1017/S0022112093003106 (cit. on pp. 22, 177).

[91] Xu, J. & Zebib, A. 'Oscillatory two- and three-dimensional thermocapillary convection'. In: *Journal of Fluid Mechanics* 364 (1998), pp. 187–209. issn: 0022-1120. doi: 10.1017/S0022112098001232. url: https://doi.org/10.1017/S0022112098001232 (cit. on p. 23).

[92] Shevtsova, V. M., Nepomnyashchy, A. A. & Legros, J. C. 'Thermocapillary-buoyancy convection in a shallow cavity heated from the side'. In: *Phys. Rev. E* 67 (6 June 2003), p. 066308. doi: 10.1103/PhysRevE.67.066308. url: https://link.aps.org/doi/10.1103/PhysRevE.67.066308 (cit. on p. 23).

[93] Bucchignani, E. 'Numerical characterization of hydrothermal waves in a laterally heated shallow layer'. In: *Physics of Fluids* 16.11 (2004), pp. 3839–3849. doi: 10.1063/1.1776963. eprint: https://doi.org/10.1063/1.1776963. url: https://doi.org/10.1063/1.1776963 (cit. on p. 23).

[94] Garner, F. H. & Nissan, A. H. 'Rheological Properties of High-Viscosity Solutions of Long Molecules'. In: *Nature* 158.4018 (1946), pp. 634–635. issn: 1476-4687. doi: 10.1038/158634a0. url: https://doi.org/10.1038/158634a0 (cit. on p. 24).

[95] Tanner, R. I. 'A new inelastic theory of extrudate swell'. In: *Journal of Non-Newtonian Fluid Mechanics* 6.3 (1980), pp. 289–302. ISSN: 0377-0257. DOI: https://doi.org/10.1016/0377-0257(80)80007-3. URL: http://www.sciencedirect.com/science/article/pii/0377025780800073 (cit. on p. 24).

[96] James, D. F. 'Open Channel Siphon with Viscoelastic Fluids'. In: *Nature* 212.5063 (1966), pp. 754–756. ISSN: 1476-4687. DOI: 10.1038/212754a0. URL: https://doi.org/10.1038/212754a0 (cit. on p. 24).

[97] Metzner, A. B. 'Behavior of suspended matter in rapidly accelerating viscoelastic fluids: The Uebler effect'. In: *AIChE Journal* 13.2 (1967), pp. 316–318. DOI: 10.1002/aic.690130222. URL: https://doi.org/10.1002/aic.690130222 (cit. on p. 24).

[98] Fredrickson, A. G. *Principles and applications of rheology*. Prentice-Hall, 1964 (cit. on p. 24).

[99] Gordon, R. J. & Balakrishnan, C. 'Vortex inhibition: A new viscoelastic effect with importance in drag reduction and polymer characterization'. In: *Journal of Applied Polymer Science* 16.7 (1972), pp. 1629–1639. DOI: 10.1002/app.1972.070160704. URL: https://doi.org/10.1002/app.1972.070160704 (cit. on p. 24).

[100] Green, T. 'Oscillating Convection in an Elasticoviscous Liquid'. In: *The Physics of Fluids* 11.7 (1968), pp. 1410–1412. DOI: 10.1063/1.1692123. eprint: https://aip.scitation.org/doi/pdf/10.1063/1.1692123. URL: https://aip.scitation.org/doi/abs/10.1063/1.1692123 (cit. on p. 24).

[101] Vest, C. M. & Arpaci, V. S. 'Overstability of a viscoelastic fluid layer heated from below'. In: *Journal of Fluid Mechanics* 36.3 (May 1969), pp. 613–623. DOI: 10.1017/S0022112069001881 (cit. on p. 25).

[102] Sokolov, M. & Tanner, R. I. 'Convective Stability of a General Viscoelastic Fluid Heated from Below'. In: *The Physics of Fluids* 15.4 (1972), pp. 534–539. DOI: 10.1063/1.1693945. eprint: https://aip.scitation.org/doi/pdf/10.1063/1.1693945. URL: https://aip.scitation.org/doi/abs/10.1063/1.1693945 (cit. on p. 25).

[103] Larson, R. G. 'Instabilities in viscoelastic flows'. In: *Rheologica Acta* 31.3 (May 1992), pp. 213–263. ISSN: 1435-1528. DOI: 10.1007/BF00366504. URL: https://doi.org/10.1007/BF00366504 (cit. on pp. 25, 197).

[104] Alves, M. A., Oliveira, P. J. & Pinho, F. T. 'Numerical Methods for Viscoelastic Fluid Flows'. In: *Annual Review of Fluid Mechanics* 53.1 (2021), pp. 509–541. DOI: 10.1146/annurev-fluid-010719-060107. eprint: https://doi.org/10.1146/annurev-fluid-010719-060107. URL: https://doi.org/10.1146/annurev-fluid-010719-060107 (cit. on pp. 25, 64, 65, 210).

[105] Martínez-Mardones, J. & Pérez-García, C. 'Linear instability in viscoelastic fluid convection'. In: *Journal of Physics: Condensed Matter* 2.5 (Feb. 1990), pp. 1281–1290. ISSN: 09538984. DOI: 10.1088/0953-8984/2/5/019. URL: https://iopscience.iop.org/article/10.1088/0953-8984/2/5/019 (cit. on pp. 25, 26, 71, 107, 129).

[106] Park, H. M. & Lee, H. S. 'Hopf bifurcations of viscoelastic fluids heated from below'. In: *Journal of Non-Newtonian Fluid Mechanics* 66.1 (1996), pp. 1–34. ISSN: 0377-0257. DOI: https://doi.org/10.1016/0377-0257(96)01458-9. URL: http://www.sciencedirect.com/science/article/pii/0377025796014589 (cit. on pp. 25, 26).

[107] Li, Z. & Khayat, R. E. 'Finite-amplitude Rayleigh–Bénard convection and pattern selection for viscoelastic fluids'. In: *Journal of Fluid Mechanics* 529 (2005), pp. 221–251. DOI: 10.1017/S0022112005003563 (cit. on pp. 25, 26, 59, 109, 129, 156).

[108] Eltayeb, I. A. 'Nonlinear thermal convection in an elastico-viscous layer heated from below'. In: *Proceedings of the Royal Society of London. A. Mathematical and Physical Sciences* 356.1685 (1977), pp. 161–176. DOI: 10.1098/rspa.1977.0127. eprint: https://royalsocietypublishing.org/doi/pdf/10.1098/rspa.1977.0127. URL: https://royalsocietypublishing.org/doi/abs/10.1098/rspa.1977.0127 (cit. on p. 26).

[109] Rosenau, P. 'Extending hydrodynamics via the regularization of the Chapman-Enskog expansion'. In: *Phys. Rev. A* 40 (12 Dec. 1989), pp. 7193–7196. DOI: 10.1103/PhysRevA.40.7193. URL: https://link.aps.org/doi/10.1103/PhysRevA.40.7193 (cit. on pp. 26, 40).

[110] Martínez-Mardones, J. & Pérez-García, C. 'Bifurcation analysis and amplitude equations for viscoelastic convective fluids'. In: *Il Nuovo Cimento D* 14.9 (Sept. 1992), pp. 961–975. ISSN: 0392-6737. DOI: 10.1007/BF02451680. URL: https://doi.org/10.1007/BF02451680 (cit. on pp. 26, 109, 129).

[111] Parmentier, P., Lebon, G. & Regnier, V. 'Weakly nonlinear analysis of Bénard–Marangoni instability in viscoelastic fluids'. In: *Journal of Non-Newtonian Fluid Mechanics* 89.1 (2000), pp. 63–95. ISSN: 0377-0257. DOI: https://doi.org/10.1016/S0377-0257(99)00031-2. URL: http://www.sciencedirect.com/science/article/pii/S0377025799000312 (cit. on pp. 26, 129).

[112] Khayat, R. E. 'Chaos and overstability in the thermal convection of viscoelastic fluids'. In: *Journal of Non-Newtonian Fluid Mechanics* 53 (1994), pp. 227–255. ISSN: 0377-0257. DOI: https://doi.org/10.1016/0377-0257(94)85051-8. URL: https://www.sciencedirect.com/science/article/pii/0377025794850518 (cit. on p. 27).

[113] Park, H. M. & Ryu, D. H. 'Rayleigh–Bénard convection of viscoelastic fluids in finite domains'. In: *Journal of Non-Newtonian Fluid Mechanics* 98 (Mar. 2001), pp. 169–184. DOI: 10.1016/S0377-0257(01)00104-5 (cit. on p. 29).

[114] Park, H. M. & Park, K. S. 'Rayleigh-Bénard convection of viscoelastic fluids in arbitrary finite domains'. In: *International Journal of Heat and Mass Transfer* 47.10-11 (2004), pp. 2251–2259. doi: 10.1016/j.ijheatmasstransfer.2003.11.022 (cit. on p. 29).

[115] Lyubimov, D. V., Kovalevskaya, K. V. & Lyubimova, T. P. 'Bifurcations in the problem of thermal convection of viscoelastic fluid in a closed cavity with free boundaries heated from below'. en. In: *Izvestiya VUZ. Applied Nonlinear Dynamics* 19.3 (2011), pp. 16–25. issn: 0869-6632. doi: 10.18500/0869-6632-2011-19-3-16-25. url: https://andjournal.sgu.ru/sites/andjournal.sgu.ru/files/text-pdf/2019/03/2011no3p016.pdf (cit. on p. 29).

[116] Lyubimov, D., Kovalevskaya, K. & Lyubimova, T. 'Bifurcation analysis of a viscoelastic fluid heated from below'. In: *Communications in Nonlinear Science and Numerical Simulation* 17.9 (Sept. 2012), pp. 3521–3532. doi: 10.1016/j.cnsns.2012.01.002 (cit. on p. 29).

[117] Park, H. M. & Ryu, D. H. 'Hopf bifurcation in thermal convection of viscoelastic fluids within finite domains'. In: *Journal of Non-Newtonian Fluid Mechanics* 101.1 (2001), pp. 1–19. issn: 0377-0257. doi: https://doi.org/10.1016/S0377-0257(01)00145-8. url: http://www.sciencedirect.com/science/article/pii/S0377025701001458 (cit. on pp. 29, 129).

[118] Park, H. M. & Ryu, D. H. 'Nonlinear convective stability problems of viscoelastic fluids in finite domains'. In: *Rheologica Acta* 41 (Aug. 2002), pp. 427–440. doi: 10.1007/s00397-001-0223-x (cit. on p. 29).

[119] Krapivina, E. N. & Lyubimova, T. P. 'Nonlinear regimes of convection of an elasticoviscous fluid in a closed cavity heated from below'. In: *Fluid Dynamics* 35.4 (July 2000), pp. 473–478. issn: 1573-8507. doi: 10.1007/BF02698115. url: https://doi.org/10.1007/BF02698115 (cit. on p. 29).

[120] Park, H. M., Shin, K. S. & Sohn, H. S. 'Numerical simulation of thermal convection of viscoelastic fluids using the grid-by-grid inversion method'. In: *International Journal of Heat and Mass Transfer* 52.21 (2009), pp. 4851–4861. issn: 0017-9310. doi: https://doi.org/10.1016/j.ijheatmasstransfer.2009.05.027. url: http://www.sciencedirect.com/science/article/pii/S0017931009003597 (cit. on p. 29).

[121] Park, H. M. & Lim, J. Y. 'A new numerical algorithm for viscoelastic fluid flows : The grid-by-grid inversion method'. In: *Journal of Non-Newtonian Fluid Mechanics* 165.5 (2010), pp. 238–246. issn: 0377-0257. doi: https://doi.org/10.1016/j.jnnfm.2009.12.006. url: http://www.sciencedirect.com/science/article/pii/S0377025709002365 (cit. on p. 29).

[122] Kovalevskaya, K. V. & Lyubimova, T. P. 'Onset and nonlinear regimes of convection of an elastoviscous fluid in a closed cavity heated from below'. In: *Fluid Dynamics* 46.6 (Oct. 2011), pp. 854–863. doi: 10.1134/s0015462811060020 (cit. on p. 29).

[123] Park, H. M. 'Peculiarity in the Rayleigh-Bénard convection of viscoelastic fluids'. In: *International Journal of Thermal Sciences* 132 (2018), pp. 34–41. ISSN: 1290-0729. DOI: https://doi.org/10.1016/j.ijthermalsci.2018.05.044. URL: http://www.sciencedirect.com/science/article/pii/S1290072917310761 (cit. on p. 29).

[124] Zhang, W. C., Zhang, H. N., Li, Y., Yu, B. & Li, F. 'Role of elasto-inertial turbulence in viscoelastic drag-reducing turbulence'. In: *Physics of Fluids* 33.8 (2021), p. 081706. DOI: 10.1063/5.0056047. eprint: https://doi.org/10.1063/5.0056047. URL: https://doi.org/10.1063/5.0056047 (cit. on pp. 29, 198).

[125] Kolodner, P. 'Oscillatory convection in viscoelastic DNA suspensions'. In: *Journal of Non-Newtonian Fluid Mechanics* 75.2-3 (Mar. 1998), pp. 167–192. DOI: 10.1016/s0377-0257(97)00095-5 (cit. on pp. 29, 205).

[126] Albaalbaki, B. & Khayat, R. E. 'Pattern selection in the thermal convection of non-Newtonian fluids'. In: *Journal of Fluid Mechanics* 668 (Jan. 2011), pp. 500–550. DOI: 10.1017/s0022112010004775 (cit. on p. 29).

[127] Métivier, C., Brochard, F., Darbouli, M. & Magnin, A. 'Oscillatory Rayleigh–Bénard Convection in elasto-viscoplastic gels'. In: *Journal of Non-Newtonian Fluid Mechanics* 286 (2020), p. 104428. ISSN: 0377-0257. DOI: https://doi.org/10.1016/j.jnnfm.2020.104428. URL: https://www.sciencedirect.com/science/article/pii/S0377025720301798 (cit. on pp. 29, 118, 206).

[128] Lebon, G., Parmentier, P., Teller, O. & Dauby, P. C. 'Bénard-Marangoni instability in a viscoelastic Jeffreys' fluid layer'. In: *Rheologica Acta* 33.4 (July 1994), pp. 257–266. ISSN: 1435-1528. DOI: 10.1007/BF00366952. URL: https://doi.org/10.1007/BF00366952 (cit. on pp. 30, 31, 74, 75, 129).

[129] Getachew, D. & Rosenblat, S. 'Thermocapillary instability of a viscoelastic liquid layer'. In: *Acta Mechanica* 55.1 (Apr. 1985), pp. 137–149. ISSN: 1619-6937. DOI: 10.1007/BF01267986. URL: https://doi.org/10.1007/BF01267986 (cit. on p. 30).

[130] Lebon, G. & Cloot, A. 'An extended thermodynamic approach to non-Newtonian fluids and related results in Marangoni instability problem'. In: *Journal of Non-Newtonian Fluid Mechanics* 28.1 (Jan. 1988), pp. 61–76. ISSN: 0377-0257. URL: https://www.sciencedirect.com/science/article/pii/0377025788800107 (cit. on p. 30).

[131] Dauby, P. C., Parmentier, P., Lebon, G. & Grmela, M. 'Coupled buoyancy and thermocapillary convection in a viscoelastic Maxwell fluid'. In: *Journal of Physics: Condensed Matter* 5.26 (June 1993), pp. 4343–4352. ISSN: 0953-8984. DOI: 10.1088/0953-8984/5/26/007. URL: https://doi.org/10.1088/0953-8984/5/26/007 (cit. on p. 30).

[132] Ramkissoon, H., Ramdath, G., Comissiong, D. & Rahaman, K. 'On thermal instabilities in a viscoelastic fluid'. In: *International Journal of Non-Linear Mechanics* 41.1 (Jan. 2006), pp. 18–25. issn: 0020-7462. url: https://www.sciencedirect.com/science/article/pii/S0020746205000624 (cit. on p. 30).

[133] Siddheshwar, P. G., Sekhar, G. N. & Jayalatha, G. 'Surface tension driven convection in viscoelastic liquids with thermorheological effect'. In: *International Communications in Heat and Mass Transfer* 38.4 (Apr. 2011), pp. 468–473. issn: 0735-1933. url: https://www.sciencedirect.com/science/article/pii/S0735193310003325 (cit. on p. 30).

[134] Hernández Hernández, I. J. & Dávalos-Orozco, L. A. 'Competition between stationary and oscillatory viscoelastic thermocapillary convection of a film coating a thick wall'. In: *International Journal of Thermal Sciences* 89 (2015), pp. 164–173. issn: 1290-0729. doi: https://doi.org/10.1016/j.ijthermalsci.2014.11.003. url: https://www.sciencedirect.com/science/article/pii/S1290072914003159 (cit. on p. 30).

[135] Lappa, M. & Ferialdi, H. 'Multiple solutions, oscillons, and strange attractors in thermoviscoelastic Marangoni convection'. In: *Physics of Fluids* 30.10 (2018), p. 104104. doi: 10.1063/1.5040562. eprint: https://doi.org/10.1063/1.5040562. url: https://doi.org/10.1063/1.5040562 (cit. on pp. 30, 97, 99, 121, 172, 182, 191, 193).

[136] Hu, K. X., He, M. & Chen, Q. S. 'Instability of thermocapillary liquid layers for Oldroyd-B fluid'. In: *Physics of Fluids* 28 (Mar. 2016), p. 033105. doi: 10.1063/1.4943971 (cit. on pp. 30, 172, 177).

[137] Hu, K. X., Liu, R., He, M. & Chen, Q. S. 'Elastic instability in the thermocapillary convection at low Reynolds numbers'. In: *Journal of Non-Newtonian Fluid Mechanics* 250 (2017), pp. 43–51. issn: 0377-0257. doi: https://doi.org/10.1016/j.jnnfm.2017.10.009. url: https://www.sciencedirect.com/science/article/pii/S0377025717303555 (cit. on pp. 30, 172, 177).

[138] Hu, K. X., He, M., Chen, Q. S. & Liu, R. 'On the stability of thermocapillary convection of a Bingham fluid in an infinite liquid layer'. In: *International Journal of Heat and Mass Transfer* 122 (2018), pp. 993–1002. issn: 0017-9310. doi: https://doi.org/10.1016/j.ijheatmasstransfer.2018.02.048. url: https://www.sciencedirect.com/science/article/pii/S0017931017349554 (cit. on pp. 30, 172, 177).

[139] Patne, R., Agnon, Y. & Oron, A. 'Thermocapillary instability in a viscoelastic liquid layer under an imposed oblique temperature gradient'. In: *Physics of Fluids* 33.1 (Jan. 2021), p. 012107. issn: 1070-6631. doi: 10.1063/5.0036202. url: https://doi.org/10.1063/5.0036202 (cit. on pp. 31, 172).

[140] Patne, R., Agnon, Y. & Oron, A. 'Thermocapillary instabilities in a liquid layer subjected to an oblique temperature gradient'. In: *Journal of Fluid Mechanics* 906 (2021). A12, A12. ISSN: 0022-1120. DOI: 10.1017/jfm.2020.747. URL: https://doi.org/10.1017/jfm.2020.747 (cit. on pp. 31, 172).

[141] Yang, W. M. 'Stability of viscoelastic fluids in a modulated gravitational field'. In: *International Journal of Heat and Mass Transfer - INT J HEAT MASS TRANSFER* 40 (Apr. 1997), pp. 1401–1410. DOI: 10.1016/S0017-9310(96)00194-9 (cit. on pp. 32, 123, 154).

[142] Lyubimova, T. & Kovalevskaya, K. 'Gravity modulation effect on the onset of thermal buoyancy convection in a horizontal layer of the Oldroyd fluid'. In: *Fluid Dynamics Research* 48.6 (Nov. 2016), p. 061419. DOI: 10.1088/0169-5983/48/6/061419. URL: https://doi.org/10.1088%2F0169-5983%2F48%2F6%2F061419 (cit. on pp. 32, 33, 72, 123, 135, 154, 159).

[143] Kirkwood, J. G. 'The Statistical Mechanical Theory of Transport Processes I. General Theory'. In: *The Journal of Chemical Physics* 14.3 (1946), pp. 180–201. DOI: 10.1063/1.1724117. eprint: https://doi.org/10.1063/1.1724117. URL: https://doi.org/10.1063/1.1724117 (cit. on p. 34).

[144] Irving, J. H. & Kirkwood, J. G. 'The Statistical Mechanical Theory of Transport Processes. IV. The Equations of Hydrodynamics'. In: *The Journal of Chemical Physics* 18.6 (1950), pp. 817–829. DOI: 10.1063/1.1747782. eprint: https://doi.org/10.1063/1.1747782. URL: https://doi.org/10.1063/1.1747782 (cit. on pp. 34, 35).

[145] Oberbeck, A. 'Ueber die Wärmeleitung der Flüssigkeiten bei Berücksichtigung der Strömungen infolge von Temperaturdifferenzen'. In: *Annalen der Physik* 243.6 (1879), pp. 271–292. DOI: https://doi.org/10.1002/andp.18792430606. eprint: https://onlinelibrary.wiley.com/doi/pdf/10.1002/andp.18792430606. URL: https://onlinelibrary.wiley.com/doi/abs/10.1002/andp.18792430606 (cit. on p. 45).

[146] Boussinesq, J. *Théorie analytique de la chaleur: mise en harmonie avec la thermodynamique et avec la théorie mécanique de la lumière*. Vol. 2. Gauthier-Villars, 1903 (cit. on p. 45).

[147] Bird, R. B., Curtiss, C. F., Armstrong, R. C. & Hassager, O. *Dynamics of polymeric liquids — Vol. 2, 2nd ed.* Vol. 91. 12. 1987, pp. 1397–1398. DOI: 10.1002/bbpc.19870911222. eprint: https://onlinelibrary.wiley.com/doi/pdf/10.1002/bbpc.19870911222. URL: https://onlinelibrary.wiley.com/doi/abs/10.1002/bbpc.19870911222 (cit. on pp. 49, 52, 53, 208, 210).

[148] Larson, R. G. 'CHAPTER 2 - Classical Molecular Models'. In: *Constitutive Equations for Polymer Melts and Solutions*. Butterworths Series in Chemical Engineering. Butterworth-Heinemann, 1988, pp. 29–57. ISBN: 978-0-409-90119-1. DOI: https://doi.org/10.1016/B978-

0-409-90119-1.50007-5. URL: https://www.sciencedirect.com/science/article/pii/B9780409901191500075 (cit. on p. 49).

[149] Hameduddin, I., Meneveau, C., Zaki, T. & Gayme, D. F. 'Geometric decomposition of the conformation tensor in viscoelastic turbulence'. In: *Journal of Fluid Mechanics* 842 (2018), pp. 395–427. DOI: 10.1017/jfm.2018.118 (cit. on p. 210).

[150] Kramers, H. A. 'The Behavior of Macromolecules in Inhomogeneous Flow'. In: *The Journal of Chemical Physics* 14.7 (1946), pp. 415–424. DOI: 10.1063/1.1724163. eprint: https://doi.org/10.1063/1.1724163. URL: https://doi.org/10.1063/1.1724163 (cit. on p. 210).

[151] Shaqfeh, E. S. G. & Khomami, B. 'The Oldroyd-B fluid in elastic instabilities, turbulence and particle suspensions'. In: *Journal of Non-Newtonian Fluid Mechanics* 298 (2021), p. 104672. ISSN: 0377-0257. DOI: https://doi.org/10.1016/j.jnnfm.2021.104672. URL: https://www.sciencedirect.com/science/article/pii/S0377025721001579 (cit. on pp. 53, 198).

[152] Castillo Sánchez, H. A., Jovanović, M. R., Kumar, S., Morozov, A., Shankar, V., Subramanian, G. & Wilson, H. J. 'Understanding viscoelastic flow instabilities: Oldroyd-B and beyond'. In: *Journal of Non-Newtonian Fluid Mechanics* 302 (2022), p. 104742. ISSN: 0377-0257. DOI: https://doi.org/10.1016/j.jnnfm.2022.104742. URL: https://www.sciencedirect.com/science/article/pii/S0377025722000015 (cit. on p. 53).

[153] Peterlin, A. 'Einfluß der endlichen moleküllänge auf die gradientenabhängigkeit des staudinger-index'. In: *Die Makromolekulare Chemie* 44.1 (1961), pp. 338–346. DOI: https://doi.org/10.1002/macp.1961.020440129. eprint: https://onlinelibrary.wiley.com/doi/pdf/10.1002/macp.1961.020440129. URL: https://onlinelibrary.wiley.com/doi/abs/10.1002/macp.1961.020440129 (cit. on p. 53).

[154] Peterlin, A. 'Gradientenabhängigkeit der Viskositätszahl in nichtidealen Lösungsmitteln'. In: *Kolloid-Zeitschrift und Zeitschrift für Polymere* 182.1 (May 1962), pp. 110–115. ISSN: 1435-1536. DOI: 10.1007/BF01499747. URL: https://doi.org/10.1007/BF01499747 (cit. on p. 53).

[155] Chilcott, M. D. & Rallison, J. M. 'Creeping flow of dilute polymer solutions past cylinders and spheres'. In: *Journal of Non-Newtonian Fluid Mechanics* 29 (1988), pp. 381–432. ISSN: 0377-0257. DOI: https://doi.org/10.1016/0377-0257(88)85062-6. URL: http://www.sciencedirect.com/science/article/pii/0377025788850626 (cit. on p. 53).

[156] Moukalled, F., Mangani, L. & Darwish, M. *The Finite Volume Method in Computational Fluid Dynamics: An Advanced Introduction with OpenFOAM® and Matlab®*. Vol. 113. Oct. 2015, pp. XXIII, 791. ISBN: 978-3-319-16873-9. DOI: 10.1007/978-3-319-16874-6 (cit. on pp. 60, 63).

[157] Raw, M. 'Robustness of coupled Algebraic Multigrid for the Navier-Stokes equations'. In: *34th Aerospace Sciences Meeting and Exhibit*. American Institute of Aeronautics and Astronautics, Jan. 1996. doi: 10.2514/6.1996-297 (cit. on p. 61).

[158] Rhie, C. M. & Chow, W. L. 'Numerical study of the turbulent flow past an airfoil with trailing edge 09aration'. In: *AIAA Journal* 21.11 (1983), pp. 1525–1532. doi: 10.2514/3.8284. eprint: https://doi.org/10.2514/3.8284. url: https://doi.org/10.2514/3.8284 (cit. on pp. 61, 78, 105, 125, 173).

[159] Ladyzhenskaya, O. A. *The Mathematical Theory of Viscous Incompressible Flow*. Mathematics and its apllications. Gordon and Breach, 1969. url: https://books.google.co.uk/books?id=rKU8xgEACAAJ (cit. on p. 61).

[160] Comini, G., Croce, G. & Nobile, E. *Fondamenti di termofluidodinamica computazionale*. S.G.E., 2014. isbn: 8889884290 (cit. on p. 61).

[161] Issa, R. I. 'Solution of the implicitly discretised fluid flow equations by operator-splitting'. In: *Journal of Computational Physics* 62.1 (1986), pp. 40–65. issn: 0021-9991. doi: https://doi.org/10.1016/0021-9991(86)90099-9. url: https://www.sciencedirect.com/science/article/pii/0021999186900999 (cit. on p. 63).

[162] Holzmann, T. *Mathematics, numerics, derivations and OpenFOAM®*. Loeben, Germany: Holzmann CFD, 2016 (cit. on p. 63).

[163] Renardy, M. 'High Weissenberg Number Asymptotics and Corner Singularities in Viscoelastic Flows'. In: *IUTAM Symposium on Non-linear Singularities in Deformation and Flow*. Ed. by D. Durban & J. R. A. Pearson. Dordrecht: Springer Netherlands, 1999, pp. 13–20. isbn: 978-94-011-4736-1 (cit. on pp. 64, 93).

[164] Bonito, A., Clément, P. & Picasso, M. 'Viscoelastic Flows with Complex Free Surfaces: Numerical Analysis and Simulation'. In: *Numerical Methods for Non-Newtonian Fluids*. Ed. by R. Glowinski & J. Xu. Vol. 16. Handbook of Numerical Analysis. Elsevier, 2011, pp. 305–369. doi: https://doi.org/10.1016/B978-0-444-53047-9.00003-4. url: http://www.sciencedirect.com/science/article/pii/B9780444530479000034 (cit. on pp. 64, 93).

[165] Demir, H., Willianms, R. W. & Akyildiz, F. T. 'The Singularities Near the Corner of a Viscoelastic Fluid in a 2D Cavity'. In: *Mathematical and Computational Applications* 4.1 (1999), pp. 39–44. doi: 10.3390/mca4010039. url: https://www.mdpi.com/2297-8747/4/1/39 (cit. on pp. 64, 93).

[166] Siginer, D. *Stability of Non-Linear Constitutive Formulations for Viscoelastic Fluids*. SpringerBriefs in Applied Sciences and Technology, Jan. 2014. isbn: 978-3-319-02416-5. doi: 10.1007/978-3-319-02417-2 (cit. on pp. 64, 93).

[167] Owens, R. G. & Phillips, T. N. *Computational Rheology*. Imperial College Press, 2002. doi: 10.1142/p160. eprint: https://www.worldscientific.com/doi/pdf/10.1142/p160. url: https://www.worldscientific.com/doi/abs/10.1142/p160 (cit. on pp. 64, 93).

[168] Lappa, M. 'Thermally-Driven Flows in Polymeric Liquids'. In: *Reference Module in Materials Science and Materials Engineering*. Elsevier, Jan. 2020. isbn: 978-0-12-803581-8. url: https://www.sciencedirect.com/science/article/pii/B9780128203521000171 (cit. on pp. 64, 73, 165).

[169] Joseph, D. D. *Fluid Dynamics of Viscoelastic Liquids*. Springer New York, 1990. doi: 10.1007/978-1-4612-4462-2 (cit. on p. 64).

[170] Afonso, A. M., Pinho, F. T. & Alves, M. A. 'The kernel-conformation constitutive laws'. In: *Journal of Non-Newtonian Fluid Mechanics* 167-168 (2012), pp. 30–37. issn: 0377-0257. doi: https://doi.org/10.1016/j.jnnfm.2011.09.008. url: https://www.sciencedirect.com/science/article/pii/S0377025711002370 (cit. on p. 64).

[171] Guénette, R. & Fortin, M. 'A New Mixed Finite Element Method for Computing Viscoelastic Flows'. In: *Journal of Non-Newtonian Fluid Mechanics* 60 (Oct. 1995), pp. 27–52. doi: 10.1016/0377-0257(95)01372-3 (cit. on p. 64).

[172] Favero, J. L., Secchi, A. R., Cardozo, N. S. M. & Jasak, H. 'Viscoelastic flow analysis using the software OpenFOAM and differential constitutive equations'. In: *Journal of Non-Newtonian Fluid Mechanics* 165.23 (2010), pp. 1625–1636. issn: 0377-0257. doi: https://doi.org/10.1016/j.jnnfm.2010.08.010. url: http://www.sciencedirect.com/science/article/pii/S0377025710002417 (cit. on p. 64).

[173] Fattal, R. & Kupferman, R. 'Constitutive laws for the matrix-logarithm of the conformation tensor'. In: *Journal of Non-Newtonian Fluid Mechanics* 123.2 (2004), pp. 281–285. issn: 0377-0257. doi: https://doi.org/10.1016/j.jnnfm.2004.08.008. url: https://www.sciencedirect.com/science/article/pii/S0377025704002630 (cit. on p. 65).

[174] Pimenta, F. & Alves, M. A. 'Stabilization of an open-source finite-volume solver for viscoelastic fluid flows'. In: *Journal of Non-Newtonian Fluid Mechanics* 239 (2017), pp. 85–104. issn: 0377-0257. doi: https://doi.org/10.1016/j.jnnfm.2016.12.002. url: https://www.sciencedirect.com/science/article/pii/S0377025716303329 (cit. on pp. 66, 106, 174).

[175] Afonso, A. M., Oliveira, P. J., Pinho, F. T. & Alves, M. A. 'The log-conformation tensor approach in the finite-volume method framework'. In: *Journal of Non-Newtonian Fluid Mechanics* 157.1-2 (Mar. 2009), pp. 55–65. doi: 10.1016/j.jnnfm.2008.09.007 (cit. on p. 66).

[176] Palhares, I. L. J., Oishi, C. M., Afonso, A. M., Alves, M. A. & Pinho, F. T. 'Numerical study of the square-root conformation tensor formulation for confined and free-surface viscoelastic fluid flows'. In: *Advanced Modeling and Simulation in Engineering Sciences* 3.1 (Feb. 2016). doi: 10.1186/s40323-015-0054-4 (cit. on p. 66).

[177] Pimenta, F. & Alves, M. A. *rheoTool*. https://github.com/fppimenta/rheoTool. 2016 (cit. on p. 66).

[178] Chen, Q. S. & Hu, W. R. 'Influence of liquid bridge volume on instability of floating half zone convection'. In: *International Journal of Heat and Mass Transfer* 41.6 (1998), pp. 825–837. issn: 0017-9310. doi: https://doi.org/10.1016/S0017-9310(97)00183-X. url: https://www.sciencedirect.com/science/article/pii/S001793109700183X (cit. on pp. 66, 67).

[179] Kasperski, G., Batoul, A. & Labrosse, G. 'Up to the unsteadiness of axisymmetric thermocapillary flows in a laterally heated liquid bridge'. In: *Physics of Fluids* 12.1 (2000), pp. 103–119. doi: 10.1063/1.870286. eprint: https://doi.org/10.1063/1.870286. url: https://doi.org/10.1063/1.870286 (cit. on pp. 66, 67).

[180] Lappa, M. 'Well-posed problems for the Navier-Stokes equations in the microgravity environment'. In: *Microgravity and Space Station Utilization* 3 (Feb. 2002), pp. 51–62 (cit. on pp. 66, 67, 73).

[181] Lappa, M. *Fluids, Materials and Microgravity: Numerical Techniques and Insights into the Physics*. English. 1st ed. United Kingdom: Elsevier Science, Dec. 2004. isbn: 978-0-08-044508-3. doi: 10.1016/B978-0-08-044508-3.X5000-2 (cit. on pp. 68, 73).

[182] Wanschura, M., Kuhlmann, H. C. & Rath, H. J. 'Three-dimensional instability of axisymmetric buoyant convection in cylinders heated from below'. In: *Journal of Fluid Mechanics* 326 (Nov. 1996), pp. 399–415. doi: 10.1017/s0022112096008373 (cit. on pp. 68, 69).

[183] Boronska, K. & Tuckerman, L. S. 'Standing and travelling waves in cylindrical Rayleigh–Bénard convection'. In: *Journal of Fluid Mechanics* 559 (July 2006), p. 279. doi: 10.1017/s0022112006000309 (cit. on p. 69).

[184] Rocha, G. N., Poole, R. J., Alves, M. A. & Oliveira, P. J. 'On extensibility effects in the cross-slot flow bifurcation'. In: *Journal of Non-Newtonian Fluid Mechanics* 156.1-2 (Jan. 2009), pp. 58–69. doi: 10.1016/j.jnnfm.2008.06.008 (cit. on pp. 70, 71).

[185] Paulo, G. S., Oishi, C. M., Tomé, M. F., Alves, M. A. & Pinho, F. T. 'Numerical solution of the FENE-CR model in complex flows'. In: *Journal of Non-Newtonian Fluid Mechanics* 204 (Feb. 2014), pp. 50–61. doi: 10.1016/j.jnnfm.2013.11.003 (cit. on pp. 70, 71).

[186] Lappa, M. 'Patterning behavior of gravitationally modulated supercritical Marangoni flow in liquid layers'. In: *Phys. Rev. E* 93 (5 May 2016), p. 053107. doi: 10.1103/PhysRevE.93.053107. url: https://link.aps.org/doi/10.1103/PhysRevE.93.053107 (cit. on pp. 73, 74).

[187] Lappa, M., Savino, R. & Monti, R. 'Three-dimensional numerical simulation of Marangoni instabilities in liquid bridges: influence of geometrical aspect ratio'. In: *International Journal for Numerical Methods in Fluids* 36.1 (2001), pp. 53–90. doi: https://doi.org/10.1002/fld.120. eprint: https://onlinelibrary.wiley.com/doi/pdf/10.1002/fld.120. url: https://onlinelibrary.wiley.com/doi/abs/10.1002/fld.120 (cit. on p. 73).

[188] Lappa, M. 'On the gravitational suppression of hydrothermal modes in liquid layers with a blockage on the bottom wall'. In: *International Journal of Thermal Sciences* 145 (2019), p. 105987. issn: 1290-0729. doi: https://doi.org/10.1016/j.ijthermalsci.2019.105987. url: https://www.sciencedirect.com/science/article/pii/S1290072919305022 (cit. on p. 73).

[189] Crewdson, G. & Lappa, M. 'The Zoo of Modes of Convection in Liquids Vibrated along the Direction of the Temperature Gradient'. In: *Fluids* 6.1 (2021). issn: 2311-5521. doi: 10.3390/fluids6010030. url: https://www.mdpi.com/2311-5521/6/1/30 (cit. on pp. 75, 108, 116, 117, 130, 132).

[190] Crewdson, G. & Lappa, M. 'Spatial and temporal evolution of three-dimensional thermovibrational convection in a cubic cavity with various thermal boundary conditions'. In: *Physics of Fluids* 34.1 (2022), p. 014108. doi: 10.1063/5.0078270. eprint: https://doi.org/10.1063/5.0078270. url: https://doi.org/10.1063/5.0078270 (cit. on pp. 75, 116, 188).

[191] Lappa, M. 'Some considerations about the symmetry and evolution of chaotic Rayleigh–Bénard convection: The flywheel mechanism and the "wind" of turbulence'. In: *Comptes Rendus Mécanique* 339.9 (2011), pp. 563–572. issn: 1631-0721. doi: https://doi.org/10.1016/j.crme.2011.05.002. url: http://www.sciencedirect.com/science/article/pii/S1631072111000878 (cit. on p. 82).

[192] Oliveira, M. S. N., Oliveira, P. J., Pinho, F. T. & Alves, M. A. 'Effect of contraction ratio upon viscoelastic flow in contractions: The axisymmetric case'. In: *Journal of Non-Newtonian Fluid Mechanics* 147.1 (2007), pp. 92–108. issn: 0377-0257. doi: https://doi.org/10.1016/j.jnnfm.2007.07.009. url: http://www.sciencedirect.com/science/article/pii/S0377025707001656 (cit. on p. 89).

[193] Oliveira, P. J. & Pinho, F. T. 'Analytical solution for the fully developed channel flow of a Phan- Thien and Tanner fluid.' In: *Journal of Fluid Mechanics* 387 (May 1999), pp. 271–280. doi: 10.1017/S002211209900453X (cit. on p. 95).

[194] Oliveira, P. J. 'An exact solution for tube and slit flow of a FENE-P fluid'. In: *Acta Mechanica* 158.3 (Sept. 2002), pp. 157–167. issn: 1619-6937. doi: 10.1007/BF01176906. url: https://doi.org/10.1007/BF01176906 (cit. on p. 95).

[195] Oliveira, P. J. & Pinho, F. T. 'Some observations from analytical solutions of viscoelastic fluid motion in straight ducts'. In: *Proc. XIIIth International Congress on Rheology*. Vol. 2. Brit. Soc. Rheo. 2000, pp. 374–376 (cit. on p. 95).

[196] Paul, S., Wahi, P. & Verma, M. 'Bifurcations and chaos in large-Prandtl number Rayleigh–Bénard convection'. In: *International Journal of Non-Linear Mechanics* 46.5 (2011), pp. 772–781. issn: 0020-7462. doi: https://doi.org/10.1016/j.ijnonlinmec.2011.02.010. url: http://www.sciencedirect.com/science/article/pii/S0020746211000217 (cit. on p. 98).

[197] Kitano, M., Yabuzaki, T. & Ogawa, T. 'Symmetry-recovering crises of chaos in polarization-related optical bistability'. In: *Phys. Rev. A* 29 (3 Mar. 1984), pp. 1288–1296. doi: 10.1103/PhysRevA.29.1288. url: https://link.aps.org/doi/10.1103/PhysRevA.29.1288 (cit. on p. 98).

[198] Grebogi, C., Ott, E. & Yorke, J. A. 'Crises, sudden changes in chaotic attractors, and transient chaos'. In: *Physica D: Nonlinear Phenomena* 7.1 (1983), pp. 181–200. issn: 0167-2789. doi: https://doi.org/10.1016/0167-2789(83)90126-4. url: http://www.sciencedirect.com/science/article/pii/0167278983901264 (cit. on p. 98).

[199] Arnolf, V. I., Afraimovich, V. S., Il'yashenko, Y. & L.P., S. 'Dynamical Systems V: Bifurcation Theory and Catastrophe Theory'. In: Berlin, Heidelberg: Springer Berlin Heidelberg, 1994. isbn: 978-3-540-65379-0. doi: 10.1007/978-3-642-57884-7. url: https://doi.org/10.1007/978-3-642-57884-7 (cit. on p. 98).

[200] Li, D. X., Liu, W. & Hao, D. 'Vibration Antiresonance Design for a Spacecraft Multifunctional Structure'. In: *Shock and Vibration* 2017 (Aug. 2017), pp. 1–10. doi: 10.1155/2017/5905684 (cit. on pp. 99–101).

[201] Asir, M. P., Jeevarekha, A. & Philominathan, P. 'Multiple vibrational resonance and anti-resonance in a coupled anharmonic oscillator under monochromatic excitation'. In: *Pramana-J Phys* 93.3 (2019), p. 43. issn: 0973-7111. doi: 10.1007/s12043-019-1802-7. url: https://doi.org/10.1007/s12043-019-1802-7 (cit. on p. 100).

[202] Xie, Z., Shepard, W. & Woodbury, K. 'Design Optimization for Vibration Reduction of Viscoelastic Damped Structures Using Genetic Algorithms'. In: *Shock and Vibration* 16 (Jan. 2009), pp. 455–466. doi: 10.1155/2009/136913 (cit. on p. 101).

[203] Duarte, A. S. R., Miranda, A. I. . & Oliveira, P. J. 'Numerical and analytical modeling of unsteady viscoelastic flows: The start-up and pulsating test case problems'. In: *Journal of Non-Newtonian Fluid Mechanics* 154.2 (2008), pp. 153–169. issn: 0377-0257. doi: https://doi.org/10.1016/j.jnnfm.2008.04.009. url: http://www.sciencedirect.com/science/article/pii/S037702570800092X (cit. on p. 102).

[204] Zhang, M., Zhang, W., Wu, Z., Shen, Y., Wu, H., Cheng, J., Zhang, H., Li, F. & Cai, W. 'Modulation of viscoelastic fluid response to external body force'. In: *Scientific Reports* 9.1 (June 2019), p. 9402. issn: 2045-2322. doi: 10.1038/s41598-019-45612-2. url: https://doi.org/10.1038/s41598-019-45612-2 (cit. on p. 102).

[205] Zheng, X., Hagani, F., Boutaous, M., Knikker, R., Xin, S. & Siginer, D. A. 'Pattern selection in Rayleigh-Bénard convection with nonlinear viscoelastic fluids'. In: *Phys. Rev. Fluids* 7 (2 Feb. 2022), p. 023301. doi: 10.1103/PhysRevFluids.7.023301. url: https://link.aps.org/doi/10.1103/PhysRevFluids.7.023301 (cit. on p. 118).

[206] Borońska, K. & Tuckerman, L. S. 'Extreme multiplicity in cylindrical Rayleigh-Bénard convection. I. Time dependence and oscillations'. In: *Physical Review E* 81.3 (Mar. 2010), p. 036320. doi: 10.1103/physreve.81.036320 (cit. on p. 121).

[207] Rogers, J. L., Pesch, W., Brausch, O. & Schatz, M. F. 'Complex-ordered patterns in shaken convection'. In: *Phys. Rev. E* 71 (6 June 2005), p. 066214. doi: 10.1103/PhysRevE.71.066214. url: https://link.aps.org/doi/10.1103/PhysRevE.71.066214 (cit. on pp. 122, 143, 149, 151, 169).

[208] Rogers, J. L., Schatz, M. F., Brausch, O. & Pesch, W. 'Superlattice Patterns in Vertically Oscillated Rayleigh-Bénard Convection'. In: *Phys. Rev. Lett.* 85 (20 Nov. 2000), pp. 4281–4284. doi: 10.1103/PhysRevLett.85.4281. url: https://link.aps.org/doi/10.1103/PhysRevLett.85.4281 (cit. on pp. 143, 145, 149, 151, 169).

[209] Rogers, J. L., Schatz, M. F., Bougie, J. L. & Swift, J. B. 'Rayleigh-Bénard Convection in a Vertically Oscillated Fluid Layer'. In: *Phys. Rev. Lett.* 84 (1 Jan. 2000), pp. 87–90. doi: 10.1103/PhysRevLett.84.87. url: https://link.aps.org/doi/10.1103/PhysRevLett.84.87 (cit. on pp. 143, 149, 151, 169).

[210] Rogers, J. L., Pesch, W. & Schatz, M. F. 'Pattern formation in vertically oscillated convection'. In: *Nonlinearity* 16.1 (Dec. 2002), pp. C1–C10. doi: 10.1088/0951-7715/16/1/401. url: https://doi.org/10.1088/0951-7715/16/1/401 (cit. on pp. 143, 149, 151, 169).

[211] Clever, R. M. & Busse, F. H. 'Steady and oscillatory bimodal convection'. In: *Journal of Fluid Mechanics* 271 (1994), pp. 103–118. doi: 10.1017/S0022112094001709 (cit. on p. 145).

[212] Busse, F. H. 'The Sequence-of-Bifurcations Approach towards Understanding Turbulent Fluid Flow'. In: *Surveys in Geophysics* 24.3 (May 2003), pp. 269–288. ISSN: 1573-0956. DOI: 10.1023/A:1024860722683. URL: https://doi.org/10.1023/A:1024860722683 (cit. on p. 145).

[213] Morozov, A. & Spagnolie, S. E. 'Introduction to Complex Fluids'. In: *Complex Fluids in Biological Systems: Experiment, Theory, and Computation*. Ed. by S. E. Spagnolie. New York, NY: Springer New York, 2015, pp. 3–52. ISBN: 978-1-4939-2065-5. DOI: 10.1007/978-1-4939-2065-5_1. URL: https://doi.org/10.1007/978-1-4939-2065-5_1 (cit. on pp. 146, 167).

[214] Pismen, L. M. & Rubinstein, B. Y. 'Quasicrystalline and dynamic planforms in nonlinear optics'. In: *Chaos, Solitons and Fractals* 10.4 (1999), pp. 761–776 (cit. on p. 150).

[215] Lifshitz, R. 'Theory of color symmetry for periodic and quasiperiodic crystals'. In: *Rev. Mod. Phys.* 69 (4 Oct. 1997), pp. 1181–1218. DOI: 10.1103/RevModPhys.69.1181. URL: https://link.aps.org/doi/10.1103/RevModPhys.69.1181 (cit. on p. 151).

[216] Kang, Q., Wu, D., Duan, L., Hu, L., Wang, J., Zhang, P. & Hu, W. 'The effects of geometry and heating rate on thermocapillary convection in the liquid bridge'. In: *Journal of Fluid Mechanics* 881 (2019), pp. 951–982. DOI: 10.1017/jfm.2019.757 (cit. on p. 171).

[217] Shevtsova, V., Melnikov, D. E. & Nepomnyashchy, A. 'New Flow Regimes Generated by Mode Coupling in Buoyant-Thermocapillary Convection'. In: *Phys. Rev. Lett.* 102 (13 Apr. 2009), p. 134503. DOI: 10.1103/PhysRevLett.102.134503. URL: https://link.aps.org/doi/10.1103/PhysRevLett.102.134503 (cit. on p. 171).

[218] Lyubimova, T. P., Lyubimov, D. V. & Parshakova, Y. N. 'Implications of the Marangoni effect on the onset of Rayleigh–Benard convection in a two-layer system with a deformable interface'. In: *The European Physical Journal Special Topics* 224.2 (Mar. 2015), pp. 249–259. ISSN: 1951-6401. DOI: 10.1140/epjst/e2015-02357-3. URL: https://doi.org/10.1140/epjst/e2015-02357-3 (cit. on p. 171).

[219] Gaponenko, Y., Yasnou, V., Mialdun, A., Nepomnyashchy, A. & Shevtsova, V. 'Hydrothermal waves in a liquid bridge subjected to a gas stream along the interface'. In: *Journal of Fluid Mechanics* 908 (2021). A34, A34. ISSN: 0022-1120. DOI: 10.1017/jfm.2020.901. URL: https://doi.org/10.1017/jfm.2020.901 (cit. on p. 171).

[220] Lappa, M. & Ferialdi, H. 'On the oscillatory hydrodynamic instability of gravitational thermal flows of liquid metals in variable cross-section containers'. In: *Physics of Fluids* 29.6 (2017), p. 064106. DOI: 10.1063/1.4985197. eprint: https://doi.org/10.1063/1.4985197. URL: https://doi.org/10.1063/1.4985197 (cit. on pp. 191, 193).

[221] Lappa, M. & Ferialdi, H. 'Gravitational thermal flows of liquid metals in 3D variable cross-section containers: Transition from low-dimensional to high-dimensional chaos'. In: *Chaos: An Interdisciplinary Journal of Nonlinear Science* 28.9 (2018), p. 093114. doi: 10.1063/1.5040580. eprint: https://doi.org/10.1063/1.5040580. url: https://doi.org/10.1063/1.5040580 (cit. on pp. 191–193, 197).

[222] Kolmogorov, A. N. 'The local structure of turbulence in incompressible viscous fluid for very large Reynolds numbers'. In: *Dokl. Akad. Nauk SSSR* 30 (1941), pp. 299–303 (cit. on p. 197).

[223] Kolmogorov, A. N. 'Dissipation of energy in the locally isotropic turbulence'. In: *Dokl. Akad. Nauk SSSR* 32 (1941), pp. 19–21 (cit. on p. 197).

[224] Kraichnan, R. H. 'On Kolmogorov's inertial-range theories'. In: *Journal of Fluid Mechanics* 62.2 (1974), pp. 305–330. doi: 10.1017/S002211207400070X (cit. on p. 197).

[225] Larson, R. G., Shaqfeh, E. S. G. & Muller, S. J. 'A purely elastic instability in Taylor–Couette flow'. In: *Journal of Fluid Mechanics* 218 (1990), pp. 573–600. issn: 0022-1120. doi: 10.1017/S0022112090001124. url: https://doi.org/10.1017/S0022112090001124 (cit. on p. 197).

[226] Groisman, A. & Steinberg, V. 'Mechanism of elastic instability in Couette flow of polymer solutions: Experiment'. In: *Physics of Fluids* 10.10 (1998), pp. 2451–2463. doi: 10.1063/1.869764. eprint: https://doi.org/10.1063/1.869764. url: https://doi.org/10.1063/1.869764 (cit. on pp. 197, 198).

[227] Morozov, A. N. & Saarloos, W. van. 'Subcritical Finite-Amplitude Solutions for Plane Couette Flow of Viscoelastic Fluids'. In: *Phys. Rev. Lett.* 95 (2 July 2005), p. 024501. doi: 10.1103/PhysRevLett.95.024501. url: https://link.aps.org/doi/10.1103/PhysRevLett.95.024501 (cit. on p. 197).

[228] Lappa, M. 'On the Nature of Fluid-dynamics'. In: *Understanding the Nature of Science*. Ed. by P. L. Editor. Series: Science, Evolution and Creationism. Nova Science Publishers Inc, Apr. 2019. Chap. 1, pp. 1–64. isbn: 978-1-53616-016-1 (cit. on p. 197).

[229] Groisman, A. & Steinberg, V. 'Elastic turbulence in a polymer solution flow'. In: *Nature* 405.6782 (May 2000), pp. 53–55. issn: 1476-4687. doi: 10.1038/35011019. url: https://doi.org/10.1038/35011019 (cit. on p. 198).

[230] Fouxon, A. & Lebedev, V. 'Spectra of turbulence in dilute polymer solutions'. In: *Physics of Fluids* 15.7 (2003), pp. 2060–2072. doi: 10.1063/1.1577563. eprint: https://doi.org/10.1063/1.1577563. url: https://doi.org/10.1063/1.1577563 (cit. on p. 198).

[231] Steinberg, V. 'Scaling Relations in Elastic Turbulence'. In: *Phys. Rev. Lett.* 123 (23 Dec. 2019), p. 234501. doi: 10.1103/PhysRevLett.123.234501. url: https://link.aps.org/doi/10.1103/PhysRevLett.123.234501 (cit. on p. 198).

[232] Gupta, S., Chauhan, A. & Sasmal, A. 'Influence of elastic instability and elastic turbulence on mixed convection of viscoelastic fluids in a lid-driven cavity'. In: *International Journal of Heat and Mass Transfer* 186 (2022), p. 122469. issn: 0017-9310. doi: https://doi.org/10.1016/j.ijheatmasstransfer.2021.122469. url: https://www.sciencedirect.com/science/article/pii/S0017931021015672 (cit. on p. 198).

[233] Samanta, D., Dubief, Y., Holzner, M., Schäfer, C., Morozov, A. N., Wagner, C. & Hof, B. 'Elasto-inertial turbulence'. In: *Proceedings of the National Academy of Sciences* 110.26 (2013), pp. 10557–10562. doi: 10.1073/pnas.1219666110. eprint: https://www.pnas.org/doi/pdf/10.1073/pnas.1219666110. url: https://www.pnas.org/doi/abs/10.1073/pnas.1219666110 (cit. on p. 198).

[234] Dubief, Y., Terrapon, V. E. & Soria, J. 'On the mechanism of elasto-inertial turbulence'. In: *Physics of Fluids* 25.11 (2013), p. 110817. doi: 10.1063/1.4820142. eprint: https://doi.org/10.1063/1.4820142. url: https://doi.org/10.1063/1.4820142 (cit. on p. 198).

[235] Shekar, A., McMullen, R. M., McKeon, B. J. & Graham, M. D. 'Self-sustained elastoinertial Tollmien–Schlichting waves'. In: *Journal of Fluid Mechanics* 897 (2020), A3. doi: 10.1017/jfm.2020.372 (cit. on p. 198).

[236] Zhang, W. H., Shao, Q. Q., Li, Y. K., Ma, Y., Zhang, H. N. & Li, F. C. 'On the mechanisms of sheet-like extension structures formation and self-sustaining process in elasto-inertial turbulence'. In: *Physics of Fluids* 33.8 (2021), p. 085107. doi: 10.1063/5.0057181. eprint: https://doi.org/10.1063/5.0057181. url: https://doi.org/10.1063/5.0057181 (cit. on p. 198).

[237] Hiller, W., Koch, S. & Kowalewski, T. 'Three-dimensional structures in laminar natural convection in a cubic enclosure'. In: *Experimental Thermal and Fluid Science* 2.1 (1989), pp. 34–44. issn: 0894-1777. doi: https://doi.org/10.1016/0894-1777(89)90047-2. url: http://www.sciencedirect.com/science/article/pii/0894177789900472 (cit. on p. 202).

[238] Schladow, S. G., Patterson, J. C. & Street, R. L. 'Transient flow in a side-heated cavity at high Rayleigh number: a numerical study'. In: *Journal of Fluid Mechanics* 200 (1989), pp. 121–148. issn: 0022-1120. doi: 10.1017/S0022112089000595. url: https://doi.org/10.1017/S0022112089000595 (cit. on p. 202).

[239] Kowalewski, T. A. 'Experimental validation of numerical codes in thermally driven flows'. In: *Advances in Computational Heat Transfer. Proceedings of the International Symposium*. Begel House Inc. 1997. doi: 10.1615/ICHMT.1997.IntSymLiqTwoPhaseFlowTranspPhenCHT.20 (cit. on p. 202).

[240] Melnikov, D. E. & Shevtsova, V. M. 'Liquid Particles Tracing in Three-dimensional Buoyancy-driven Flows'. In: *Fluid Dynamics & Materials Processing* 1.2 (2005), pp. 189–200. ISSN: 1555-2578. DOI: 10.3970/fdmp.2005.001.189. URL: http://www.techscience.com/fdmp/v1n2/24205 (cit. on p. 202).

[241] Lappa, M. & Burel, T. 'Symmetry breaking phenomena in thermovibrationally driven particle accumulation structures'. In: *Physics of Fluids* 32.5 (2020), p. 053314. DOI: 10.1063/5.0007472. eprint: https://doi.org/10.1063/5.0007472. URL: https://doi.org/10.1063/5.0007472 (cit. on p. 205).

[242] Kuhlmann, H. C., Lappa, M., Melnikov, D., Mukin, R., Muldoon, F. H., Pushkin, D., Shevtsova, V. & Ueno, I. 'The JEREMI-Project on Thermocapillary Convection in Liquid Bridges. Part A: Overview of Particle Accumulation Structures'. In: *Fluid Dynamics Materials Processing* 10.1 (2014), pp. 1–10. DOI: 10.3970/fdmp.2014.010.001. URL: http://www.techscience.com/fdmp/v10n1/24552 (cit. on p. 205).

[243] Capobianchi, P. & Lappa, M. 'Particle accumulation structures in noncylindrical liquid bridges under microgravity conditions'. In: *Physical Review Fluids* 5.8 (Aug. 2020), p. 084304. DOI: 10.1103/physrevfluids.5.084304 (cit. on p. 205).

[244] Capobianchi, P. & Lappa, M. 'Particle Accumulation Structures in a 5 cSt Silicone Oil Liquid Bridge: New Data for the Preparation of the JEREMI Experiment'. In: *Microgravity Science and Technology* 33.2 (Apr. 2021). DOI: 10.1007/s12217-021-09879-3 (cit. on p. 205).

[245] Lappa, M. 'On the Propagation of Hydrothermal Waves in a Fluid Layer with Two-Way Coupled Dispersed Solid Particles'. In: *Fluids* 7.7 (June 2022), p. 215. DOI: 10.3390/fluids7070215 (cit. on p. 205).

[246] Fernandes, C., Faroughi, S., Carneiro, O., Nóbrega, J. M. & McKinley, G. 'Fully-resolved simulations of particle-laden viscoelastic fluids using an immersed boundary method'. In: *Journal of Non-Newtonian Fluid Mechanics* 266 (Apr. 2019), pp. 80–94. DOI: 10.1016/j.jnnfm.2019.02.007 (cit. on p. 205).

[247] Shevtsova, V., Lyubimova, T. P., Saghir, Z., Melnikov, D., Gaponenko, Y., Sechenyh, V., Legros, J. C. & Mialdun, A. 'IVIDIL: on-board g-jitters and diffusion controlled phenomena'. In: *Journal of Physics: Conference Series* 327 (Dec. 2011), p. 012031. DOI: 10.1088/1742-6596/327/1/012031. URL: https://doi.org/10.1088/1742-6596/327/1/012031 (cit. on p. 206).

[248] Shevtsova, V., Mialdun, A., Melnikov, D., Ryzhkov, I., Gaponenko, Y., Saghir, Z., Lyubimova, T. & Legros, J. C. 'The IVIDIL experiment onboard the ISS: Thermodiffusion in the presence of controlled vibrations'. In: *Comptes Rendus Mécanique* 339.5 (May 2011),

pp. 310–317. ISSN: 1631-0721. URL: https://www.sciencedirect.com/science/article/pii/S1631072111000350 (cit. on p. 206).